NORTHWESTERN UNIVERSITY

Computational Design and Analysis of High Strength Austenitic TRIP Steels for Blast Protection Applications

A DISSERTATION

SUBMITTED TO THE GRADUATE SCHOOL
IN PARTIAL FULFILLMENT OF THE REQUIREMENTS

for the degree

DOCTOR OF PHILOSOPHY

Field of Materials Science and Engineering

By

Padmanava Sadhukhan

EVANSTON, ILLINOIS

December 2008

This research is dedicated to my parents

Smt. Prakriti Sadhukhan (Mother)

&

Shri. Dev Kumar Sadhukhan (Father)

Mom and Dad, your love and warmth in raising and educating me is the sole reason I am who I am …

"Life seldom gives what you want,
But then, you have to fight for it!"

"The most exciting phrase to hear in science, the one that heralds new discoveries, is not 'Eureka!' but 'that's funny...' ..."

-Isaac Asimov

ABSTRACT

Computational Design and Analysis of High Strength Austenitic TRIP Steels for Blast-Protection Applications

Padmanava Sadhukhan

Recent assessment of material property requirements for blast resistant applications, especially for the naval ship hulls, has defined the need to design steels with high stretch ductility and fragment penetration resistance, along with high strength and adequate toughness. Using a system based computational materials design approach, two series of austenitic (γ) steels have been designed – ***BA120*** to exhibit high uniform ductility in tension (>20%) and ***SA120*** to exhibit high tensile (>20%) and shear strains (>50%), with both alloys maintaining high levels of yield strength (120 ksi/827 MPa) at room temperature under Tensile and Shear stress states. BA120 is low chromium (4 wt %) high nickel (23.5 wt %) alloy while the SA120 is a high chromium design (10 wt %), both designed for non-magnetic behavior.

The Thermo-Calc computational thermodynamics software in conjunction with a Ni-DATA 7 thermodynamic database has been used to model precipitation strengthening of the alloy, by quantifying the dependence of yield stress of austenitic steels on the mole fraction of the precipitated γ' (Gamma Prime) Ni_3(Ti, Al) phase. The required high strength has been achieved by the precipitation of spheroidal intermetallic γ' – phase of optimum diameter (15 nm) in equilibrium with the matrix at the standard aging temperature. Adequate Al and Ti with respect

to the Ni in the matrix ensure enough γ' phase fraction and number density of precipitates to provide the necessary strength. The predicted **γ'** precipitation strengthening to 120-130 ksi for both BA120 and SA120 has been validated through both microhardness as well as static and dynamic tensile and shear tests conducted at room temperature. 3-D LEAP analysis of the aged specimens has shown the expected size and distribution of γ' – precipitates with good compositional accuracy of predicted values from the thermodynamic models, for both matrix austenite and γ'.

Metastable austenitic steels have been known to exhibit high uniform elongation, tensile strength under static and dynamic loads, and high fracture toughness due to mechanically induced martensitic transformation. The phenomenon of Transformation-Induced Plasticity (***TRIP***) arising from the FCC → BCC martensitic transformation has been used to create theoretical parametric models of matrix stability, flow stabilization and fragment resistance under tension and shear loads which were then applied to obtain significant improvements in uniform ductility for both stress states. These stability models have then been calibrated through experimental data from static and dynamic/adiabatic tensile tests and characteristic $\boldsymbol{M_S^{\sigma}}$ temperature measurements from an earlier TRIP prototype to support the new alloy designs. BA120 and SA120 alloys are designed to undergo stress-assisted martensite transformation at a pre-determined critical temperature ($\boldsymbol{M_S^{\sigma}}$) thereby optimizing transformation plasticity to achieve the desired performance improvements.

The new prototype alloy BA120 has demonstrated improved mechanical properties with a high strength of 124 ksi (845 MPa) and ~ 150 ksi (1040 MPa) under static and dynamic tensile loading at room temperature. The measured uniform ductility for BA120 under quasi-static

tensile loading is 21% at room temperature with high strain hardening leading to UTS of 246 ksi (1696 MPa). The UTS under dynamic loading is ~ 195 ksi (1344 MPa). The uniform ductility is consistent (21% - 24%) over a wide range of temperature (25^{o}C – 65^{o}C). Mechanical testing demonstrates the required M_S^{σ} temperature, and 3-D LEAP microanalysis confirms the predicted matrix composition as well as the particle size and distribution of strengthening precipitates. FSI simulation experiments conducted on BA120 to analyze the material behavior under actual blast loading have shown promising results in terms of strains exceeding 40%. A prescribed simple heat treatment process comprising of solutionizing treatment at 950^{o}C for 1 hour followed by a single-step temper at 750^{o}C for 10 hr has achieved the desired performance goals of strength and uniform ductility.

Principal Advisor: Professor Gregory B. Olson June *13th, 2008*

Department of Materials Science and Engineering

Northwestern University, Evanston, IL, 60208, USA

ACKNOWLEDGEMENTS

Throughout my journey of successfully completing the doctoral degree program at the *Department of Materials Science and Engineering* at Northwestern University, I have come across people who have not only helped me with my thesis research and experiments, but have also made the three and half years I have spent extremely memorable. It is with a sincere and heartfelt sense of gratitude that I express my thanks to all those who have made the past few years of my life so special. When I look back, I believe I could not have survived the stresses involved in a PhD research without the support of people who have been, directly or indirectly, involved.

Professor Greg Olson, you have been a wonderful advisor and a fabulous teacher. Coming to Northwestern, I had only a faint idea what field of research would really interest me. I still remember speaking to you the first day at NU at the student-faculty meetings and I knew there itself you were my first choice. I have never seen you without a cheerful attitude and a sense of humor. Every instance I have interacted with you, from the simple explanations of complicated design models to every kind of paperwork, you have always been kind, understanding and encouraging. Your infinite knowledge, vast experience, friendly nature and always having a positive outlook makes me proud to be associated with you, and to be known as your student. I will always cherish the moment you saw the first tensile results of BA120 and shook my hands. Selecting you as my advisor and working with you has undoubtedly been the best decision I have made in the past 4 years. I thank you from the bottom of my heart for being the wonderful teacher and person you truly are. I wish you and your family good health and success forever.

My Parents, my Mom and my Dad, you are the two pillars of strength in my life. You have been the constant source of inspiration throughout. Every moment of my life is filled with gratitude, love, affection and respect for what you have brought in my life. Whenever I feel happy or a little sad, you somehow get to know without my having to say and you have always been there for me every step guiding me through myriad expectations, stresses and challenges that life throws upon us. You have taught me everything I know as a person, and every success I have achieved so far in my life, you are the primary reason behind them.

My doctoral thesis committee members, *Professor David Dunand, Professor Horacio Espinosa and Professor Morris Fine*; Thank you for agreeing to be my committee and providing your thoughtful insights and suggestions for the betterment of this research. My thanks to Professor Fine for agreeing to be on my committee on such a short notice. Professor Espinosa: for helpful discussions on Blast structures and dynamic testing. My sincerest thanks to *Professor David Seidman* for being on my original committee and providing inputs during my Candidacy Exam. I am much grateful for your suggestions throughout for LEAP usage.

My thanks to the *Department of Materials Science and Engineering, at Northwestern University* for accepting me as a graduate student in their highly revered and coveted PhD program and awarding me the Walter P. Murphy fellowship: being one of the first international students to receive the honor.

My sincerest thanks to *Professor Seshadri Seetharaman*, Chairman, Department of Metallurgy, KTH (Royal Institute of Technology, Stockholm, Sweden). You opened my eyes to the world of research in Material Science. My research internship at KTH at the end of my junior year was one of the most exciting phases of my life, being exposed to research at a high level in a new environment and believing in myself to be capable of a career in scientific design and exploration. The confidence I received from working under your tutelage was the decisive factor in my opting for the challenging quest for PhD degree.

My *alma-mater, Indian Institute of Technology (IIT), Roorkee*: Being selected to the Indian Institute of Technology (IIT) was the happiest moment of my life. All the recognition I have as an engineer, is mostly because of my being an *IIT'ian* and I will always be proud of it. I thank my teachers and professors at IIT as well as my school (BHS, Calcutta) where I learnt the value of education, science and technology.

My thanks to *Professor Kathleen Stair*: for helping me out with metlab processes.

My sincerest thanks to *Dr. Mike Johnson* and *Don Sherman* at Advanced Materials Technology group and *Karen Huber* and *Kalyana Bhamidi* at Advanced Structures group, in Caterpillar for giving me the opportunity of interning in their groups and learning about new manufacturing techniques. Don: thank you for your support and inputs on the carbide precipitation study. I look forward to collaborating with you on a research publication in this topic. My appreciation and thanks to *Dr. Raj Naik* for his valuable mentorship at the '*Insight Engineering and Science, 2007*' event hosted by Mckinsey & Company.

Members of Questek LLC: *Chris Kern, Jason Sebastian, Abhijit Misra and Dr. Jou* for being so helpful and friendly whenever I was there at the Questek office running innumerable Thermo-calc and CMD simulations. Chris: thank you for answering all those questions about TC and CMD and also with the ordering process of the new alloys. Jason: thank you for teaching me so many cool stuff about the LEAP Atom probe and the envelope program.

Dr. Sungsoo Lee's assistance in the initial dynamic testing initiative of earlier prototype specimens is greatly appreciated. *Lapo Mori and Dr. Felix Latourte* from Professor Espinosa's research group have contributed a lot in testing my new alloy designs using their FEM and ABAQUS simulations for dynamic tension and torsion specimens. My collaboration with Lapo and Dr. Latourte, especially in the last two months, has been critical to studying the performance of the new alloys. I thank them for their efforts. I wish Lapo the very best for his Doctoral thesis.

Thang Bui, Jim, Jeff and Jeffrey Sundvall in the Instrument Shop: I owe so much to you for providing me with all the samples I needed throughout my graduate studies, especially in the last few months before my PhD defense. My thanks to *Mark Seniw* for all the help for my tensile tests on the MTS machine in the mechanics lab. Thanks to *Rick Kraemer* in the SRG lab, for helping me with all the vacuum heat treatments in the induction furnace.

My sincerest thanks to *Dr. Dieter Isheim* for many valuable inputs towards operating 3D – LEAP effectively for the best results. Thanks to *Richard Karnesky* and *Mike Mulholland* in the Seidman Research group for providing critical inputs for Laser LEAP operation.

I have had the privilege to lead and work with so many talented and enthusiastic group of undergraduate design teams during my graduate work at NU. My interactions with these teams have not only helped me get valuable insight to how different people approach engineering problems, but also understand and learn newer techniques of design. My appreciation goes out to the MSE 390, IDEA 298/398 and Civil Shield/BlastTruss teams of 2005 – 2008.

My thanks to *Peggy Adamson, Farrin Abott and staff* in the MSE office. You always made all the administrative paperwork so easy.

During my stay in Evanston, I have been fortunate to be able to make so many great friends. I carry many fond memories of all the good times. From adventure road trips to game nights, music jam sessions to Opera and Theatre trips, all-night hangouts on the lakeshore to the Holy '*Bhagwad Gita*' sessions every weekend; every moment has been special. Thank you for being my friends.

Some of my finest moments at Northwestern came from my being a member of the Northwestern Table Tennis Team. My thanks to NUTT group: *Tariff, Bobby, Lim and Yuan*, you guys have been awesome. I will always remember our first trip to the U.S Nationals tournament in Rochestor. The NUTT leadership is in good hands, and I wish you the very best in life.

Finally, my thanks to the past and present members of the SRG for being such a fantastic group of people to interact with. *David Bryan and Abhijit Misra*: for introducing me to the group culture. *Michele:* Congratulations on your faculty position at Florida, my best wishes to you in shaping the future of materials design; *Ben Tiemens and Yana Qian*: you were always so kind and helpful. I loved sharing the office with you and playing 'basketball hoops'. I miss the free-throw shooting contests with Ben and David. Ben: thank you for introducing me to the Atom Probe and helping me out initially. My best wishes to you and Aleta. Yana: for your valuable inputs during X-ray diffraction measurements and sharing so many idle talks in the office. My congratulations to *Matt Bender* on his successful doctoral defense, I wish you and Erin the very best in life. *Les*, my good wishes to you on your thesis defense and a successful career ahead. *Jamie*: good luck with your research. *Dennis:* your expertise in TC and computational modeling are a boon to the group. *Stephanie*, congratulations on your NSF fellowship; you have a very bright future ahead and I want to see you become very successful in everything you do. I really enjoyed the myriad discussions we have had on so many topics, which I am going to miss for sure. Good luck with your research. *Zack, Tengfei and Ryan*: hope you all had a great first year. Zack, my alloys are now in your hands. Ryan, it was great working with you on 390. Don't let your injury stop you from being the next Mat. Sci. soccer legend. Tengfei, best wishes for your successful research.

TABLE OF CONTENTS

LIST OF FIGURES

Figure 4.2.1.1 Austenite matrix grains of solutionized EX425 specimen as seen using an inverted optical microscope at a) 100X and b) 400X magnification. Etchant used is 2% Nital.

Figure 4.2.2.1 X-Ray diffraction intensity per scanning angle showing observed Austenite {220} peaks in solution treated EX425 specimen

Figure 4.2.3.1 (a) 3-D Reconstruction of a fully austenized EX425 [70nm X 80 nm X 30 nm]

Figure 4.2.3.1 (b) Clipped 3D - LEAP image of the fully austenized EX425 specimen as observed along the z-axis vertically. The figure shows a cylindrical bin with a diameter of 20 nm used to encapsulate an equal volume of ions for generation of 1-D composition profile [70nm X 80 nm X 30 nm]

Figure 4.2.3.1 1-D Composition profile of major elements for figure 4.2.3.1 (b) measured using 3-D LEAP Tomography. The length of 30 nm is for analysis along z-axis.

Figure 4.3.1.1 Temperature dependence of the mole fraction of gamma prime precipitate phase in equilibrium with matrix FCC austenite for EX425

Figure 4.3.2.1.1 (a) Pulsed laser 3D- LEAP reconstructed images for an EX425 specimen aged at 700^{o}C for 60 hours with **γ' –** precipitates shown in red iso-concentration surfaces and (b) a cylindrical analysis area to calculate 1D profile [10 Million ions analyzed] [70 nm X 60 nm X 40 nm]

Figure 4.3.2.1.2 (a) 1D Composition Profile of EX425 aged at 700^{o}C for 60 hr **(b)** Proxigram analysis of all TiNi interfaces (red) shown in figure 4.3.2.1.1 (b)

Figure 4.3.2.1.3 (a) Pulsed Laser LEAP image of an EX425 aged at 736oC for 16.25 hours showing TiNi iso-surfaces in red for **γ' –** precipitates and green Ni ions in matrix **[**14 M ions**]** [60nm X 60nm X 40nm], and (b) Voltage LEAP image [8 M ions] [80nm X 70nm X 30nm]

Figure 4.3.2.1.4 (a) 1D Composition Profile of EX425 aged at 736^{o}C for 16.25 hr **(b)** Proxigram analysis of all TiNi interfaces shown in figure 4.3.2.1.3(a)

Figure 4.3.2.1.5 (a) Laser LEAP image of EX425 aged at 750^{o}C for 10 hours showing TiNi iso-surfaces in red for **γ' –** precipitates and green Ni ions in matrix **[**25 M ions**]** [70nm X 70nm X 80nm], and **(b)** Voltage LEAP image of red Ti ions and blue matrix Fe ions [10 M ions] [80nm X 80nm X 35nm]

Figure 4.3.2.1.6 (a) 1D Composition Profile of EX425 aged at 750^{o}C for 10 hr **(b)** Proxigram analysis of all TiNi interfaces (red) shown in figure 4.3.2.1.5 (a)

Figure 4.3.2.1.7 Voltage LEAP image of EX425 aged at 800^{o}C for 10 hours showing (**a)** formation of **η –** precipitate plates/bands **[**45 M ions**]** [60nm X 60nm X 250nm] **(b)** Ti Ni Iso-

surfaces shown in yellow along with a cylindrical 1D profile surface, with Fe and Ti ions of matrix

Figure 4.3.2.1.8 1D Composition Profile of EX425 aged at 800^{o}C for 10 hr showing the thickness of the two Eta precipitates seen in figure 4.3.2.1.7

Figure 4.3.2.1.9 (a) Laser LEAP image of EX425 aged at 750^{o}C (10 hr) + 700^{o}C (20 hr) + 650^{o}C for 25 hours showing TiNi iso-surfaces in red for **γ' –** precipitates and blue Fe ions in matrix [25 M ions**]** [70nm X 70nm X 80nm], and **(b)** Voltage LEAP image of red Ti ions and blue matrix Fe ions [10 M ions] [80nm X 80nm X 35nm]

Figure 4.3.2.1.10 (a) 1D Composition Profile of EX425 aged at 650^{o}C for 25 hr **(b)** Proxigram analysis of all TiNi interfaces (red) shown in figure 4.3.2.1.9 (a)

Figure 4.3.2.1.11 (a) 1D Composition Profile of EX425 aged at 800^{o}C (10hr) – 720^{o}C (30hr) – 641^{o}C (100hr) **(b)** 1D Composition Profile related to figure in (a)

Figure 4.3.2.1.11 Determination of optimum precipitate diameter using normalized stress function with respect to measured gamma prime phase function. This is based on strengthening model of single and double dislocation cutting in section 2.4, figure 2.4.2

Figure 4.4.1 Variation of surface Vicker's microhardness with aging time for EX425 specimens aged at 700^{o}C

Figure 4.4.2 Variation of Vickers microhardness with aging time for EX425 aged at **a)** 800^{o}C and **b)** 800^{o}C (10 hours) + 720^{o}C. The arrow marks the aging time selected for that temperature

Figure 4.4.3 Variation of Vickers microhardness with aging time for EX425 aged at **a)** 800^{o}C (10) + 720^{o}C (30) + 680^{o}C and **b)** 800^{o}C (10) + 720^{o}C (60) + 680^{o}C

Figure 4.5.1.1 Comparison of static uniaxial tensile tests for EX425 specimens aged at 736^{o}C for 16.25 hours. The test temperature is indicated in bold across each curve. The solid curves indicate the elastic range and the dotted lines show the plastic strain till the point of fracture, thereby indicating final fracture strain

Figure 4.5.1.2 Comparison of static uniaxial tensile tests for EX425 specimens aged at 736^{o}C for 16.25 hours.

Figure 4.5.1.3 Comparison of static uniaxial tensile tests for EX425 specimens aged at 736^{o}C for 16.25 hours.

Figure 4.5.2.1 Comparison of static uniaxial tensile tests and dynamic Kolsky tensile test for EX425 specimens aged at 736^{o}C for 16.25 hours and BA160 aged at 550^{o}C for 30 minutes + 450^{o}C for 5 hours.

Figure 6.1.4 As-received ingot of SA-120 showing incipient melting and wide-cracks

Figure 6.3.1.1 Comparison of the measured surface microhardness for 'as-received' and solution treated specimens of BA120, SA120 and EX425 to compare the relative internal stress build up during forging/rolling in new alloys

Figure 6.3.1.2 Aging time dependence of surface Vickers Microhardness of for BA120 and SA120 specimens solution treated at 950^{o}C for 1 hr and then aged at 750^{o}C

Figure 6.3.2.1 Optical microscopy of solution treated fully austenitic microstructure of BA120 using a) light etching with 2% Nital showing austenite grain boundaries and b) etching with 10% Nital to show formation of twinned austenite grains

Figure 6.3.2.2 Optical microscopy of solution treated fully austenitic microstructure of SA120 using light etching with 2% Nital showing austenite grain boundaries a) magnification of 25X and b) magnification of 100X

Figure 6.4.1.1 3-D LEAP reconstructed image of the distribution of Gamma Prime γ' precipitates (Red) within the austenite matrix for BA120. The γ' precipitates are separated from the matrix by an iso-concentration surface defined by a 50% TiNi concentration boundary. **[**40 M ions**]** [80nm X 80nm X 70nm]

Figure 6.4.1.2 (a) A 2D view of the Gamma Prime γ' precipitates (Red) within the austenite matrix as viewed along the Z-axis for BA120

Figure 6.4.1.2 (b) live image recorded during actual LEAP run showing the Detector Ion map. The evaporation of ions from the Gamma Prime γ' precipitates (pink) within the Blue Fe ions of austenite matrix is clearly demonstrated

Figure 6.4.1.3 Proxigram analysis of BA120 for all TiNi interfaces shown in figure 6.4.1.1

Figure 6.4.1.4 Comparison of the effectiveness of Envelope method in separating clusters matching the original iso-concentration surfaces: **a)** 3D reconstructed image from LEAP for isolated 50% TiNi iso-concentration surfaces from figure 6.4.1.1 **b)** Reconstructed Clusters of Ti with separation distance of 50 using the Envelope Program

Figure 6.4.1.5 3-D LEAP reconstructed image of the distribution of Gamma Prime γ' precipitates (Red) within the austenite matrix for SA120. The γ' precipitates are separated from the matrix by an iso-concentration surface defined by a 50% TiNi concentration boundary. **[**28 M ions**]** [70nm X 70nm X 70nm]

Figure 6.4.1.6 A 3D view of the Gamma Prime γ' precipitates (Red) within the austenite matrix as viewed along the Z-axis [25 M ions], and **(b)** live image recorded during actual LEAP run showing the Detector Ion map. The evaporation of ions from the Gamma Prime γ' precipitates (pink) within the Blue Fe ions of austenite matrix is clearly demonstrated

Figure 6.4.1.7 Proxigram analysis of SA120 for all TiNi interfaces shown in figure 6.4.1.5

Figure 6.4.1.8 Observed Mass Spectrum for BA120 using Laser mode for 3D-LEAP run at 60K and using 500 Pulse rate and 0.6nJ of Pulse energy for the laser beam

Figure 6.5.1.1 Comparison of True Stress-Strain static uniaxial tensile tests for BA120 specimens aged at 750^{o}C for 10 hours. The test temperature is indicated in bold across each curve. The solid curves indicate the elastic range and the dotted lines show the plastic strain till the point of fracture, thereby indicating final fracture strain

Figure 6.5.1.2 Comparison of Engg. Stress-strain static uniaxial tensile tests for BA120 specimens aged at 750^{o}C for 10 hours. The test temperature is indicated in bold across each curve

Figure 6.5.1.3 Comparison of True Stress-strain static uniaxial tensile tests at room temperature for BA120 and EX425 specimens of comparative Yield Stress

Figure 6.5.1.4 Comparison of observed transformed martensite in BA120 fractured quasi-static tensile specimens aged at 750^{o}C for 10hours and tested at (a) 25^{o}C and (b) – 5^{o}C. The darker regions represent the transformed martensite. Etchant used: 0.5 gm of Sodium Metabisulfite, 33 cc HCL and 167 cc H_2O [166]

Figure 6.5.2.1 Stress Strain plot for the determination of M_s^{σ} temperature for BA120 using Richman and Bolling's method of loading and unloading stress cycles at successively decreasing temperatures. The peak yield stress is the measure of the M_s^{σ} temperature

Figure 6.5.2.2 Temperature dependence of Yield Stress for BA120 from the Iso-thermal tensile tests data. Linear trends to the data points if fitted and the intercept is taken as the M_s^{σ} temperature

Figure 6.5.2.3 Stress Strain plot for the determination of M_s^{σ} temperature for BA120 using Richman and Bolling's method of loading and unloading stress cycles at successively decreasing temperatures.

Figure 6.5.2.4 Temperature dependence of Yield Stress for BA120 from the Iso-thermal tensile tests data to determine the M_s^{σ} temperature

Figure 6.5.3.1 Comparison of the modified Austenite Stability Parameter model for Tension and Shear stress states with the earlier model. The new model is shown in red (Tension) and Brown (Shear). The black solid points represent the calculated ASP values for BA120 and SA120 from the measured M_s^{σ} temperatures of 36^{o}C and 21^{o}C, respectively

Figure 6.5.4.1 Comparison of True Stress-strain curves for Dynamic tensile and Torsion/Shear tests for BA120 and HSLA100 at room temperature [160]

Figure 6.5.4.2 SEM Micrographs of the fractured end of dynamic tensile test specimens for BA120 [160]

Figure 6.5.4.3 Comparison of observed transformed martensite in fractured BA120 dynamic-static tensile specimens aged at 750^{o}C for 10hours and tested at room temperature using a strain rate of (a) 1017 s^{-1} (b) 500 s^{-1}. The darker regions represent the transformed martensite. Etchant used: 0.5 gm of Sodium Metabisulfite, 33 cc HCL and 167 cc H_2O [166]

Figure 6.5.4.4 Dynamic Torsion/Shear BA120 test specimen with marked grid-lines in the inner wall as shown before and after the test [160]

Figure 6.5.4.5 SEM Micrographs of the fractured face of the BA120 Shear specimens [160]

Figure 6.5.5.1 Deflection profiles obtained for BA120 post FSI-ballistic tests on subsequent impulses a) showing deflection profile post 1st impulse and b) deflection profile post second impulse. The lowermost figure shows the combined effect of the impulses, with the calculated difference in impulses [160]

LIST OF TABLES

CHAPTER 1: INTRODUCTION

The constant search and ever-increasing need for improved mechanical properties has defined materials design over centuries, be it steels, polymers, ceramics or any other class of materials. The advancement in new systems-based design methodology which accelerates the total product development life-cycle while achieving new levels of product reliability has led to rapid innovations in steel technology and design. In an effort to create materials with maximum durability for varied applications ranging from Hull steels for Naval warships, aircraft landing gears to high performance engines, most of recent steel research initiatives have mainly focused on achieving extremely high strength or toughness or combinations of both accompanied with good weldability and corrosion resistance. However, in the wake of current needs of the Navy in specific where high blast impulse resistance coupled with fragmentation/shear resistance is desired for any new alloy design, it has been recognized that an ideal performance criterion in addition to high strength would be to have high uniform ductility under both tension and shear loads.

1.1 MOTIVATION

With the increase in terrorist activity in the past ten years, there has been a fervent search for new ways to protect innocents from harm. The September 11^{th} terrorist attacks against the U.S. resulted in a sustained and amplified civilian awareness of the increasing threat of terrorism across the globe. In a 2002 US census report, 66 out of the 77 terrorist attacks against the US were bombings. This preference for explosive attacks provided an impetus for joint research programs at Northwestern and Harvard by the Office of Naval Research (ONR) to provide

methods for improved blast protection. With the creation of the Department of Homeland Security (DHS), it was made clear that sustained efforts would be taken to actively work against the plots of terrorist organizations to secure the safety of civilian and military personnel worldwide. In that spirit, an increased focus on scientific and engineering research into defense-based anti-terrorism applications has ensued. In the field of materials science and engineering, advanced engineering materials are being sought for lightweight, high strength and blast resistant applications, among other desirable properties. Since the attack on the USS Cole in 2000, the Office of Naval Research (ONR) along with the Department of Homeland Security (DHS) has created a multi-institutional research initiative to explore the next generation of naval hull steels, including designing new materials as well as complementary structures with improved blast resistance. A set of design goals has been defined for this project. Some of these goals were based on the ongoing *CyberSteel 2020* project at Northwestern University, which is supported by the ONR "*Naval Materials by Design*" Grand Challenge. The CyberSteel 2020 project is concerned with creating ultrahigh toughness levels in the processable plate steels desired for impact resistant naval hull applications. Figure 1.2.1 charts the ONR project initiative and the concurrent research of materials and structures.

1.2 STEEL RESEARCH GROUP AND ONR INITIATIVE

The Steel Research Group (SRG), founded in 1985, is a multi-institutional university, government and industry interdisciplinary program directing its research at the scientific principles for the design of new classes of steels motivated by specific property objectives of importance to the government and industry [1]. The objective of this initiative was to build the

methods, tools and databases to support the rapid systems design of materials within a modern systems engineering framework.

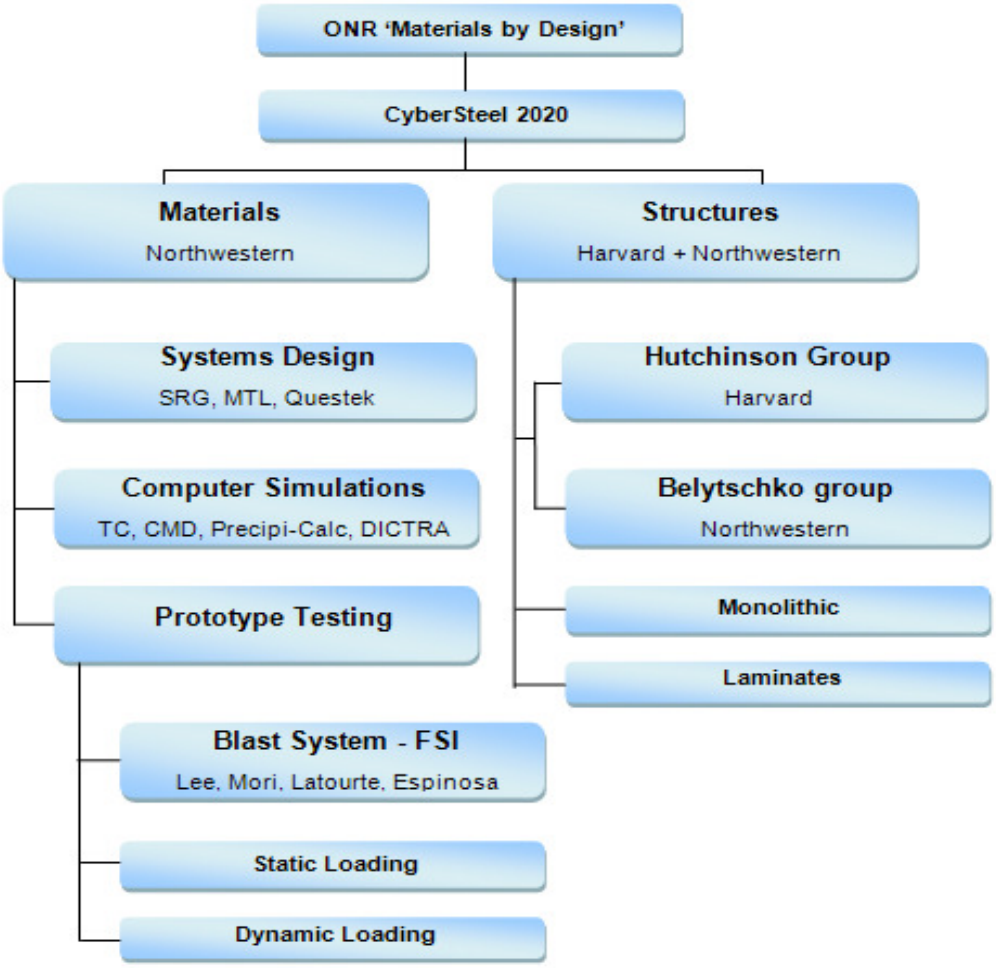

Figure 1.2.1: Project ONR "*Materials by Design – CyberSteel 2020*" Flow Chart

SRG has successfully adapted such a systems methodology to the science-based design of materials for the production of high-performance alloy steels. The research has integrated physical and process metallurgy, ceramics, applied mechanics, quantum physics, chemistry, mechanical engineering, and management science [2]. A major Materials Technology Lab/SRG initiative on materials and structures for antiterrorism blast protection is conducted under the ONR (Office of Naval Research, U.S Navy) Grand Challenge 2020 Project. SRG focuses on

fundamental research in advanced steels which show higher toughness and ductility than current available commercial steels and a design course in the undergraduate level has been developed on the same [5-6]. Graduate research and undergraduate design projects in multi-scale materials design are closely coordinated with mechanical engineering research on novel blast protection structures, while interdisciplinary undergraduate team projects explore civilian adaptation of the new technology for homeland security applications [3-4]. The primary objective of the ONR initiated CyberSteel project is to design Ultra-high toughness levels in Weldable and Processable plate steels –

a. Extreme dynamic fracture toughness ($K_{Id} \geq 200ksi\sqrt{in}$)
b. High strength levels ($150ksi \leq s_y \leq 200ksi$)
c. High resistance to hydrogen stress corrosion cracking ($K_{ISCC}/K_{IC} > 0.5$).

Under this research initiative, the first prototype BlastAlloy 160 was designed by Dr. Arup Saha which consisted of a mixed Bainite/Martensite microstructure and was compositionally optimized for extreme high toughness ($K_{ID} > 200$ ksi.in$^{1/2}$ – 220 MPa.m$^{1/2}$) and high yield strength (150 – 180 ksi, 1034 – 1241 MPa) at room temperatures [8]. The high toughness was obtained through transformation via precipitated nickel-stabilized dispersed austenite and the strength mechanism involved precipitation of both M_2C carbides and BCC Cu particles of optimum size.

1.3 CURRENT CONTEXTS AND GOALS

While the doctoral research of Saha [8] conducted under the CyberSteel 2020 project successfully demonstrated the high toughness “Blast Alloy 160” (BA160) martensitic steel, recent efforts have focused on greater exploitation of Transformation-induced plasticity (TRIP)

[9] in fully austenitic steels to achieve enhanced mechanical properties like uniform ductility and shear resistance, while maintaining high strength and toughness. The martensitic transformation of austenite during mechanical loading has been known for quite a long time [10-12].

The particular challenge of the current design problem is to achieve both strength and fracture toughness while maintaining high uniform ductility and shear resistance at room temperature; usually with the gain of one comes the loss of the other. The use of austenitic Transformation-Induced Plasticity (TRIP) steels designed earlier allows plastic flow stabilization that can be applied to either uniform ductility or toughness. This austenite to martensite transformation is influenced by temperature, applied stress, composition of the alloy, strain-rate, stress-state and any prior deformation of parent austenite [13]. The mechanism of the transformation and the kinetics governing it have been well established [discussed in Chapter 2] and have been used to generate constitutive equations and models [discussed in Chapter 5] to determine the stability of the parent matrix phase, which is critical in determining ideal transformation temperature and other parameters. The transformation to martensite provides resistance to necking in tension thereby increasing not only the uniform ductility but also the ultimate tensile strength (UTS) [14]. The transformation behavior is dependent on the stability of the austenite matrix and its influence on the mechanical properties of TRIP steels have been extensively studied by Bhandarkar et al. [15].

A previously designed experimental prototype alloy EX425 has been used as the starting calibration point where we begin our design optimizations for the new alloy designs. Alloy EX425 is a TRIP steel developed by Dr. Frode Stavehaug for his doctoral thesis at MIT [13]. It

was developed to study transformation toughening at high strength levels achieved by a combination of warm working and γ'-precipitation strengthening in metastable composition based on modification of the stable austenitic A286 commercial γ'-precipitation strengthened stainless steel. The composition of this EX425 alloy has been compared with that of A286 in Table 1.4.1.

Alloy	Cr	Ni	Mo	Ti	V	Al	C	Mn	Fe
EX425	3.93	25.04	1.25	2.97	0.22	0.16	0.005	0.09	Balance
A286	14.50	25.00	1.25	2.10	0.30	0.15	0.04	0.20	Balance

Table 1.3.1: Alloys EX425 and commercial A286 austenitic stainless steel, compositions are listed in weight percent

Earlier, integration of the previously designed blast resistant martensitic steel BA160 into sandwich plate truss structures was done to establish the feasibility of weight efficient blast protection for use in civilian anti-terrorism applications. For ground transportation systems, finite element modeling (FEM) conducted by undergraduate design teams [16] predicted a 50% increase in blast impulse resistance for the new material and structure combination over a conventionally armored vehicle of equivalent weight. These results have been discussed later in section 1.6. While the initial blast resistant steel design focused on achieving high toughness at high strength levels, the FEM simulations indicates that uniform ductility at high strength is the critical property for blast impulse resistance, provided a critical toughness level is maintained to avoid shattering. This reassessment of requirements led to added focus on designing an austenitic steel which has 30% uniform elongation, a tensile yield strength of 100-120ksi, a fracture toughness of at least 90ksi√in (98.9 MPa√m) to resist shattering, while being non-ferromagnetic at use temperature and easily weldable with high resistance to hydrogen stress corrosion cracking ($K_{ISCC}/K_{IC} > 0.5$).

Recent advances in computer and software technology have made it possible to accurately model the behavior of multi-component metal alloys. Both Thermo-Calc and the QuesTek CMD design software have become powerful tools, allowing researchers to control the phenomena of both strengthening mechanisms and TRIP effects more quantitatively than ever. These tools, which allow materials engineers to design more advanced steels that meet very specific needs more rapidly and at a much lower cost to a research facility, have been thoroughly utilized in the design process.

In a broader picture, the current research has involved undergraduate teams every year working on improving the design aspects using computational tools like ThermoCalc (TCW) and CMD to generate equilibrium compositions for different alloy combinations and to insure purposeful modeling activities supporting the materials design strategy of the SRG. Studies have been conducted on the 3-dimensional Atom Probe (LEAP tomography) at Northwestern University's Centre for Atom Probe Tomography (*NUCAPT*) facilities to determine the characteristics and distribution of γ' strengthening phase and composition validation of the matrix phase. Additional blast impulse tests have been conducted on sandwich plate structures with collaborating researchers in the ballistic testing lab in the Department of Mechanical Engineering at Northwestern University. The materials design integration in this research has integrated these models with the full set of design models such as precipitation strengthening and martensite transformation kinetics to come up with the two prototype alloy series named BA120 and SA120, for application under Tension and Shear loading conditions respectively.

1.4 PROPERTY OBJECTIVES and OVERVIEW

While the martensitic BlastAlloy160 steel was designed based on the initial assumption that toughness is the critical factor in blast protection, recent computer simulations and failure analysis [16] have indicated that uniform ductility is the limiting property for impulse resistance, provided a critical toughness is maintained to avoid shattering. This reassessment of requirements has changed the goals of the current design to develop a prototype which has improved ductility at high yield stress levels with just sufficient fracture toughness. These objectives should be met while maintaining the other properties desirable for naval hull steels, such as non-ferromagnetism (for reduced magnetic signature at use temperatures), good weldability, and resistance to hydrogen-stress-corrosion cracking. Based on these requirements, the following property objectives have been defined:

1. To achieve Yield Strength of ~120 ksi and UTS > 130 ksi.
2. To achieve at least 20% uniform elongation under tension and shear loading conditions at room temperature, with significant necking (>50% in Reduction of Area)
3. To maintain a high fracture toughness (greater than 90 ksi/in$^{0.5}$) – Since the main goal of this design is improved ductility, the fracture toughness requirements have been lowered. However these values are still higher than commercial A286 austenitic steel.
4. To be non-magnetic at use temperatures – The design will constrain the Curie temperature of the alloy composition below room temperature.
5. To be easily weldable
6. To be resistant to environmental hydrogen and stress-corrosion cracking
7. Low Cost

Initial tensile tests under dynamic adiabatic conditions (Kolsky Bar) had demonstrated tensile yield strength of 160ksi at room temperature for the EX425 prototype [Chapter 4]. However, the

uniform elongation obtained in EX425 at room temperature was limited to~ 15% due to intergranular fracture. Therefore, additions of extra Boron and Carbon has been considered in our alloy designs in order to have grain boundary segregation and grain refinement (by formation of an optimum amount of FCC TiC phase) after solutionizing treatment, respectively. This has been discussed in detail in the sections 5.5 and 5.6. This research has focused mainly on increasing the uniform elongation to beyond 20% under both tension and shear at room temperature. The yield strength is our second most important property for the intended application. The goal of 120 ksi is still significantly higher than the Al6XN and 316L austenitic stainless steels recently explored by the Navy and a reasonable increment above the current martensitic HSLA100 steel that provides good fragment protection.

There are many secondary design objectives for the current alloy design. In order to prevent plate shattering and fragment protection, it is desirable to maintain good shear instability resistance and fracture toughness to strength ratio to have an acceptable critical flaw size at yield. Weldability is an important property since plates of the alloy will have to be joined together to create a hull. It is also important that ships minimize their electric, magnetic, and thermal signatures to increase their stealth and hence, a non-magnetic hull presents an advantage for the Navy. A microstructural approach will be used to meet the desired properties summarized in the system flowchart figure 1.6.1.

1.5 DESIGN APPROACH: Materials by Design™

The property-driven view of structure and processing for the creation of value, shared by modern materials science and ancient alchemy, embraces an essential complexity of material structure. This has motivated the development of a systems approach in the design of materials,

propounded by Smith [7] based on the universal hierarchical nature of materials structure. The systems approach of computational materials design combines materials science, quantum physics and continuum mechanics in the integration of process/structure/property/performance relations for predictive design of high performance steels as multilevel dynamic structures [2]. The materials property objectives motivating the research were developed with a property cross-plot approach, as generalized by Ashby [17] to quantify property-performance relations in a broad methodology for materials selection, as shown in figure 1.5.1

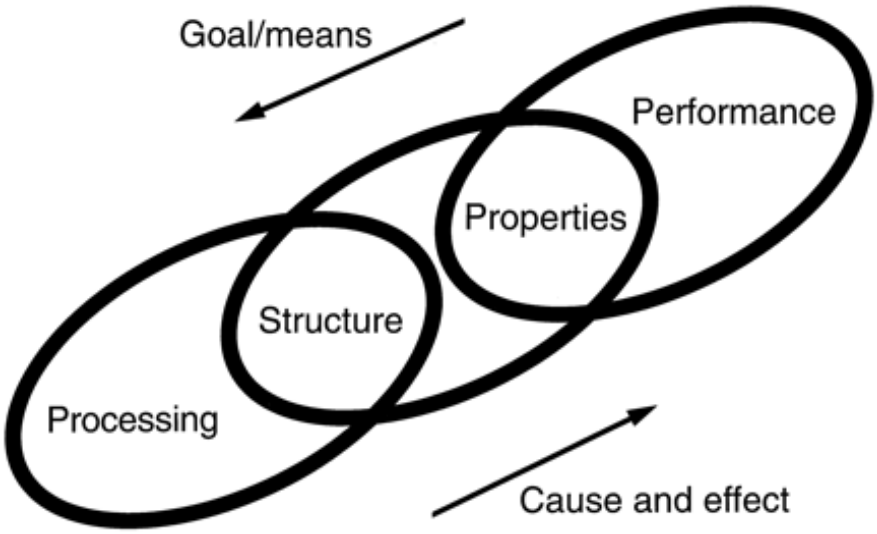

Figure 1.5.1: The SRG core underlying Materials design Principle of *Structure – Property – Performance* relationship [2]

Four primary elements are critical in materials science and engineering: processing, structure, properties, and performance [3]. The structure offers a resonant bond between the science and engineering of materials, in which the deductive cause-and-effect logic of science flows to the right, while the inductive goal-means relations of engineering flow to the left.

With the objectives set, the structure can be broken down into subsystems with graphical representation of their interactions through a system flow block diagram. Fig. 1.5.2 describes the

systems approach that will be used in this thesis to design steels with the specified strength, ductility, transformation strengthening mechanism, toughness levels as well as weldability and hydrogen resistance.

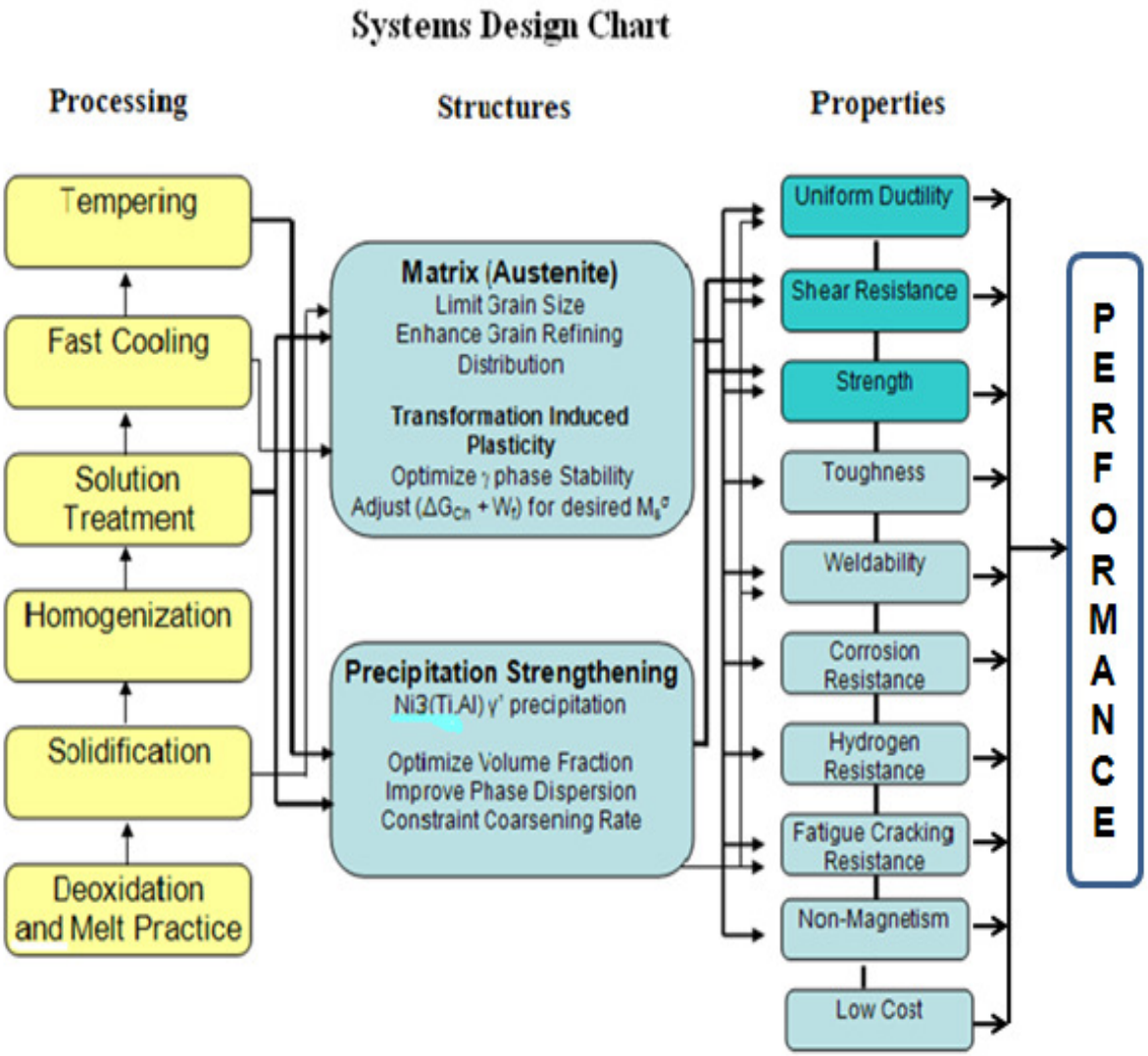

Figure 1.5.2: Systems Design Chart for new alloys for Blast and Fragmentation protection

The systems design chart links the performance of the material desired to its properties, which are in turn dictated by the micro structure of the alloys controlled by the primary processing and final heat treatment. Uniform ductility under tension as well as shear loading and tensile yield

strength at room temperature are the primary objectives of the design while corrosion resistance, ease of weldability, non - ferromagnetism etc. while important to any alloy design, are considered as secondary objectives. The matrix is kept fully austenitic (f.c.c) and the strengthening is obtained by the precipitation of gamma prime (γ') Ni_3 (Ti, Al) phase, in metastable equilibrium with the matrix austenite. The strength of the alloy is a function of the mole fraction of precipitated γ'- phase, which in turn, is controlled by the aging heat treatment temperature and time. Optimized grain size is obtained by a fine dispersion of TiC particles. Past SRG initiatives [18] have shown that fine TiC particles have a grain refining effect helpful for optimizing strength and fracture ductility by delaying the coalescence of microvoids among the primary voids during ductile fracture. Since inter-granular mode of fracture was detected in EX425 which limited its uniform ductility (low necking and < 25% reduction in fracture area) [section 4.2] at room temperature, addition of extra Boron have been considered in the current design context for improved grain boundary cohesion. This is discussed in detail in chapter 2 section 2.5.

The austenite grain size control is important as it is one of the primary factors to optimize austenite stability for the desired martensite transformation characteristics which is critical to the alloy design. The stability of the austenite matrix is dependant not only on the composition of the alloy, but also on the temperature and stress state. M_s^σ is the critical temperature for martensitic transformation assisted by the application of an external stress, and optimizing this critical M_s^σ temperature is a major focus for austenite stability in optimizing the transformation at the temperature desired. As shown in the design chart, mathematically, austenite stability is a function of the total Gibb's free energy associated with the martensitic transformation and the

frictional work of martensite interface motion. While Al and Ti are optimized initially for γ' strengthening, the quantities of Ni and Cr are varied to determine the optimum levels of both Gibb's free energy and interface frictional work. The goal is to initiate a martensitic transformation at an optimum pre-determined temperature so as to achieve improved mechanical properties like uniform ductility and strength under both tension and shear stress states.

Secondary properties like corrosion resistance and weldability are controlled by both the matrix and dispersion control with alloying elements carbon and chromium playing a major role. For any structural material, the heat-affected zones (HAZ) adjacent to the welded joints are considered to be the weakest links. The current design has low carbon levels so as to avoid formation of any secondary carbide (other than optimum quantities of TiC for grain refinement) as they are known to induce brittle character to the alloys. Two alloys designs are considered, one a non-stainless design and the other a high chromium design, the latter can be specifically optimized for shear/fragmentation resistance by adjusting its heat treatment. The processing and heat treatments for all designs are kept the same, at an optimum level of 750^{o}C for 10 hours, with the alloys undergoing the standard homogenization process post re-melting, followed by complete austenization prior to aging heat treatment.

1.6 Blast Resistant Structures and Simulations

FSI (Fluid-Structure Interaction) physical simulations of actual prototype test plates have been carried out at Northwestern's ballistics-testing lab by Lee, Espinosa et al. [19] in the department of Mechanical Engineering. It has been well known [20] that laminate "*sandwich plate*" type structures have demonstrated performance benefits over monolithic plates in static loading applications requiring high strength and stiffness. This realization has led research teams to

evaluate laminate structures under dynamic loading conditions where both high strength and energy absorption are critical to performance, as is the case for naval ship hulls under strong blast loads. Using a refined 3-Dimensional computer simulation to model the deflection response to a blast for these structures, Hutchinson et al. at Harvard University predicted reduced deflection for laminate truss structures over monolithic plates under blast loading conditions [21]. In order to corroborate the Hutchinson result, a 2-Dimensional computer simulation based on the work of Belytschko et al [22] at Northwestern was utilized. The Belytschko simulation also models the blast as an impulse incident on the front faceplate of the structure, but considers multiple structural units. The Belytschko simulation also fixes the sides parallel to the alignment of the trusses as shown in figure 1.6.1.

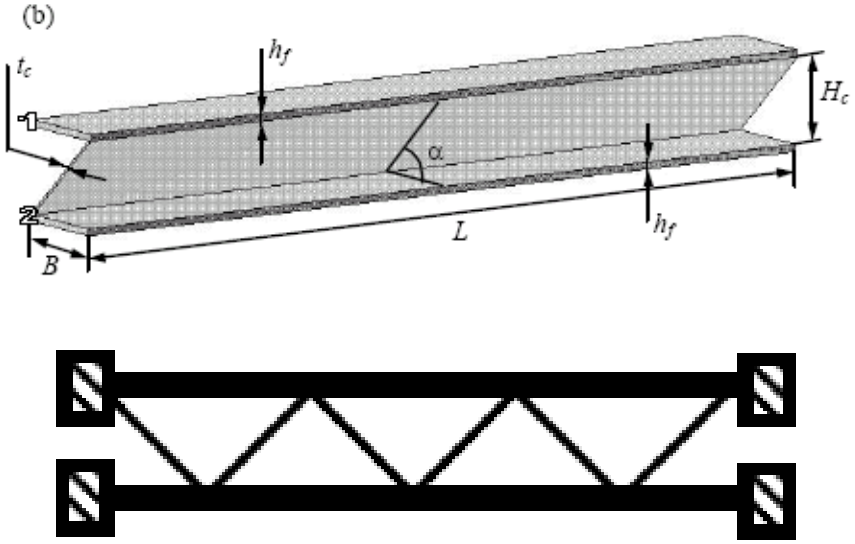

Figure 1.6.1 Profile view of Truss structures used for shock absorption FSI tests [16]

Several structures, including the square honeycomb, folded plate, and pyramidal truss were compared, by relating an applied force and their respective deformations. Using a 3-D computer simulation to model the deflection response of a blast in these structures, Hutchinson et al.

calculated reduced deflection for laminate truss structures over those of monolithic plates under dynamic blast loading conditions.

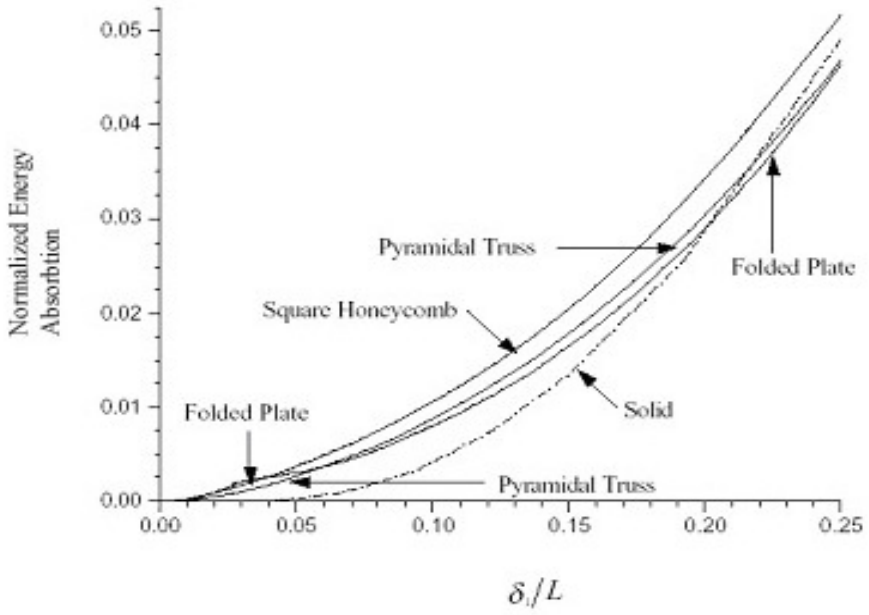

Figure 1.6.2 Plot of Normalized energy dissipation by different truss structures relative to their normal deflection levels using Belytschko Model for Front face sheet [16]

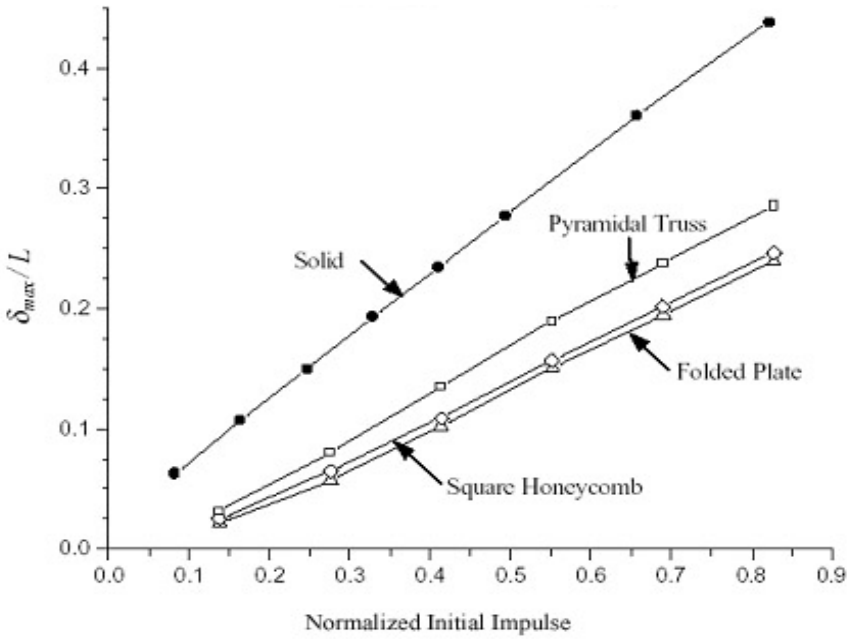

Figure 1.6.3 Plot of Deflection for different truss structures relative to their normalized Impulse levels using Belytschko Model for Bottom face sheet [16]

In these calculations, the effects of a blast on the various structures were analyzed by assigning an initial velocity to the outer surface of the laminate. This velocity is expressed as a function of the initial impulse per unit area (initial pressure times time) provided by a blast. The deflection was then calculated revealing the relative energy absorption of each structure via deformation [16]. Based on these calculations for specific sandwich laminate truss structures of the types folded, square honeycomb and pyramidal, the *folded plate structure* was selected for use in the proposed design. This is represented in figures 1.6.2 and 1.6.3. The core of the folded plate is able to dissipate more energy by transmitting less force to the bottom plate, resulting in reduced deflection. Furthermore, Belytschko [22] showed that for constant relative densities, a folded sheet outperforms more complicated crossed truss structures. A rigorous 2D FEM simulation code developed by the collaborating Belytschko group at Northwestern was utilized by senior undergraduate design teams at Northwestern [16, 23] to calculate the strain as a function of impulse in the back faceplate of a folded plate core sandwich structure with the specific dimensions devised for the proposed blast protected Hummer H2 (termed the "HB160"), and the material properties of BlastAlloy160 steel [8]. Figure 1.6.3 below shows screen captures of the ABAQUS FEM simulation used to calculate the strain values given in Figure 1.6.4 which reveals that the maximum allowable deflection of the back faceplate (and therefore the maximum impulse withstood) is constrained by the uniform ductility limit of the material. The initial energy absorption occurs in the crushing of the core material, which should be maximized by increased core shear strength. Following core compaction, biaxial stretching of the faceplates becomes the dominant deformation mechanism for sufficiently high loads. These modes are clearly apparent in our FEM simulation as noted in Figure 1.6.3. *If the face material has insufficient ductility, it will tear under stretch loading, thus decreasing the allowable impulse the*

structure can effectively withstand. Figure 1.6.5 is shown for the measured material properties of BlastAlloy160, indicating its uniform ductility of about 10% does not quite meet the requirement for a normalized deflection of 0.2. Increasing the uniform ductility of the material while maintaining a comparable yield strength level would increase the maximum deflection the structure can withstand before failure, thus providing protection from large blast impulses. This result is the incentive that has shifted the focus of our property objectives towards increasing the uniform ductility.

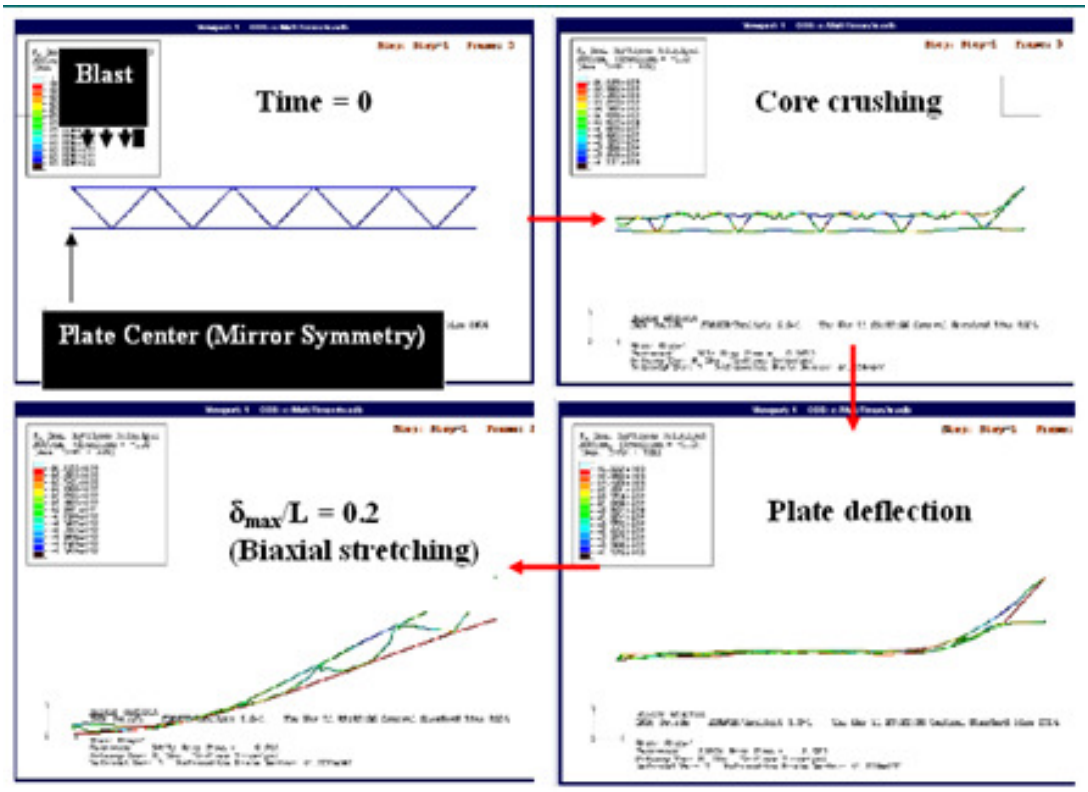

Figure 1.6.4 ABAQUS FEM screen captures show the deformation process for a folded core truss sandwich under an 18000 Pa*s impulse load applied to the Hummer HB160 structure [23]

Another study by the Hutchinson group evaluates energy dissipation of truss structures under blast loads [20]. Their analysis of the blast loading response includes two separate mechanisms that operate to deform the structure. The initial energy absorption occurs in the crushing of the

core material, which should be maximized by increased core shear strength. Following core compaction, biaxial stretching of the faceplates becomes the dominant deformation mechanism for sufficiently high loads. These modes are clearly apparent in the FEM simulation as noted in Figure 1.6.3. If the face material has insufficient ductility, it will tear [24] under stretch loading, thus decreasing the allowable impulse the structure can effectively withstand. This result is the driving force that has shifted the focus of our property objectives towards increasing the uniform ductility [25].

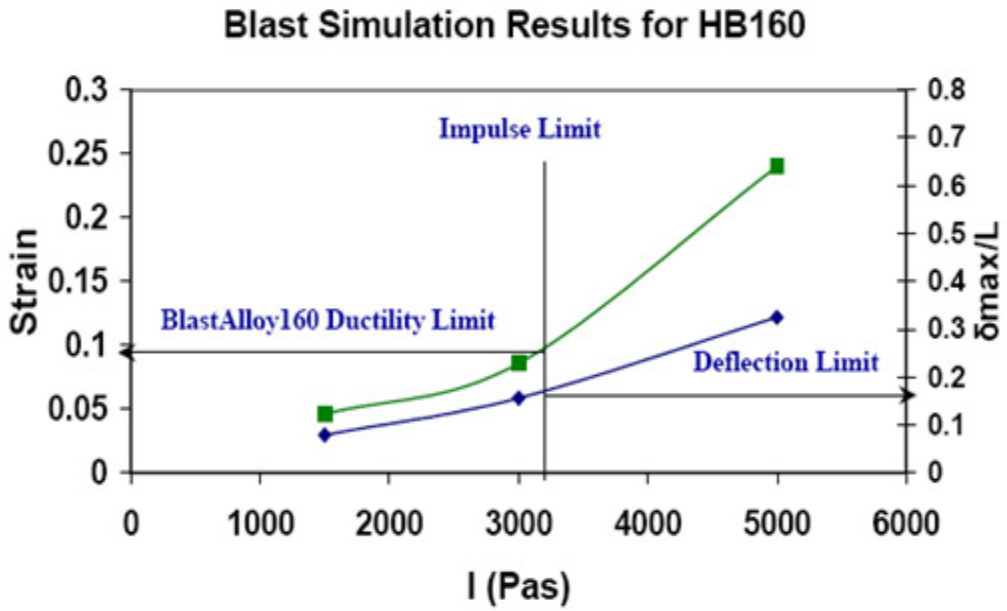

Figure 1.6.5 Dual axes plot shows strain and deflection of the back faceplate of BlastAlloy 160 folded plate core sandwich under impulse loading [16]

To compare the performance of the Saha - Olson BA160 [8] versus the other types of proposed steels, a linear trend line was added for each material as shown in figure 1.6.6.

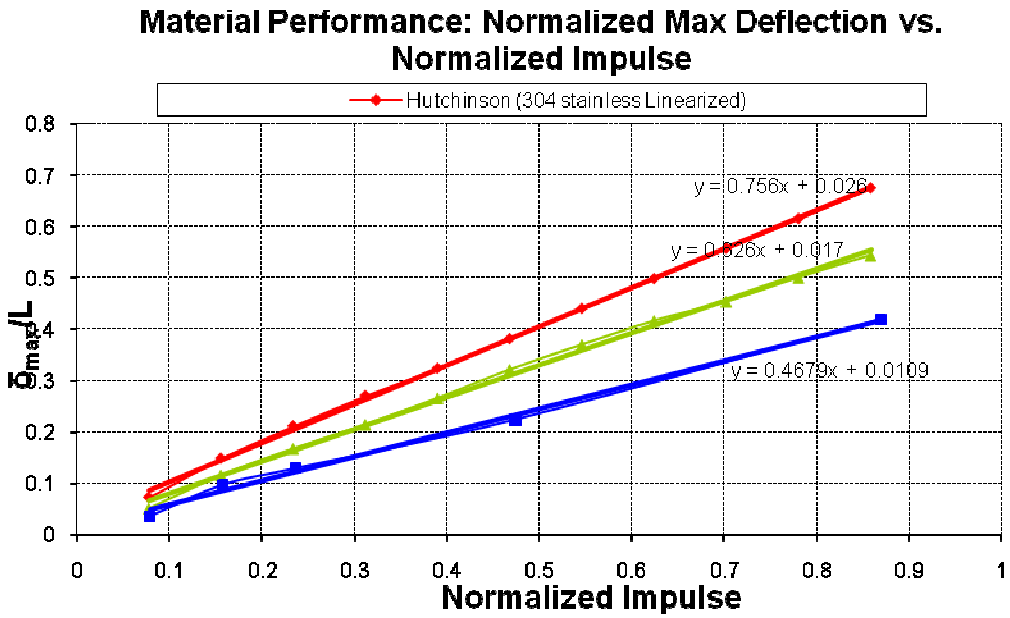

Figure 1.6.6 Plot of maximum normalized Deflection for different truss structures relative to their normalized Impulse levels using Belytschko Model for Bottom face sheet [16]

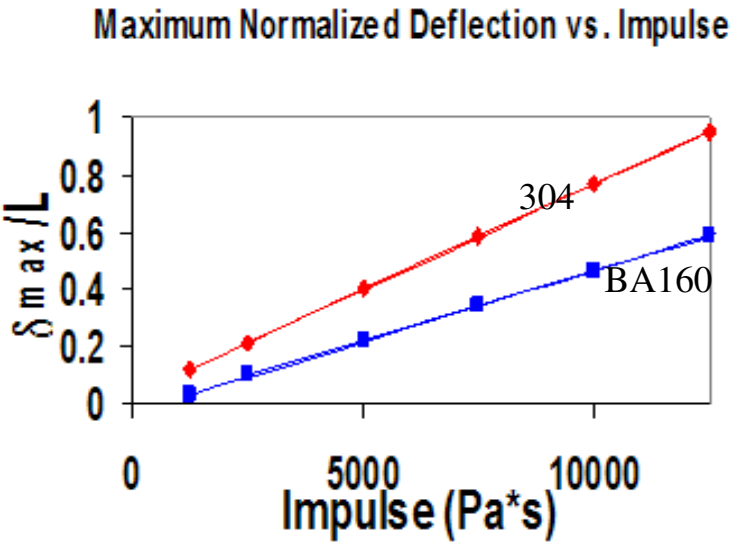

Figure 1.6.7 Comparison of maximum normalized Deflection with respect to the impulse absorption for 304 steel and BA160 martensitic alloy [16]

BlastAlloy 160 shows the best performance (i.e. least deflection for a given impulse). The average δ_{max}/L for BA160 was then compared with those for 304 stainless and AL-6XN for the normalized impulse range of 0.07 and 0.86. Using these averages, a performance gain of 38.3%

is observed using BlastAlloy-160 in place of 304 Stainless. Similarly, there is a performance gain of 25.4% in using BlastAlloy-160 instead of AL-6XN.

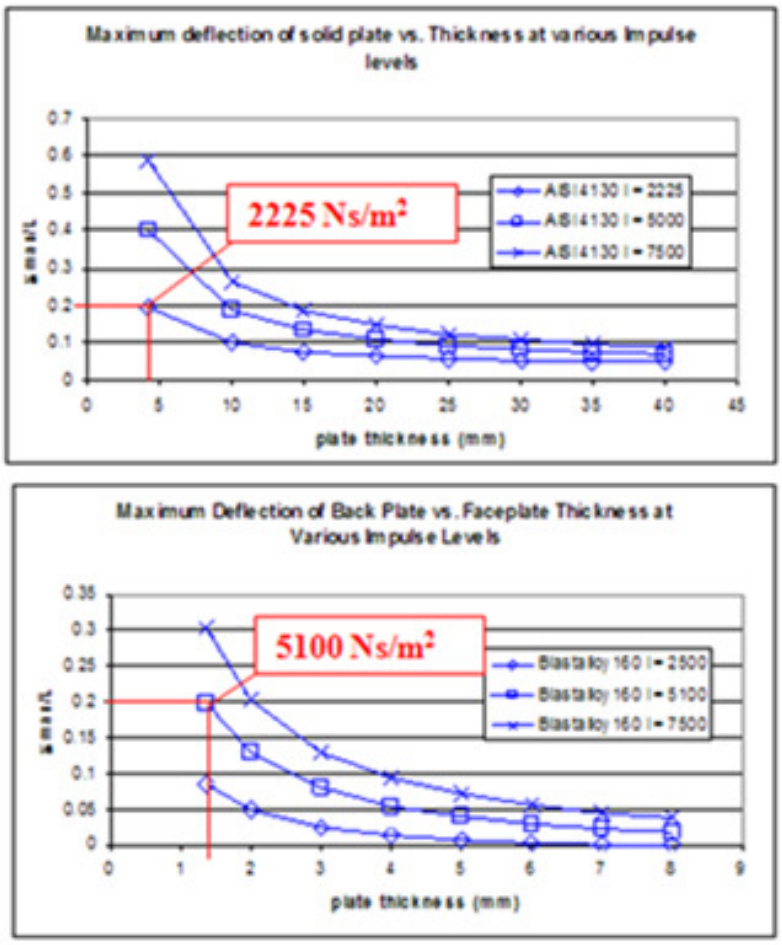

Figure 1.6.8 Comparison of maximum normalized Deflection with respect to the impulse absorption for 304 steel and BA160 martensitic alloy [23]

McCarren et al. [23] compared the projected impulse that a monolithic high-strength armor steel plate of AISI 4130 design could withstand to that of an H2 with the improved BlastAlloy160 Truss armor design. Plots of deflection vs. thickness for given impulse level were created for the two designs based on the Hutchinson model and is shown in figure 1.6.8. The model indicates that for the same weight, the Blastalloy 160 truss design can withstand a blast that is two times greater in impulse.

CHAPTER 2

BACKGROUND AND LITERATURE

As introduced earlier in section 1.4, in order to achieve the project design goals of high ductility and high shear resistance while maintaining high strength and optimum toughness levels in weldable and processable austenitic steels, we need to incorporate the concept of Transformation – Induced Plasticity (TRIP), wherein improved mechanical properties are achieved via martensitic transformation under application of an external stress. A basic review of the Olson – Cohen model for kinetics of martensitic nucleation and phase transformation is presented prior to discussing the Transformation – Induced Plasticity in detail, since this model provides the theoretical formulation of all kinetic design parameters involved in the current design. Later sections in this chapter provide a review of the concepts of stress assisted and strain induced modes of martensitic transformation leading to transformation plasticity and how this can be used to design alloys having improved ductility and strength at the temperatures we desire. Further sections provide an overview of the quantitative parameters and models to define the stability of the austenite matrix, critical to the transformation characteristics. Finally an overview of the Gamma Prime precipitation strengthening mechanism in Ni-rich austenitic steels as well as a discussion on grain refining dispersions and grain boundary cohesion for improved matrix grain size control is presented.

2.1 Kinetics of Martensitic Nucleation

Formulations of the classical nucleation theory can be applied to any system or phase which remain stable against small fluctuations for a given period of time, irrespective of their being equilibrium systems or phases [26]. The slowest step in any nucleation process is considered the rate-limiting step since it defines the nucleation kinetics and growth rate for the entire process. The Olson and Cohen model [27] of the kinetics of martensitic transformation proposed that the nucleation by growth of martensitic fault embryos in the fault plane and subsequent development and thickening of these embryos normal to the fault plane form the major rate-defining steps of the nucleation process.

2.1.1 Dislocation Motion and Embryo Formation

Olson and Cohen have developed a general mechanism of the martensitic nucleation process [27-28], whereby the nucleation process can be treated as a sequence of steps, which take the particle from maximum coherency to minimum coherency. A martensitic embryo is formed due to faulting derived from a group of pre-existing dislocations. The faulting mechanism developed by Olson and Cohen for FCC → BCC transformation is based on Boger's and Burger's '*hard sphere*' lattice deformation model [29]. Transformation kinetics due to the growth of martensitic embryos has earlier been studied in detail [30-32]. The subsequent steps in the nucleation process take place in such a way as to leave the fault plane unrotated. The possible rate-limiting steps in the total martensitic nucleation process are the growth-rate of the martensitic fault embryos in the parent fault plane and their relative thickening normal to the same fault plane. The fault energy per unit area, γ, associated with such an embryo, n atomic planes in thickness, is [33]:

$$\gamma = n\rho_A(\Delta G^{Chem} + E^{str}) + 2\sigma(n) \quad (2.1.1)$$

Where ρ_A is the density of atoms in the close packed plane in moles per unit area, ΔG^{Chem} and E^{str} are the parent product chemical free energy difference and coherency strain energy (in molar quantities) and $\sigma(n)$ is the particle/matrix interfacial energy. For spontaneous formation of an embryo from the defect, the critical condition is given by $\gamma = 0$ and equation 2.1.1 defines the size of existing defects necessary to account for embryo formation under the conditions for martensitic nucleation. The above equation further predicts that for conditions where volume energy change ($\Delta G^{Chem} + E^{str}$) is negative, the fault energy will decrease with increasing thickness (n). This term ($\Delta G^{Chem} + E^{str}$) is independent of the size of the embryo, according to Gibb's surface energy formulation [34].

For a fault embryo bounded by an array of partial dislocations of total Burger's vector nb, the force per unit length of dislocation array required to move it is $n\tau_0 b$. The required shear stress to move the dislocation is τ_0. Accordingly, the critical condition for a defect to become unstable and form a growing embryo is:

$$\gamma = -n\tau_0 b \quad (2.1.2)$$

Following Olson and Cohen [27-28], the activation energy, Q for dislocation motion under an applied shear stress, τ is expressed as [35-36]

$$Q = Q_0 - (\tau - \tau_\mu) v^* \quad (2.1.3)$$

Where Q_0 is the activation energy in the absence of any applied stress, T_μ is the athermal resistance to dislocation motion and v^* is the activation volume defined by:

$$v^* = -\left(\frac{\partial Q}{\partial \tau}\right) \qquad (2.1.4)$$

v^* is independent of strain rate. Figures 2.1.1 (a) and (b) represent the temperature dependence of the applied stress for two different strain rates and conditions of martensitic embryo formation for thermally activated motion of partial dislocations. So at high temperatures, the Olson-Cohen model implies that the applied stress necessary for dislocation motion becomes $T\mu$ and the dislocation behavior is athermal in nature.

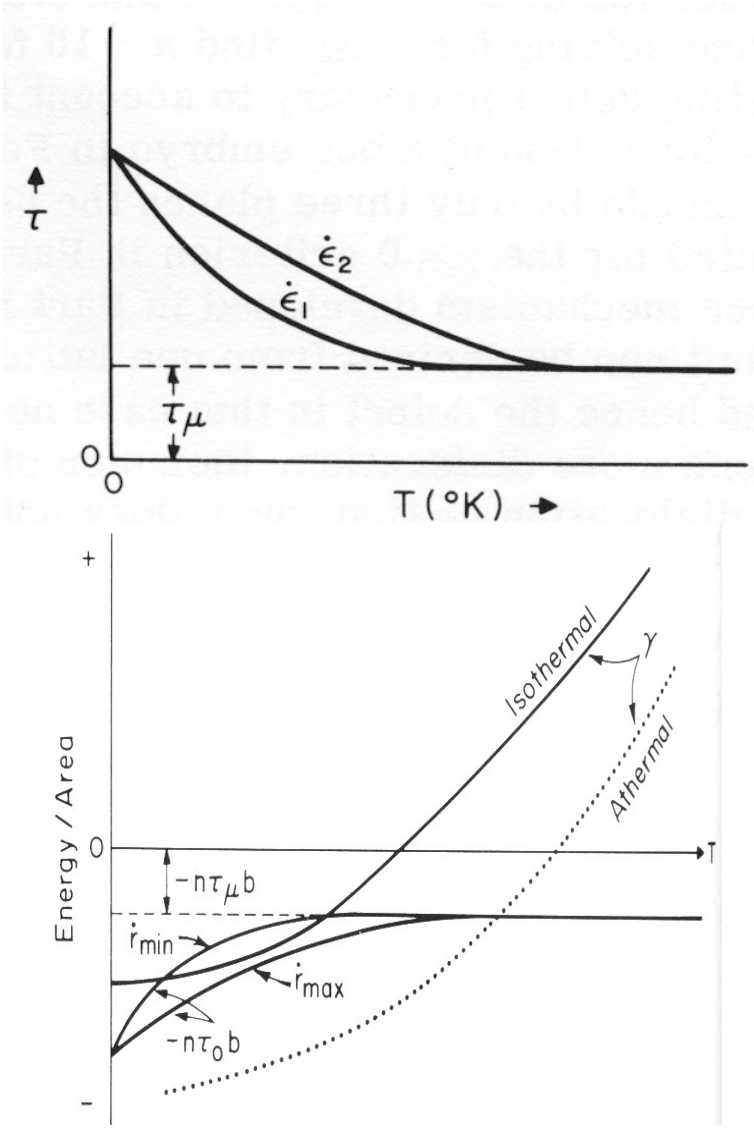

Fig 2.1.1: (a) Temperature dependence of applied stress for specific rates (b) Schematic representation of thermally activated martensitic nucleation

From equation 2.1.2, the transformational stress associated with the fault energy will be:

$$\tau = \left(\frac{-\gamma}{nb}\right) \tag{2.1.5}$$

In figure 2.1.1 (b), the solid γ curve indicates the temperature dependence of the fault energy for a defect size of n and through this, equation 2.1.2 is satisfied when the γ curve crosses into the region between the $-\eta\tau_0 b$ curves corresponding to $\gamma_{\min}$ and $\gamma_{\max}$. Thus, thermally activated motion of partial dislocations leads to isothermal growth of martensitic embryos and predicts the kinetics of growth. With the above assumption, an expression for the activation energy, Q, for isothermal martensitic nucleation can be obtained from equations 2.1.1, 2.1.3 and 2.1.5:

$$Q = Q_0 + \left\{\tau_\mu + \left(\frac{\rho_A}{b}\right) E^{Str} + \left(\frac{2\sigma}{nb}\right)\right\} v* + \left\{\left(\frac{\rho_A}{b}\right) v*\right\} \Delta G^{Chem} \tag{2.1.6}$$

Thus, the dependence of activation energy on the chemical driving force is determined by the activation volume v *. So if v * is insensitive to the temperature range of isothermal nucleation experiments (critical transformation temperatures) then this model will be in accord with the earlier obtained result of activation energy being linearly dependent on chemical driving force [37]. Thus,

$$Q = A + B\Delta G_v^{\gamma\to\alpha} \tag{2.1.7}$$

Where,

$$\Delta G_v^{\gamma\to\alpha} = \frac{(\Delta G^{Chem})}{V_m} \tag{2.1.8}$$

V_m represents the molar volume

2.1.2 Development and Growth of Martensite Embryo

According to Raghavan and Cohen [31], the mechanism of FCC → BCC embryo production also requires the formation of dislocations and that the nucleation of dislocation loops is necessary for a lattice invariant deformation. Although FCC → HCP isothermal martensitic transformation in Fe-Ni-Mn alloys have not demonstrated any lattice invariant deformation [38-39], Kaufman and Cohen [30] had proposed earlier that this phenomenon could be one of the rate limiting steps of the FCC → BCC martensitic nucleation, the kinetics of which have been studied in detail by Raghavan and Cohen [37]. Figure 2.1.2 (a) shows the interfacial structure of a martensite particle forming a new dislocation loop radially in steps of δr. Raghavan and Cohen [31] had calculated the activation energies which correctly correlated the dependence of the activation energy to the chemical driving force necessary for isothermal nucleation.

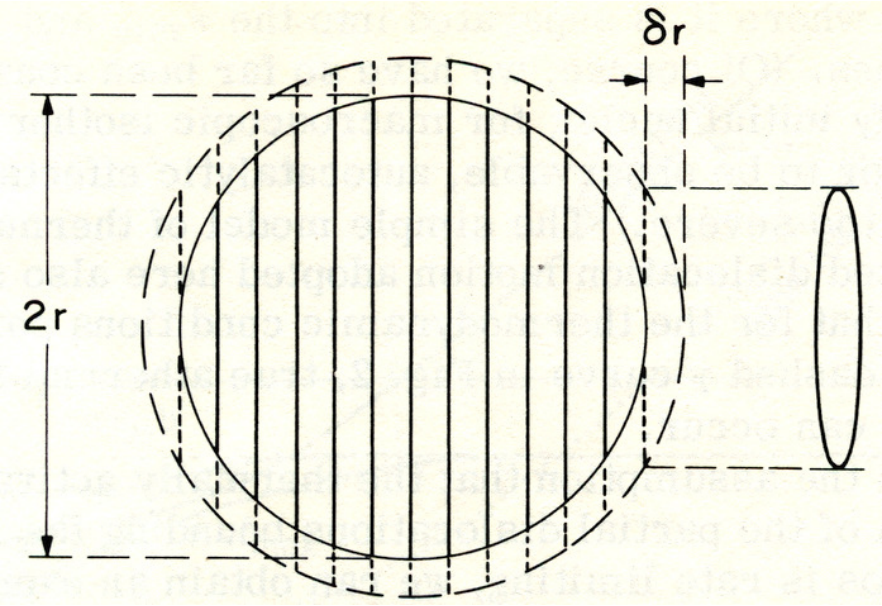

Figure 2.1.2 (a): Interfacial structure of a martensite particle [31]

Shockley partial dislocations or lattice dislocations must be formed to lower the strain energy of the embryo. A group of '*n*' dislocation sites could act as a nucleation site and can dissociate in the glide plane to form an embryo. Figure 2.1.2 (b) shows the development of the interfacial structure of the embryo from the fault plane and the formation of new dislocation loops.

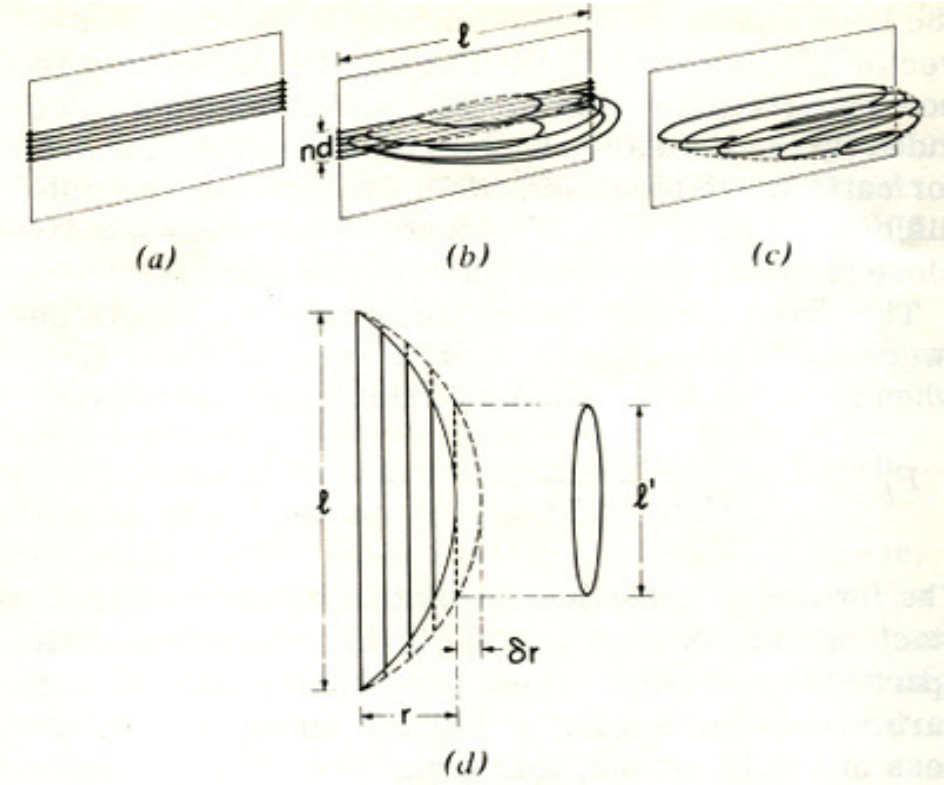

Figure 2.1.2 (b): Development of the interfacial structure of a fault embryo to form a new loop of step growth δr [40]

The figure 2.1.2 (b) shows the four steps from the dissociation of the dislocation to form the embryo to the lattice deformation and final rearrangement of loops to form a new loop of unit step δr [40]. Now, for the case of embryo thickening normal to the fault plane, new dislocations possessing long-range strain fields are needed so as to accomplish the transformational shape change, which makes the nucleation of such dislocations more difficult in terms of energy. Since it is very difficult to thermally activate new dislocation loops; it is also probable that embryo

thickening occurs by a mechanism involving a continuous increase in dislocation line length, rather than by new dislocation loops. Hence, Olson and Cohen suggested that the embryo growth occurs by a pole mechanism similar to those associated with the growth of mechanical twins [41-44].

Now, many systems which show martensitic transformations, involve softening of the linear elastic constants of the metastable parent phase with decreasing temperature. These softening effects at high strains may be associated with lattice meta-stability [45]. This softening effect does change the conditions for embryo formation, as each of the terms in equation 2.1.1 and 2.1.2 are predicted to scale with the shear modulus. Combining these terms the critical driving force required for the formation of a fault embryo from a defect size n^* is:

$$\Delta G_{n^*}^{Chem} = -\left\{\left(\frac{2\sigma n^*}{n^* \rho_A}\right) + E^{Str} + \left(\frac{\tau_0 b}{\rho_A}\right)\right\} \qquad (2.1.9)$$

The above constitutive equation 2.1.9 has been used for the potency distribution of nucleation sites under an applied elastic stress σ. Since the process of embryo thickening is basically an athermal process, it is not considered a rate limiting step in the isothermal transformation kinetics. It is to be noted that although elastic softening may assist nucleation, such softening is not necessary for the Olson-Cohen mechanism of nucleation by faulting. Although thermally activated nucleation of dislocation loops responsible for lattice deformations is a rate limiting step for some isothermal transformations, this cannot be a general case as it is not essential to all martensitic transformations. Several ideas have been put forward where a non-classical phonon mechanism of martensite nucleation though diffuse boundaries is proposed [46-47]. Detailed

calculations show that such non-classical mechanisms can only operate very close to the condition for general lattice instability where an elastic constant vanishes.

2.2 Iso-thermal Martensitic Transformation and Transformation Plasticity

As discussed previously in section 1.4, the starting point of the design process, prototype alloy EX425, is based on the concept of Transformation-Induced Plasticity (TRIP) to achieve optimal transformation at room temperature for high ductility and high strength. Precipitation hardening EX425 is a fully austenitic **γ'** [Ni_3 (Al, Ti)] strengthened non-stainless steel. Zackay and Parker [48] first introduced the concept of high-strength Transformation Plasticity steels which resulted in improved mechanical properties like high tensile ductility in medium carbon heat treatable austenitic steels, along with high strength. These properties had already been demonstrated in lower strength alloys [49]. The term TRIP was coined to express this observed transformation mechanical behavior [50]. The transformation of austenite to martensite as a result of a deformation results in high strain hardening, which is extremely important to inhibit flow instability and delay the onset of necking. Further studies [50-51] have shown that the TRIP effect greatly improves mechanical properties by allowing a high work-hardening rate that postpones plastic localization such as both tensile necking and shear bands. The positive volume change of transformation (FCC → BCC) also provides pressure-sensitive transformation strain hardening that improves the efficiency of transformation toughening. The basic mode of transformation on cooling in these classes of alloys has been determined to be isothermal [53] and stress-assisted martensitic transformation is responsible for the plastic flow at low temperatures. This has been discussed in detail in section 2.2.2.1.

This deformation-induced martensitic transformation and dispersions of metastable Austenite has shown promise for the improvement of ductility in multi-component steels [54]. The interrelationships of transformation kinetics and plastic flow behavior in TRIP steels have been studied in depth by Olson and Azrin [55] by measuring the true-stress, true-strain and martensite content during uniform as well as localized deformation. At low temperatures, the transformation kinetics is dominated by stress-assisted nucleation whereas at higher temperatures, strain-induced nucleation dominates new sites created by plastic deformation [56]. The change in the deformation mechanism around a critical point (termed M_s^{σ}) can be characterized by the difference in the transformation product morphologies: stress-assisted transformation forms relatively coarse plates while strain-induced transformation forms fine laths at intersections of shear micro-bands. This is discussed in section 2.2.2.

2.2.1 Kinetics

As described earlier the kinetics of isothermal martensitic transformation in steels is nucleation controlled and it has been demonstrated [57-58] that activation energy (Q) for isothermal nucleation is related to the transformation free-energy change per mole (ΔG):

$$Q = A + B.\Delta G \tag{2.2.1}$$

Then, the rate of transformation can be expressed by [57]:

$$f^{o} = n_s V \vartheta \exp\left\{-\frac{A+B.\Delta G}{RT}\right\} \tag{2.2.2}$$

Where f^{o} represents the transformation rate, V is the instantaneous martensite plate volume and ϑ is the nucleation attempt frequency. Then, the critical G required to achieve a given f^{o} is given by [59],

$$\Delta G_{crit}(f^o) = -\frac{1}{B}\left[A + RT\ln\left(\frac{f^o}{n_s V \vartheta}\right)\right] \quad (2.2.3)$$

which shows a linear expression for temperature dependence. Figure 2.2.1 shows the G_{crit} for different values of f^o in the $G - T$ curve. The rate of transformation at a given temperature is determined by the G_{crit} (f^o) line, which intersects the G_{ch} at that temperature. The slope of G_{ch} is given by

$$\frac{d\Delta G^{chem}}{dT} = -\Delta S_{chem} \quad (2.2.4)$$

where ΔS_{chem} is the transformation entropy change

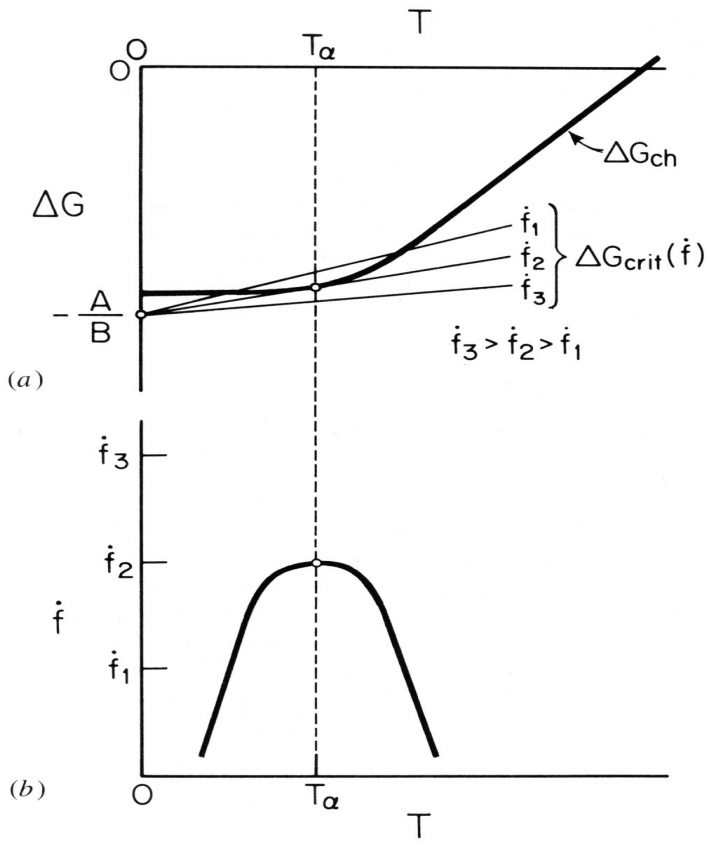

Fig 2.2.1: Schematic kinetic relationships for isothermal martensitic transformations (a) plot representing chemical free-energy change and critical free-energy change for different Transformation rates (b) Transformation rate Vs. T [59]

The nose temperature (T) at which f^o is maximum can be determined by drawing a tangent straight line at the curve for G_{ch} from the point $-A/B$ at $T = 0$ to the point of tangency and the point of tangency (intersection point with G_{ch}) gives the value of T_α. So we have,

$$\frac{\partial^2 \Delta G}{\partial T^2} = -\left(\frac{\Delta C_p}{T}\right) \tag{2.2.5}$$

Describing the non-linear $\Delta G_{ch}(T)$ with a power law of exponent n then gives,

$$T_\alpha = \left[\frac{A+BC_1}{(n-1)BC_2}\right]^{\frac{1}{n}} \tag{2.2.6}$$

This curvature of $\Delta G_{ch}(T)$ has an important influence on the plastic flow characteristics when stress-assisted martensitic transformations control the plastic flow, i.e., below the M_s^σ.

2.2.2 M_s^σ Temperature and Modes of Martensitic Transformation

As shown in figure 2.2.2, the $\sigma - T$ curve for general TRIP steels show two distinct mechanisms within the deformation interaction of martensitic transformation region → $T < M_s^\sigma$ and $T > M_s^\sigma$. The transition from low temperature *stress-assisted transformation mode* ($T > M_s$ and $T < M_s^\sigma$) to high temperature *strain-induced nucleation* ($T > M_s^\sigma$ and $T < M_d$) occurs at the M_s^σ. The designation M_s^σ comes from the work of Richman and Bolling [60] and is defined as the maximum temperature at which martensitic transformation is induced by external stress below the yield stress of the parent phase. Below M_s^σ, the induced martensitic transformation, as described in section 2.2.1, is strongly dependent on the temperature and strain rate imposed and spontaneous transformation is triggered by pre-existing nucleation sites [56].

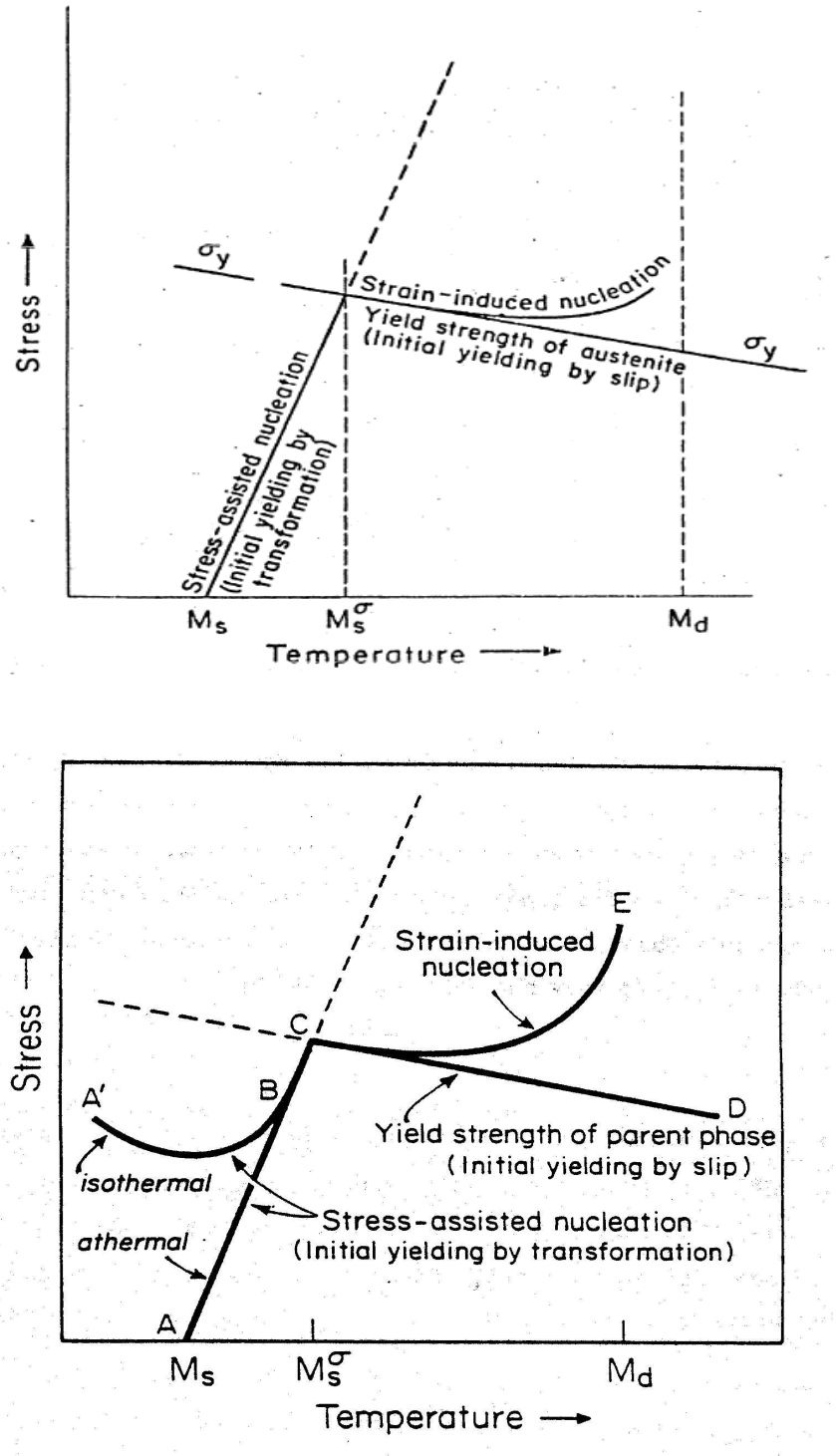

Fig 2.2.2: Schematic representation of interrelationships between stress-assisted and Strain-induced martensitic transformation [56]

In this regime, the measured yield strength is much lower than that expected for a fully stable austenite matrix. Above M_s^σ to M_d (temperature above which martensitic transformation cannot be induced by deformation), plastic strain introduces new potent nucleation sites, which trigger strain-induced nucleation. Thus significant plastic flow precedes transformation with the new nucleation sites providing an additional contribution to the transformation. As shown in figure 2.2.2, for athermal martensitic transformation below M_s^σ, the stress required for stress – assisted transformation has a linear temperature dependence approaching zero at M_s while for the isothermal transformation, the stress requires at $T < M_s^\sigma$ shows a dip and then curves upwards.

The two M_s^σ temperatures of interest here are the M_s^σ *(ut)* corresponding to uniaxial tension and the M_s^σ *(ct)* corresponding to the stress state at a crack tip. Thus M_s^σ temperature may be considered as a barometer of stability for transformation due to deformation, whereby the two modes are distinguished with one owing to nucleation on pre-existing sites responsible for transformation on cooling (Stress-Assisted) and the other due to nucleation on new sites produced by plastic strain (Strain – Induced). As a result of the transformation volume change, the M_s^σ temperature is stress-state dependant. The kinetics and transformation behavior of these two modes are described in section 2.2.2.1. The essential mechanism for Stress – Assisted and Strain – Induced heterogenous martensitic nucleation is considered to be essentially the same, following the work of Olson and Cohen [61-62]. Since the pre-existing as well as the newly formed nucleation sites due to plastic strain are considered to arise from dislocation defects, the kinetics of the nucleation process have been treated with both classical continuum descriptions [63-65] and dislocation dissociation [27-28].

2.2.2.1 Stress – Assisted Transformation

The kinetics associated with the Stress – Assisted transformation mode can be derived from the general isothermal martensitic transformation kinetics discussed in section 2.2.1 by simply accounting for the additional work done by an external applied stress. The applied elastic stress modifies the effective potency distribution of the pre-existing nucleation sites, which in turn help the transformation kinetics. According to Patel and Cohen [10], the work per unit volume done by applied stress assisting the transformation can be expressed by:

$$W = \tau\gamma_0 + \sigma_n\epsilon_0 \tag{2.2.7}$$

Where γ_0 and ϵ_0 are the shear and normal strain components and τ and σ_n are the resolved shear and normal stresses on the planes and in the direction of γ_0 and ϵ_0. The values of W obtained are in good agreement [66] with the observed dependence of the M_s Temperatures in alloys having similar athermal kinetic behavior [67]. According to the Olson-Cohen dislocation dissociation model of classical heterogeneous martensitic nucleation by elastic interactions with internal stress concentrations [68], the potency of a nucleation site can be expressed in terms of critical thickness 'n' of the nucleus for a given driving force per unit volume, given by

$$n = -\left\{\frac{\frac{2\gamma_s}{d}}{[\Delta G^{ch} + E^{str} + W_f]}\right\} \tag{2.2.8}$$

where γ_s the interfacial energy and d is the inter-planar spacing. The driving force term in the denominator is a sum of the chemical driving force ΔG^{ch}, elastic strain energy per unit volume E^{str} and frictional work of interfacial motion W_f. Based on this model and from results obtained by Cech and Turnball [69], Olson and Cohen [70] further derived the structural defect-potency distribution $N_v(n)$ as

$$N_V = N_V^0 \exp(-\alpha n) \tag{2.2.9}$$

Where N_v^0 is the total number of nucleation sites in all potencies and α is a constant. For considering the stress effects in potency distribution, the two extreme cases would be; the operative nucleation sites are of optimum orientation for maximum interaction with applied stress, i.e., $\Delta G^{\sigma} = \Delta G^{\sigma}_{max}$ based on Patel and Cohen model [71] and the other extreme is a fully random distribution treated by Tzusaki, Olson and Cohen [72]. The actual behavior should be between these two bounds and Tzusaki et al. found that the effect of applied stress is 1/3 of that predicted by the fully biased model, in the stress assisted region of transformation. Thus the potency distribution of nucleation sites under an applied elastic stress can be expressed by:

$$N_v(\sigma) = N_v^0 \exp\left\{\frac{\frac{2\alpha\gamma_s}{d}}{\Delta G^{ch} + \Delta G^{\sigma}_{max}(\sigma) + W_f + E^{str}}\right\} \tag{2.2.10}$$

where $\Delta G^{\sigma}(\sigma)$ is the mechanical driving force. So $\Delta G_{max}{}^{\sigma}$ should be equal to $(\Delta G_{max}{}^{\sigma})/3$ for a fully random distribution. At a given stress level, the value of the mechanical driving force changes with the orientation of the nucleus relative to the stress state. The mechanical driving force is again related to the applied stress through the Patel-Cohen criterion, derived from equation 2.2.7:

$$\Delta G^{\sigma} = \sigma \left(\frac{\partial \Delta G}{\partial \sigma}\right) \tag{2.2.11}$$

Thus the probability P of finding one nucleation site within a particle could be assumed to be equal to the fraction of transforming particles,

$$P = 1 - \exp(-N_V . V_p) \tag{2.2.12}$$

Where N_V is the cumulative number density of the potency sites and V_P is the average particle volume. From equation 2.2.1 and 2.2.8, the stress σ required to operate a nucleation site of potency n_0 is linearly related to a parameter Φ given by [73],

$$\Phi = \left[\sigma.\left(-\frac{\partial \Delta G}{\partial \sigma}\right) - \left(\Delta G^{ch} + G^{el} + W_f\right)\right]\left(\frac{d}{2\gamma}\right) = n_0^{-1} \qquad (2.2.13)$$

Where the fraction of transforming particles can be related to the parameter Φ by the relation

$$\Phi = \frac{\alpha}{\ln\left[-\frac{N_V V_P}{\ln(1-f)}\right]} \qquad (2.2.14)$$

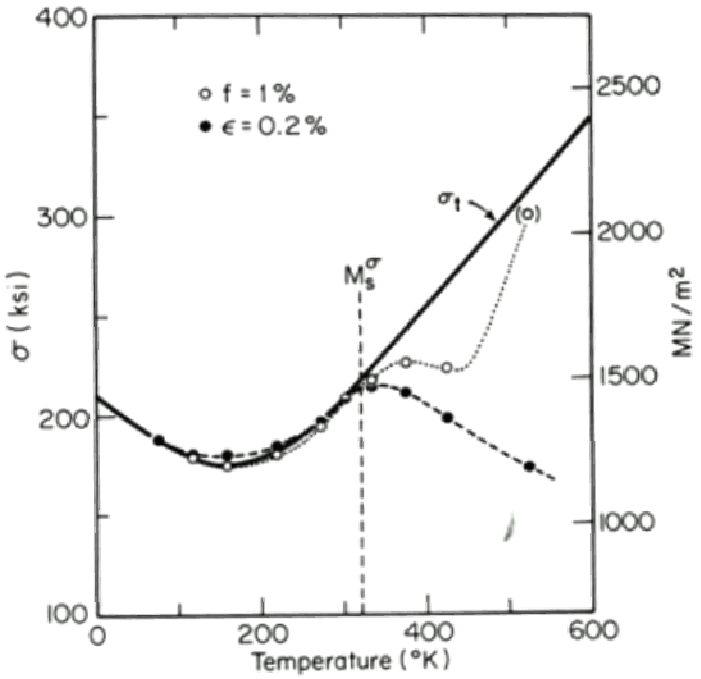

Fig. 2.2.3: Observed Temperature dependence of Yield Stress and stress at which 1% martensite is detected post transformation in a high strength TRIP Steel, with the solid line representing the ideal curve for stress-assisted transformation regime [69]

The linear equation 2.2.3 for ΔG^{crit} predicts the critical stress for stress – assisted transformation shown by the solid curve in figure 2.2.3 compared against the measured stresses

for 0.2% plastic strain and 1% transformation by volume. The heating effect at moderate strain rates can adversely affect the uniform tensile ductility associated with the stress - assisted transformation process. From the σ-T curve in figure 2.2.3, we can see that the temperature dependence of the stress – assisted transformation kinetics is zero (minimum) at ~ 150K. The temperature sensitivity to the overall transformation kinetics can be reduced by moving this minimum closer to room temperature ~ 300K.

For a fixed rate and a given extent of stress – assisted martensitic transformation, the external applied stress can be expressed as a function of the fixed rate f^o

$$\sigma\,(f^o) = -\left\{B\left(\frac{d\Delta G}{d\sigma}\right)\right\}^{-1}\,[A + B\Delta G_{ch} + RT\ln\left\{\frac{f^o}{\{(n+pf-N_v)(1-f)V\vartheta\}}\right\} \tag{2.2.15}$$

Substitution of nickel with manganese in the alloy has shown to influence the temperature sensitivity of the strain – induced transformation [74]. However the tradeoff is that increased manganese is known to decrease the final 'reduction-in-area' thereby limiting uniform ductility [75]. Following the kinetics of the isothermal martensitic transformation, a $\Delta G - T$ curve for stress-assisted transformation is shown in figure 2.2.4. The straight line through $-A/B$ represent the critical ΔG needed (ΔG_{crit}) to obtain a fixed rate of transformation f^o. $\delta\Delta G$ represents the additional free energy increment needed for transformation rate f^o from the normal case as had been shown in figure 2.2.4. A minimum occurs at a temperature T_β where the ΔG_{ch} and the ΔG_{crit} have the same slope as shown by the dashed line. This occurs when

$$\Delta S(T) = \left(\frac{R}{B}\right)\ln\left(\frac{f^o}{n_s V\vartheta}\right) \tag{2.2.16}$$

And, by approximating the $\Delta G_{chem}\,(T)$, we get the condition

$$T_\beta = \left[-\left(\frac{R}{nC_2B}\right)\ln\left(\frac{f^o}{n_sV\vartheta}\right)\right]^{\left\{\frac{1}{n-1}\right\}} \tag{2.2.17}$$

While T_α is fixed for a given alloy, T_β in the above equation is a function of the imposed transformation rate [59].

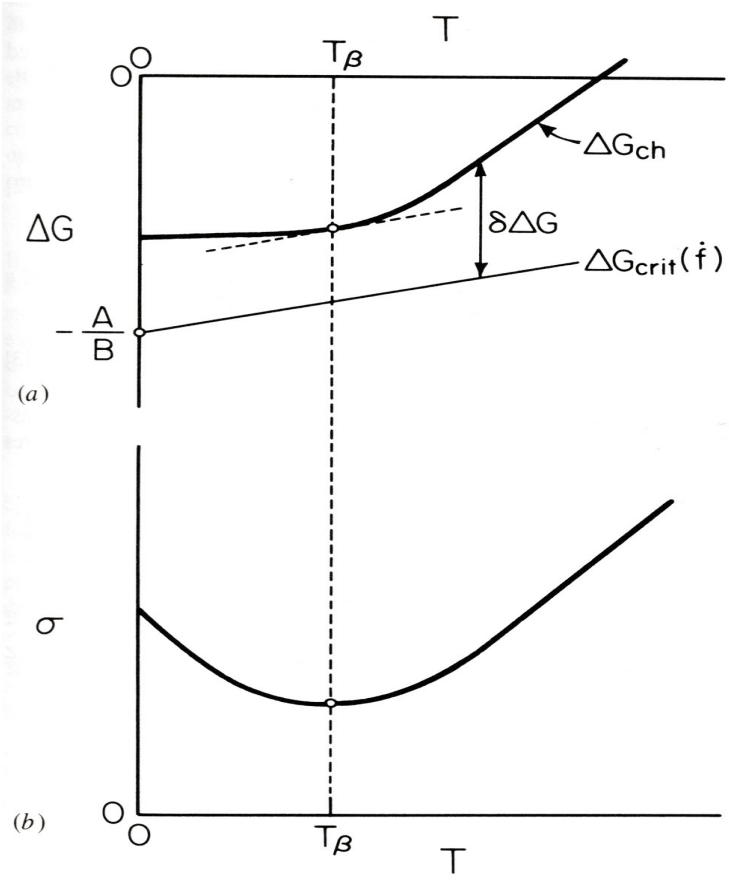

Fig. 2.2.4: Schematic kinetic relations for stress-assisted isothermal martensitic Transformations (a) plot showing additional free-energy increment ΔG for transformation Rate f (b) Stress required for maintaining f^o [59]

2.2.2.2 Strain – Induced Transformation

In the temperature range above M_s^{σ} and below M_d, when the externally applied stress becomes over the yield limit of parent austenite, significant plastic flow precedes the transformation and it is dominated by *strain-induced* nucleation on new nucleation sites created by the plastic strain [56]. It is well established that the strain-induced nucleation occurs predominantly at shear-band intersections which act as potent nucleation sites [76]. Since stress-assisted transformation ($T < M_s^{\sigma}$) takes place in the absence of any slip, it represents a softening phenomenon relative to the flow behavior of the parent phase. But for $T > M_s^{\sigma}$ where strain-induced nucleation dominates the deformation behavior, transformation and slip act in parallel. While a dynamic softening operates with transformation as a deformation mechanism, a static hardening effect also arises from the transformation product acting as an obstacle. For transformation plasticity, dynamic softening is dominant at low strains while static hardening is dominant at strains where the rate of transformation decreases [133-134]. This distorts the usual $\sigma - \varepsilon$ curve into an upward curving shape. The detailed quantitative analysis of this behavior is modeled by Olson and Cohen [74]. Narutani, Olson and Cohen [77] presented a critical assessment of the effects of the transformation by separating the 'static hardening' from the 'dynamic softening' influence of transformation as major deformation mechanisms.

Both the volume fraction of martensite (f) and the plastic strain ε are linearly related during stress – assisted transformation. But in case of the Strain – Induced transformation, the kinetics follow a sigmoidal curve [fig. 2.2.2]. The quantitative modeling of the kinetics in this stage has been based on the shear band intersections being primary nucleation sites, as discussed earlier. The volume fraction of shear bands is related to plastic strain in the form [74],

$$f^{sb} = 1 - \exp\ (-\alpha\epsilon) \tag{2.2.18}$$

where the parameter α determines the rate of shear-band formation. Now from the volume fraction of shear-bands, the number of martensitic units can be determined through the probability (***P***) that ***n*** intersections will act as a potent nucleation site. Hence the volume fraction of Strain – Induced Martensite as a function of plastic strain is derived as –

$$f = 1 - \exp\{-\beta[1 - \exp\ (-\alpha\epsilon)]^n\} \tag{2.2.19}$$

Where,

$$\beta = P\left[(no.\,of\ mart.units).\frac{k}{(average\ shear\ band\ volume)^n}\right] \tag{2.2.20}$$

and *k* is the geometric constant for the shear bands. The relation 2.2.20 gives a sigmoidal curve whose slope is determined by the parameter β. β is temperature dependant and is proportional to the probability *P* (probability of *n* nucleation sites). Figure 2.2.5 shows the fit to the equation 2.2.19 for strain – induced transformation curves for 304 austenitic steel [73]. The parameter α is the primary temperature dependant kinetic factor influencing strain induced transformation kinetics while for the stress – assisted mode of transformation is the parameter *B* (activation volume). The respective variation in the kinetic parameters α and β with temperature is shown in figure 2.2.6. So while the volume of transformed martensite phase fraction (f^o) is directly proportional to the plastic strain in the case of Stress – assisted transformation, in the case of Strain - induced nucleation, the volume fraction of martensite takes the form of equation 2.2.19.

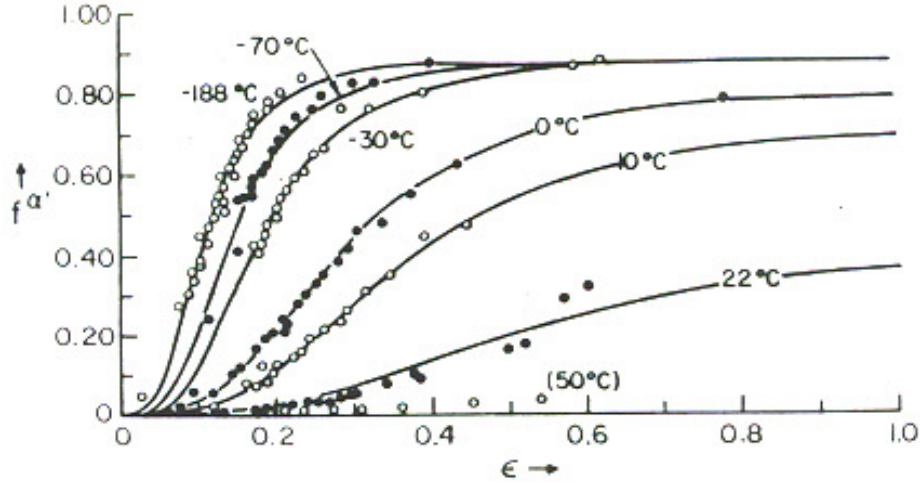

Fig. 2.2.5: Experimentally Determined Vs. Calculated strain induced transformation curves for SS304. The solid curves indicate best fit according to equations 2.2.19 and 2.2.20 for parameters α and β [74]

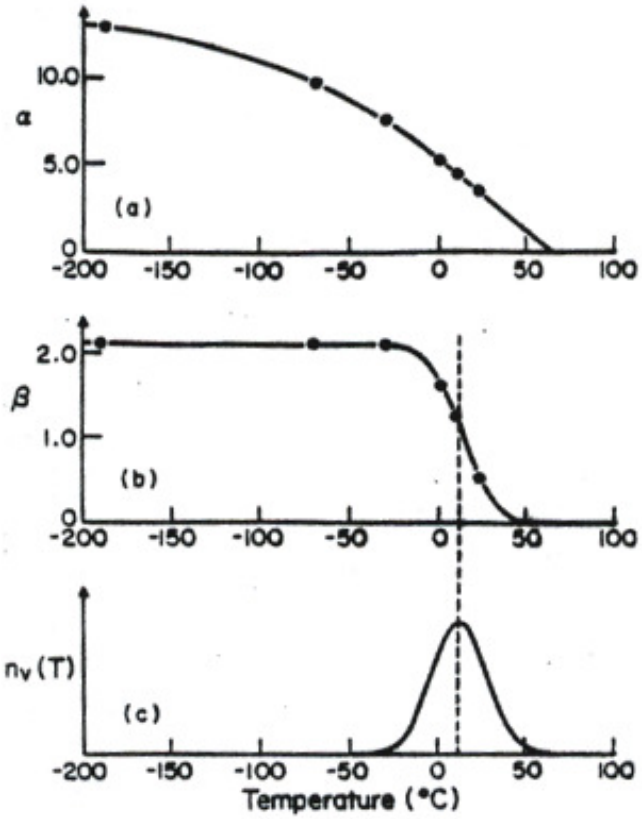

Fig. 2.2.6: Temperature dependence of kinetic parameters α and β from equations 2.2.19 and 2.2.20 and experimental data from fig 2.2.5 a) α parameter for shear-band formation, b) β for embryo formation and c) for Gaussian Distribution of Potencies [74]

The true stress – strain and associated volume fraction martensite vs. true strain at various temperatures have been measured by Olson and Cohen [53] to study the transformation characteristics and flow behavior of the TRIP steels under uniform tensile stresses. The transformation curves (σ – ε) and (f – ε) in figure 2.2.7 show the predicted sigmoidal shape at higher temperatures while at lower temperatures the curves follow a linear trend.

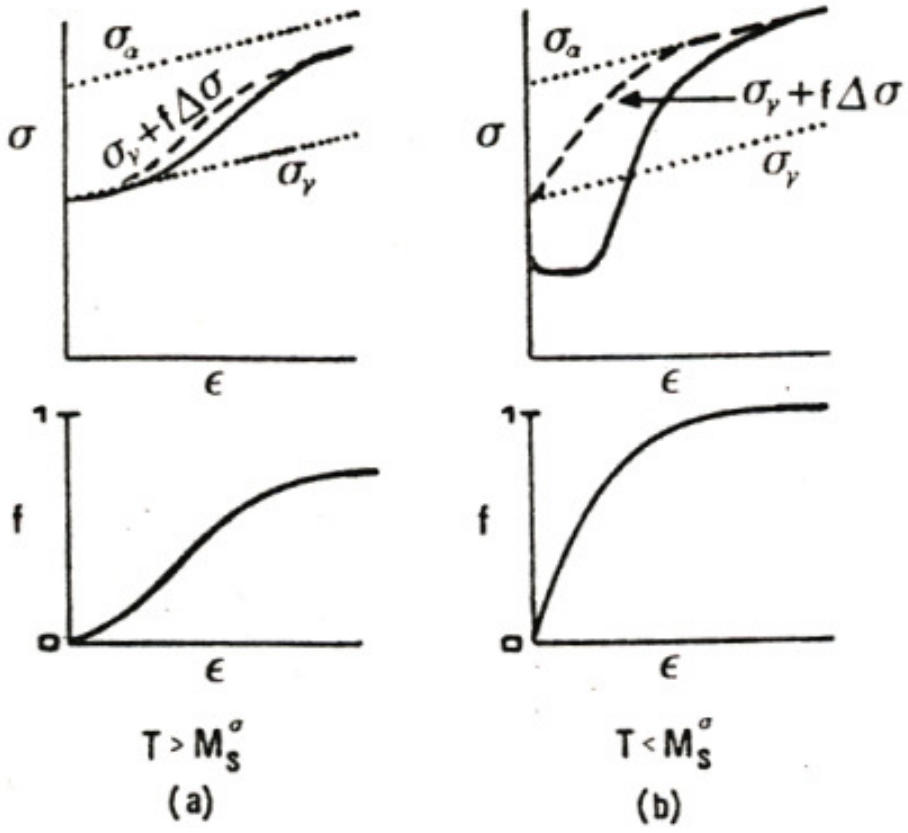

Fig. 2.2.7: Schematic True Stress – Strain and Volume Fraction Martensite – Plastic Strain plots for a) Stress-assisted and b) Strain Induced Transformation [78]

Just as in stress – assisted transformation, the dynamic softening is a dominant factor at low strains which causes the flow stress to fall below that of the stable austenite matrix. The above behavior correlates the basic change in transformation and this is also shown by the temperature dependence on the yield stress as shown in figure 2.2.8. The transformation curves (*f* vs. *ε*) in

figure 2.2.8 (a and b) have a sigmoidal shape at higher temperatures, whereas at lower temperatures, the curves approach an initially linear behavior. The above behavior correlates the basic change in transformation and this is also shown by the temperature dependence on the yield stress as shown in figure 2.2.9.

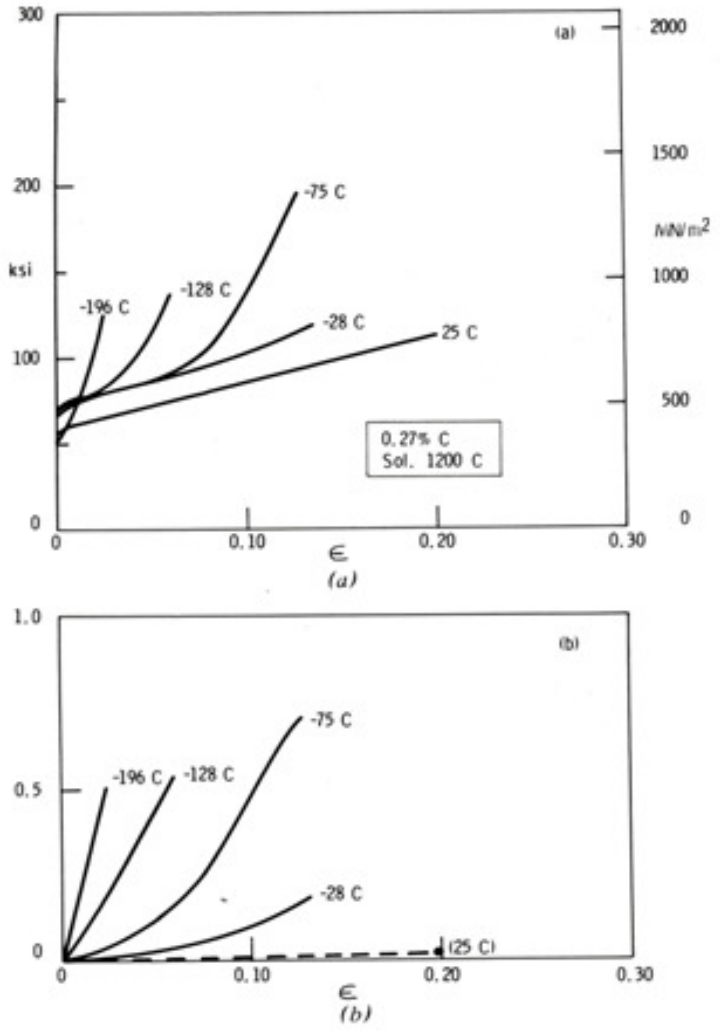

Fig. 2.2.8: Tensile properties and transformation curves for a 0.27%C TRIP steel (a) Stress-Strain (b) Volume Fraction martensite Vs. Plastic Strain [74]

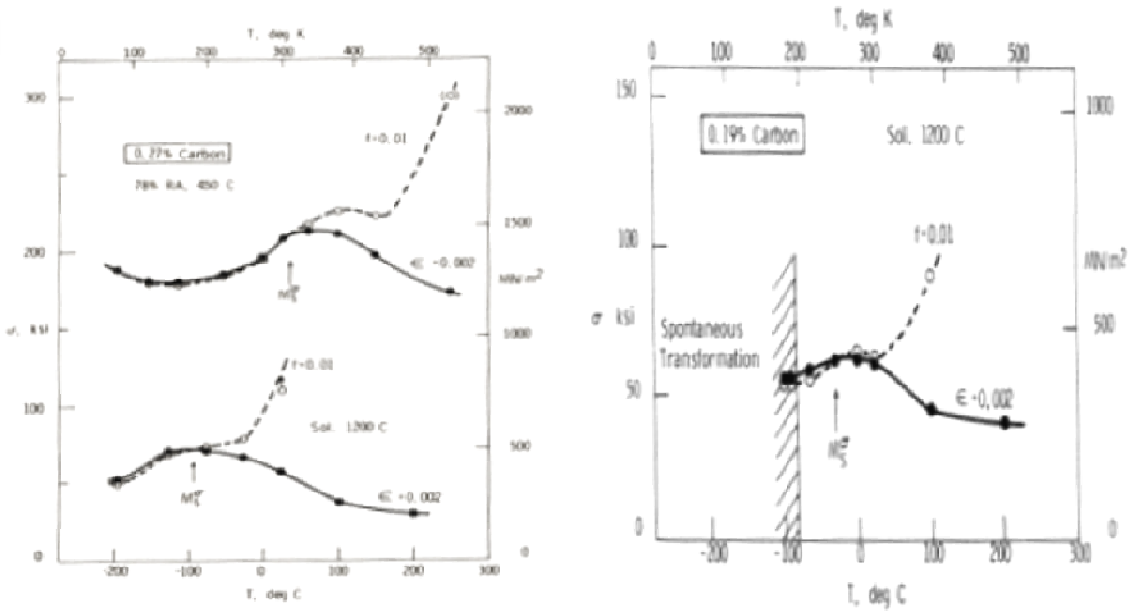

Fig. 2.2.9: (a) Temperature dependence of yield stress on and stress for martensitic Transformation in 0.27C TRIP steel warm-worked (b) 0.19C TRIP steel (solution treated) [74]

2.2.3 Transformation Volume Expansion

The positive volume change associated with the FCC → BCC martensitic transformation plays a critical role not only in controlling the shear instability of the alloy design, but is also a factor that influences the Gibb's free energies associated with the FCC and BCC phases while calculating the austenite stability under stress, as discussed in section 2.3 equation 2.3.4. Both Haidemenopoulos [80] and Grujicic [82] had developed initial models to quantify the volume expansion of transformation, which was further modified by Kuehmann [83]. The relative change in volume due to transformation can be defined as [83]

$$\frac{\Delta V}{V} = 2\left[\frac{a_{BCC}}{a_{FCC}}\right] - 1 \qquad (2.2.21)$$

Where a_{BCC} and a_{FCC} represent the BCC and FCC lattice parameter, which is composition dependant. Kuehmann fit a linear equation which described the lattice parameters as a function of the equilibrium austenite composition at the critical transformation temperature. The contribution and fit due to each alloying element for the BCC lattice parameter was determined through experimental values which were then calibrated with theoretical predictions to obtain the following relationship:

$$a_{BCC} = 2.8664X_{Fe} + 2.8884X_{Co} + 2.9483X_{Cr} + 2.6385X_{Ni} + 0.3017X_{Fe}X_{Ni} \quad (2.2.22)$$

Where X represents the atomic fraction of the underlying alloying element. The composition dependence of the FCC lattice parameter is calculated by the description of the two gamma states of the INVAR anomaly, a model which can be used for multi-component high strength steels [84]. This model assumes that the two gamma states have a specific free energy difference in equilibrium for their respective electronic states, and the probability of one state over the other is described by

$$\frac{f_1}{f_2} = \frac{g_1}{g_2}\exp\left(-\frac{\Delta E}{kT}\right) \quad (2.2.23)$$

Where f_1 and f_2 define the fraction of Fe atoms in the two respective electronic states ΔE is the energy difference and kT is the thermodynamic Boltzmann factor. A degeneracy ratio based on the atom fractions (probability) in equation 2.2.23 was used by Kuehmann based on earlier research [85-88],

$$\frac{g_1}{g_2} = \frac{A+B}{2} + \frac{A-B}{2}\tanh\left[D\left\{\frac{T}{T_C} - 1\right\}\right] \quad (2.2.24)$$

Where T_C is the Curie temperature and A (1.05) and B (3.10) are fitting parameters related to T_C. D (1.0) is the sharpness of the transition [89].

Using equations 2.2.23 and 2.2.24

$$a_{FCC} = (3.57f_1 + 3.64f_2)X_{Fe} + 3.5239X_{Ni} + 3.5440X_{Co} + 3.57X_{Cr} \quad (2.2.25)$$

Where $f_1 + f_2 = 1$.

2.2.4 Ductility Enhancement

The objective of having a deeper understanding of the kinetics of stress – assisted martensitic transformation and the factors affecting it is so that we are able to effectively control the transformation characteristics of a TRIP alloy to give us the properties we want. Earlier studies by Leal [79] and Young [81] in metastable fully austenitic steels have demonstrated that transformation plasticity can substantially enhance uniform ductility when fracture is controlled by shear instability. The effective strain hardening, as observed in figures 2.2.10 and 2.2.11 and the ability of the transformation to provide the increase in slope of the true stress – true strain curves is useful in stabilizing the plastic flow. According to Olson [50], the stress – strain curve of a transforming material can approach the ideal exponential shape $\boldsymbol{\sigma = \sigma_0 \, exp \, \varepsilon}$ where, the strain hardening rate would be just enough to maintain plastic flow, thereby maximizing the uniform ductility.

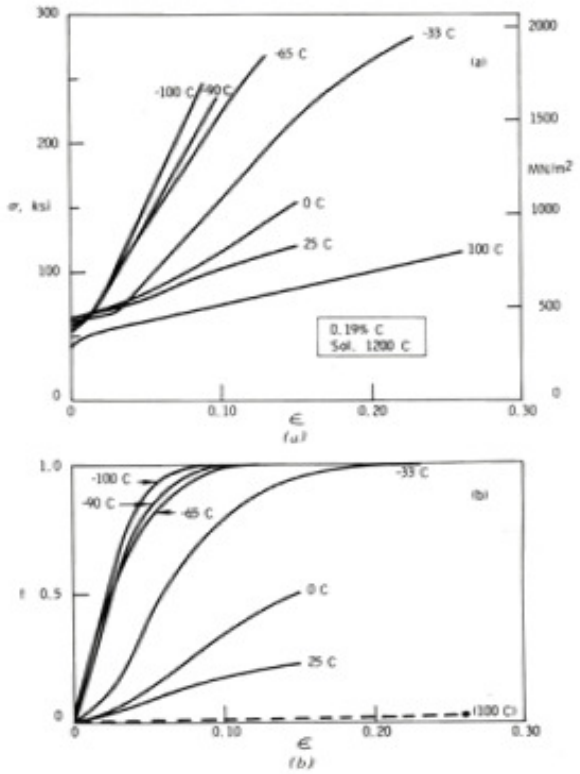

Fig. 2.2.10: Tensile properties and transformation curves for a 0.19%C TRIP steel (a) Stress-Strain (b) Volume Fraction martensite Vs. Plastic Strain [74]

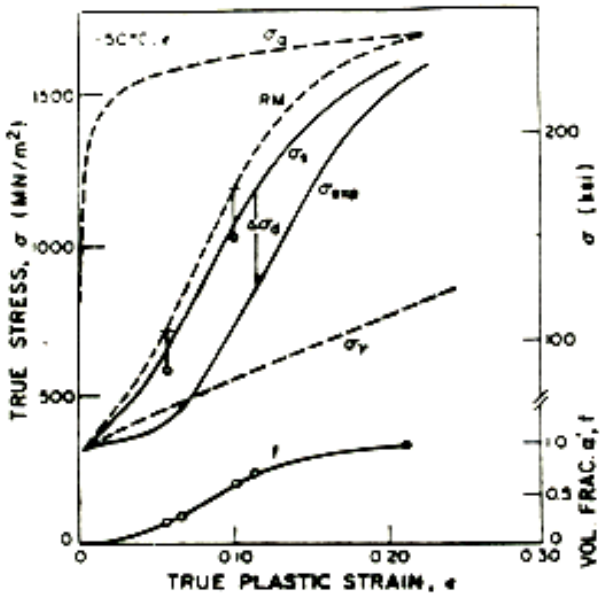

Fig. 2.2.11: Experimental Flow Stress and Volume Fraction Martensite vs. Plastic Strain for Metastable Austenitic TRIP Steel at -50C. Dashed Curves show the trend for the stable Austenite Flow Stress [77]

Figure 2.2.10 depicts the case of transformation behavior observed in low carbon austenitic TRIP steel showing that more strain hardening occurs at lower temperatures. Figure 2.2.11 shows that static hardening becomes dominant at higher strain rates. The phenomenon of using strain hardening mechanism for plastic flow to enhance ductility has been used in our alloy design for both high tensile (stretch) ductility and high shear ductility. The following two subsections describe the individual approaches to each of the above two ductile modes. The concept of shear ductility requires increasing the thermal addition to frictional work function, the concept of which is described in detail in section 2.2.3.2.

2.2.4.1 Tensile Ductility

While the theoretical foundation for the application of Transformation-Induced plasticity to promote uniform tensile ductility in austenitic steels is derived from the works of Olson and Cohen [59, 68, 73-74], the experimental work from the research of Leal [79] provided the necessary data points to create a basic model for optimum stability of the matrix with respect to transformation. Leal had studied the dependence of ductility on relative transformation stability using different austenitic TRIP alloys with varying Ni and Cr contents to vary the matrix stabilities. Figure 2.2.12 shows the results of the fractional increase in uniform tensile ductility with respect to the stable austenite matrix. The parameter θ represents the normalized temperature as defined by the expression –

$$\theta = \left\{ \frac{T - M_s^\sigma}{M_d - M_s^\sigma} \right\} \tag{2.2.26}$$

From the figure 2.2.12 (a) it is seen that the optimum transformation temperature lies between the M_s^σ (θ = 0) and the M_d (θ = 1) temperatures. Figures 2.2.12 (b) and 2.2.13 shows the

numerical values for the increment in uniform tensile ductility with temperature [79]. The peak ductility is observed at a temperature of around M_s^σ + 30°C, after which a sharp decrease in the uniform ductility is observed.

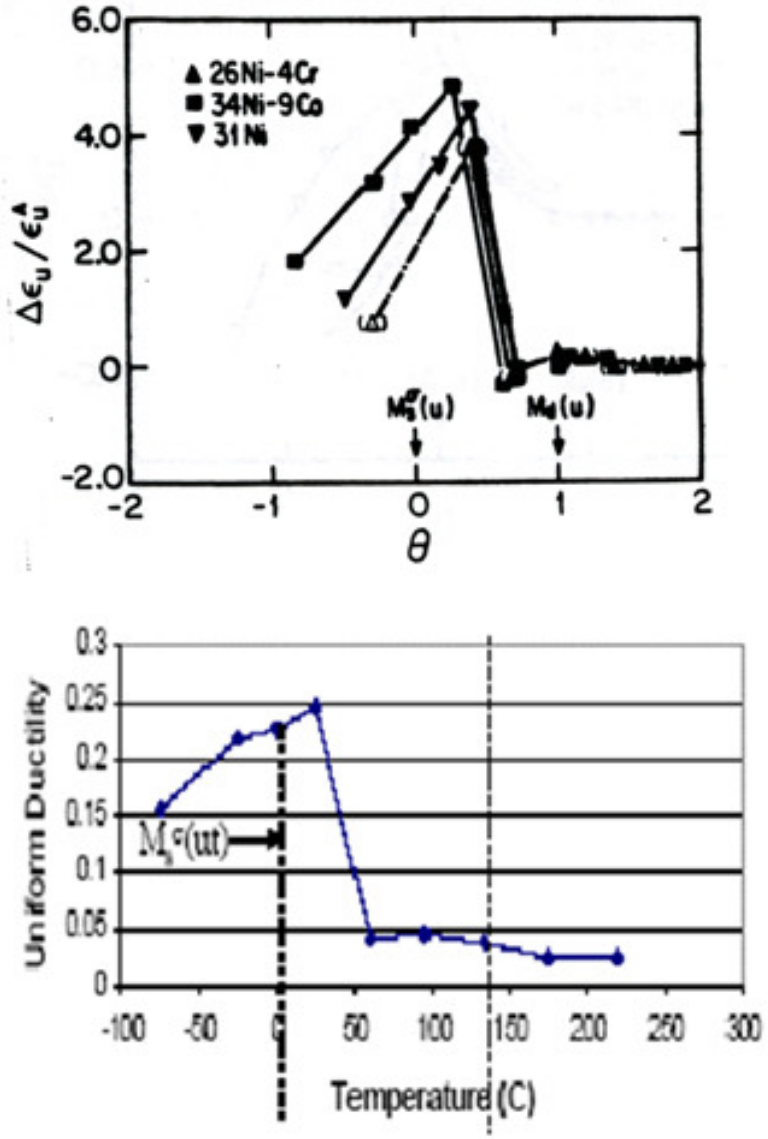

Fig. 2.2.12: a) Relative and **b)** actual Enhancement of Uniform elongation vs. Normalized temperature for various precipitation – strengthened TRIP Steels [77]

Figure 2.2.14 shows the strain to fracture dependence on normalized temperature (θ), which again shows that the optimum performance in terms of maximizing the strain-to-fracture lies between the M_s^σ ($\theta = 0$) and the M_d ($\theta = 1$) temperatures zones.

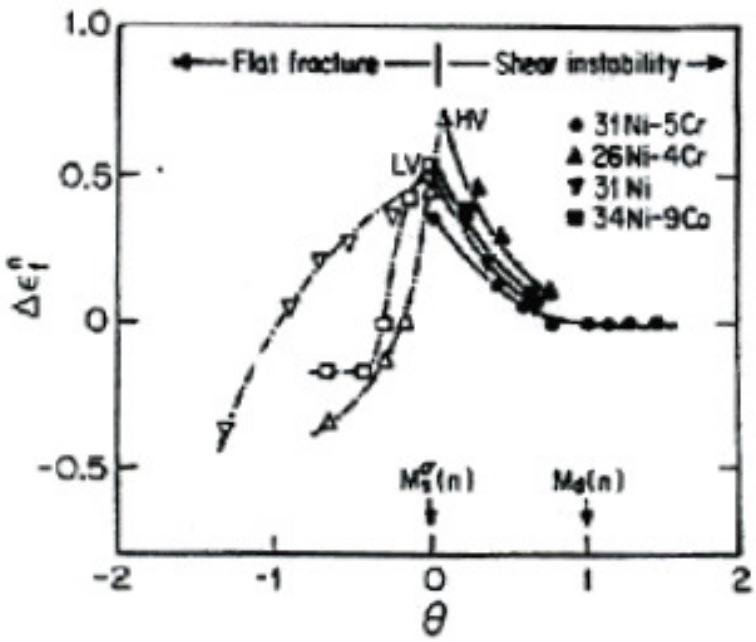

Fig. 2.2.13: Enhancement of Strain-to-Fracture vs. Normalized temperature for various precipitation – strengthened TRIP Steels [77]

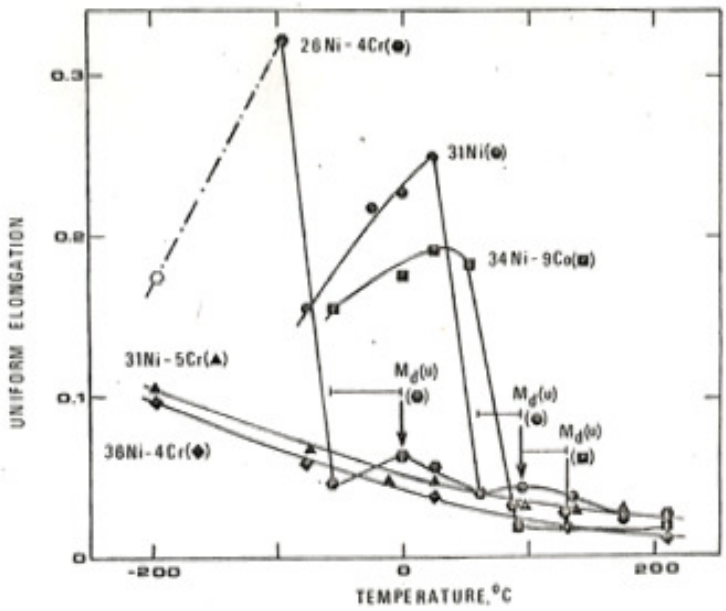

Fig. 2.2.14: Plastic Uniform Elongation vs. Temperature with dashed line showing premature failure. The expected error in measured M_d temperature is also shown [77]

The requirement for our new alloy design for Blast protection application is to have maximum uniform ductility at room temperature. Keeping this in mind, the optimum M_s^σ (θ = 0) for our design is kept at 0°C - 5°C.

2.2.4.2 Shear Ductility

For the case of designing alloys with high fragment protection, we need to consider improving the shear-instability resistance of materials. Although the structural performance of EX425 under in-plane shear loading is yet to be analyzed, we have been able to formulate preliminary designs based on the Olson-Cohen isothermal transformation model [74]. In pure shear deformation, the strain induced transformation delays shear localization to higher strains. The effects of transformation induced plasticity on shear instability have been previously studied by Haidemenopoulos [80].

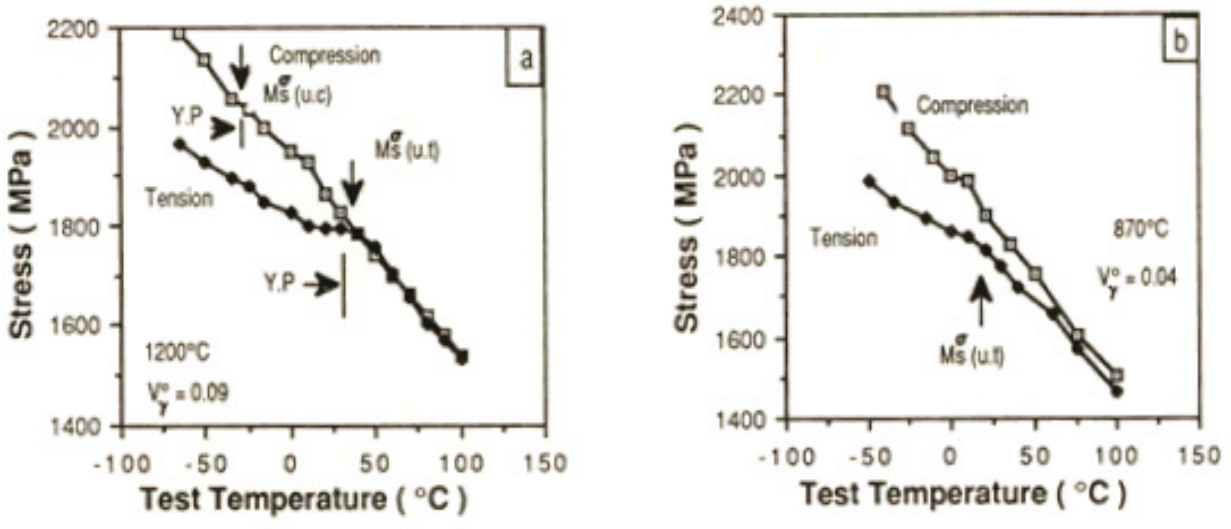

Fig. 2.2.15: Temperature dependence of Tensile and compressive flow stresses indicating the critical transformation M_s^σ temperature for specimens aged at a) 1200C and b) 870C [80]

It has been observed under both tension and compression, there is an increase in flow stresses (higher yield strength) with decrease in temperature, till a point where the stresses dip, signaling the martensitic transformation regime, and then increases again. The increase in the flow stresses in some cases after transformation is due to the composite nature of the behavior, with both austenite and martensite phases adding its own contributions to the flow stress behavior. Figure 2.2.15 shows the results of the Stress- temperature dependence using a single specimen of 4340 commercial steel with varying amount amounts of retained austenite characterizing the different flow behavior observed. The measured M_s^σ temperatures under different stress states – tension, compression and shear where compared where the shear M_s^σ temperature was taken to be the mean of the measured M_s^σ temperatures from tension and compression stress states –

$$M_s^\sigma(shear) = \left(\frac{1}{2}\right)[M_s^\sigma(tension) + M_s^\sigma(compression)] \qquad (2.2.27)$$

And the M_s^σ temperature for crack-tip state was determined by a simple extrapolation from the tension and compression states. Under shear loading, the strain induced nucleation plays a critical role since the transformation can delay the shear localization to higher strain under these conditions. Haidemenopoulos et al. [80] performed thin walled torsion tests on specimens with different levels of retained austenite at a temperature higher than the $M_s^\sigma(shear)$ and obtained the following shear stress – strain curves as shown in figure 2.2.16. The specimens with higher amounts of retained austenite showed delayed shear instability leading to a uniform shear strain increase of overall ~ 25-30%. Recently Latourte [139] calculated the shear instability values for the different austenite volume fractions from the data of Haidemenopoulos for the two $M_s^\sigma(shear)$ values. The results are shown in figure 2.2.17.

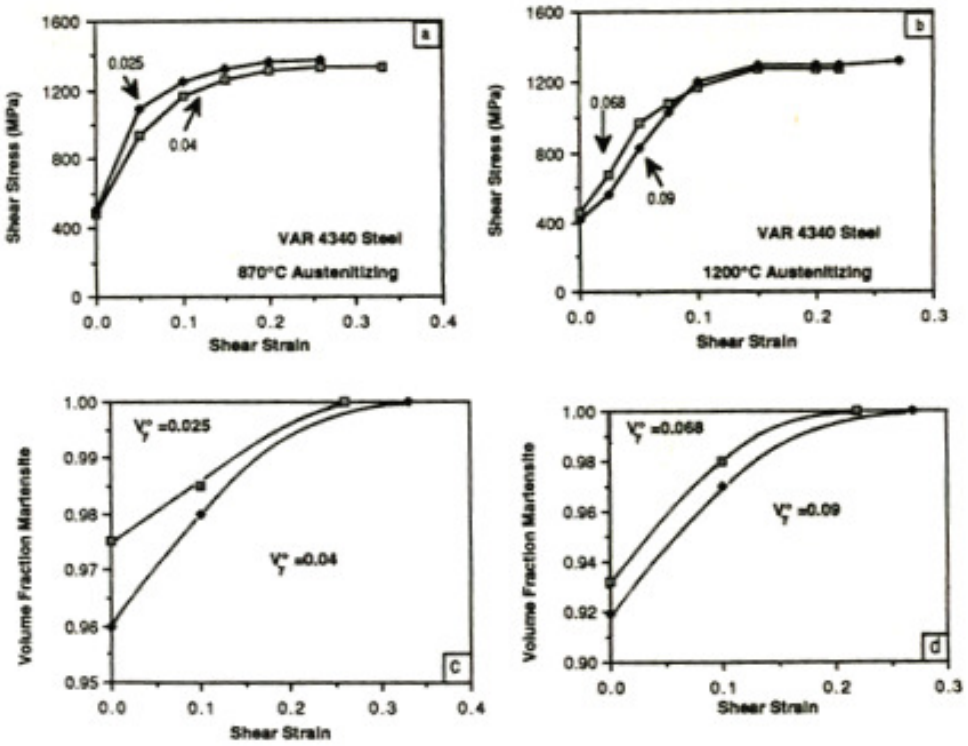

Fig. 2.2.16: Stress- Strain curves and their corresponding martensite volume fractions with respect to total plastic strain during pure shear deformation of 4340 steel aged at 870C (a, c) and 1200C (b, d) [80]

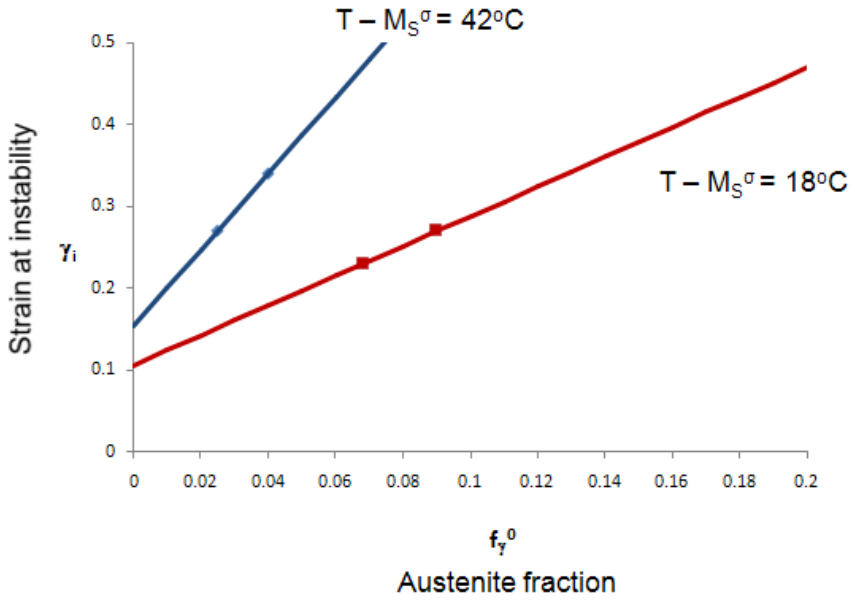

Fig. 2.2.17: Plot of shear strain at instability as a function of the measured austenite fraction showing that the optimum performance lies ~ 40C above the shear M_s^σ temperature [139]

The optimum performance is found at a temperature ~ 40°C above the $M_s^{\sigma}(shear)$ temperature where a higher instability strain - per unit austenite volume is obtained. When plastic flow is controlled by stress-assisted nucleation, our knowledge of the kinetics of isothermal martensitic transformations can be effectively used to predict the shape of stress-strain curves. Using equation 2.2.15, the temperature dependence of the transformation stress is calculated for tension and compression stress states, shown by the solid curves in figure 2.2.17, and the predicted transformation curve for a shear-stress state has been superimposed between the curves for tensile and compressive stress states, since the M_s^{σ} *(shear)* is expected to be the average for the M_s^{σ} temperatures for tensile and compressive stress states as in equation 2.2.27.

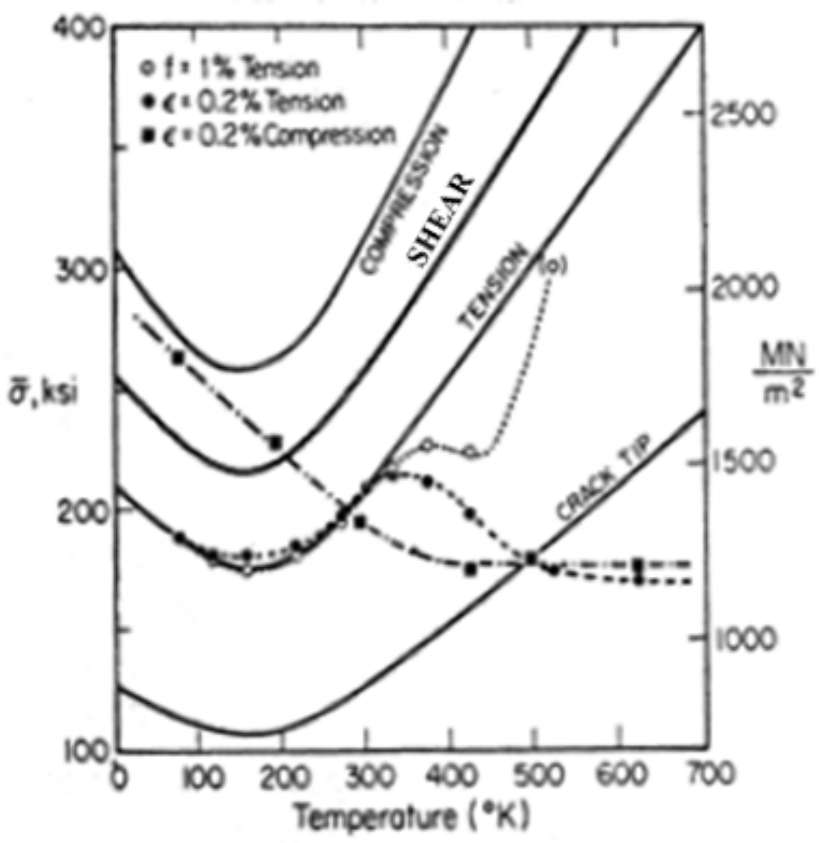

Fig. 2.2.18: Stress – Temperature dependence of TRIP steels with the solid curves showing the theoretical predictions matching with the solid dark points noting the experimental values [79]

The measured yield stress for compression and tension are shown along with the predicted shear stress state to compare the relative values for the three states. Now it is clearly seen from the figure 2.2.18 that under shear-optimized conditions, the tensile yield strength of the material will be reduced by the transformation. Below 300K there is a large strength differential effect between tension and compression stress states, which suggests while plastic flow is controlled by transformation in tension, slip is responsible for flow under compression. Figure 2.2.18 shows low yielding at 300K is controlled by transformation in tension.

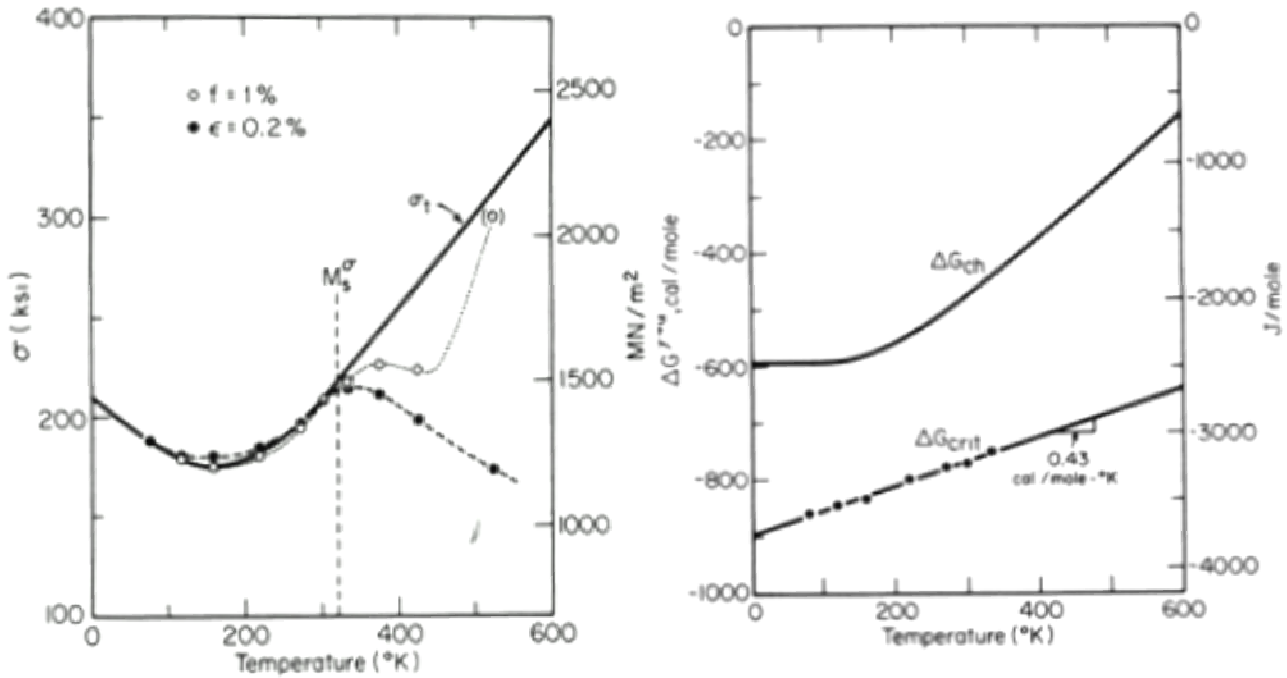

Fig. 2.2.19: The stress-temperature dependence showing the typical transformation regime defined by the M_s^{σ} temperature and the variation in the Gibb's free energy function with temperature from the Critical free energy for transformation [79]

However, above 500K, slip controls both states. This is not desirable since we want the shear alloy to also have adequate yield strength under tension in the operating temperature. This can be offset by increasing the thermal-dependence of the frictional work of martensite interfaces W_f^{Sol} – thermal, which causes isothermal transformation, thereby reducing the slope ($d\sigma/dt$) of the stress-

assisted transformation region. In this way, we can achieve the necessary yield strength performance levels under both shear and tension stress states. As will be explained later, in order to increase the W_f^{Sol}, it is needed to increase the relative amounts of Cr, thereby decreasing Ni to maintain the level of optimum austenite stability. The thermal-dependence of the frictional work of martensite interfaces W_f^{Sol} – thermal and related austenite stability considerations will be discussed in detail in section 2.3.2.

2.3 Austenite Stability

As just discussed, mechanical properties of TRIP steels like uniform ductility, toughness and transformation temperatures are dependant on the matrix (austenite) stability (ability to resist transformation). While Stavehaug [13] demonstrated the improved ductility obtained for his austenitic alloys close to M_s^{σ} temperature for uniaxial tension, Leal [79] showed the improved toughness for his martensitic alloys around the critical M_s^{σ} temperature for transformation of the retained austenite. Stavehaug varied the austenite stability by changing the alloy compositions (6 different alloys), although the matrix composition can be varied by different aging conditions. Young [81] studied the effect of volume expansion on toughness increment and used a power law to define the inter-relationship between the two.

The stability of austenite is controlled by the amount and type of the alloying element [93] and the strength of austenite influence the kinetics of transformation and martensite morphology [91-92]. The energetics of the transformation has been studied in detail by Olson, Tzusaki and Cohen [94]. In this section, a quantitative model is detailed for austenite phase stability with respect to diffusionless martensitic transformation, based on Olson and Cohen's nucleation theory.

2.3.1 Austenite Stability Parameter (ASP)

The total driving force for martensitic transformation is a function of composition and stress state for a given material condition [13]. We again write the critical driving force condition from the Olson and Cohen model as [33]:

$$\Delta G^{Chem} + G^{el} + \left(\frac{2\sigma}{nd}\right) = -(W_{Ath} + W_{Th}) \quad (2.3.1)$$

W_{Ath} and W_{Th} are the athermal (only composition dependent) and thermal (both composition and temperature dependent) components of the interfacial frictional work, respectively. In the equation 2.3.1 above, the Gibb's free energy change ΔG^{Chem} is negative while the terms G^{el}, $\left(\frac{2\sigma}{nd}\right)$ and $(W_{Ath} + W_{Th})$ are always positive. The total driving force of transformation is defined as [13]:

$$\Delta G^{Tot} = \Delta G^{Chem} + \Delta G^{\sigma} \quad (2.3.2)$$

For diffusionless phase transformation, the chemical driving force (ΔG^{Chem}) at a constant temperature is given by [95]

$$\Delta G^{Chem} = \Delta G^{Chem}_{BCC} - \Delta G^{Chem}_{FCC} \quad (2.3.3)$$

Thermo-Calc with the *Ni-data* (ver. 7) database along with the *CMD* interface with *MART5* database can be used to determine the Gibb's free energy associated with the FCC and BCC phases during transformation using equilibrium austenite composition and the difference between the two free energies gives the value of ΔG^{Chem}. ΔG^{σ} is a function of stress state and stress level, which are both defined by the Blastalloy working conditions. The dependence of

mechanical driving force of martensitic transformation on applied stress is given by the relation [97]:

$$\Delta G^{\sigma} = -[0.7183\,\sigma + 6.85\left(\frac{\Delta V}{V}\right)\sigma_h - 185.3\{1 - \exp(-0.003043\,\sigma)\}]$$

(2.3.4)

Where $\left(\frac{\Delta V}{V}\right)$ represent the volume change associated with an FCC → BCC transformation which has a typical value of ~ 4% in steels. The term σ_h is the hydrostatic stress which depends on the stress state and the respective values for tension and shear states have been shown in equation 2.3.5 and 2.3.6. There are two stress states for which we need to determine ΔG^{σ}:

Uniaxial Tension: $\sigma_h = (\frac{\sigma}{3})$, and (2.3.5)

Shear Stress state: $\sigma_h = 0$ (2.3.6)

Substituting in equation 2.3.4, the mechanical driving force for martensitic transformation for the two stress states (tension and shear) can be written as:

Under tension:

$$\Delta G^{\sigma} = -[0.7183\,\sigma + 6.85\left(\frac{\Delta V}{V}\right)\left(\frac{\sigma}{3}\right) - 185.3\{1 - \exp(-0.003043\,\sigma)\}]$$

(2.3.7)

And, under shear:

$$\Delta G^{\sigma} = -[0.7183\,\sigma - 185.3\{1 - \exp(-0.003043\,\sigma)\}]$$ (2.3.8)

To make sure that nucleation and transformation occurs at a temperature we desire, we set ΔG^{Tot} to the critical driving force required for martensitic nucleation (ΔG^{Crit}) at the required transformation temperature, which is defined from equation 2.3.1 as:

$$\Delta G^{Crit} = -\left[g_n + W_f^{Sol}\right] \quad (2.3.9)$$

Where g_n = 1010 J/mol and W_f^{Sol} is the frictional work of the martensite interface motion. The frictional work function for martensite interfacial motion will be discussed in detail in section 2.3.2. At the critical transformation temperature (M_s^{σ}), the total driving force ΔG^{Tot} is equivalent to the critical driving force ΔG^{Crit} at $\sigma = \sigma_y$, hence we get:

At M_s^{σ}, $$\Delta G^{Tot} = \Delta G^{Crit} \quad (2.3.10)$$

Therefore,

$$\Delta G^{Chem} + \Delta G^{\sigma} = -\left[g_n + W_f^{Sol}\right] \quad (2.3.11)$$

Equation 2.3.11 can be re-written as (*at* $T = M_s^{\sigma}$) (in SI Units)

$$\Delta G^{Chem} + W_f^{Sol} = -[g_n + \Delta G^{\sigma}] \quad (2.3.12)$$

Or, (as a linearized function)

$$\Delta G^{Chem} + W_f^{Sol} = -\left[g_n + \sigma_y \left(\frac{d\Delta G^{\sigma}}{d\sigma}\right)\right] \quad (2.3.13)$$

Here ΔG^{ch} and W_f are composition dependent terms and σ_y is the yield strength. For alloys without warm-work, the critical stability parameter is $\Delta G^{Chem} + W_f^{Sol}$. Equation 2.3.12 is also termed as the ***Austenite Stability Parameter (ASP)***. The right hand side of equation 2.3.12 is independent of composition for each yield stress goal and equals the critical ASP values (at M_s^{σ}). The Austenite Stability Parameter is a quantitative representation of the transformation stability of the austenite matrix and is a measure of the total (critical) energy required to drive the aforementioned FCC → BCC transformation at the critical temperature of M_s^{σ}. This parameter has been used extensively in our alloy design in section () to model the precise stress – assisted transformation temperature (M_s^{σ}).

2.3.2 Frictional Work of Martensite Interface Motion

The approach to martensitic nucleation theory has adapted theory of slip deformation to the transformation dislocation motion to nucleate a martensite embryo [82]. The compositional dependency of the frictional force arising due to the slip deformation have been investigated by Arsenault et al. [98] whereby a $X_i^{0.5}$ dependence of the frictional stress for dislocation motion was established, assuming a random solution structure. Ghosh and Olson [95] have further investigated this dependence in a much more detailed analysis of the critical driving force for both athermal and thermal nucleation, the basis of which stems from Olson and Cohen's original dislocation based embryo formation kinetic theory of FCC → BCC heterogeneous martensitic nucleation.

The total interfacial friction work (W_f^{Sol}) is defined as the sum of the athermal (W_{Ath}, only composition dependent) and thermal (W_{Th}, both composition and temperature dependent) components of the interfacial frictional work, respectively [95]

$$W_f^{Sol} = W_{Ath} + W_{Th} \tag{2.3.14}$$

2.3.2.1 Athermal Frictional Work of Nucleation

Although Arsenault et al. correctly formulated the compositional dependence of the frictional stress for slip dislocation motion as being of the form of $X_i^{0.5}$, the relation does not take into full account the long range interaction frictional forces prevalent at finite temperatures. This was corrected by Ghosh and Olson [95] whereby experimental data points of the required Athermal stress for slip deformation for both FCC and BCC alloys were taken into consideration to form a

constitutive equation defining the total athermal frictional work at any given temperature. Based on this approach, the athermal frictional work opposing the motion of martensitic interfaces due to solid solution strengthening is modeled by linear superposition:

$$W_{Ath} = \sqrt{\sum_{i} (K_{\mu}^{i} X_{i}^{0.5})^2} + \sqrt{\sum_{j} (K_{\mu}^{j} X_{j}^{0.5})^2} + \sqrt{\sum_{k} (K_{\mu}^{k} X_{k}^{0.5})^2} + K_{\mu}^{Co} X_{Co}^{0.5} \quad (2.3.15)$$

where *X* is in mole fraction. The elements represented by '*i*' are C and N, while '*j*' represents Cr, Mn, Mo, Nb, Si, Ti, and V, and '*k*' represents Al, Cu, Ni, and W. The equation 2.3.15 above is divided into four groups depending upon the alloying elements and their respective values of relative obstacle strength, K_{μ} which represents the strengths of different solutes for the fcc/bcc martensite interface. The effect of cobalt is added separately since it is known to reduce the interface frictional work due to reduction in shear modulus [174]. Table 2.3.1 lists the values of the athermal strengths of different constitutional elements for the fcc/bcc martensite interface,

J/mol	**Al**	**Ti**	**Cr**	**Ni**	**Mo**	**V**	**C**	**N**	**B**	**Fe**
K_{μ} - ath	280	1473	1868	172	1418	1618	1409	3097	0	N/A

Table 2.3.1: Athermal strength of different solutes for the fcc/bcc martensitic interface [95]

2.3.2.2 Thermal Activation Frictional Work of Nucleation

While the athermal mode of martensitic transformation starts at a pre-fixed temperature of M_s and then follows a linear trend, the isothermal mode of martensitic transformation proceeds as a function of time at a fixed temperature, fig 2.2.2. The isothermal mode of transformation has

been studied before by Raghavan [31]. Ghosh and Olson [96] have extended the analysis to the kinetics at sub-zero temperatures to account for the thermal and compositional dependence of the interfacial frictional work for low temperature martensitic transformation. Assuming similar $X^{0.5}$ concentration dependence of frictional work for multi-component systems and using the same superposition law as in section 2.3.2.1, the thermal component of interfacial friction is given as [96]

$$W_o = W_o^{Fe} + \sqrt{\sum_i (K_0^i X_i^{0.5})^2} + \sqrt{\sum_j (K_0^j X_j^{0.5})^2} + \sqrt{\sum_k (K_0^k X_k^{0.5})^2} + K_0^{Co} X_{Co}^{0.5} \quad (2.3.16)$$

Where X is mole fraction of each component. The elements represented by 'i' are C and N, while 'j' represents Cr, Mn, Mo, Nb, Si, Ti, and V, and 'k' represents Al, Cu, Ni, and W. W_0^{Fe} is the level of for pure Fe and is taken to be ~ 836 J/mol [96]. The K_0 coefficients determine the thermal components of the interfacial work due to various solute atoms at absolute zero and their respective values for each of the components have been given in table 2.3.2.

J/mol	**Al**	**Ti**	**Cr**	**Ni**	**Mo**	**V**	**C**	**N**	**B**	**Fe**
K_0 - Th	576	3031	3923	345	2918	3330	21216	16986	0	0

Table 2.3.2: Thermal Strength of different solutes for the fcc/bcc martensitic interface [96]

From table 2.3.1 it is seen that Cr is effective in increasing the W_0 thermal term since its K_0 value is 3923 J/mol. The K_0 coefficients determine the thermal contributions to the interfacial work due to various solute atoms referenced at absolute zero. According to Arsenault et al. both size and modulus effects contribute to solid solution strengthening to evaluate the thermal dependencies. Using Arrhenius's strain rate relationship, Kocks et al. [92] studied the stress dependence of

activation energy for rigid barriers for any given barrier height. Using the same analogy Ghosh and Olson provided the thermal dependence of the total work for interfacial motion which included W_o, the composition part of the work function, as

$$W_{Th} = W_o \left[1 - \left(\frac{T}{T_\mu}\right)^{\frac{1}{q}}\right]^{\frac{1}{p}} \quad (2.3.17)$$

where W_0 is calculated according to equation (previous). The T_μ temperature is associated with the base thermal barrier (Q_O in Arrhenius strain relationship) and is taken to be in the range 500 – 510 K and is interfacial rate dependent. For our studies, the values of the coefficients 'p' and 'q' have been taken to be ½ and $^3/_2$, as has been predetermined by Kocks, Argon and Ashby [92] for dislocation obstacle interaction mechanism by Strain. This corresponds to a weakly non-linear form of the linearized relation from equation (2.2.7).

2.4 Gamma Prime (γ′) - Strengthening Mechanism

Many Ni- based alloys are age-hardenable by a fine dispersion of γ' precipitates. The strengthening mechanism employed in this alloy design is the precipitation of the same γ' intermetallic phase which impedes dislocation shear through APB formation. The γ', represented as Ni_3 (Ti, Al), is an ordered super lattice phase and has an $L1_2$ structure (ordered face centered cubic) [99]. Mechanical properties such as yield strength, UTS and creep resistance are strongly dependent upon the size and distribution of the γ' precipitates [99-100]. The low energy of its coherent interface with the matrix promotes precipitation by homogenous nucleation reaction. The coherency strain resulting from a lattice mismatch and existence of order in the particles is the major contributor to the strengthening mechanism. Earlier studies [101] of high strain hardening due to θ – particles have shown that these precipitates are not cut by the dislocations

due to deformation. The study on precipitation-hardened alloys with small coherent precipitates such as γ' in high Ni alloys have shown that precipitates are usually sheared by dislocations. Figure 2.4.1 above shows a TEM (BF) image of an aged sample of a Ni-base alloy at a true strain of 0.15 showing the shearing of γ' precipitates by dislocation pairs. Ham proposed a model whereby when one dislocation cuts an ordered particle, the anti-phase boundary energy created must be balanced by the force on the dislocation. According to Najafi and Asgari [99], in such cases, the required stress to cut the particle is less than Orowan bowing stress, which is necessary to bow a dislocation line between two rigid particles. In the case of dislocation pairs, the stress necessary to cut the ordered particle is even less than the stress required for single dislocation cutting.

.

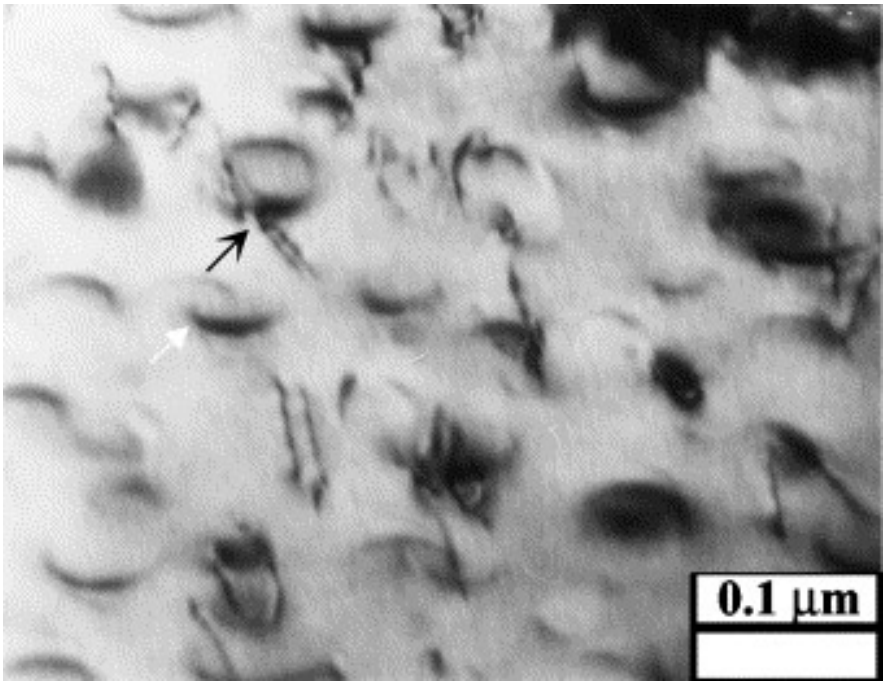

Fig. 2.4.1: Bright-field (BF) image of an aged sample at a true strain of 0.15 showing the cutting of γ' - precipitates by dislocation pairs. [99]

The method of dislocation bypass is important to determine the ideal size of the precipitates. For smaller precipitates, it is generally energetically favorable for dislocations to shear precipitates than to bypass them. The difficulty of shearing, however, increases dramatically with the size of the precipitates and eventually other mechanisms such as the Orowan bypass become more energetically favorable than dislocation cutting.

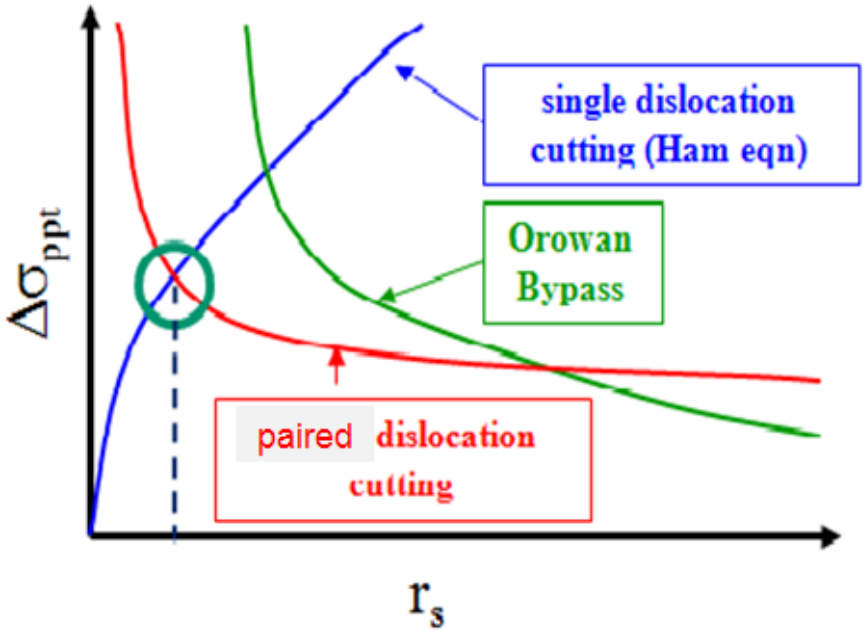

Fig. 2.4.2: Schematic representation of the optimum radius required for peak strengthening using Ham model for single and paired dislocation cutting

Additionally, in the case of ordered precipitates, the phenomenon of paired-dislocation cutting, also known as 'super-dislocation cutting' may become favorable as well. In this case, the dislocations travel in pairs, which offset the formation of anti-phase boundary when ordered precipitates are sheared. In the case for the γ' precipitates; the greatest strength contribution is achieved at the intersection of single and paired cutting, as shown in figure 2.4.2.

Brown and Ham [102] also showed that the more the APB is cut by trailing dislocation, the less effective the particles become as obstacles [102-104]. The cutting of γ′ precipitates, shown in figure 2.4.2, does imply that precipitates do not play a major role in the increasing strain hardening rate of aged γ' strengthened specimens. A decrease in matrix stacking fault energy (SFE) results in a wide separation of partials and a higher stress is required to recombine the widely separated partials. Shearing of γ′ precipitates by deformation twins should be very similar in nature to the shearing process by partial dislocations in $L1_2$ structures [99]. It has been reported that partial dislocations may easily shear $L1_2$ structures and produce stacking faults during this process [105]. The room temperature deformation process has shown shearing of γ′ precipitates by partial dislocations [106].

The quantitative effect of the strengthening due to γ′ precipitation in austenitic steels is documented by Silcock and Williams [97] on the commercial A286 austenitic steel. Their results provide a relationship between aging time, aging temperature, solution treatment temperature, and γ′ particle size, which is used to calibrate our strength model, based on the works of Ham et al. [102-103] for shear strength in a two-phase alloy involving particles of the strengthening phase impeding dislocation shear. The equation defining the shear strength is represented as

$$\Delta\tau = \left(\frac{\gamma_0}{2b}\right)\left[\frac{1}{\left\{\left(\frac{8\gamma_0 r_s f}{\pi G b^2}\right)\right\}^{\frac{1}{2}} - f}\right] \tag{2.4.1}$$

And

$$\tau = \tau_0 + \Delta\tau \tag{2.4.2}$$

where

f: volume fraction of γ'

b: matrix dislocation Burger's vector = 2.5 angstroms

γ_0: antiphase boundary (APB) energy of γ' phase

r_s: average radius of the particles

G: matrix shear modulus =76.54e9 N/m^2

τ_0: calibration point for strength without precipitates (fully austenitic specimen)

Keeping r_s fixed at its optimum size, the phase fraction of γ' can be determined to obtain the required yield stress objective. Yield stress is related to shear stress by

$$\sigma = M\tau \tag{2.4.3}$$

Where M is the polycrystalline Taylor factor is taken to be equal to 3 in this case. The optimum particle size was found from the aging time that obtained a maximum hardness, corresponding to a particle diameter of ~15 nm. This optimal point is known to represent the transition point of a change from a single dislocation shear cutting mechanism to a paired dislocation cutting of the particles as represented in figure 2.4.2. Equation 2.4.1 and 2.4.2 have been used to generate the gamma prime strength model shown in figure 7.1.1 along with experimental data points.

2.5 Grain Boundary Cohesion and Grain Refining Dispersion

Grain boundary cohesion and the presence of a refining dispersion to enable optimum matrix grain size go a long way in controlling and increasing the limit of fracture ductility in high strength austenitic TRIP steels [107]. Intergranular embrittlement is associated with the prior segregation of impurity atoms or substitutional atoms towards the grain boundaries [108-111]. A complete understanding of the influence of metallic alloying elements is necessary to predict and control the grain boundary embrittlement (GBE) in order to achieve the maximum ductility possible under various stress states [112]. Although early research [113-118] focused on building

simple thermodynamic models of the behavior of these alloying elements on the grain boundary, both empirical [119-120] as well as first principle quantum-mechanical models [121-122] have been brought forward to explain the effect of segregants on the grain boundary fracture resistance.

2.5.1 Alloying effects on Grain Boundary (GB) Cohesion

Geng, Freeman and Olson [123-127] have used rigorous first-principles methods to study the surface thermodynamic energy difference identified earlier [118] as related to premature GB fracture. The effect of Mo and Pd on substitutional segregation on σ_3-Fe was analyzed [127] as part of this research using the full-potential linearized augmented plane wave method [128], and using their thermodynamic models, Olson et al. showed that elements like Mo has a significant beneficial effect on the Fe grain boundary cohesion. Pd, on the other hand, increases the probability of embrittlement, although very weakly.

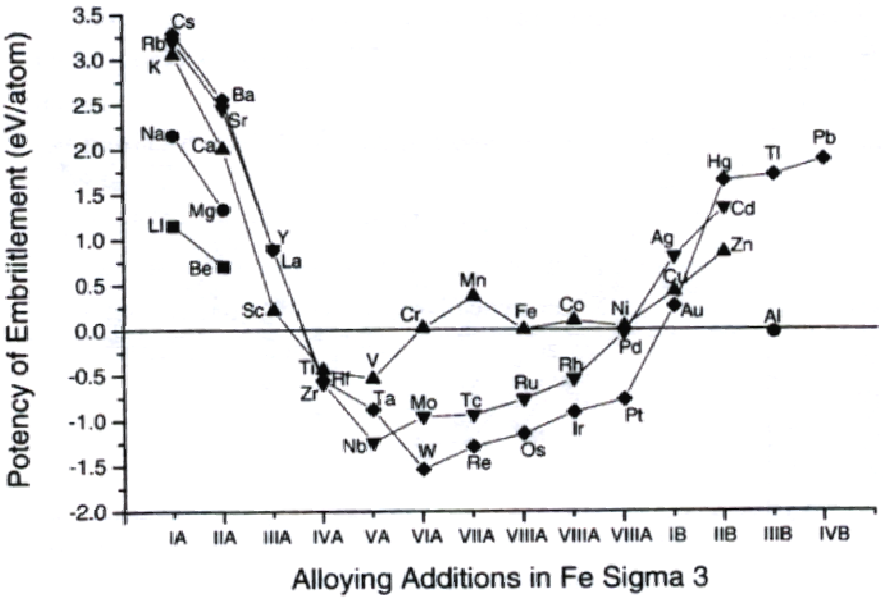

Figure 2.5.1: Embrittlement potency of substitutional additions on the Fe Σ3 (111) GB [112]

It is important to have an optimum atomic size to fit well within the substitutional sites along the grain boundary. The bonding character in both grain boundary and free surface environments have shown to define the behavior of the segregants in the grain boundaries. Figure 2.5.1 shows the relative potency of embrittlement (energy per atom) for various alloying elements grouped together according to their place in the periodic table. The addition should preferably have negative embrittlement potency.

Krasko and Olson [129] presented results of spin-polarized calculations of the atomic structure of Boron, Carbon, Phosphorus and Sulfur in an environment typical of that of a Fe atom where it is shown that boron atoms tend to occupy the center of a trigonal prism formed by Fe atoms in the core of the grain boundary. They also showed that boron and carbon have a different effect on the grain boundary bonding from that of Sulfur and phosphorus. While boron and carbon tend to strengthen the bonding of the Fe atoms in the grain boundary plain and across it thereby improving pinning properties to help reduce inter-granular fracture, sulfur and phosphorus on the other hand decreased the bonding strength across the grain boundary thereby leading to decrease in uniform ductility through premature inter-granular fracture [129].

2.5.2 Grain Refining Dispersion

The presence of a small volume fraction of a stable phase (at solutionizing temperature) is very useful in preventing the excessive grain growth of austenite during solutionizing treatment. Austenitic grain boundary refinement through grain boundary pinning is a critical factor in improving the fracture ductility of the steels. This can be achieved by having an austenitic grain refining dispersion which must be stable enough to remain out of solution during solution treatment of the alloy and must be fine enough (<1μm) with minimal volume fraction for

reduced interaction between the particles. They must also resist coarsening so that a fine and optimum austenite grain size can be maintained with a minimum of the dispersed boundary pinning phase [80]. It has been shown earlier [130] that microvoid nucleation on submicron (secondary carbides) dispersions is the cause of reduced ductility in many high strength TRIP steels, however these dispersions always have shown a positive effect by helping to pin the migrating grain boundaries maintaining optimum grain sizes. This pinning behavior was observed and quantitatively analyzed by Zener [131] where it was derived that the grain size is directly proportional to the ratio of the particle size and the volume fraction of the dispersed phase. Gore, Olson and Cohen [132] studied the thermal activation of boundary unpinning as well as microvoid nucleation resistance of several alloys to determine the quantitative effects of these dispersed secondary phases. The alloy design in this research involves adding just enough carbon to allow the precipitation of this specific secondary carbide dispersion necessary to achieve the optimum austenite grain size post solutionizing treatment. Proper control of the amount of grain-refining dispersion can be achieved through varying the austenizing or solutionizing temperature. Proper sizes of these dispersions are also extremely important since particles smaller than 20 nm are predicted not to offer any substantial resistance to grain boundary migration [132]. Thus, for achieving high fracture ductility by minimizing the probability of inter granular fracture, we need a combination of a fine dispersion of secondary carbide to pin the migrating grain boundaries and optimum austenite matrix grain size. Control of carbon leading to optimum amount of FCC TiC as a dispersed phase to control the matrix grain size has been used as a design parameter in our alloys. This will be discussed in section 5.4 in the chapter Alloy Design.

CHAPTER 3

MATERIALS, TOOLS AND EXPERIMENTAL PROCEDURES

3.1 MATERIALS

The material used in all experimental processes to form the basis of the new Blastalloy designs is the alloy EX425, which as previously described in section 1.4, is a TRIP steel developed at MIT by Dr. Frode Stavehaug as part of his doctoral research. The full composition of EX425 is shown in table 3.1. It has a fully austenite (γ) matrix and is strengthened by the precipitation of the intermetallic γ' Ni_3 [Ti, Al] phase upon tempering and the strength level is dependent on the phase fraction of γ' in equilibrium with the austenite γ matrix, under existing conditions.

	Ni	Cr	Ti	Mo	Al	V	Mn	C	B	Fe
EX425	25.04	3.93	2.91	1.25	0.16	0.32	0.09	.005	.009	Bal

Table 3.1: Composition of TRIP prototype alloy EX425 in wt%

Experimental runs on the EX425 has provided critical calibration points in regards to both strengthening mechanism (phase fraction of γ' in equilibrium at given tempering temperature) as well as the stability of the austenite γ matrix (which is critical in order to optimize the martensitic transformation characteristics). Calculations of volume fraction transformed martensite after the FCC → BCC transformation have also been determined on EX425 as a calibration for new TRIP Blastalloy design. Studies on kinetics of gamma prime precipitate nucleation over time in EX425 has been done using 3-D Atom Probe Tomography to determine the optimum conditions for precipitate size and distribution (volume fraction) for desired strength and stability of matrix.

3.2 MODELLING TOOLS and DATABASES

To quantitatively evaluate the interaction between the different subsystems, system design requires the use of different computational methods and models. The modeling tools that have been used here are listed below and described:

3.2.1 ThermoCalc™

ThermoCalc is a thermo-chemical database and application developed in 1981 by the Royal Institute of Technology (KTH) in Sweden to perform thermodynamic and phase diagram calculations. This includes metastable and equilibrium calculations, driving force calculations using sublattice models to describe thermodynamic parameters based on activity, enthalpy and specific heat measurements, which are expressed as functions of temperature, pressure and chemical composition [135]. This can calculate arbitrary phase diagram sections and property diagrams in multicomponent systems. ThermoCalc works on the principles of Gibb's energy minimization function to calculate an assortment of most stable phases in a heterogeneous equilibrium (i.e., multicomponent and multiphase equilibrium). The equations of mass balance, mass action, and conservation of electrons are satisfied through both thermodynamic free-energy and mathematical mass balance solutions. We can also use it to calculate many other types of diagrams like CVD depositions, Scheil-Gulliver solidification simulations, partial pressures in gases, Pourbaix diagrams, etc [138]. Thermo-Calc provides better understanding of the factors that affect material behavior and helps reduce costs by quickly identifying variations in control parameters or alloy compositions. Thermo-Calc consists of the following seven interconnected basic modules [138]:

(1) TDB for database retrieval and management
(2) GES for thermodynamic handling of models and data
(3) TAB for tabulations of thermodynamic properties
(4) POLY for multicomponent heterogeneous equilibrium calculations
(5) POST for processing of various phase diagrams
(6) PARROT for parameter optimizations, and
(7) ED_EXP for editing of experimental points

The POST module is a sub-module of the POLY module, and ED_EXP is a sub-module of the PARROT module. In addition, Thermo-Calc currently has six highly specialized modules, developed for very specific types of calculations and numerical simulations:

(1) BIN for binary phase diagram calculations
(2) TERN for ternary phase diagram calculations
(3) POT for potential diagram calculations
(4) POURBAIX for Pourbaix diagram calculations
(5) SCHEIL for Scheil-Gulliver solidification simulations, and
(6) REACTOR for steady-state reaction simulations.

ThermoCalc – Classic

The basic thermo-calc model is a general-purpose Unix-based program to retrieve thermodynamic/mobility quantities after the equilibrium calculation for a closed system (fixed mass). It needs temperature as an additional model input besides material composition. This model relies on the extra input to configure the calculation. It requires at least one extra input name. The first extra input name (ENT PH) has to be a list of interested phase name(s) that go into the equilibrium calculation. The optional second extra input name (Dor PH) represents a name list of dormant phases. In this context, a dormant phase is defined as a phase that is

allowed to participate in the energy minimization but not allowed to have any mass (i.e. driving force).

ThermoCalc – Windows

Thermo-Calc for Windows (TCW) is the family name of the Windows versions of Thermo-Calc. It has a graphical user interface, which allows for calculations of multi-component phase diagrams and property diagrams through the use of menus, buttons and input values e.g. compositions. Thermo-Calc for windows uses the same thermodynamic databases as Thermo-Calc Classic, although not all functions are available in the windows version.

3.2.2 *CMD*^{TM} – Computational Materials Dynamics

The process of materials design involves a large amount of equilibrium calculations using different models/databases as discussed in this section in order to study trade-offs and to perform optimization of design strategies. *CMD*^{TM} is a Linux-based computational materials design software system developed by *QuesTek Innovations LLC*, Evanston [136]. QuesTek's CMD platform has been successfully used for computer-aided systems design and optimization of QuesTek's high performance alloys, and has provided the foundation of accelerated materials qualification for both government and commercial market applications [137]. Currently this interface calculates basic thermodynamic quantities, martensite start temperature, solution temperature, and carbide driving force, carbide coarsening rate, solidification segregation and more. The user has to establish the materials design criteria for using the CMD model programs.

For alloy design in this research, CMD has been used to optimize the stability of the austenite matrix at the designed critical temperature by determining the Gibb’s free energy of FCC and

BCC phases. Input variables consist of the composition of the austenite matrix phase in equilibrium at any given temperature and output gives the Gibb's free energy associated with the phase at a critical temperature.

3.2.3 Thermodynamic Databases

The following thermodynamic databases have been used extensively for the calculation of equilibrium and para-equilibrium compositions in multi-component systems.

Ni-DATA (version 7): Ni-DATA is thermodynamic database developed by Thermotech Corporation (*Sente Software*) for the calculation of phase equilibria in Ni-based superalloys containing high amount of Fe, with version 7 being the latest edition which incorporates high accuracy level in computing equilibrium for multi-component systems. Ni-based databases include an accurate description of the γ' strengthening phase. The full database contains the elements: Ni, Al, Co, Cr, Fe, Hf, Mo, Mn, Nb, Re, Ru, Si, Ta, Ti, W, Zr, B, C and N. The database has good standards for accuracy in thermodynamic calculations of multi-component alloys. It can be used for all Ni-based or NiFe-based alloys. Only **FCC** (#1 – Matrix and #2 – TiC dispersed phase) and **Gamma_Prime (γ')** phases were used for calculations at equilibrium aging temperature.

MARTENSITE (MART) 5: MART-5 is modified version of SGTE – SSOL thermodynamic database (developed by Scientific Group Thermodata Europe (SGTE)). SGTE is a consortium of research centers in Europe developing databases for inorganic chemistry and metallurgy. MART-5 was developed and modified from SSOL by Ghosh and Olson [95] to calculate the martensite start temperature and includes modified low temperature thermodynamic parameters for FCC

and BCC phases for Fe-based systems, since the original SSOL database is based on high-temperature thermodynamics. This database incorporates low temperature thermodynamic assessment parameters and models for Fe-based systems and can be used to accurately determine Gibb's free energies at low temperatures.

3.2.4 Thermodynamic Models

BASIC Model: The Basic Model is a general purpose program which is used in conjunction with *CMD* to calculate the thermodynamic free energies and critical transformation temperatures, post equilibrium computation. It retrieves thermodynamic mobility quantities for a closed system (fixed mass in equilibrium). Basic Model can be used in the *CMD* interface along with MART5 or any other appropriate database to determine the critical driving force or transformation temperature for the equilibrium system. It needs temperature as an additional model input beside the equilibrium composition and requires atleast one extra input. The first and necessary input is the ENT PH, or the Entered Phase, which is a list of phase names that are to be considered for equilibrium computation. The second and third input can be either dormant phases (DOR PH) which don't participate in the equilibrium calculations or the POLY3 (P3 CMD) for multi-phase heterogeneous equilibrium. This P3 input maybe a complex function or command to generate specific driving forces, and thus requires the use of the symbol '$' to specify different commands (outputs) within a single input.

3.3 EXPERIMENTAL PROCEDURES

The experimental equipments, methods and procedures used in the research have been described in this section –

3.3.1 Vacuum Seal-Off

Prior to any solutionizing process or any aging heat treatment, all specimens were vacuum encapsulated in glass tubes of diameter 0.6 inch to prevent oxidation and formation of oxides and nitride layers on the surface of the specimens during heat treatments. The presence of oxides and nitrides affect the austenite microstructure by formation of inclusions and voids, which is undesirable. The Seal-Off station is attached to a vacuum system operating on three pumps – a mechanical pump, a roughing pump and a diffusion pump. The mechanical and roughing pumps are used first to evacuate most of the gases in the tube. During this process the tube is back filled with Argon two to three times and pumped again to enable smoother evacuation of gases. Finally the diffusion pump is used to evacuate the trace gases and reach the final vacuum of < 5 microns (5 mTorr). A fully vacuum sealed specimen in a glass tube is shown in figure 3.3.1.

Fig 3.3.1: Tensile bars vacuum encapsulated and sealed in a glass tube prior to aging. A small piece of tantalum foil can be seen at the left corner to absorb the trace oxygen in the system

A small piece of Tantalum foil is often put in the sealed tube along with the specimens. This is because Tantalum has a very high affinity for oxygen, and any trace oxygen left inside the sealed tube is absorbed by the tantalum, instead for forming oxides on the surface of the specimens. For quenching process, the glass sealed tube is removed from the furnace and dropped into a container full of quench oil. The seal is then broken inside the container to avoid any contact of specimen with air prior to quench. The contents are filtered to re-use the oil and separate the specimen.

3.3.2 Heat Treatment and Furnaces

Three types of furnaces have been used in this research depending on the temperature and time of heat-treatment and sample size and quantity. These have been briefly described –

Barnstead International FB1400: The FB1400 furnace from Barnstead is a general purpose laboratory heat-treatment furnace. The optimum temperature ranges for usage are 100C (212F) to 982C (1800F) for continuous use of more than 3 hours or upto 1100C (2012F) for intermittent use or shorter time heat treatments of less than 3 hours. The unit consists of a single heating chamber and a digital controller. The heating chamber dimensions are 5.00” W by 4.25” H by 6.00” D. Due to its small size and good temperature accuracy and balance (low temperature variance with distance from wall), it is extensively used for smaller specimens for solutionizing and general heat treatments. However, for larger sized specimens, we have used the larger Lindberg Box and Tube furnaces.

Lindberg 1700C Tube Furnace: The Lindberg 1700C laboratory tube furnace provides good temperature uniformity and thermal efficiency throughout the radiant temperature range and

'heat-zone'. It consists of long-life molybdenum disilicide heating elements for ideal heat-up and uniformity requirements. Elements resist thermal shock and can be subjected to rapid cycling over long periods of time. The maximum diameter of the tube inserted can be 3" made of ceramic. This furnace has been used for longer specimens with high temperature heat treatments for long periods.

Vacuum Induction and Quench Furnace: The fully automated Vacuum Induction Quench Furnace in the SRG lab at Northwestern University has been custom manufactured by *Materials Research Furnaces (MRF) Corporation*, New Hampshire. The system consists of two furnace chambers, sharing a diffusion pumping system and an HMI (Human Machine Interface) for automated computer control of the furnace. The first furnace chamber is a front-loading Quench Laboratory furnace capable of reaching extreme high temperatures of ~ 2000 – 2500^{o}C in a vacuum or gas atmosphere. The hot zone consists of a tungsten mesh heating element and there is a manual quench cup below the hot zone which allows for rapid cooling of specimens by dropping them into a quench liquid like oil or water. The diffusion pump enables the furnace to reach a vacuum of ~ 10^{-6} Torr. The second furnace chamber consists of a 10 ton Hot Press Furnace system which includes an additional pressing kit to that of the quench furnace. Based on current research needs, only the first quench furnace has been used.

3.3.3 Sample Preparation Techniques for Metallography

It is essential to prepare properly mounted finely finished material specimens in order to study them under an optical microscope to investigate their surface substructure or to measure its hardness. Complete sample preparation steps for metallographic studies include precision cutting of thin materials specimens, mounting them on a polymer base using an automated mechanical

heat press, grinding the specimens and polishing them to a clean and fine finish. The following equipment have been used for metallographic sample preparation in this research –

Automated Precision Cutting: Accutom 5, manufactured by *Struers Inc.*, has been used for advanced precision cutting of small slices of specimens for metallographic studies. It is a precision table top cut-off machine and grinding machine for precise and deformation-free cutting. It has a pre-set constant feed speed in the range of 0.005 - 3.00 mm/s. The most important aspect is that this can be programmed to automatically cut series of slices from the same samples, thus maintaining uniform dimensional accuracy in all specimens studied.

Mounting: *Struers Hot mounting LaboPress-1* has been used for mounting the precision cut material specimens. The aim of mounting is to handle small or odd shaped specimens and to protect fragile materials as well as to provide good edge retention. Mounting produces specimens with uniform size so that it is easier to handle. The specimen is mounted using powdered polymer or acrylic which melts under heat and pressure in a hot mounting press and finally solidifies on cooling to form a flat round base.

Grinding and Polishing: In order to obtain a highly reflective surface that is free from scratches and deformation, the specimens must be carefully grinded and polished before they can be examined under the microscope or used for hardness measurements. Each of the mounted specimens was ground through three stages using sand paper with grid sizes of – 180, 320 and 600. After grinding, a Buehler Ecomet – 4 variable speed automatic grinder-polisher was used to polish to a final finish of 1 µm. The polishing was carried out using oil-based polishing etchant and cloth with grid sizes starting with 15 µm, 9 µm, 6 µm and finally 1 µm. After polishing, the

mounted specimens were cleansed before being loaded for viewing on an optical microscope or for measuring micro-hardness.

Cleansing: Post grinding and cleansing, it is important to clean the surface of the specimen very gently to remove skunks and fine debris. Ultrasonic cleansing methods are faster, more consistent, and safer than any other cleaning processes. An ultrasonic cleaning system from *Buehler (Branson SPC)* has been used for 2 minutes post polishing for all specimens. After ultrasonic cleaning, the surface of the specimen is dabbed with cotton wool smeared with ethanol. Any etchant necessary for analysis is applied thereafter.

3.3.4 Vickers Micro-Hardness Testing:

Hardness is a good measure of a materials ability to resist plastic deformation under application of an external compressive load. Vicker's micro-hardness has been measured for model prototypes in this research for varying heat treatment temperatures and times in an effort to study the variation of hardness and Yield strength with temper times. Although measuring hardness using Vicker's method is significantly equivalent to a compressive deformation process, Saha [8] provided a relationship for uniaxial tensile yield strength dependence on Vicker's hardness number (VHN) through the equation,

$$VHN = 6.11571 \times (YS)^{0.81841} \tag{3.3.1}$$

Where VHN is in Kg/mm^2 and YS (yield strength) is in ksi. This relation gives a direct estimate of the Tensile Yield strength of the material from the VHN number without needing to run tensile tests on every specimen condition.

A Buehler Micromet II micro hardness tester was used to measure the Vicker's number for each specimen condition. This method conforms to the prescribed method in ASTM standard E384. The indenter used in the Vickers test is ground in the shape of a square-based pyramid whose opposite sides meet at the apex at an angle of 136º. The diamond indentor is pressed into the surface of the material (which is polished to atleast 1 µm finish) at a set load of 200 gram-force for 10 seconds and the size of the impression is measured with the aid of a calibrated microscope at 400X preset magnification. The Vickers Hardness Number is the ratio of the load applied by the indentor to the surface area of the indentation [140].

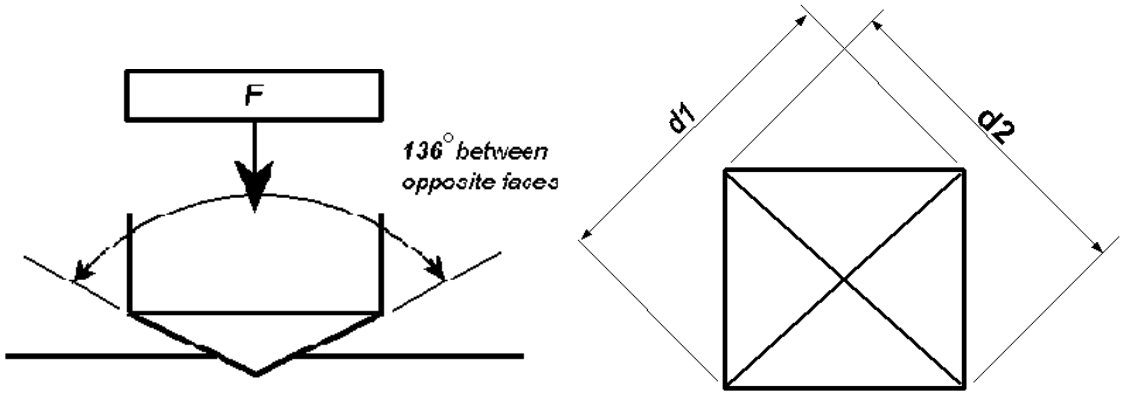

Fig. 3.3.4.1: Indentor configuration and indent geometry obtained for a typical Vicker's Microhardness test [140]

VHN is calculated using the following formula:

$$VHN = 2F\frac{\sin\left(\frac{\theta}{2}\right)}{D^2} \tag{3.3.2}$$

or,

$$VHN = 1.854 \times \left(\frac{F}{D^2}\right) \tag{3.3.3}$$

Where F is the applied load (measured in kilograms-force) and D is the arithmetic mean of the two diagonals, *d1* and *d2* in mm. The load applied (200 gram-force) and the time of load application (10s) has been kept constant for all specimens and all conditions in the current work.

3.3.5 Tensile Tests

Mechanical properties like Yield Strength (YS), Ultimate Tensile Strength (UTS), Uniform Ductility and Strain Hardening, Fracture Strain, temperature dependence of YS and stretch ductility under tension have been studied through tensile tests on model prototypes. Both Static Isothermal tensile tests and Dynamic adiabatic tensile tests have been carried out to determine performance under ideal conditions. Since the new alloy designs are primarily for blast protection, it is important to evaluate the performance and process parameters under dynamic adiabatic loading. The specimen geometry and dimensions differ for each of the two modes of tensile tests conducted – Static and Dynamic. Details of specimen configuration and equipment used have been described -

3.3.5.1 Static Tensile Testing:

Static uniaxial tensile tests on both earlier model prototype EX425 and newly designed alloy (BA120 and SA120) specimens were performed at different temperatures in the range of 100^{o}C to -196^{o}C, using a computer controlled Sintech (MTS) 20/G screw driven mechanical testing machine. The tensile test system and related software (Testworks 3.03) is available from *MTS System Corp, Sintech Division*. The system has a maximum capacity of 100,000 N (20,000 lbf). These tests fully conform to the ASTM Test Method D638-95. For tensile tests at lower than room temperatures, an automated temperature controlled metallic cooling chamber with liquid nitrogen gas cooling system was used. Tests could be conducted at as low as –196^{o}C using this system. Specimens for the static tensile tests were machined from blanks cut from the model prototype slab along the rolling direction. The geometry and dimensional specifications are shown in figure 3.3.5.1

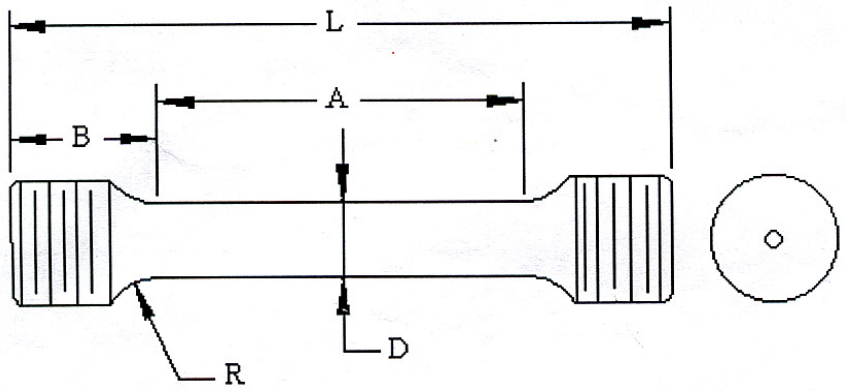

Fig. 3.3.5.1: Geometry and Specification of a Static Tensile test Specimen. The values for the denotations are: L = 1.5540, A = 0.7416, D = 0.1259, R = 0.2000, B =0.3804. Thread size is ¼-28. All units are in Inches.

A load cell of 20,000 lb at a constant cross-head speed of 1.0 mm/min has been used as a standard mechanism for all Iso-thermal static tensile tests in this research. For M_S^{σ} measurements using the Richman and Bolling method [13] however, the strain rate used is 0.1 mm/min. This method is described later in section 4.5.4. The load cell has been calibrated prior to every test using the machine software calibration test. To have an accurate measure of the true elongation of the gage length of the tensile specimens, an extensometer with a gage length of 1" was attached to the sample length during testing. The extensometer was then calibrated to zero reading just before start of test, in unison with the crosshead's initial coordinates. The instantaneous strain values from the gage are determined directly from the extensometer, which enables calculation of True Stress-Strain curves for the test. The MTS software incorporated to the Sintech System gives instantaneous stress – strain curves which can be related to both engineering and true stress - strain plots by incorporating the initial radius of the specimen. Area reduction of fracture surface is measured manually after the test.

3.3.5.2 Dynamic Tensile Tests (Adiabatic)

The Kolsky bar setup is one of the most popular configurations for measuring the response of materials at high strain rates. A stored-energy Kolsky bar (or, a split Hopkinson bar) apparatus has been used in this research to perform dynamic adiabatic tensile tests to simulate actual deformation characteristics during a blast. Hopkinson originally used an elastic bar for pressure wave propagation to measure the stress profiles during dynamic loading of materials [161].

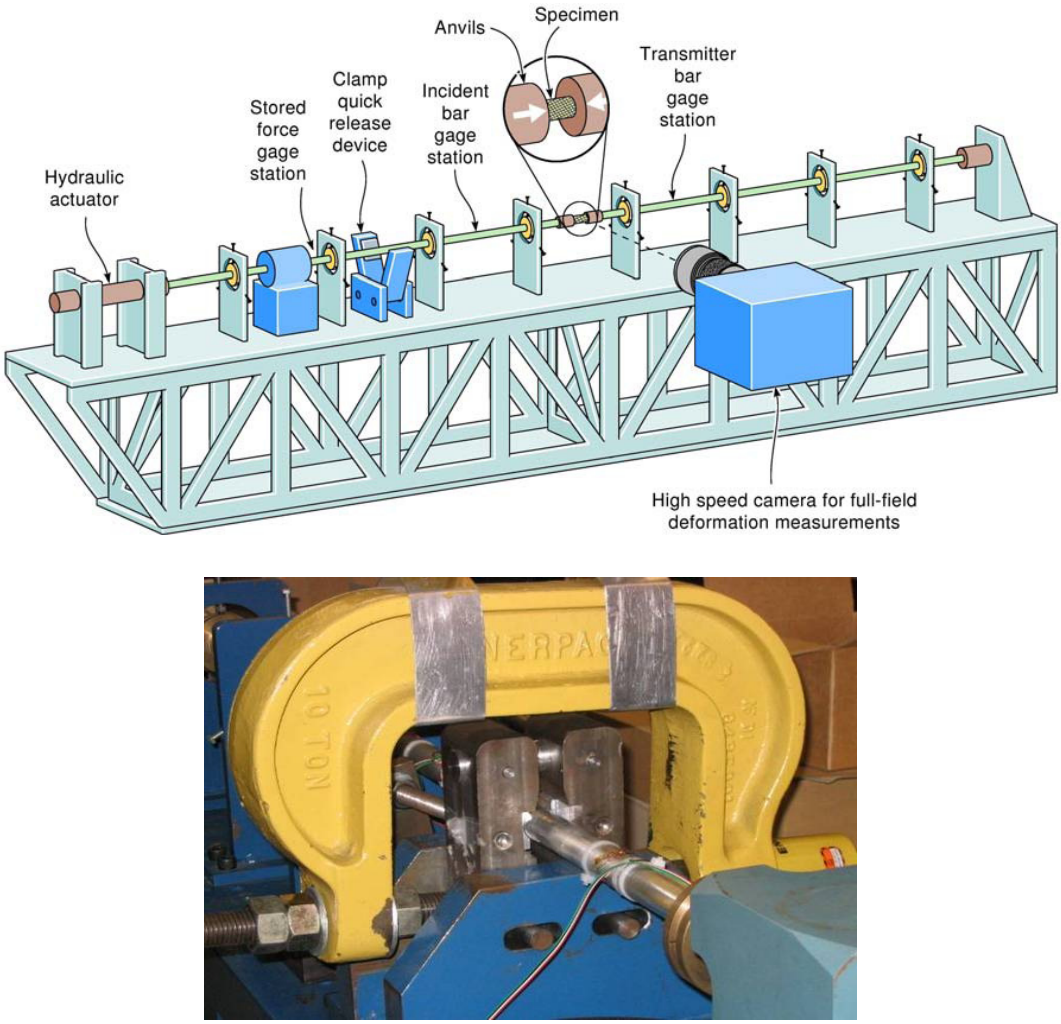

Fig. 3.3.5.2: Kolsky apparatus set-up for Dynamic Adiabatic Tension and Shear/Torsion tests showing the use of a high-speed camera to capture fracture images in intervals of 40-80 μs [19]

This bar was modified by Davies [162-163] and Kolsky [164-165] by adding a second pressure bar in series with the first one, to measure the strain profile under the applied dynamic propagating stress. A compressive wave is passed to the incident bar and the returning elastic waves in the incident and transmitted waves are measured [160]. Using the two bar setup, Kolsky [164] showed that the part of the incident wave that is transmitted through the specimen provides a measure of the average axial stress in the specimen and the magnitude of the reflected wave is proportional to the strain rate [160]. Nominal strain rates of 200-1200 s^{-1} (typically, ~ 450 s^{-1} and 800 s^{-1} for low and high strain rate tests respectively) have been used. The apparatus setup is shown in figure 3.3.5.2 [141]. The specimen is placed between two 1" diameter aluminium bars mounted on linear bearings. To store the energy, the incident aluminium bar is clamped and a compressive load is applied using a hydraulic actuator. A steel pin holds the compressive force due to the clamping and by releasing the clamp, the pin breaks and releases all the stresses in wanes along the bar and into the specimen and transmitter attached to the bar.

Strain gage stations at different locations on the bars are connected to a signal conditioning and amplification system. Assuming elastic deformation in the pressure bars and force equilibrium at the two interfaces of the specimen, the force-time history applied to the specimen was computed by Lee et al. [19],

$$F(t) = E_{Al}\left(\frac{\pi D^2}{4}\right)\varepsilon_t(t) \qquad (3.3.4)$$

where E_{Al} is the Young's modulus of the aluminum employed in the pressure bars, D is the pressure bar diameter, and $\varepsilon(t)$ is the strain history measured using a Wheatstone bridge at the strain gage station installed on the transmitter pressure bar. Lee further calculated the overall deformation mathematically as

$$\delta_N(t) = 2c_{Al}\int_0^t [\varepsilon_i(t) - \varepsilon_t(t)]d\tau \quad (3.3.5)$$

where c_{Al} is the sound speed in aluminium and $\varepsilon_i(t)$ is the strain measured on the incident bar.

A high speed camera has been used to capture images at regular intervals to observe the deformation process for digital correlation with data. The time interval between two frames was varied from 40 μs to 80 μs and the exposure time was set between 5 μs to 20 μs [19]. The dynamic test results have been directly compared to those of the static tests and the results have been discussed in sections 4.4.2 and 6.4.3. The specimen geometry and dimensional specifications have been shown in figure 3.3.5.3. The dimensions are in inches.

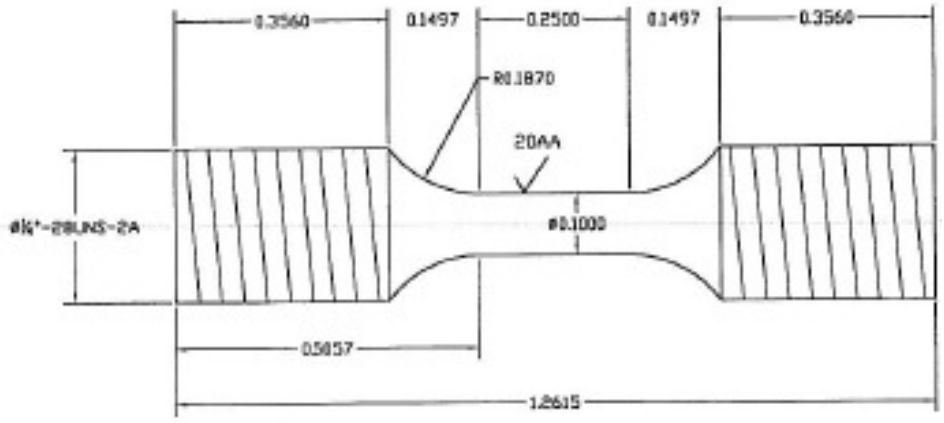

Fig. 3.3.5.3: Geometry and Specification of a Dynamic Kolsky bar Tensile test Specimen. All units are in inches.

The alignment of the two bars needs to be verified before screwing the specimen to ensure that no bending and shear stress components arise during the test. In order to achieve high strain rate, the gage length '*l*' has to be as small as possible, however too small a gage length can lead to distortion of stress-state [160].

3.3.6 Shear/Torsion Tests

The evaluation of the Shear/Torsion Stress response have been performed on prototype austenitic TRIP alloys to demonstrate their fragmentation resistance under static and dynamic shear loading at room temperature. Shear tests were performed on a similar Kolsky bar apparatus as shown in figure 3.3.5.2. The axial components of the stress and displacement vectors were replaced by angular displacement and shear stress (τ_{xy}). Mori et al. [160] calculated the shear stress-strain curve for any specimen by combining the shear stress waves measured by the strain gages on both sides of the specimen and by integrating the strain rate over time. The specimen geometry is shown in figure 3.3.6.1 consists of cylindrical ends joined by a thin round wall for shear failure.

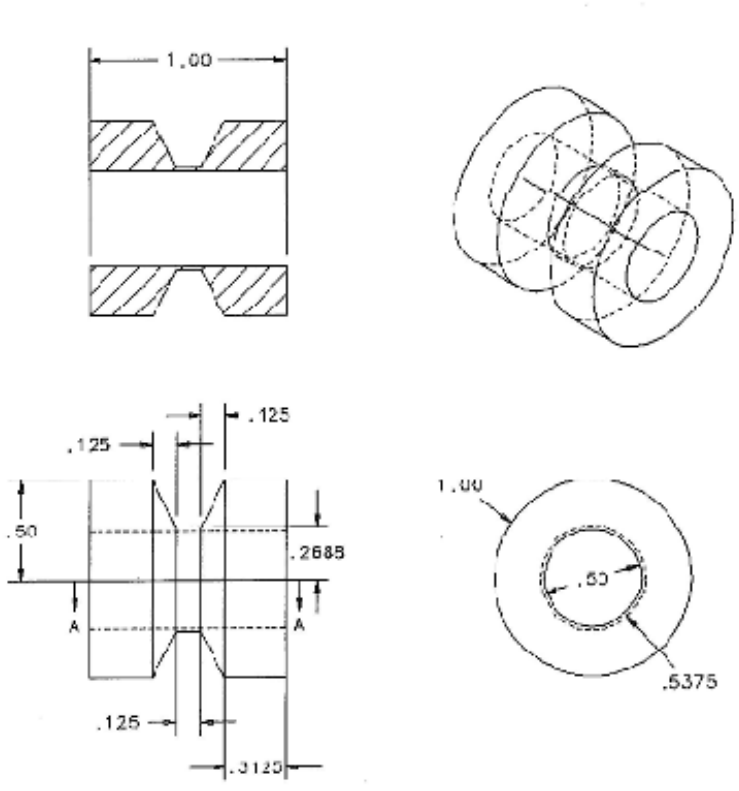

Fig. 3.3.6.1: Geometry and Specification of a Static and Dynamic Kolsky bar Torsion/Shear test Specimen. All units are in inches.

This wall has grids on it to measure the true shear strain. The gage section of the specimen is machined on a lathe with a specifically manufactured conformed tool that allows controlling the rounds at the two ends of the gage section to make sure that the material localizes at the middle of the gage section. The specimen is glued between input and output bars. A torque is applied on the Kolsky bar which is transmitted to the specimen. The compression/tension and shear loading pulses are generated with the sudden release of elastic energy stored the incident bar. For the dynamic test, the torque is stored between the torque actuator and the mechanical clamp, and suddenly released by the fracture of an aluminum pin. The energy is stored in the first half of the incident bar by means of a clamp that holds the desired torque and compression/tension force without slipping and then releases the elastic energy with a sharp-fronted stress pulse travelling towards the specimen [160]. Upon release of the stored torque, a torsional stress wave traveled down the input bar to the specimen. For the quasi-static tests (which was performed at *Illinois Institute of Technology, Chicago*) a hydraulic lever arm and a platen attached to it were installed on the output bars, and the input bar was clamped together with an aluminum pin holding the bars to the clamp. Weights were added on the platen to increase the torque by small amounts as needed. The transmission of the torque to the specimen was verified using an automated signal-generated strain gage. For both quasi-static and dynamic tests, pictures of the surface can be taken at different loading stages. For the quasi-static test these pictures can be triggered manually (at each load increment), and for the dynamic case the strain gage, upon arrival of the wave, triggers the high-speed camera [145]. Adequate timing allows taking high-speed pictures at different stages of the rising pulse of the wave. Dark and bright features on the specimen surface are used to correlate the pictures with each other, allowing the determination of the strain in the specimen. However in the absence of a high-speed camera, the grid method is

commonly used to measure the true shear strain for both quasi-static and dynamic torsion loading. The thin-wall cross-section is marked with grids of equivalent separation distances and the displacement is measured pre- and post fracture.

3.3.7 Ballistic FSI tests

Since the ultimate goal of the Navy's research initiative through the CyberSteel 2020 program is to design materials with high resistance to underwater blast impulses for its ship hull structures, the final performance evaluation of any new prototype made has to be done on an experimental setup which closely resembles the above scenario. Lee and Espinosa [19] designed a novel *Fluid-Structure-Interaction* (FSI) experiment to simulate the underwater blast impulse loading of material structures and investigate deformation of these structural plates subjected to the blast loading by studying their deformation profiles, histories and fracture mechanism. The same setup has been used to evaluate the final blast impulse resistance performance of BA120 and SA120 alloys. Lee's experimental design is shown in figure 3.3.7.1.

The setup consists of a water chamber made of steel which has the structural model prototype plate fixed at one end. On the other end, we have a water piston which is impacted by a flyer-plate attached to a gas-gun system. When the flyer plate hits the water piston, the energy of the impulse is transferred in form of exponentially decaying pressure waves, to resemble a blast occurring under water due to a sudden and high release of energy [142]. The pressure waves travel through the water chamber and hit the panel prototype structure, thereby inducing deformation and probable fracture. The impact velocity of the flyer plate is measured by a contact-pin type velocity sensor [19].

The pressure history in the water is recorded by dynamic high pressure transducers and a digital oscilloscope. Figure 3.3.7.2 shows the gas gun barrel system with the Anvil tube attached to the specimen panel.

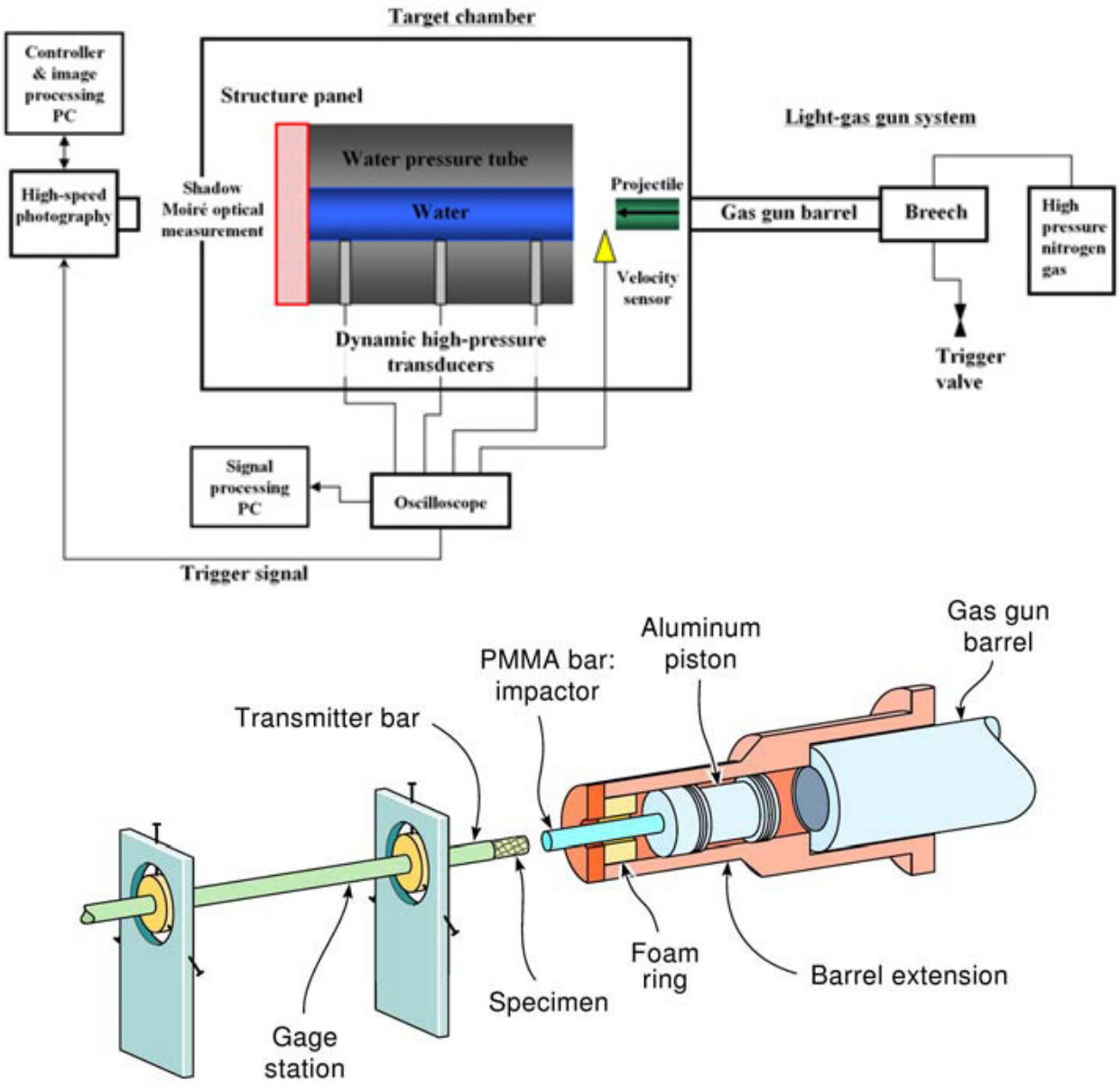

Fig. 3.3.7.1: a) Schematic diagram of the FSI Ballistic Test Gas-Gun Apparatus used for impulse impact deformation tests b) Schematic of direct impact tests [19]

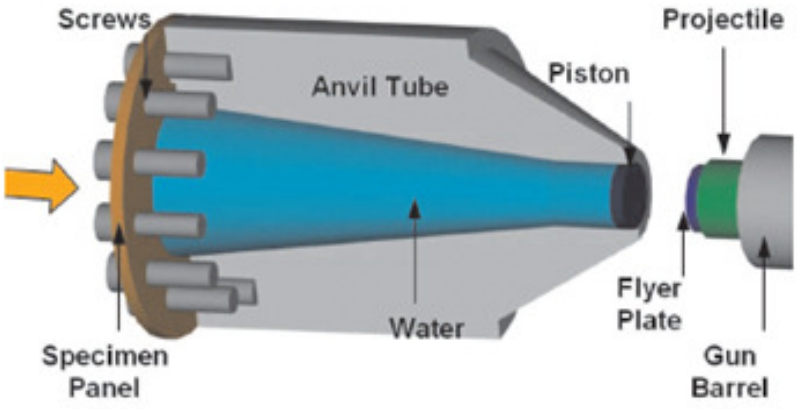

Fig. 3.3.7.2: Schematic of the projectile flyer-plate with the Anvil tube system attached to the Specimen Panel [142]

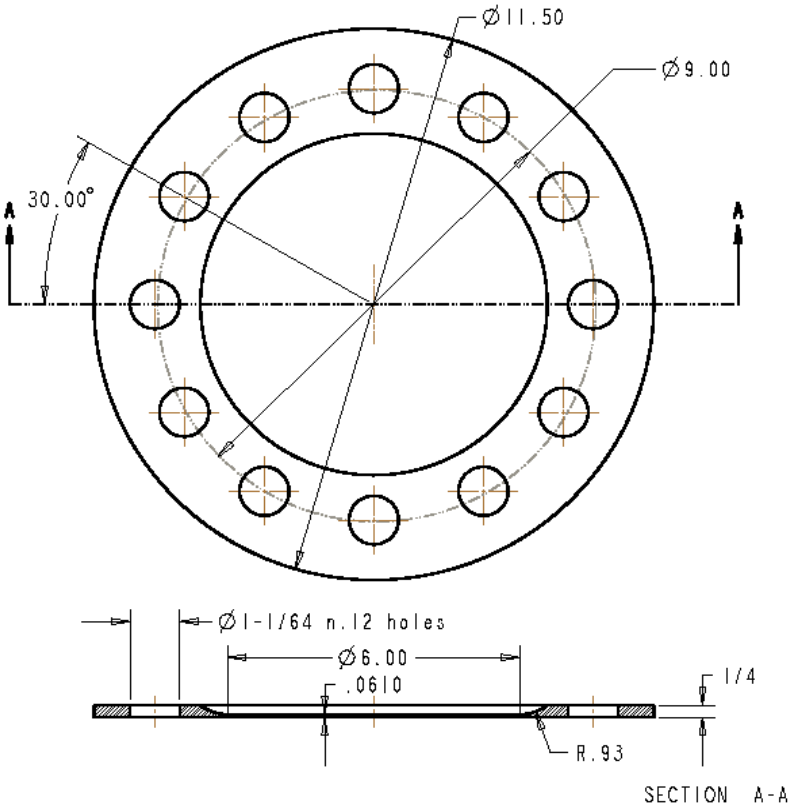

Fig. 3.3.7.3: Geometry and Specification of an FSI Ballistic Gas Gun test Structure. All units are in inches.

Standard deformation characteristics of the model prototype plates have been studied by Lee as well as Mori et al. [142] using high speed camera to obtain shadow moiré fringes at different

time intervals. Earlier comparison of the recorded deformation profiles with dynamic finite element analysis has shown a very good agreement [144]. FSI ballistic tests have been done on new alloy designed in this research and compared with those of 304 Stainless steel monolithic plates.

3.3.8 X-Ray Diffraction

The volume fraction of transformed martensite under application of external stress (post tensile tests) has been measured using X-Ray diffraction technique. The tempered and quenched specimens were first lightly polished upto 15μm prior to irradiating it with X-rays. A Scintag XDS2000 automated diffraction system with four-circle pole-figure and residual stress device, thin film diffraction attachment and solid-state detector has been used to measure the relative intensities of the Austenite and Martensite diffraction peaks. The specimen was irradiated By Cu K_α radiation at ~ 40kV and 20mA and the diffraction peaks observed were calibrated and compared with peaks obtained from standard powder diffraction files. The data was collected for a step size of 0.01^o for both austenite and martensite peaks with wide-angle reflection (2θ) scanned to a max of 90^o. Once the appropriate peaks were identified, the desired peaks for calculations were scanned at a smaller interval with a slow scan. The maximum intensities were measured for (220) reflection for Austenite (γ) for scanned angle range 49^o to 53^o and (200) reflection of Martensite for scanned angle range 80^o to 85^o. Quantitative analysis of the volume fraction of martensite and retained austenite were measured based on the ratio of their integrated intensities. According to Cullity [146], the ratio of the diffraction intensities of Austenite and Martensite can be related directly to the ratio of their respective volume fractions –

$$\frac{I^{fcc}}{I^{bcc}} \; \alpha \; \frac{f^{fcc}}{f^{bcc}} \tag{3.3.6}$$

$$\cong \; f^{bcc} = R_{fcc-bcc} \cdot f^{fcc} \left(\frac{I^{fcc}}{I^{bcc}} \right) \tag{3.3.7}$$

where I^{fcc}, I^{bcc}, f^{fcc} and f^{bcc} are the integrated intensities and volume fractions of austenite and martensite respectively. $R_{fcc-bcc}$ is the proportionality constant which combines all factors including structure factor for the specimen calibrated to a standard austenite-ferrite material, temperature, polarization, multiplicity and scanning (2θ) rotation area.

3.3.9 Microscopy

Surface microscopy and sub-surface sub-micron imaging has been done to analyze the specimens pre and port heat treatment. The three levels of microscopy used in this research are – Optical Microscopy to study the surface characteristics of polished and etched specimens to differentiate martensite regions from the dominant austenite areas, Scanning Electron Microscopy analysis for fracture mechanics in tensile specimens and intergranular fracture and finally 3-D Local Electrode Atom Probe (LEAP) tomography has been used to study the para equilibrium **γ - γ'** structure, measure the composition profiles across **γ** and **γ'** phases for all components and to obtain details of **γ'** precipitate clusters (geometry, radii, volume fraction, number density and composition profile). These methodologies have in described in detail –

3.3.9.1 Optical Microscopy

Optical microscopy has been used mainly to study the etched surface of specimens in order to identify the transformed martensite regions. Preliminary austenite grain size and distribution have also been carried out with light microscopy. A Nikon Epiphot inverted metallographic

microscope has been used with built-in interlocking aperture diaphragm to automatically adjust during brightfield/darkfield changeover. The specimen is mounted, ground, polished and etched prior to loading on the microscope system. The objective lens has magnification upto 500X. The system uses a 2V-100W halogen illuminator with three 45mm filters. Digital camera capability has been added to the system to automatically scan high quality images.

The etchants used in light microscopy in this research has been a) 10% Nital solution (10% Nitric Acid in Ethyl Alcohol) to reveal Austenite grain boundaries and study matrix grain size and distribution, and b) a solution of 0.5 gm of Sodium Metabisulfite, 33 cc HCL and 167 cc H_2O which has been found to be very effective in differentiating the martensite regions (by darkening them) from the austenite phase [53].

3.3.9.2 Scanning Electron Microscopy

Scanning Electron Microscopy (SEM) has been used for fractography to study the fracture surface of tensile specimens to evaluate occurrence of intergranular fracture as well as the microstructure (transformed martensite regions). A Hitachi S-3400N variable pressure high vacuum tungsten-filament SEM system at Northwestern University's *NUANCE* centre has been used in this research. For loading, the samples of appropriate height were fixed to a metal holder using a graphite conducting tape and inserted into high vacuum of $< 10^{-6}$ torr inside the chamber. Both secondary electrons and back scattering modes have been used to study the microstructure for a better contrast of images. The machine has a resolution of 3nm for secondary electron scan and 5nm for back scattering mode with a total magnification of x300K. This SEM has automated

functions for filament saturation, gun alignment, brightness, contrast and stigmatism for auto-image corrections and good image contrast and quality.

3.3.9.3 3-D Local Electrode Atom Probe Tomography (*LEAP^{TM}*)

A high resolution 3D Local Electrode Atom Probe (LEAP^{TM}) tomography has been used in this research to study the characteristics and distribution of the γ' precipitates, composition profiles of matrix (γ) and precipitates (γ') and the nucleation (growth) of the precipitates with increasing temper times. *The Northwestern University Centre for Atom Probe Tomography* (*NUCAPT*) houses the next generation Atom Probe microscopes, including the LEAP, manufactured by *Imago Scientific Instruments Ltd., Madison, WI, USA*. 3-D Atom Probe tomography uses a combination of time-of-flight mass spectroscopy to identify individual atoms and elements using their atomic numbers and common isotopes, and point-projection microscopy to determine the 3D coordinates of the exact prior location of the atom/ion in the specimen.

Figure 3.3.9.1 shows a schematic of the ions being pulsed by a DC Voltage accompanies by an augmented Laser Pulse. Materials are examined by removing and analyzing individual atoms, thus providing chemical analysis at the atomic level [147]. This is extremely valuable in analyzing nanoscale volumes of materials thus allowing studies of small precipitates and other phases by identifying individual atoms within the phase [147-148]. Atoms are removed by a combination of a high electrical field and either: (1) an ultra-fast voltage pulse or (2) an ultra-fast laser pulse [149].

The specimens (microtips) are first electro-polished to a very fine sharp edge with diameter of ~ 50nm and shaped like a needle as shown in figure 3.3.9.2 and 3.3.9.5. Under high vacuum (~ 10^{-}

^{12} torr) and extreme low temperatures (< 100K), a high electric field is generated by application of a positive voltage pulse to the detector or a laser pulse to the needle-shaped specimen leading to instant field-evaporation/ionization of the ions located on the tip of the needle.

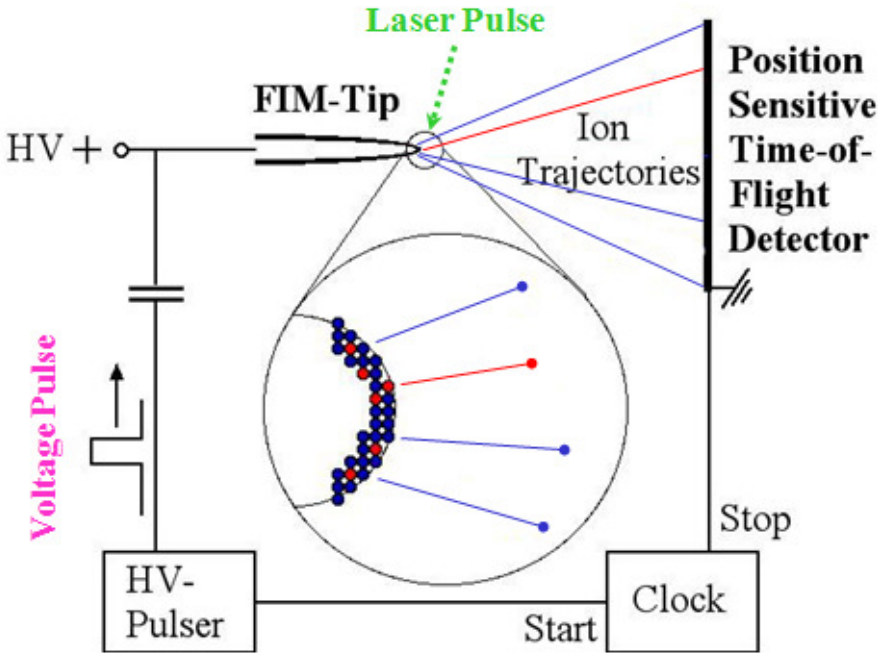

Fig 3.3.9.1: Schematic diagram of the application of Voltage and laser pulsing for tip evaporation operation in a 3D LEAP [147]

Due to the high voltage differential, these evaporated ions are pulled towards a 2D detector located ~100nm from the electrode. The detector used is a single-ion detector with timing devices to record the hit time (arrival time) of the ions and thus multiple hits (2 or more ions hitting the same spot at the same time) are not considered ideal and are subsequently not used in the final analysis. The system uses the time-of-flight trajectory of the ion to determine its mass-to-charge ratio and identify it chemically as an element and isotope and uses this information for all single ions hitting the detector to create the mass spectrum for composition profiling. The

position (x-y coordinates) of the 'hit' (recorded by the delay-line detector) is directly related to the original position of the ion in the specimen and the z-axis position is dependant on the 'delay' or time lag of ions hitting the detector.

The development and use of a Local Electrode Atom Probe (LEAP) technology in the 3-D Atom Probe has revolutionized all aspects of instrument performance and enabled analysis volumes to be increased by more than three orders of magnitude. During analysis, the local electrode is positioned close or local to the specimen, with the electrodes aperture centered over the specimen tip. Since the electrode is located close to the specimen tip, the required electric field and pulse energy or fraction to evaporate the ions at a given rate is much lesser than for traditional Atom probes at a higher mass resolution (1/500 full width at half maximum (FWHM)) and to reconstruct high volumes ($>10^6$ nm^3).

Voltage and Laser Pulse Modes:

The Voltage pulse method is the traditional mode of initialize filed-ion evaporation via a high electric field. A pulse frequency of around 200 kHz is applied with a pulse fraction varying from 0.15 to 0.20 ($\Delta V/V$), though a PF of 0.20 is preferred as lower pulse fractions have shown lower evaporation of preferred elements like Ni. Traditionally atom probe tomography (APT) has used voltage pulsing as the mechanism for field-emission ionization, which limited its use to specimens with good electrical conductivity. However, laser pulsing allows ionization of specimens via a thermal effect. In the Voltage mode, the pulse provides all the energy needed to evaporate the ions at a given temperature. Since this mode has been used since long and has been well calibrated and documented, it is taken as a standard operation mode for 3DAP and LEAP.

Figure 3.3.9.2 shows the micro-tip centered and positioned ~ 100nm from the electrode in the Voltage only mode while running.

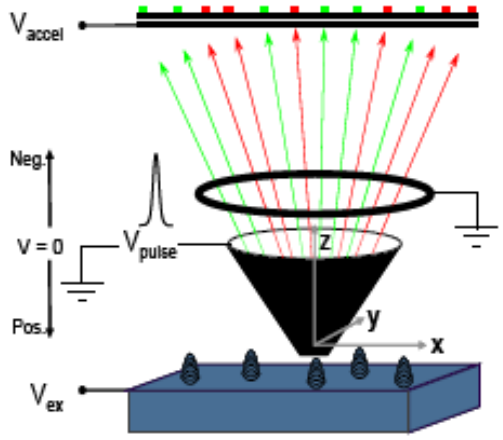

(a)

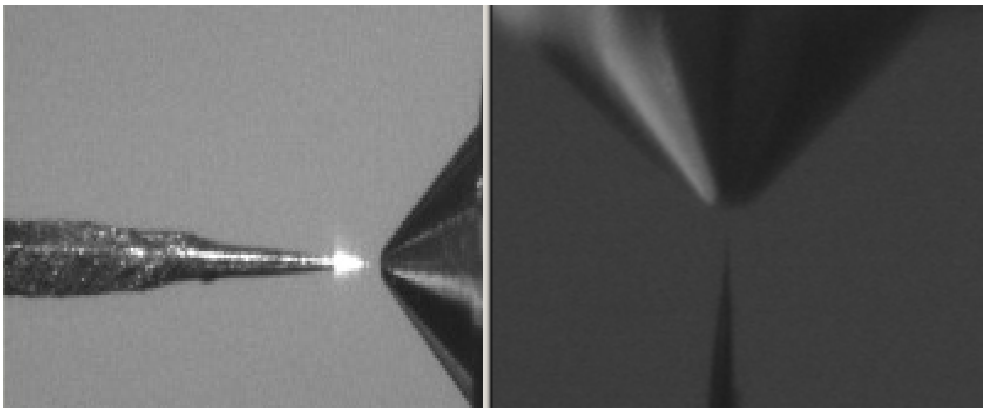

(b)

Fig 3.3.9.2: **a)** Schematic of Voltage Pulsing [Courtesy: Imago], **b)** In-operation image of a fully austenized EX425 micro-tip using Voltage-only pulsing in a 3D LEAP Atom probe. Image taken using IVAS 3.0

The laser pulsing technique of operation of LEAP is relatively very new and it uses an ultra-fast laser pulse along with a static electric field to ionize the specimen at the tip. The LEAP used in this research combines a laser unit with a high pulse repetition rate (upto 500 kHz), pulse energy variations and optical alignment to enable very good mass resolution and a high evaporation rate.

Laser mode has been used frequently in conditions where the specimens are very fragile (thin films) and high accuracy is needed for composition profiling (sharper mass spectrum than voltage mode) and a high volume of data/ions is needed for ion reconstruction. However, it has been observed that the laser mode generates distorted and elongated γ'precipitates upon reconstruction. Figure 3.3.9.3 shows an in-operation image of an EX425 micro-tip being irradiated radially with laser beam of pulse 500 kHz. It is observed that a faint diffraction pattern is observed in the background for the tip due to laser beam hitting the ionic crystals.

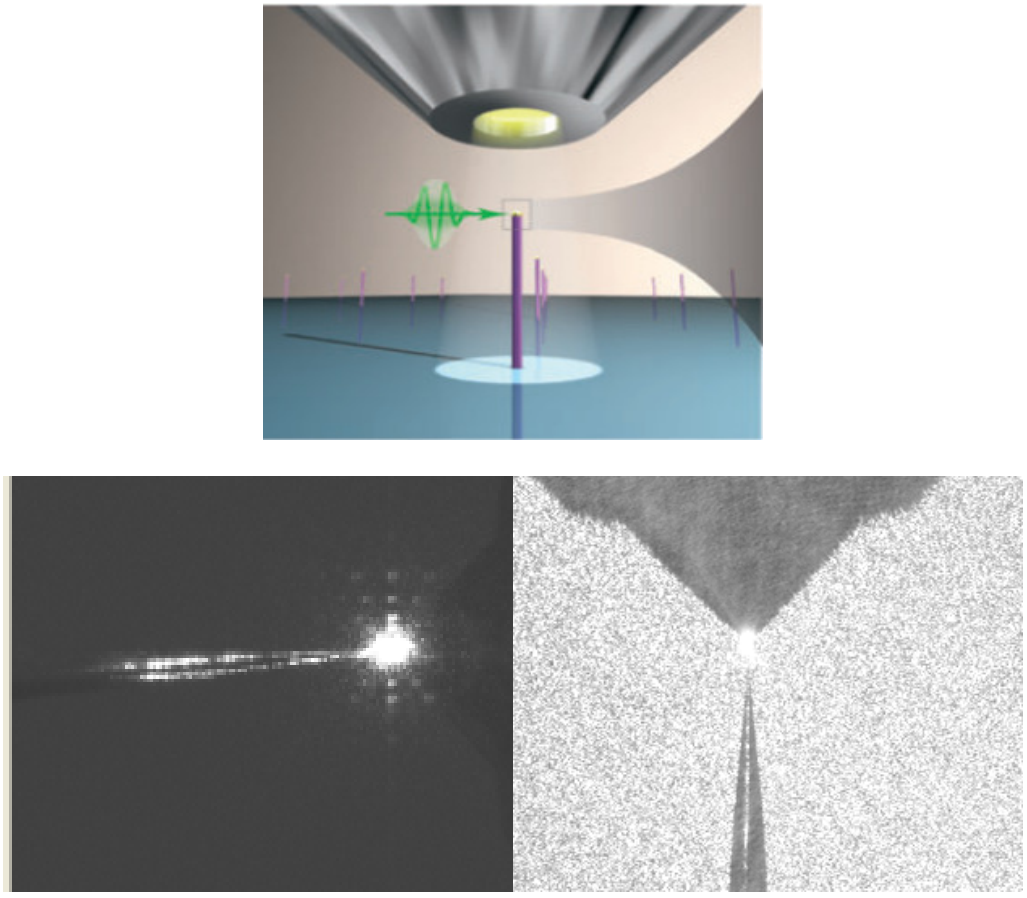

Fig 3.3.9.3: In-operation image of a fully austenized EX425 micro-tip using Laser pulsing in a 3D LEAP Atom probe [Courtesy: Seidman group, Northwestern University]. The bright zones are the reflection of the leaser beam from the surface of the tip section. Image taken using IVAS 3.0 [155]

Specimen Tip Preparation:

Figure 3.3.9.4 provides a schematic representation of the steps of preparing a Atom Probe LEAP tip manually. Specimens have been prepared manually because it gives a greater control of tip polishing and final finish for metallic strips than using FIB, which is more useful for nanowires and semi-conductors. Thin sections of 0.2 mm X 0.2 mm cross section were first cut from larger specimen blanks using precision wire saws. The length of the sections was ~ 10 mm. These were then fixed into small copper crimps and sealed at one end. Then micro tips were prepared using electropolising in two steps – first step involved macro-polishing using 10% perchloric acid in butoxyethanol solution at room temperature with a DC voltage of ~ 10-16 V enabling a steady current of 0.1-0.2 mA to form a slight taper. After this, the tip is washed very delicately with ethanol solution prior to micro-polishing. Once a nice thin taper is formed, in second stage of micro-polishing, we switch to a 2% perchloric acid in Butoxyethanol with a DC starting voltage of 7-9 V for final necking and slowly bringing down the applied voltage to 4-5V till a very fine layer is formed. At this moment, we switch from automatic voltage control to manual short-pulsing for a better control of the final breaking of the tip edge for a perfect finish of around ~ 25 – 50 nm.

After the lower portion breaks and falls off, the tip is cleaned using ethanol solution. The tip in the copper crimp is then loaded into the '*load lock*' chamber of the LEAP at an initial vacuum of ~ 10^{-8} torr from where it is finally transferred to the '*analysis*' chamber at an operating vacuum of 10^{-11} torr. The operating temperature ranges from 30K – 120K for most cases. Higher temperatures lead to better specimen runs (lower fracture risk) but results in a very high noise in the observed mass spectrum.

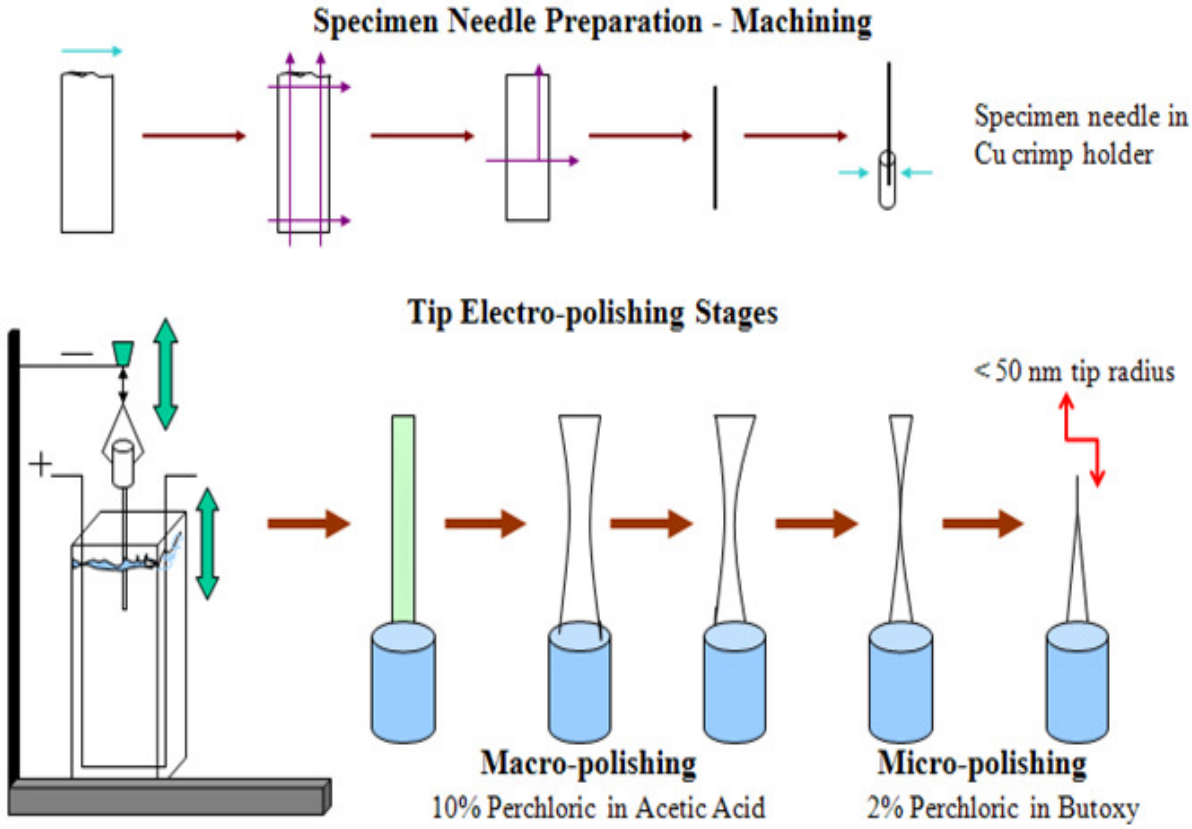

Fig 3.3.9.4: Schematic of all steps showing both macro- and Micro - polishing of specimen tips used in 3D Atom Probe Tomography. Final finish of the tips is ~ 25-50nm.

Operating Conditions:

The operating conditions for Voltage and Laser pulse modes have been shown in table 3.3.9.3. The specimens have been run at a constant super cooled temperature of 60K throughout and a vacuum of < 10^{-11} Torr for both Voltage and Laser pulse modes. Extreme low temperatures around 25-30K generally give very clear spectrums and are used for semi-conductor and thin-films analysis. However low temperature (<40K) operation has shown loss of Ni and Ti ions in EX425 specimens.

A starting voltage of 500V (~10V/nm) was applied to start the field ionization process and evaporate the ions from the tip. Automated evaporation control is used to monitor the evaporation rate of the ions and keep it fixed at a specified rate. The pulse fraction (Pulse to DC Voltage ratio) used is 0.20 for all runs except for initial calibration runs where the pulse fraction was varied from 0.15 – 0.20 to determine the optimum evaporation condition for EX425 TRIP prototype. At the start the evaporation rate is kept at 0.20 for voltage pulsing.

CONDITIONS	VOLTAGE PULSE	LASER PULSE
TEMPERATURE	60 ± 3K	60 ± 3K
PULSE FRACTION	0.20	-
PULSE ENERGY	-	0.60 ± 0.01 NJ
PULSE FREQUENCY	200 KHZ	250-500 KHZ
SPECIMEN VOLTAGE	500-14000 V	500-14000 V
OPERATING PRESSURE	$< 10^{-11}$ TORR	$< 10^{-11}$ TORR

Table 3.3.9.1: 3D –LEAP Atom Probe Tomography Operating conditions for Voltage and Laser mode for all specimens

For Laser pulse mode, the starting evaporation rate used is 0.20 (for pulse repetition rate of 250 kHz) and 0.50 (for pulse repetition rate of 500 kHz). The maximum evaporation rate allowed depends on the pulse frequency/repetition rate. Till the specified steady state evaporation rate is achieved, the voltage keeps increasing (automated control) and then ideally the curve of Voltage vs. Time almost flattens with a very small slope, as shown in figure 3.3.9.5. The maximum voltage allowed in the system configuration is ~15 kV. The evaporation rate can be increased in

steady steps for a faster ion collection (up to a maximum of 3.0 for 500 kHz Laser operation and upto 8.0 for 200 kHz Voltage operation) which might in turn lead to increase in conducting voltage depending on the evaporate state of the specimen tip.

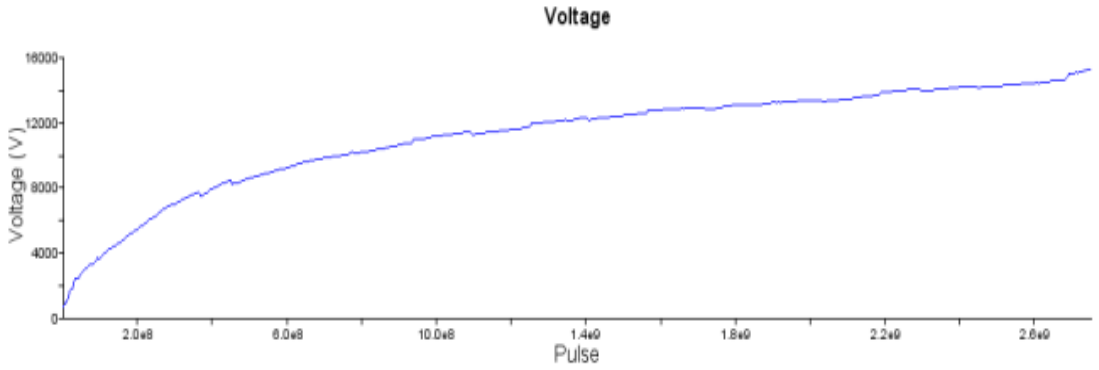

Fig 3.3.9.5: Typical voltage history during a good run showing gradual taper of the pulsed DC voltage with time. Once the adequate evaporation rate is achieved, the slope flattens out.

One of the major advantages of using the Laser mode other than its ability to amass high volume datasets in smaller times is the better compositional accuracy it provides by virtue of its better mass spectrum and low noise accompanying it. Section 4.2.3 shows the difference in observed mass-spectrum for fully austenized EX425 specimens using Voltage and Laser pulsing modes in the LEAP. The Laser mode of operation also provides the added capability to progressively scan the tip at any time during operation to automatically calibrate the optimum position and pulse fraction for the specimen tip, which highly optimizes the ion evaporation process and reduces the possibility of premature tip fracture. However, recent studies [154] of M_2C carbides and *BCC-Cu* precipitation study of Blastalloy160 [8] using Laser LEAP operation have shown distortion of precipitate images due to which the conventional Voltage mode is still the preferred mode of analysis.

Software and Analysis

Analysis of the data obtained the LEAP is done through the software IVAS^{TM} 3.03 developed by *IMAGO Scientific Instruments*. IVAS gives us the option of selecting ions hit on all or any part of detector (circular) region and uses a series of automatic time-of-flight and flight path corrections to calculate each ion 'hit' trajectories. Subsequently upon identification of the peaks in the mass spectrum, it gives a reconstructed image of the specimen showing each element/ion type in a specific color. Any precipitates or phase differentials are easily observed due to the color contrasts. IVAS allows excellent precipitate analysis using the *Envelope* method [151, 175-178], interface analysis and composition profiling. Detailed discussion of the Envelope method of precipitate analysis is given in Appendix I. Composition estimation is done by two different methods – a) 1D composition profiling, and b) Proxigram analysis of Iso-concentration surfaces. For calculating the 1D composition file, a pre-shaped section (Cylindrical, Cube or Sphere) can be selected with specific diameter/width to encapsulate any region of the reconstructed volume and all ions/atoms within that region selected is used to compute the 1D composition profile (Composition vs. Distance from edge). In this research, a cylindrical section of 2 nm diameter has been used in all 1D profiles generated. Where more detailed composition analysis (of precipitates or specific phases) is required, an Iso-concentration Proxigram method is used [152]. In this method, for a specific threshold concentration of a single or group of ions, the program creates contour plots of 3D regions highlighting volumes within the reconstruction where the minimum boundary concentration is restricted by the threshold concentration of ions specified. This method uses bins to identify each ion within their boundary, and computes the contours based on concentration differentials. Due to the complexity, it usually takes lot more

computational time (several minutes) for larger datasets. The standard deviation of the measured compositions of each ion/atom is calculated using the following equation [153].

$$\sigma = \sqrt{\frac{c(1-c)}{N}} \tag{3.3.8}$$

Where c is the measured composition of the specific ion and N is the total number of ions. Number density, Volume fraction of Gamma Prime precipitates and inter-precipitate distances (IPD) is determined by the Envelope method [151]. Detailed description of the methodologies and equations for determining these numbers by separation of clusters using the *envelope* method has been provided in Appendix I.

Color Convention

The different colors used in LEAP reconstructed images throughout this document are consistent with the following representation (although in most images only Ti, Ni and Fe ions have been shown)–

Fe ions: Blue, **Ni ions**: Green, **Ti ions**: Red, **Mo ions**: Light Green, **V ions**: Brown, **Cr ions**: Orange, **Al ions**: Light/Sky Blue, **B ions**: Purple. Other trace components such as **N**, **C** etc. are not selected in the LEAP re-construction.

CHAPTER 4

EVALUATION OF TRIP PROTOTYPE: EX425

As previously described in section 3.1, the starting material for all mechanical testing and austenite matrix stability calculations and calibrations for our new designs is the experimental model prototype alloy EX425. EX425 is a fully austenitic (**γ**) steel strengthened by precipitation of intermetallic **γ'** Ni_3 [Ti, Al] precipitates. In this section, various processing and experimental results of evaluation of EX425 have been discussed in detail. The composition of EX425 has been reported in table 3.1. As reported by Stavehaug [13], the original EX425 was melted by Vacuum Induction at Carpenter Technology Corp into 100 lb ingots which were homogenized at 1190^{o}C for 24 hours, cooled to 1149^{o}C and forged into 3-inch square bars. They were further reduced in form of billets of 2.875 X 1.5 inch cross section.

4.1 Solutionizing and Heat Treatments

Using Thermo-Calc, two phase γ - γ' equilibrium condition was established for varying temperatures as shown in figure 4.1.1. The temperature where the alloy is in homogeneous single solid-phase equilibrium is considered to be the solutionizing temperature. It is seen from figure 4.1.1 that gamma prime phase fraction goes to zero ~ 855^{o}C. Although the gamma prime phase (γ') fraction goes to zero at 855^{o}C, it is generally recommended to have a solutionizing treatment atleast 50^{o}C above the single solid phase point. Solutionizing at temperatures above 950^{o}C had previously shown embrittlement due to excessive grain growth while for lower temperatures have shown presence of duplex grain size [13]. From this an ideal solutionizing temperature was determined ~ 950^{o}C for 1 hour to obtain single phase matrix austenite (γ) composition dissolving

all other phases. Prior to solutionizing, the specimens are vacuum encapsulated in quartz tube as described in section 3.3.1. After solutionizing, the specimens are quenched in an oil bath at room temperature to avoid direct oxidation. The presence of the second FCC phase TiC in solution with matrix is desirable as it leads to austenite grain refinement.

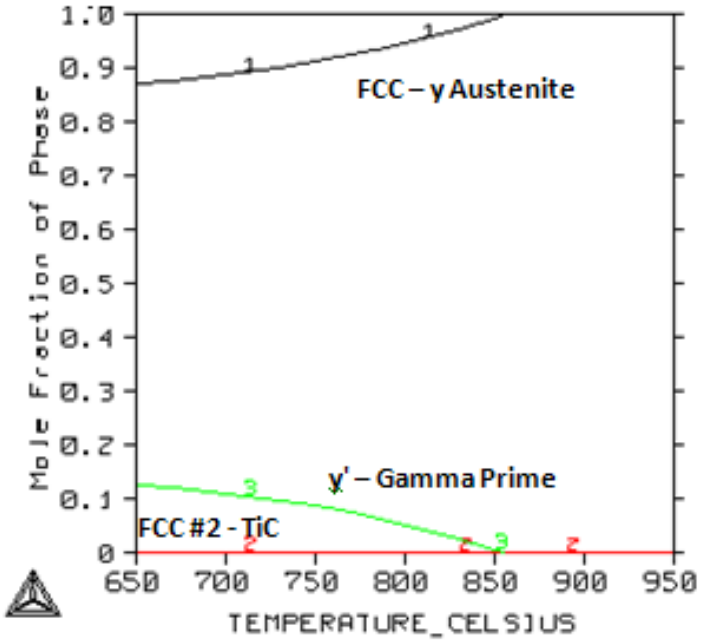

Figure 4.1.1: Temperature dependence of equilibrium phase fractions for EX425 calculated using Thermo-Calc and Ni-data 7 thermodynamic database. The phases considered in equilibrium are FCC and Ni-rich Gamma Prime.

Stavehaug had previously studied the optimum aging temperature-time dependence of EX425 for attaining peak hardness. The following two reference points of peak hardness for EX425 were set based on optimum radius of **γ'** precipitates – a) 700°C for 60 hours, and b) 750°C for 10 hours. Figure 4.1.2 shows an Arrhenius curve of the natural logarithm of the inverse of time to the inverse of temperature (Kelvin) fit to the two data points for extrapolation of peak hardness aging conditions. The times for all heat treatment temperatures have been set according to the curve in figure 4.1.2, including that of the final prototype alloy design.

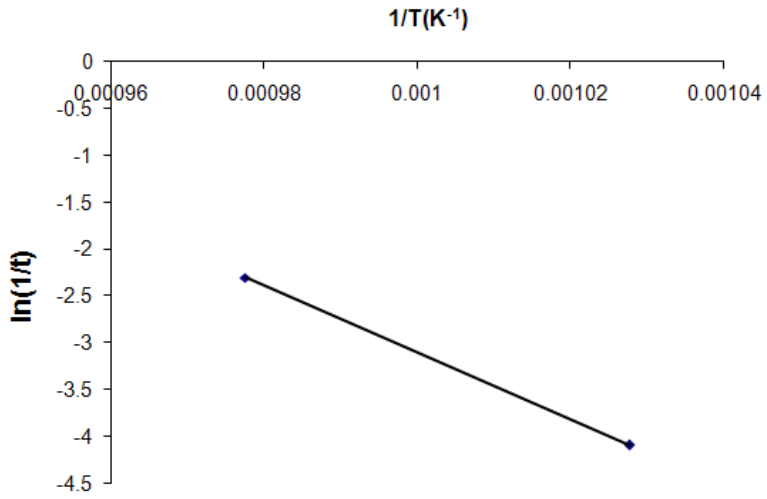

Figure 4.1.2: Arrhenius curve for relation between aging temperature and aging time for peak hardness based on optimum gamma prime particle radius of ~ 15 nm.

4.2 Matrix Microstructure Evaluation

4.2.1 Optical Microscopy:

Microstructure evaluation by light microscopy has been performed on solution treated and quenched EX425 specimen to study the fully austenitic microstructure. Smaller pieces of the EX425 billets were solution treated at 950^{o}C and oil-quenched. They were then cut to thin slices of 10 mm X 10 mm cross section and ~ 1 mm thickness and then mounted, ground, polished and rubbed lightly with etchant solution, as discussed in section 3.3.9.1. Figure 4.2.1.1 (a) and (b) show the microstructure and austenite grain boundaries obtained. The linear grid intercept method conforming to ASTM E112-96 [156] has been used to determine the average size of the austenite grains. The average austenite grain size, as observed, is 30μm.

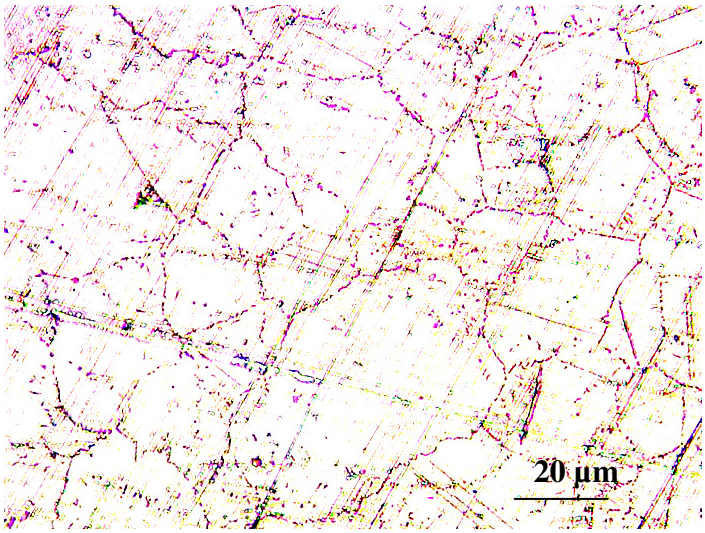

Figure 4.2.1.1 Austenite matrix grains of solutionized EX425 specimen as seen using an inverted optical microscope at 100X magnification. Etchant used is 2% Nital.

4.2.2 X-Ray Diffraction Analysis of Matrix

X-Ray diffraction has been performed for solution treated and quenched EX425 specimens to confirm the presence of a fully austenitic microstructure. Feinberg [157] has done quantitative assessment by measuring the intensity of the austenite {220} reflections and comparing them with the standard austenite power diffraction peaks from tables. The analysis was performed for a 2θ range of $45^{o} – 55^{o}$. Figure 4.2.2.1 shows the {220} Austenite diffraction peak obtained -

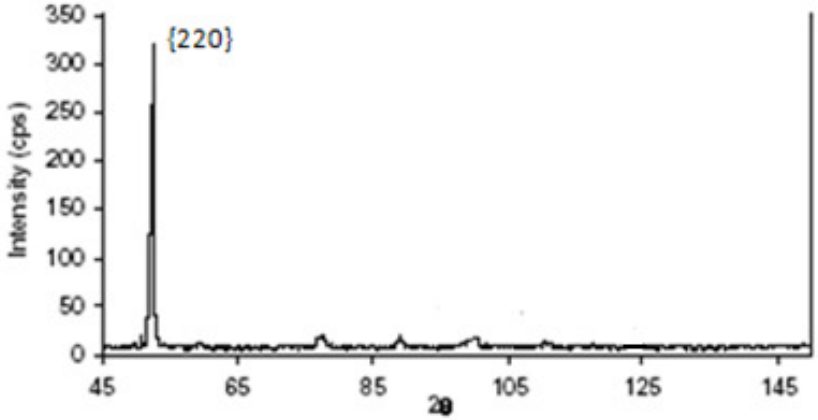

Figure 4.2.2.1: X-Ray diffraction intensity per scanning angle showing observed Austenite {220} peaks in solution treated EX425 specimen

The figure 4.2.1.1 shows only austenite peaks corresponding to Austenite {220} reflections confirming that the structure are fully austenitic after solution treatment at 950^{o}C for 1 hr and quenching to room temperature thereafter.

4.2.3 LEAP Analysis and Composition Validation of Austenite Matrix

3-D Local Electrode Atom probe has been used to study the matrix austenite phase after solution treatment (950^{o}C for 1 hr) and quench. It has been used to determine the austenite composition using 1-D cylindrical profiling parallel to the z-axis direction. The iso-concentration Proxigram method has not been used in this case since for solution treated specimens we do not have any gamma prime (γ') precipitates to create iso-surfaces or bound surfaces with specified composition boundary conditions. Figure 4.2.3.1 (a) and (b) shows a reconstructed 3D LEAP atom probe image of the pure Austenite matrix. It shows a fully austenitic microstructure as expected and without any Ti ion segregation implying absence of gamma prime precipitates.

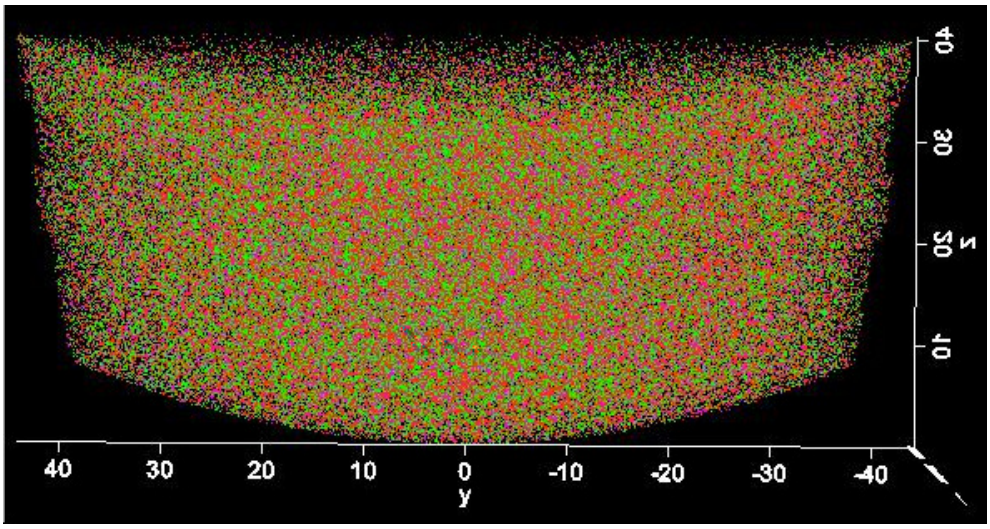

Figure 4.2.3.1 (a): 3-D Reconstruction of a fully austenized EX425 [70nm X 80 nm X 30 nm]

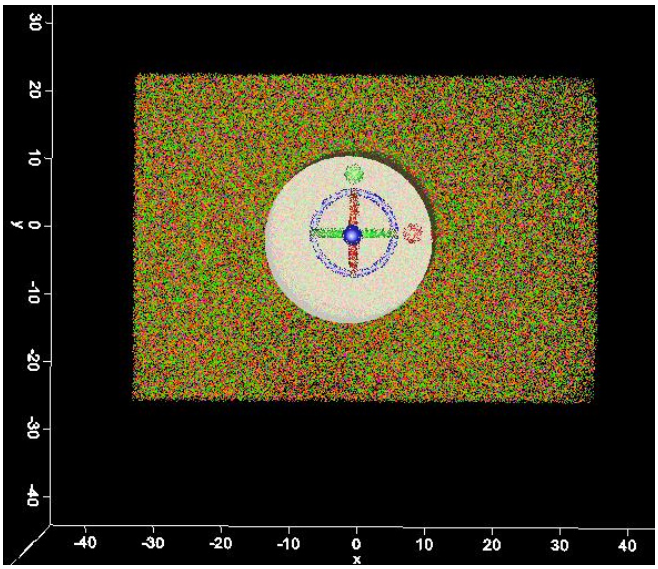

Figure 4.2.3.1 (b) Clipped 3D - LEAP image of the fully austenized EX425 specimen as observed along the z-axis vertically. The figure shows a cylindrical bin with a diameter of 20 nm used to encapsulate an equal volume of ions for generation of 1-D composition profile [70nm X 80 nm X 30 nm]

Total number of ions/atoms in the construction is 8.1 Million. Figure 4.2.3.1 (b) shows the cylindrical volume of diameter 20 nm used to bind a region for 1D composition analysis. Table 4.2.3.1 lists the comparison of equilibrium austenite matrix compositions determined by Thermo-Calc and the measured compositions using LEAP at the solutionizing temperature of 950^{o}C.

γ (atomic fraction)	**Fe**	**Ni**	**Cr**	**Mo**	**Al**	**Ti**	**V**
Predicted (TC)	0.668	0.240	0.043	0.007	0.003	0.035	0.003
Measured	0.670 ± 0.023	0.241 ± 0.021	0.044 ± 0.011	0.007 ± 0.004	0.003 ± 0.002	0.034 ± 0.014	0.003 ± 0.001

Table 4.2.3.1: Comparison of Calculated thermo-calc equilibrium matrix composition with that of measured austenite composition for a fully austenized EX425 specimen using 3-D LEAP tomography

The error factor in the calculation of ionic composition is determined by equation 3.3.8 in section 3.3.9.3. Figure 4.2.3.2 shows the 1D composition profile of the bounded volume shown in figure 4.2.3.1 (b) for the austenite matrix showing uniform levels of main components Ni, Fe, Cr and Ti without many variations.

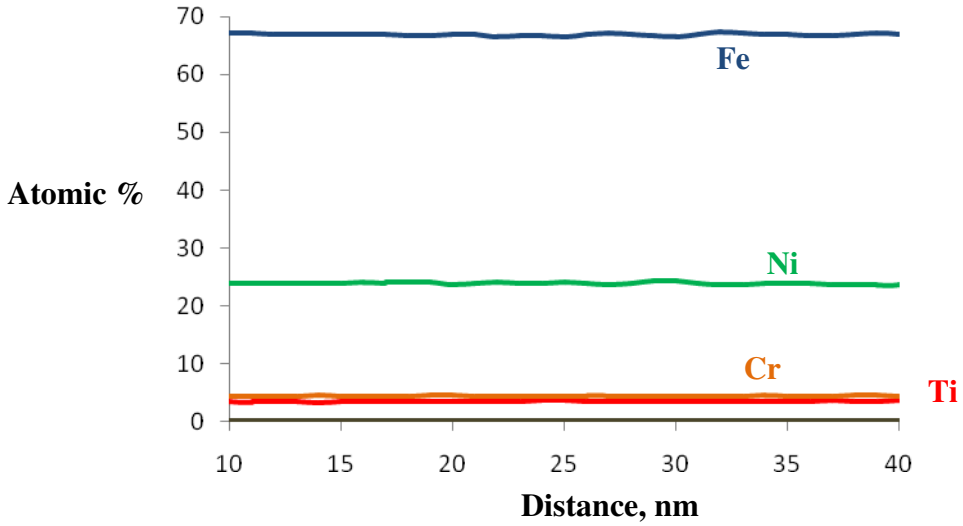

Figure 4.2.3.2: 1-D Composition profile of major elements for figure 4.2.3.1 (b) measured using 3-D LEAP Tomography. The length of 30 nm is for analysis along z-axis.

4.3 Gamma Prime (γ') Precipitate Analysis

LEAP analysis of EX425 has been used to not only to evaluate the distribution and properties of the gamma prime precipitates at various temperature of interest in the range from 650°C – 800°C, but also to study the kinetics of nucleation and growth of Gamma Prime **γ'** strengthening phase precipitates. The specimens were tempered to temperatures ranging from 600°C to 800°C for times determined by their peak hardness criteria based on the Arrhenius relationship shown in figure 4.1.2.

4.3.1 Temperature Dependence of Gamma Prime γ' Phase Fraction

Using the Ni-data7 database with Thermo-Calc, we calculate the ideal equilibrium matrix austenite and gamma prime phase fractions and composition at different aging temperatures. Figure 4.3.1.1 shows the variation of gamma prime phase fraction with temperature for EX425 alloy composition for the temperature range 500°C to 1000°C.

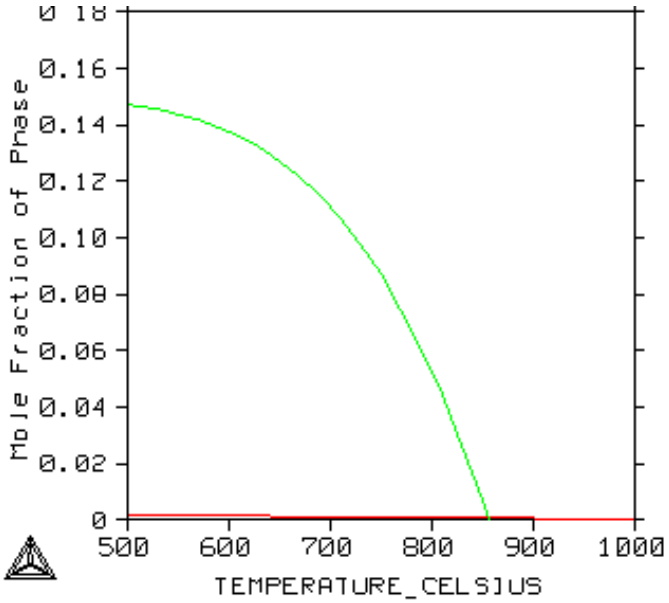

Figure 4.3.1.1: Temperature dependence of the mole fraction of gamma prime precipitate phase in equilibrium with matrix FCC austenite for EX425

As discussed previously, the Gamma Prime fraction goes to zero at 855°C marking the start of solutionizing temperature zone. As the gamma prime phase fraction decreases with increasing temperature, accordingly the hardness and yield strength of EX425 also decreases for increasing aging temperature. This has been shown in section 4.4. Above 600°C, the gamma prime phase fraction decreases very rapidly till the specimen has a single homogenous matrix austenite phase. This is very important in determining the ideal aging conditions for EX425 as a minor increment in aging temperature would lead to lower yield strength of the specimen.

4.3.2 LEAP Analysis of Gamma Prime (γ') Precipitates

The 3-D Local Electrode Atom Probe (LEAP) is one of the most important tool used to characterize the gamma prime **γ'** precipitates in EX425 prototype. The nano-scale size of these precipitates makes them very difficult to analyze in detail using standard SEM and TEM characterization techniques. The need to view the precipitate distribution on a large scale and get quantitative analysis of its size, population density and intrinsic composition makes the 3-D LEAP much more viable option than a TEM or any other high resolution microscopy technique.

4.3.2.1 Characterization of Gamma Prime γ' precipitates

The distribution of gamma prime precipitates **γ'** has been studied for both a) single step tempers at 700^{o}C, 736^{o}C, 750^{o}C and 800^{o}C as well as for b) multi-stage heat treatments. For single step temper, the time of heat treatment for a given aging temperature is determined according to the Arrhenius model for peak hardness (related to optimum particle radius) condition, as discussed in section 4.1. For the multi-stage tempers, the time for heat-treatments is dependant on the final goal; either higher than the normal peak hardness times for over-aging in specimens to reduce hardness/Yield Strength in each step or to age for lesser times in each stage to attain maximum hardness.

Figure 4.3.2.1.1 (a) and (b) shows the 3D LEAP reconstruction of a single step aging at 700^{o}C for 60 hours using laser pulse mode. This aging treatment condition gives an estimated yield strength of 138 ksi based on phase fraction of **γ'** vs. yield strength calibration based on hardness profile shown in section 4.4. Ti ions are represented in red and the spheroids represent the iso-concentration surfaces encapsulating all surfaces with a Ti-Ni minimum boundary concentration

of 50%, or namely, a 50% TiNi Iso-concentration surface. The critical value of the iso-concentration surface is determined by step-by-step incrementing of the TiNi boundary concentration value till the bounded regions have a clear separation. The background represents the austenite matrix with blue dots showing the Fe ions and green dots showing the Ni ions.

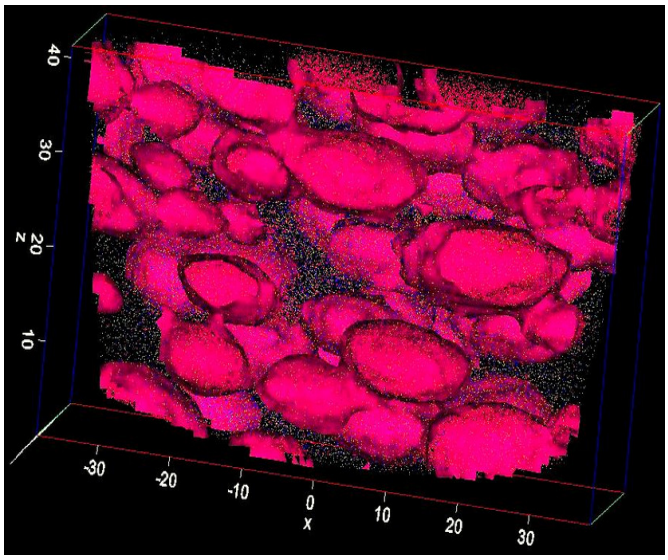

(a)

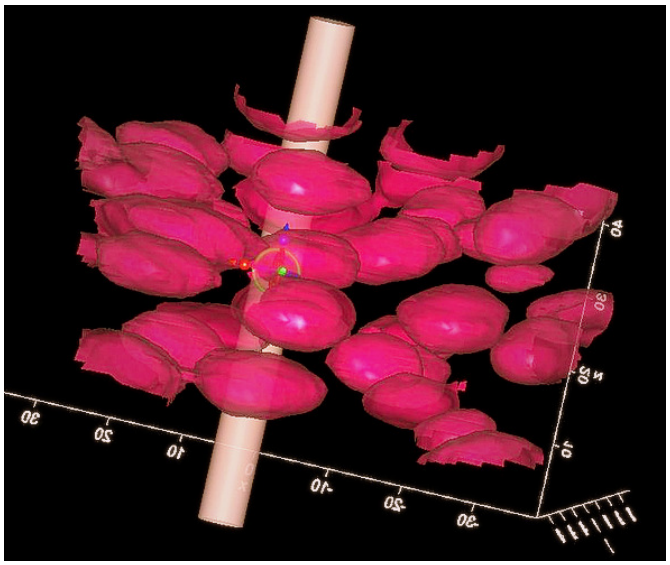

(b)

Figure 4.3.2.1.1: (a) Pulsed laser 3D- LEAP reconstructed images for an EX425 specimen aged at 700°C for 60 hours with **γ' –** precipitates shown in red iso-concentration surfaces and (b) a cylindrical analysis area to calculate 1D profile [10 Million ions analyzed] [70 nm X 60 nm X 40 nm]

Figures 4.3.2.1.1 (a) represents a TiNi – 40 % iso-surface created which is lower than the critical value of 50%. The image clearly shows the red bounded regions of Gamma Prime still diffusing out of each other while figure 4.3.2.1.1 (b) represents TiNi 50% iso-surface bounded volumes showing the clear demarcation between the precipitate particles.

Figure 4.3.2.1.2 (a) and (b) show the composition estimation of the gamma prime regions using 1D profiling and concentration Proxigram method, respectively.

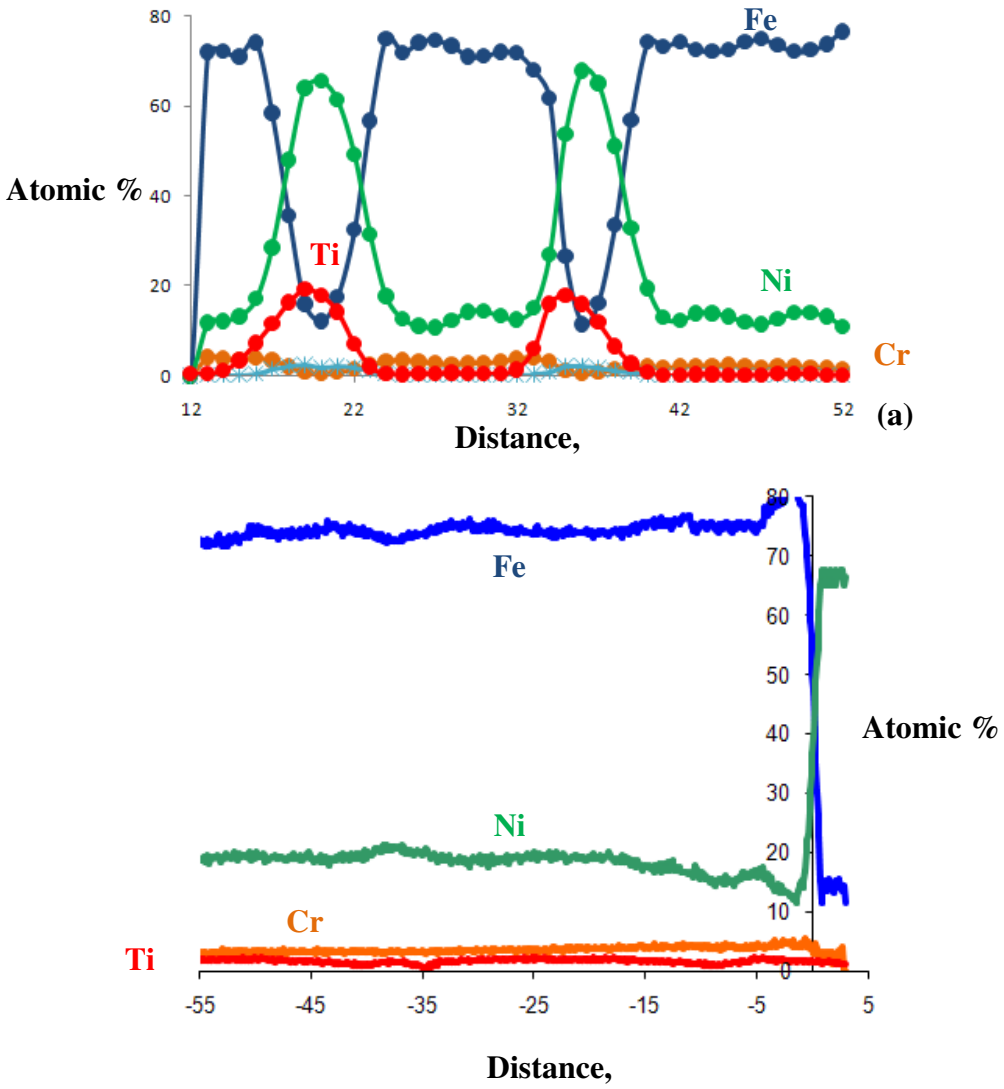

Figure 4.3.2.1.2 (a): 1D Composition Profile of EX425 aged at 700°C for 60 hr **(b)** Proxigram analysis of all TiNi interfaces (red) shown in figure 4.3.2.1.1 (b)

All 1D composition analysis has been done along the z-direction for precipitates aligned normally to the z-axis as shown in figure 4.3.2.1.1 (b). A detailed analysis of the kinetics of gamma prime **γ'** nucleation has been done at this aging temperature (700^{o}C) to understand the growth rate, changes in size, number density and also volume fraction of the precipitates in this class of TRIP steel. This analysis has been described in detail in Appendix I.

Although 1-D profiling is not considered to be a very accurate measure of the composition of the gamma prime precipitate phase in the 3D – LEAP reconstructed images due to their high density and varying size and interfaces, it gives a very fair estimate of the same and also for the width of the precipitates along the direction of analysis. This is because if the number density of precipitates is very large, as in figure 4.3.2.1.1, the cylindrical bins cut through multiple precipitates and interfaces, thereby leading to high variances in compositional accuracy. Thus, all composition validation done in section 4.3.2.3 use data calculated using the Proxigram method [152] for 50% NiTi Iso-concentration surfaces using only laser mode.

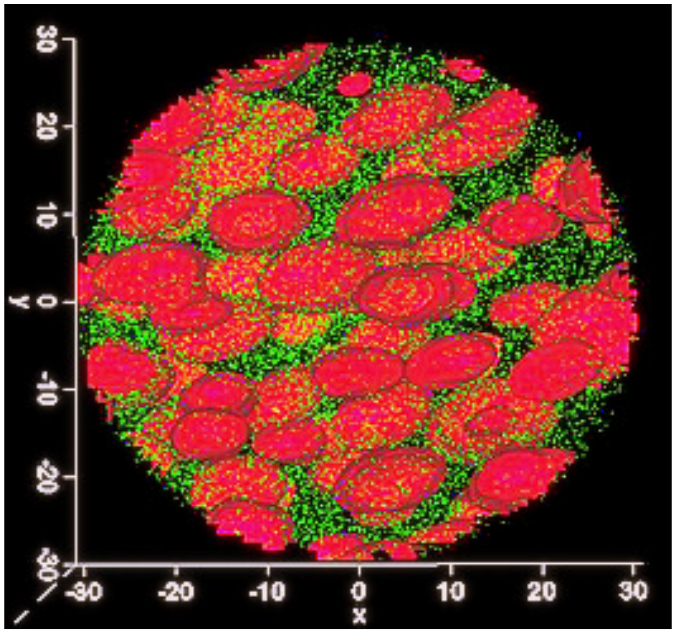

Fig 4.3.2.1.3: (a)

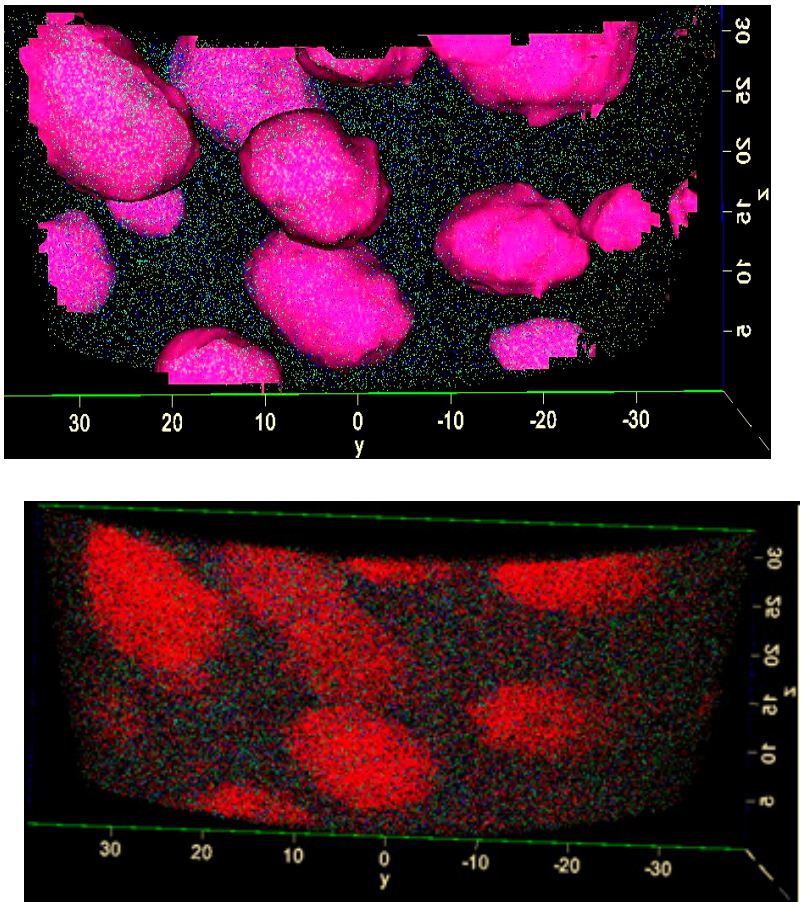

(b)

Figure 4.3.2.1.3: (a) Pulsed Laser LEAP image of an EX425 aged at 736oC for 16.25 hours showing TiNi iso-surfaces in red for **γ' –** precipitates and green Ni ions in matrix **[**14 M ions**]** [60nm X 60nm X 40nm], and (b) Voltage LEAP image [8 M ions] [80nm X 70nm X 30nm]

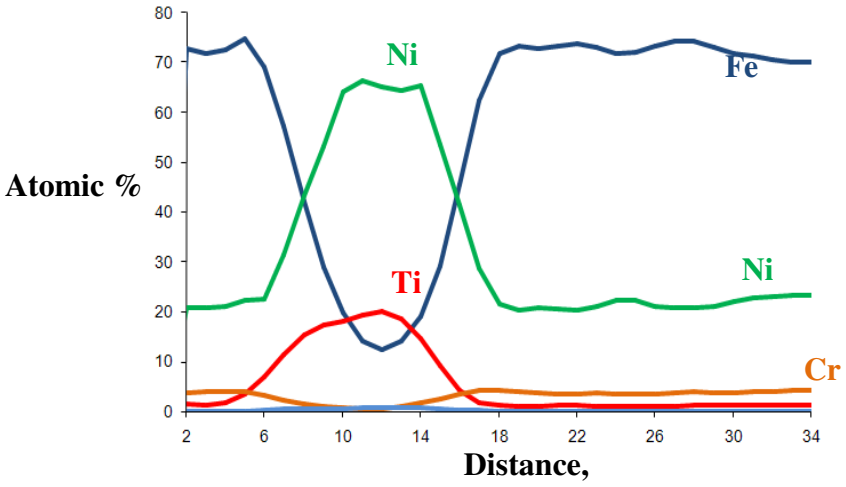

Figure 4.3.2.1.4: (a): 1D Composition Profile of EX425 aged at 736^{o}C for 16.25 hr

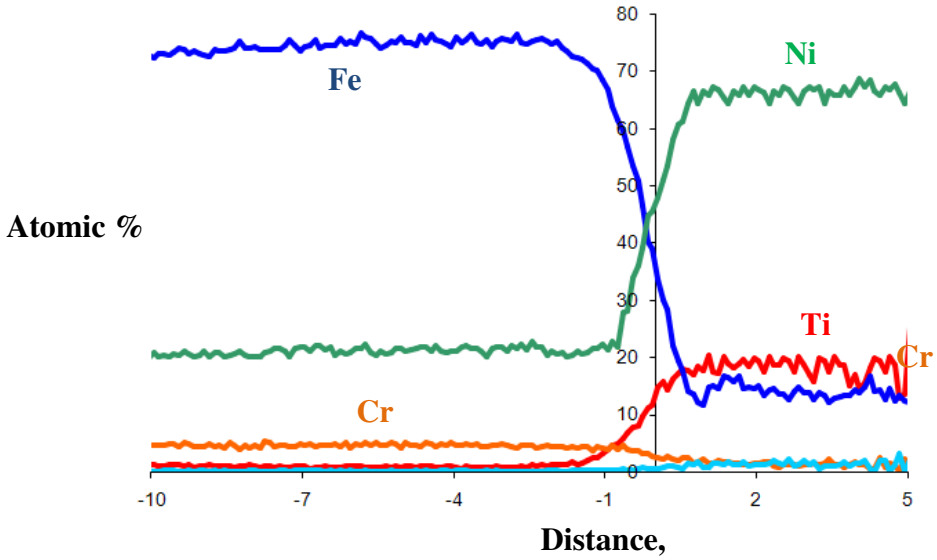

Fig 4.3.2.1.4: (b) Proxigram analysis of all TiNi interfaces shown in figure 4.3.2.1.3(a)

The Proxigram composition profile for figure 4.3.2.1.1 is shown in figure 4.3.2.1.2 (b). Figure 4.3.2.1.3 and 4.3.2.1.5 shows the LEAP reconstruction images for tempers done at 736^{o}C for 16.25 hours and 750^{o}C for 10 hours respectively. The calculated yield strength at these heat-treatment conditions are 130 ksi and 125 ksi respectively. These show the evolution, size and distribution contrasts of gamma prime precipitates with increasing tempering temperatures. The respective compositional analysis using 1D and Proxigram methods is also shown in figures 4.3.2.1.4 and 4.3.2.1.6. It can be observed from the 1D profile of figure 4.3.2.1.4 that the width of the gamma prime precipitate can be determined by the width of profile trough. To determine the final composition of the gamma prime precipitate using 1D profiling, a 95% statistical confidence interval is first calculated for all measured data points along the coordinates of flat part of the curve between the two intersection troughs for any ion species, then using the same length coordinates, the confidence interval for other ions is calculated. The interval denotes the range of statistical variance for the concentration of the ions and the mean value for the range is taken to be the measured concentration.

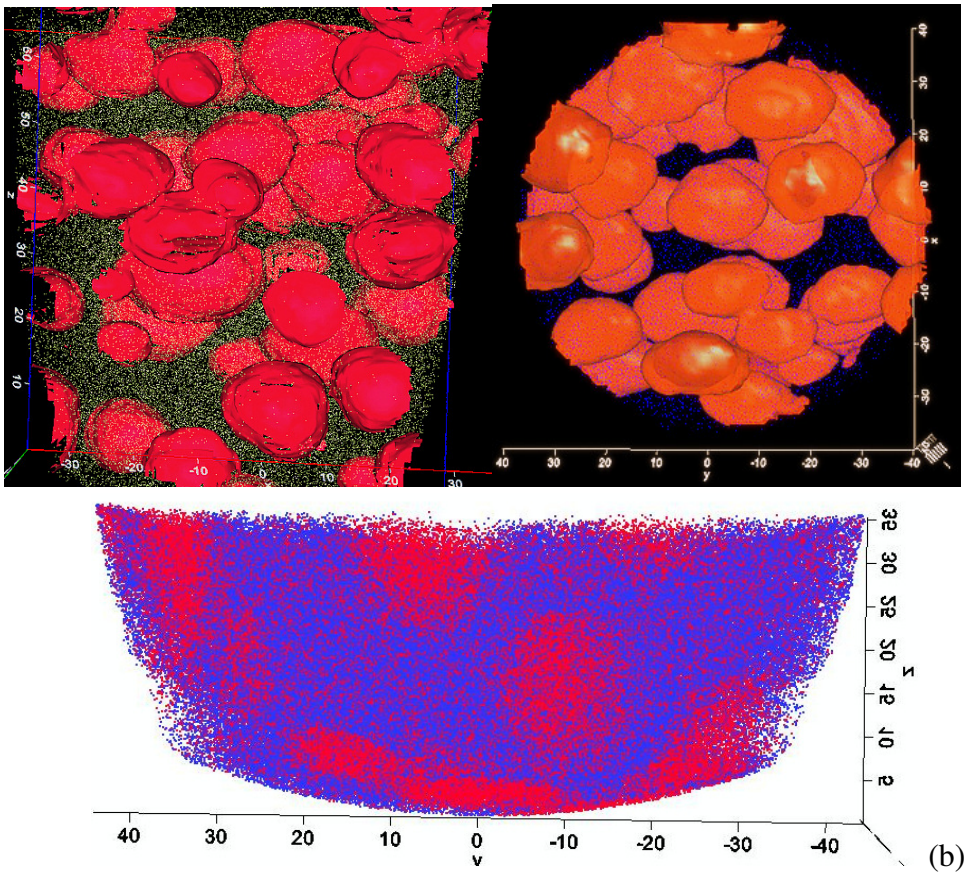

Figure 4.3.2.1.5: (a) Laser LEAP image of EX425 aged at 750°C for 10 hours showing TiNi iso-surfaces in red for **γ' –** precipitates and green Ni ions in matrix **[**25 M ions**]** [70nm X 70nm X 80nm], and **(b)** Voltage LEAP image of red Ti ions and blue matrix Fe ions [10 M ions] [80nm X 80nm X 35nm]

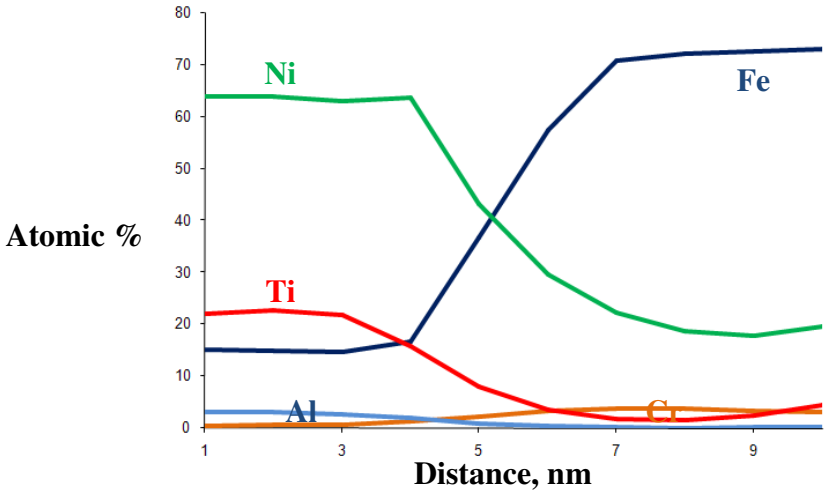

Figure 4.3.2.1.6 (a)

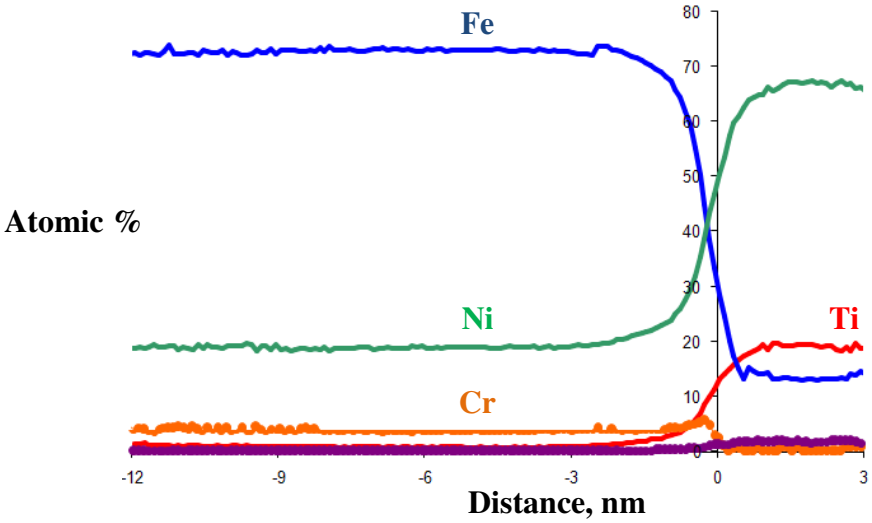

Figure 4.3.2.1.6: (a): 1D Composition Profile of EX425 aged at 750°C for 10 hr **(b)** Proxigram analysis of all TiNi interfaces (red) shown in figure 4.3.2.1.5 (a)

High temperature (> 780°C) heat treatment of EX425 TRIP prototype has shown formation of **η** precipitates which are plate-shaped particles. Under the effect of high temperatures (>780C) for prolonged aging periods, **γ**' Ni_3 (Ti, Al) phase is known to transforms into hcp '**η**' phase. Under these circumstances, the LEAP tomography showed the phase to appear in bands, as shown in red (Ni-rich regions) in the figure 4.3.2.1.7. This phase is unwanted as it reduces the uniform ductility.

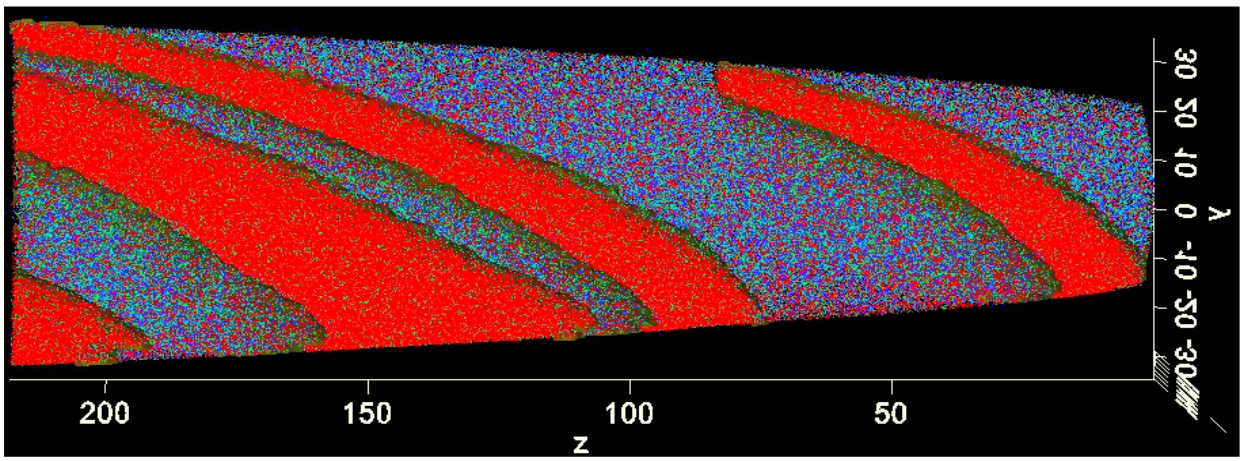

Figure 4.3.2.1.7: (a)

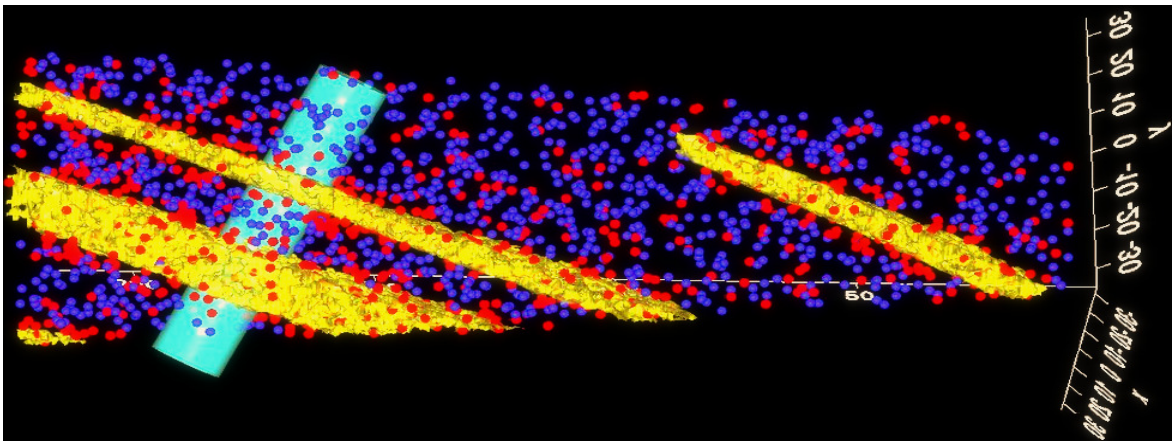

(b)

Figure 4.3.2.1.7: Voltage LEAP image of EX425 aged at 800°C for 10 hours showing (**a**) formation of **η –** precipitate plates/bands **[**45 M ions**]** [60nm X 60nm X 250nm] **(b)** Ti Ni Iso-surfaces shown in yellow along with a cylindrical 1D profile surface, with Fe and Ti ions of matrix

The yellow bands represent the 50% NiTi iso-concentration for Gamma prime precipitates.

Figure 4.3.2.1.8 shows the composition using 1D.

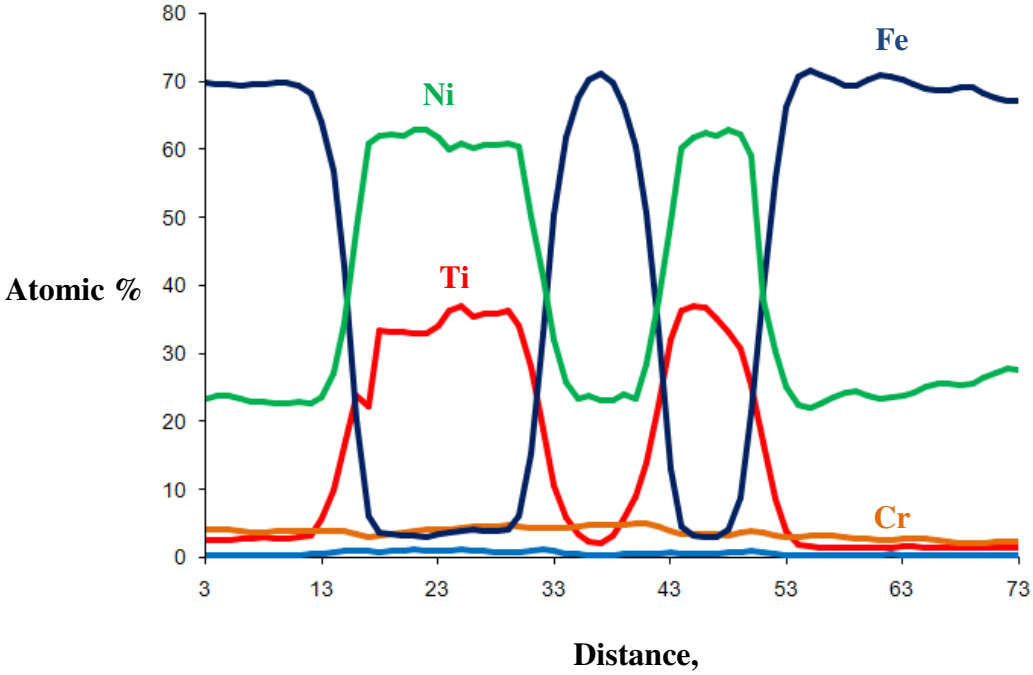

Figure 4.3.2.1.8: 1D Composition Profile of EX425 aged at 800°C for 10 hr showing the thickness of the two Eta precipitates seen in figure 4.3.2.1.7

Since the precipitates appear as plates/bands, the 1D composition profile is much more accurate than in general cases for spheroidal gamma prime precipitates. The two intersection widths in the 1D profile give an accurate estimate of the widths of the two η plates formed - ~ 16 nm and 8 nm respectively. The transformation of γ' spheroids to η plates have been seen to occur at temperatures above 780^{o}C for aging time ~ 10 hours, although presence of spheroids highly elongated along the z-axis (~ 30 nm) have been confirmed [159] even at lower temperatures ~ 700^{o}C for prolonged aging times (>100 hours). The compositional analysis of these precipitates using Proxigram method has shown these precipitate regions to be higher in Ni and Ti and lower in Al than predicted by Thermo-calc for $\gamma - \gamma'$, leading support to the theory that they are leading towards a $\gamma - \eta$ equilibrium state rather than a $\gamma - \gamma'$ equilibrium as expected. Both laser and voltage modes have confirmed the presence of large egg-shaped precipitates in EX425 specimens aged at 700^{o}C for 200 hours [159]. This has been discussed in further detail in the kinetics study of gamma prime nucleation in Appendix I.

Two multi-stage heat-treatments have been carried with specific objectives. A first multi-stage heat treatment has been done in order to maximize the hardness. Since higher phase fractions of gamma prime is attained at lower temperatures where the kinetics is slow, the multi-stage heat treatment involves starting with a higher temperature for peak hardness aging time and then decreasing the temperatures in the later stages. A three stage heat treatment with 750^{o}C (10 hr) – 700^{o}C (20 hr) – 650^{o}C (25hr) was adopted and the 3D LEAP reconstruction of the precipitates and matrix post the 3rd stage is shown in figure 4.3.2.1.9.

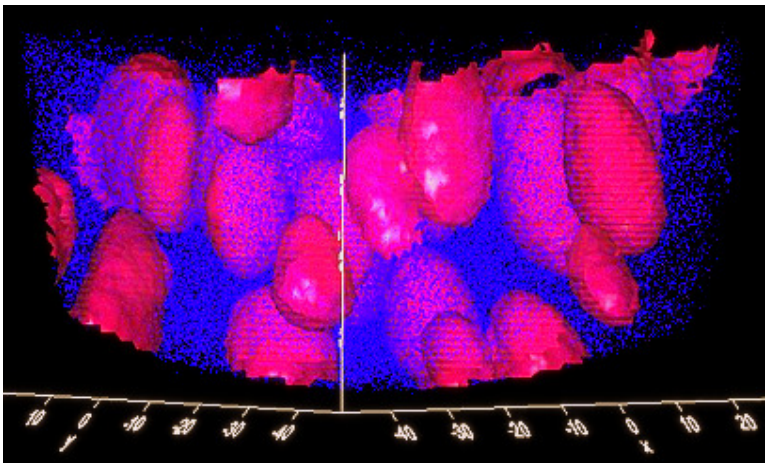

Fig 4.3.2.1.9: (a)

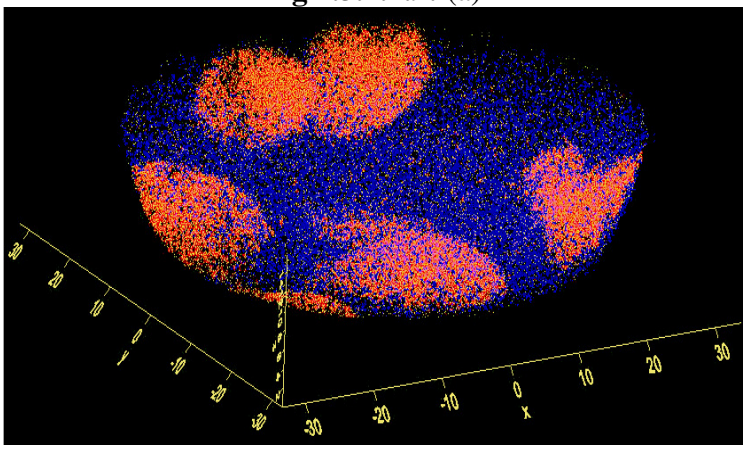

Figure 4.3.2.1.9: (a) Laser LEAP image of EX425 aged at 750°C (10 hr) + 700°C (20 hr) + 650°C for 25 hours showing TiNi iso-surfaces in red for **γ' –** precipitates and blue Fe ions in matrix [25 M ions**]** [70nm X 70nm X 80nm], and **(b)** Voltage LEAP image of red Ti ions and blue matrix Fe ions [10 M ions] [80nm X 80nm X 35nm]

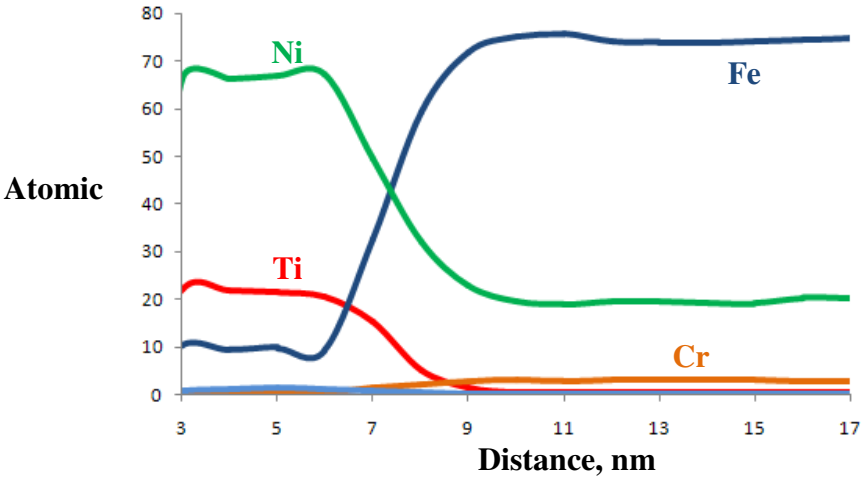

Fig 4.3.2.1.10: (a)

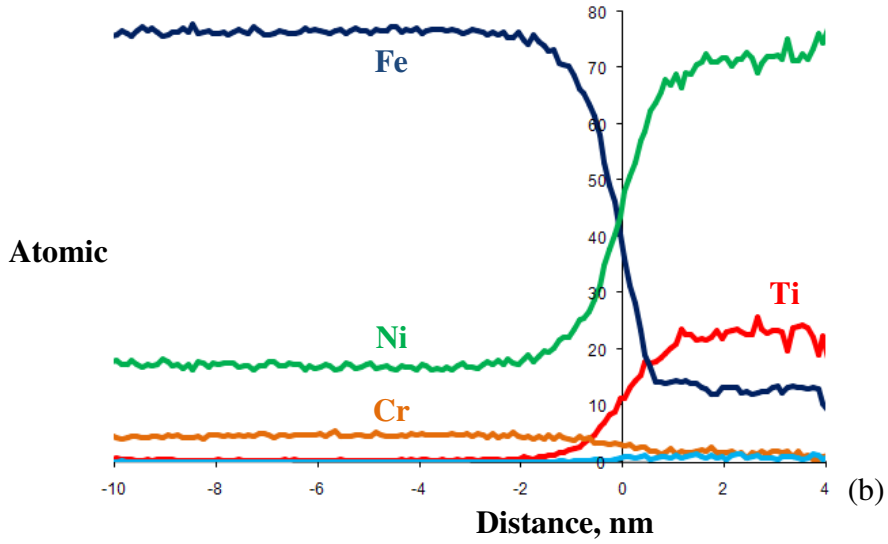

Figure 4.3.2.1.10: (a): 1D Composition Profile of EX425 aged at 650°C for 25 hr **(b)** Proxigram analysis of all TiNi interfaces (red) shown in figure 4.3.2.1.9 (a)

The second multi-stage heat treatment is the 800°C(10hr) – 720°C(30hr) – 641°C (100hr) three step temper process with the goal of optimizing the stability of the matrix austenite to have an M_S^{σ} temperature close to room temperature, and maintain strength levels ~ 120 ksi (827 MPa) by overaging. The 3D LEAP reconstructed images were taken after the 3rd stage of 641C (100hr). The LEAP images, as seen in figure 4.3.2.1.11 (a), do not show the presence of any precipitates or they might be too small to be resolved. The Ti rich regions from the precipitates slowly disperse towards the grain boundaries in this state with prolonged aging, leading to reduced strength and ductility of the material in this state.

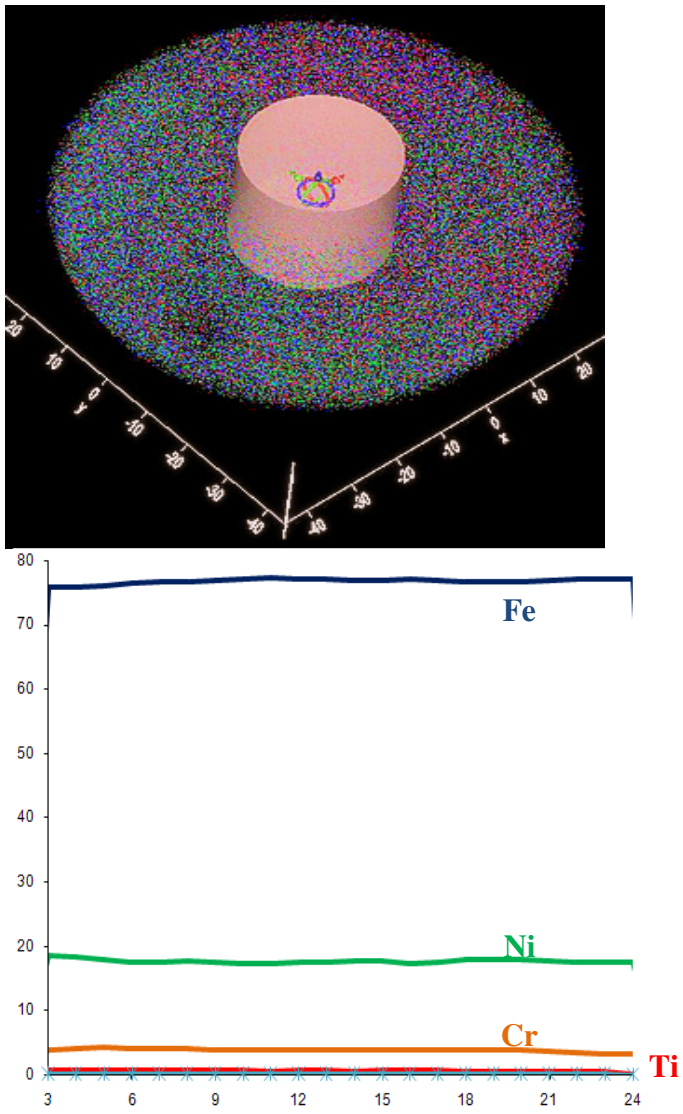

(a) (b)

Figure 4.3.2.1.11: (a): 1D Composition Profile of EX425 aged at 800°C (10hr) – 720°C (30hr) – 641°C (100hr) **(b)** 1D Composition Profile related to figure in (a)

4.3.2.2 Optimum Size of Gamma Prime Precipitates

It is important to determine the optimum size of the gamma prime precipitates to achieve the efficient strengthening of the alloys. The strengthening model of intersection of single and double dislocation cutting of gamma prime particles at the optimum radius has been detailed in

section 2.4 figure 2.4.1. Using the same approach, the variation of a normalized precipitation strengthening term using phase fraction of gamma prime with respect to Precipitate radius is calculated in figure 4.3.2.2.1. The normalized strength of EX425 is calculated for the measured precipitate cluster diameter. The precipitate diameter is determined by first calculating the average effective volume of the clusters in each state, with Ti ions acting as the differentiating constituent from the matrix. Then using equivalent sphere geometry for each cluster, the average cluster radius is calculated. Figure 4.3.2.2.12 shows the intersection of the best fit $r^{1/2}$ and $1/r$ curves for optimum radius. The optimum precipitate radius for maximum strengthening is calculated to be ~ 7.4 nm.

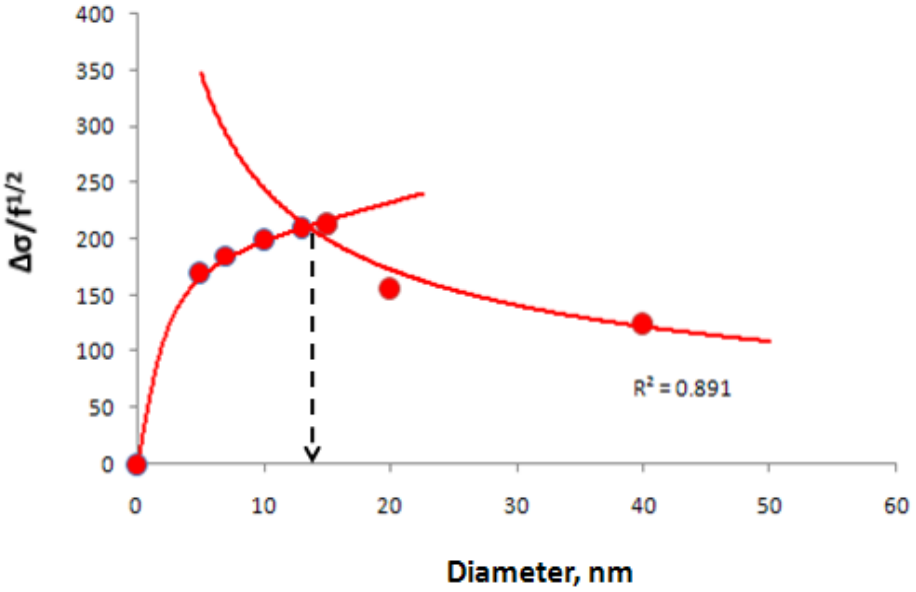

Figure 4.3.2.2.1: Determination of optimum precipitate diameter using normalized stress function with respect to measured gamma prime phase function. This is based on strengthening model of single and double dislocation cutting in section 2.4, figure 2.4.2

The optimum diameter of 14.8 nm calculated using this model is related to the peak hardness assumption for similar classes of austenitic TRIP steels and is based on the Arrhenius time-temperature relation shown in figure 4.1.2.

4.3.2.3 Composition Validation

Table 4.3.2 compares the measured composition of the gamma prime precipitates by 3-D LEAP tomography with the calculated equilibrium gamma prime composition using Thermo-Calc and Ni-Data7 database. For the case of the specimen aged at 800°C, where the presence of the η-precipitates have been confirmed, the measured precipitate composition is compared to that of the calculated η phase composition in Thermo-Calc for the $\boldsymbol{\gamma - \eta}$ equilibrium state rather than a $\boldsymbol{\gamma - \gamma'}$ equilibrium as in other cases. The standard error, σ for compositions measured using atom probe is calculated using binomial statistics to account for the statistical uncertainty associated with small sampling sizes according to the equation 3.3.8 [158] in section 3.3.9.3.

Temperature (C)	Calculated γ' (Thermo-Calc)	Measured γ' (3D – LEAP - Laser/Proxigram)
700	$(Ni_{0.822}Fe_{0.176}Cr_{0.002})_3\ (Ti_{0.913}Al_{0.087})$	$(Ni_{0.825}Fe_{0.173}Cr_{0.002})_3\ (Ti_{0.908}Al_{0.092})$
736	$(Ni_{0.804}Fe_{0.193}Cr_{0.003})_3\ (Ti_{0.913}Al_{0.087})$	$(Ni_{0.813}Fe_{0.183}Cr_{0.004})_3\ (Ti_{0.910}Al_{0.090})$
750	$(Ni_{0.798}Fe_{0.200}Cr_{0.002})_3\ (Ti_{0.913}Al_{0.087})$	$(Ni_{0.805}Fe_{0.192}Cr_{0.003})_3\ (Ti_{0.908}Al_{0.092})$
800*	$(Ni_{0.853}Fe_{0.146}Cr_{0.001})_3\ (Ti_{0.992}Al_{0.008})$	$(Ni_{0.860}Fe_{0.139}Cr_{0.001})_3\ (Ti_{0.988}Al_{0.012})$

* represents γ – η equilibrium

Table 4.3.2: Comparison of calculated and measured composition of Gamma Prime/Eta precipitates observed in EX425 at selected aging temperatures

The comparison shows reasonable agreement of intermetallic phase composition with those predicted/calculated using Thermo-Calc and Ni-Data7 thermodynamic database. Table 4.3.3 charts the comparison between the calculated (Thermo-Calc) and measured (3D-LEAP – Laser Pulsing – Proxigram Method) concentrations of individual ions in the matrix. Similar to the case in table 4.3.2, for the case of the specimen aged at 800°C, the measured precipitate composition

is compared to that of the calculated η phase composition in Thermo-Calc for the $\gamma - \eta$ equilibrium state rather than a $\gamma - \gamma'$ equilibrium.

	Aging Temperature, Celsius									
		700		736		750		800 *		
At %	Elements	Calculated	Measured	Calculated	Measured	Calculated	Measured	Calculated	Measured
	Fe	73.550	74.312 ± 2.341	72.328	73.511 ± 3.022	71.796	72.451 ± 2.888	71.453	72.210 ± 3.141
	Ni	19.311	18.752 ± 2.452	20.215	19.251 ± 1.975	20.595	19.743 ± 2.665	20.755	19.980 ± 3.063
	Cr	4.774	4.468 ± 0.897	4.685	4.442 ± 1.453	4.656	4.325 ± 1.264	4.603	4.316 ± 1.13
	Ti	1.035	1.103 ± 0.621	1.445	1.688 ± 0.874	1.622	1.855 ± 0.557	1.725	1.962 ± 0.883
	Al	0.105	0.090 ± 0.232	0.143	0.137 ± 0.234	0.163	0.148 ± 0.143	0.344	0.277 ± 0.241
	Mo	0.824	0.833 ± 0.354	0.809	0.817 ± 0.522	0.802	0.813 ± 0.753	0.793	0.801 ± 0.607
	V	0.397	0.413 ± 0.134	0.392	0.412 ± 0.271	0.387	0.421 ± 0.234	0.382	0.396 ± 0.180

* represents γ – η equilibrium

Table 4.3.3: Comparison of calculated and measured composition of matrix Austenite in EX425 at selected aging temperatures

4.4 Variations in Micro-Hardness and Yield Strength

Figure 4.4.1 charts the variation of Vicker's micro-hardness as a function of aging time for a constant aging temperature of 700°C for EX425 specimen blanks. The specimens were solution treated prior to aging. As seen in figure 4.4.1, the phase fraction of gamma prime decreases with increase in temperature which affects the overall hardness and yield strength of the EX425 alloy since gamma prime is the main strengthening phase. Vickers harness measurements have been taken for various tempering temperatures and times to study the variation of the hardness and resulting changes in yield strength.

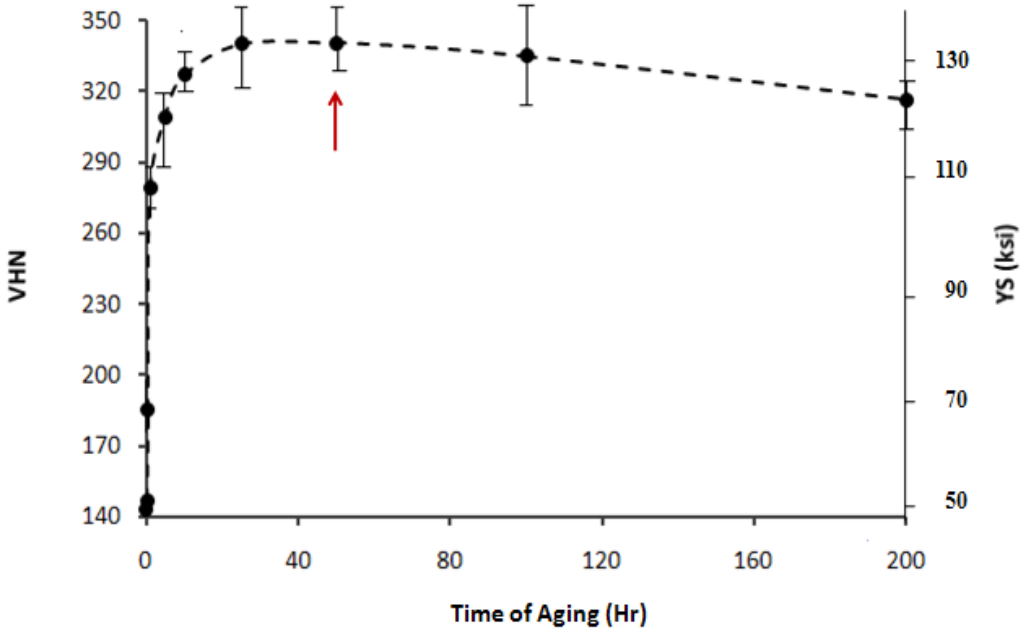

Figure 4.4.1: Variation of surface Vicker's microhardness with aging time for EX425 specimens aged at 700°C

Several multi-stage heat treatments have also been conducted on EX425 to study the stability of the austenite matrix under varying conditions. In order to reduce the stability of the austenite for transformation at higher temperatures, tempering at low temperatures is needed (< 700°C for M_s^{σ}

> 0^{o}C). However at lower temperatures, it is difficult to attain equilibrium **γ – γ'** microstructure since the kinetics is very slow and hence requires aging for prolonged periods. So a multi-stage temper process was utilized, starting with the high temperature of 800^{o}C for 10 hour to speed up the equilibrium **γ – γ'** phase fractions and then over-aging at 720^{o}C and 641^{o}C for 30 hours and 120 hours respectively to keep the final strength level ~ 120 ksi (MPa) and at the same time lower the stability of the matrix to have a stress-assisted transformation temperature close to room temperature.

Figure 4.4.2 (a) shows the dual-axis plot of Hardness profile (VHN vs. Time of aging) for the first stage: 800^{o}C and the converted yield strength using Saha's [8] Yield Strength – Vicker's hardness relationship.

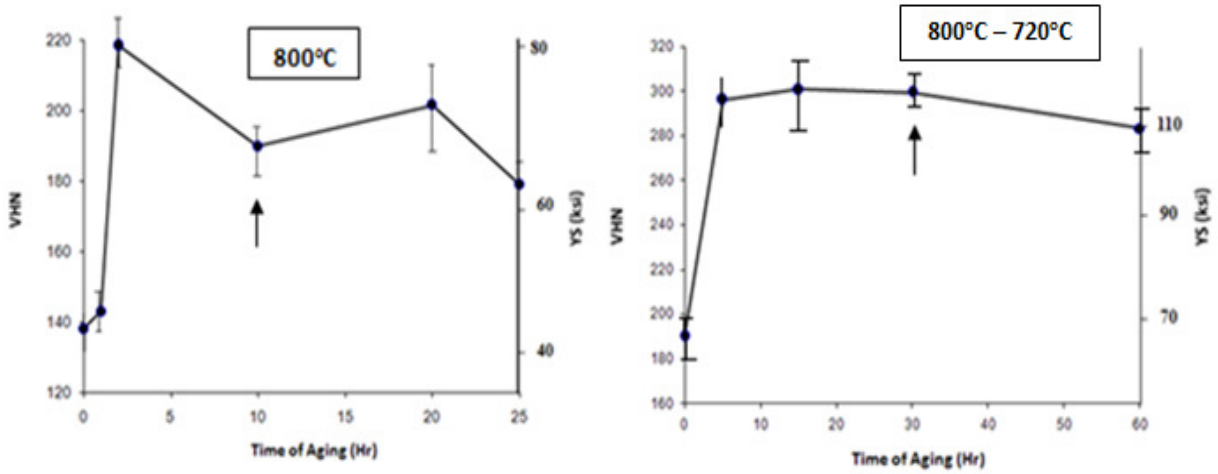

Figure 4.4.2: Variation of Vickers microhardness with aging time for EX425 aged at **a)** 800^{o}C and **b)** 800^{o}C (10 hours) + 720^{o}C. The arrow marks the aging time selected for that temperature

The zero hour denotes the fully solutionized and quenched austenitic specimen which has a hardness of 138.2 VHN corresponding to base yield strength of ~ 46 ksi (317 MPa) for the matrix. It is noted that the peak hardness of 219 VHN (~ 80 ksi – 552 MPa) occurs at about 2

hours of aging at 800°C, which is as predicted from the aging temperature – time model for peak hardness for TRIP steels from Stavehaug's data [13] discussed in section 4.1. An optimum over-aged time of 10 hours was selected for this stage 1 temper, which gives hardness of 190 VHN corresponding to yield strength of ~ 66.5 ksi (458.5 MPa). Figure 4.4.2 (b) shows the hardness profile for specimens post stage 2: 720°C for times upto 60 hours. The zero hour signifies that the specimen has undergone only the first stage of temper (800°C for 10 hours). As seen from the figure 4.4.2 (b), the peak hardness occurs ~ 16 hours of temper. Over-aging to 30 hours and 60 hours do not lead to much decrease in hardness. So a second stage time of 30 hours is chosen, which builds up the hardness to ~ 300 VHN and Yield Strength to ~ 116 ksi (800 MPa).

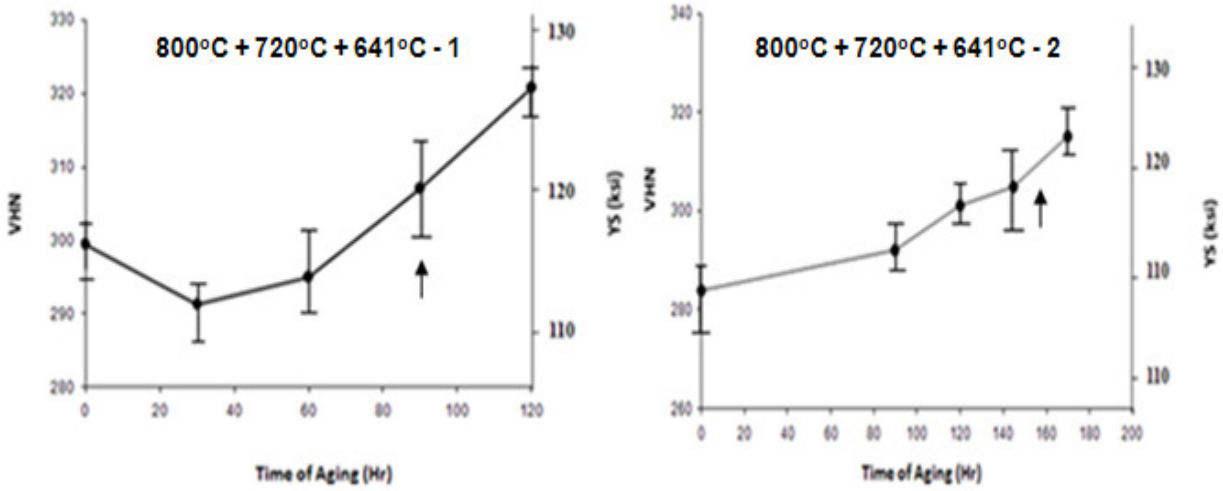

Figure 4.4.3: Variation of Vickers microhardness with aging time for EX425 aged at **a)** 800°C (10) + 720°C (30) + 680°C and **b)** 800°C (10) + 720°C (60) + 680°C

Figure 4.4.3 (a) and (b) shows a comparison of hardness and corresponding estimated yield strength on a dual axis plot for the following two steps -

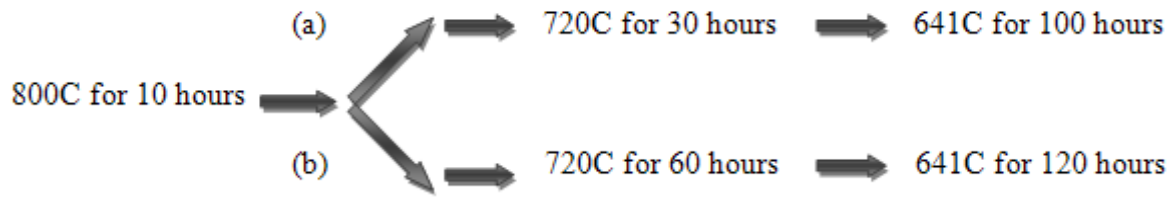

4.5 Mechanical Testing and Analysis

Tensile properties of EX425 have been evaluated using both the quasi static uniaxial tensile testing as well as the dynamic/adiabatic Kolsky bar (modified Hopkinson bar) apparatus, at different temperatures for different heat treatments. These tests were performed not only measure the Yield Stress (YS) and Uniform ductility (ε_y) at various aging as well as test temperatures, but also to measure the M_s^{σ} temperature in a unique method as described later in section 4.5.4. The specimens have been heat treated to different aging temperatures and times. These aging conditions determine not only the gamma prime phase fraction (for desired strength), but also the matrix stability which affects transformation characteristics. The test process and system have been discussed earlier in section 3.3.5.1. The specimen geometry and dimensions have been shown in figures 3.3.5.1 and 3.3.5.2 for static and dynamic tensile tests respectively. The fracture surface of the specimens has been investigated by SEM to observe the details of the fracture mechanism.

4.5.1 Quasi Static Tensile Tests

Quasi static tensile tests have been conducted for both single-step tempered specimens as well as multi-stage tempered specimens to determine their Yield Strength and uniform ductility. Single Step tempers were done at 736^{o}C for 16.25 hours based on the peak hardness condition for

EX425 as derived from the Arrhenius Time-Temperature relation in section 4.1. The temperature of 736°C was chosen as it gives an equilibrium phase fraction of gamma prime required to have yield stress of 130 ksi at room temperature. Uniaxial tensile tests were done at temperatures in the range -196C to room temperature of 27C. An extensometer was fitted across the gage-length of the tensile specimens and the MTS system was calibrated to measure the strain based on the extensometer readings. The actual gage strain extensometer data makes it possible to calculate accurate true stress-strain curves, since the diameter of the gage is already know. Figure 4.5.1.1 shows the True stress – True strain curves for the tensile tests conducted at various temperatures, with a 0.2% offset, all specimens aged at the same temperature of 736°C for 16.25 hours.

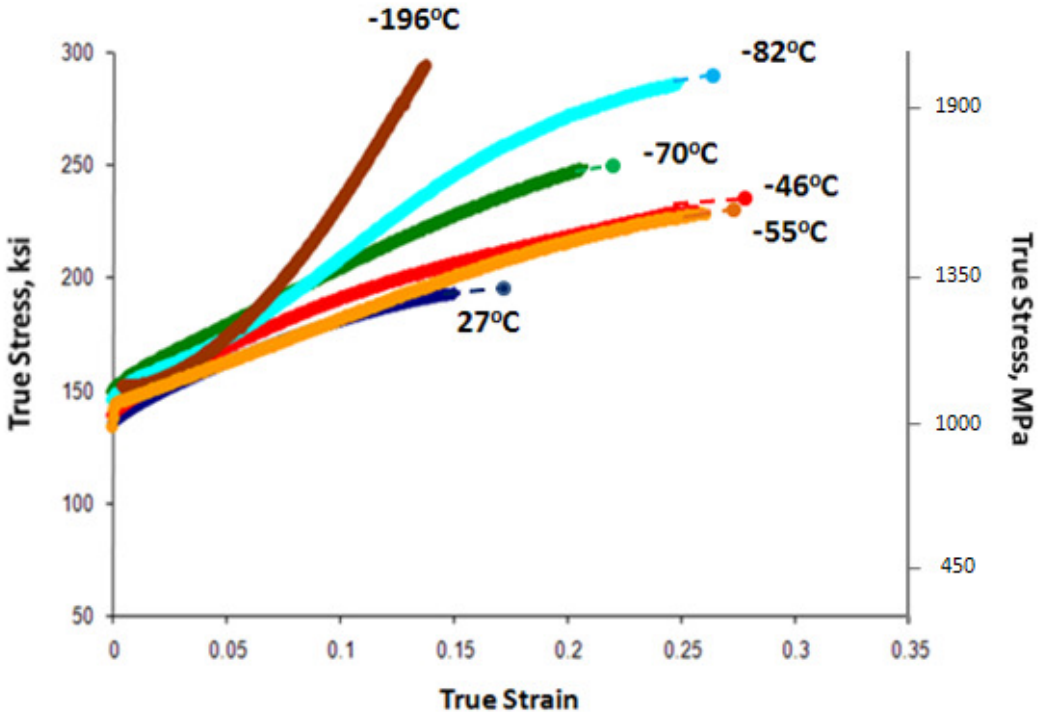

Figure 4.5.1.1: Comparison of static uniaxial tensile tests for EX425 specimens aged at 736°C for 16.25 hours. The test temperature is indicated in bold across each curve. The solid curves indicate the elastic range and the dotted lines show the plastic strain till the point of fracture, thereby indicating final fracture strain

The range of temperature used for the iso-thermal tensile tests is from room temperature (27^oC) to the lowest temperature of -196^oC. The solid curves represent the region of uniform ductility upto the onset of necking in the specimens while the dotted curves indicate fracture strain. These tests are based on the transformation curves discussed in figure 2.2.8 in section 2.2.2.2 which have a sigmoidal shape at higher temperatures, whereas at lower temperatures, the curves approach an initially linear behavior. This behavior correlates the basic change in transformation. It is evident from the stress-strain curves obtained that the strain hardening increases at lower temperatures.

The maximum uniform ductility of ~ 25% has been observed at the temperature regime of -45^oC to -55^oC for the current heat treatment (736^oC for 16.25 hours). As discussed earlier in section 2.2.4.1, the uniform ductility increases with increase in test temperature till around the M_S^σ temperature and then decreases again for temperature higher than M_S^σ. The maximum ductility has been seen to occur at temperatures 25-30^oC above M_S^σ (section 2.2.4.1). This suggests that the M_S^σ temperature for EX425 would be close to -70^oC. A common methodology of measuring the M_s^σ temperature has been proposed by Richman and Bolling [60] and the same has been used to validate the M_s^σ temperatures of all prototype alloys. This has been discussed later in section 4.5.4. The highest yield stress of the material must be at the M_S^σ temperature, which separates the transformation region from the slip region. Hence by this definition, the M_S^σ temperature should be close to -70^oC as the green curve for -70^oC in figure 4.4.1.1 shows the highest value of Yield Stress measured (~ 150 ksi) for EX425, for any temperature within the test range of -196^oC to 27^oC.

Figure 4.5.1.1 also shows that achieving a uniform ductility of ~ 25% is definitely achievable under ideal and optimum conditions. To obtain the same performance at room temperature however, is the challenge for our new alloy designs. The stress-strain curves from figure 4.5.1.1 also show that similar to uniform ductility, the yield stress also increases when temperature is reduced from room temperature till a critical point (M_S^{σ} = -70°C) and then tends to decrease following the iso-thermal behavior as detailed by Olson and Cohen [56] as described earlier in section 2.2.2.2. Table 4.5.1.1 shows the primary data corresponding to the tests and stress-strain curves represented in figure 4.5.1.1.

Test Temperature	YS (ksi)	UTS (ksi)	YS/UTS	Uniform Elongation	Reduction in Area
27°C	130	185	0.703	0.158	0.174
-46°C	144	218	0.661	0.261	0.282
-55°C	145	217	0.668	0.265	0.277
-70°C	151	244	0.619	0.207	0.225
-82°C	150	275	0.545	0.251	0.268
-196°C	151	291	0.519	0.138	0.138

Table 4.5.1.1: Static Uniaxial tensile test properties of EX425 aged at 736°C for 16.25 hours

The ratio of UTS to YS gives an estimate of the strain hardening for the material. From table 4.5.1.1, it is seen that the YS/UTS ratio decreases with decrease in test temperature, which implies higher strain hardening at lower temperatures, which is expected. The strain hardening behavior is observed close to M_S^{σ} temperature, which is a result of the stress-assisted transformation. The reduction in area of the fracture surface is a good measure of the true fracture strain of the material and can be determined from a simple measure of the fracture radius and comparing it to the original radius of the gage and calculating the effective reduction of area.

This fracture strain data point can be used in the True Stress-Strain curve as a final point in the curve to express the limit of plastic strain post necking. The uniform elongation can also be determined from the broken tensile specimen by measuring the reduction in radius of the gage section of the tensile specimen. From the reduction in area data in the table 4.5.1.1, we conclude that the fracture strain for EX425 is not very high as those seen for A286 or martensitic BA160 [8] and HSLA 100, where the total reduction in fracture surface area is close to 65%. Thus there is very little necking, which is not desirable since it limits the overall toughness and fracture ductility required for alloys used in blast protection applications. Since both fracture and stretch ductility are important quantitative measures of the performance of a material under tensile loading, having good fracture ductility is important to the success of the new alloy designs. The fracture seen in EX425 is brittle throughout the test temperature range (even for the max. ductility region of -50^{o}C) and on further investigation by SEM imaging; the main cause is shown to be Inter-granular fracture. This has been discussed in section 4.5.3.

Static uniaxial tensile tests have also been carried out on the multi-stage tempered specimens which had earlier shown peak hardness in EX425. Figures 4.5.1.2 and 4.5.1.3 show the engineering stress-strain and True stress-strain curves of for EX425 specimens for varied tempered conditions and test temperatures, including the multi-step tempers. The solid dot on the engineering stress – strain curve indicate the onset of plastic necking strain, which is also represented in the True Stress-Strain curves by the solid lines. The 3-step multi-stage tempered specimens were the ones aged at 750^{o}C (10hours) + 700^{o}C (20 hours) + 650^{o}C (25 hours). Other single step tempered specimens were aged at 781^{o}C corresponding to a calculated yield stress of 105 ksi (724 MPa).

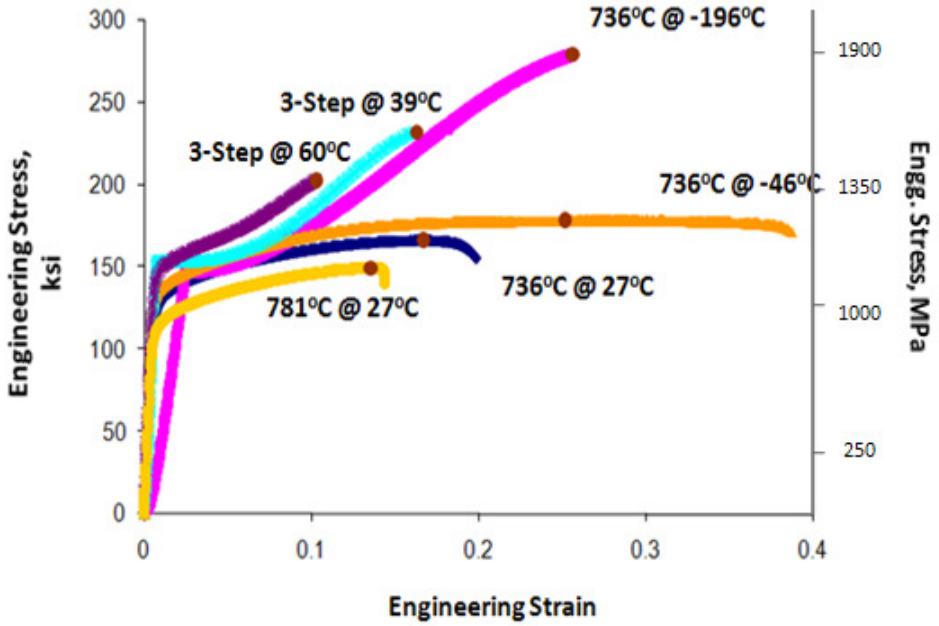

Figure 4.5.1.2: Comparison of static uniaxial tensile tests for EX425 specimens aged at 736°C for 16.25 hours. The curve for -196°C is to be taken as a qualitative measure only since the extensometer used to determine the strain has a range till -100°C only. The modulus in this case is not the true elastic modulus

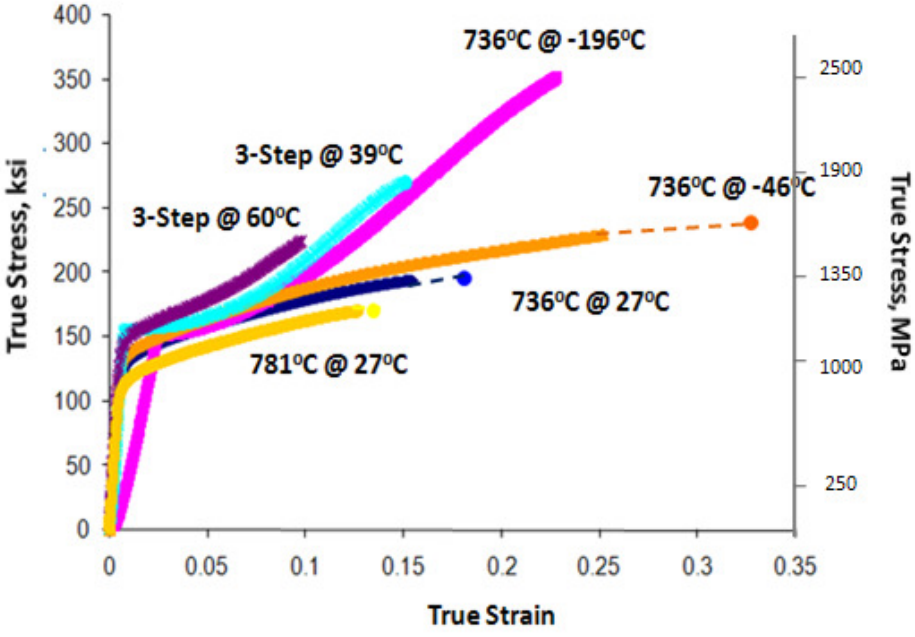

Figure 4.5.1.3: Comparison of static uniaxial tensile tests for EX425 specimens aged at 736°C for 16.25 hours. The curve for -196°C is to be taken as a qualitative measure only since the extensometer used to determine the strain has a range till -100°C only. The modulus in this case is not the true elastic modulus

Table 4.5.1.2 lists the data from the figure 4.5.1.3 for true stress-strain plots.

Aging Condition	Test Temperature	YS (ksi)	UTS (ksi)	YS/UTS	Uniform Elongation	Reduction in Area
781°C	27°C	110	155	0.71	0.137	0.142
750°C (10hours) + 700°C (20 hours) + 650°C (25 hours)	39°C	151	258	0.585	0.154	0.154
750°C (10hours) + 700°C (20 hours) + 650°C (25 hours)	60°C	150	217	0.691	0.11	0.097

Table 4.5.1.2: Static Uniaxial tensile test properties of EX425 aged at different conditions

4.5.2 Dynamic Tensile Tests

To simulate actual dynamic loading under adiabatic conditions, a standard stored-energy Kolsky bar setup has been used [141]. The experimental setup and conditions have been detailed in section 3.3.5.2. The specimen geometry and dimensions differ from the static tensile test specimens, and is shown in figure 3.3.5.2. The tests have been conducted at room temperature for EX425 and compared with that of martensitic BA160. The EX425 specimens for both Static and Dynamic (Kolsky bar) tests were tempered at 736°C for 16.25 hours with a measured static uniaxial tensile yield strength of 130 ksi (896 MPa) at room temperature. The BA160 specimens were first solution treated at 900°C for 1 hour and followed by water quench and liquid nitrogen cooling and then heat treated to the its standard two step tempering condition of 550°C for 30 minutes and 450°C for 5 hours [8]. Figure 4.5.2.1 shows the True stress-strain plots for the

EX425 and compared to those of BA160 for both static tensile and dynamic adiabatic Kolsky bar setup. It is clearly observed from figure 4.5.2.1 that the dynamic loading conditions lead to higher Yield Stress and higher Ultimate Tensile Strength for both EX425 Austenitic TRIP prototype as well as BA160 martensitic steel. This means higher strain hardening for both alloys although the uniform ductility level remains relatively similar for both loading conditions. The solid line represents the limit of uniform ductility and the onset of necking (Plastic strain).

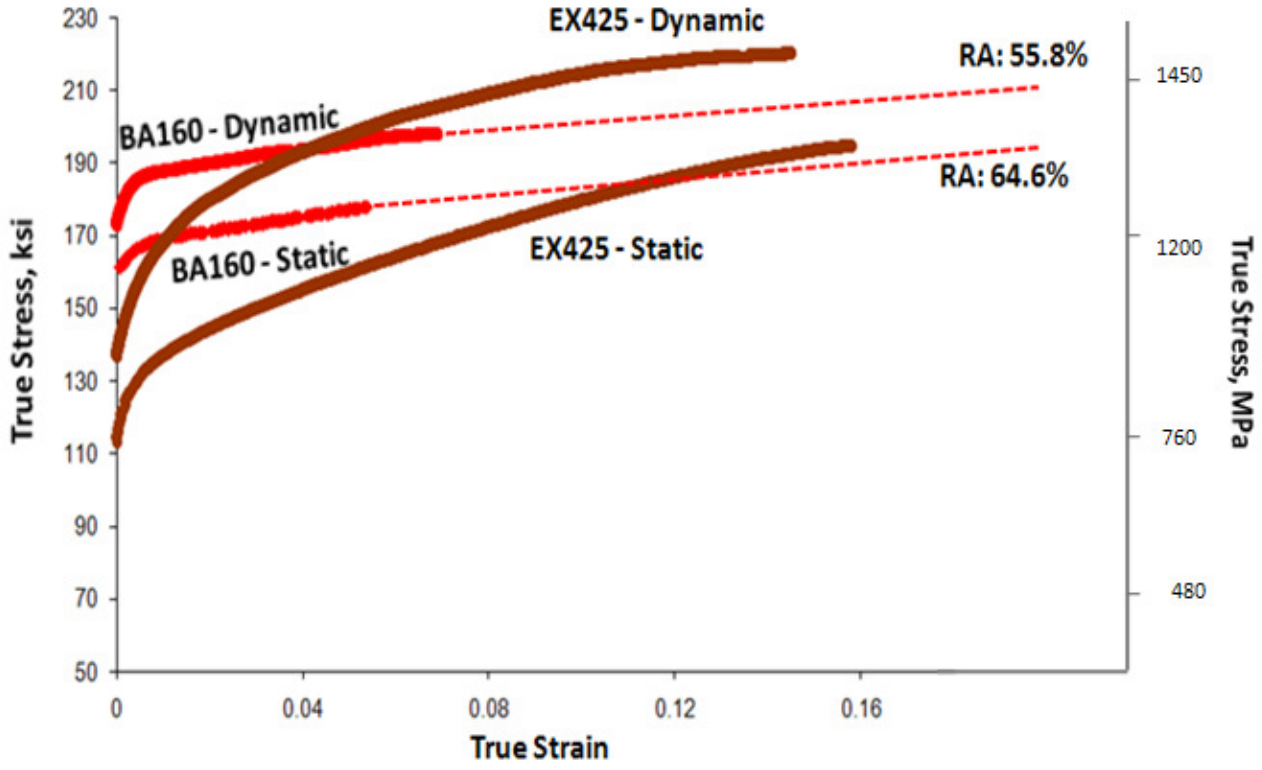

Figure 4.5.2.1: Comparison of static uniaxial tensile tests and dynamic Kolsky tensile test for EX425 specimens aged at 736°C for 16.25 hours and BA160 aged at 550°C for 30 minutes + 450°C for 5 hours.

The BA160 shows a very high reduction in area of its fracture surface (~ 65%) due to its high necking strain. Hence the dotted lines extend a long way for the BA160 curves. On the other hand, EX425 has a brittle (inter-granular) mode of fracture which restricts its uniform ductility

and therefore has low reduction in area of its fracture surface. The stress-strain plots in the figure 4.5.2.1 have a 0.2% cutoff to account for the machine setup anomaly.

4.5.3 Evaluation of Fracture Mode

The fracture surface of the broken tensile specimens has been investigated using a SEM to study the failure mechanism, post quasi-static uniaxial and dynamic Kolsky bar tests. The maximum uniform ductility at room temperature for the EX425 TRIP alloy under both static and dynamic loading conditions has been limited to ~ 15 - 16%. Figure 4.5.3.1 shows the SEM secondary electron image of the fracture surface from a specimen fracture after a uniaxial tensile test.

The SEM images reveal that the fracture mode has been essentially that of Inter-granular in nature, with grain boundaries being clearly marked on the fracture surface. Due to this, although the EX425 shows high yield strength (130ksi) at room temperature, its uniform ductility is limited. BA160, on the other hand, exhibits a high reduction in area of its fracture surface leading to ductile failure mode although the martensite matrix limits its stretch ductility. To avoid this, we need an austenitic grain-refining dispersion for grain boundary pinning. This has been discussed in the alloy design section 2.5.2. In this regard, addition of Boron has been considered as one of the important design parameters as Boron is known to improve grain boundary cohesion thereby reducing inter-granular fraction. The amount of boron in EX425 is 0.009 wt% which is much less that 120-150 ppm levels for the common commercially used austenitic TRIP steels.

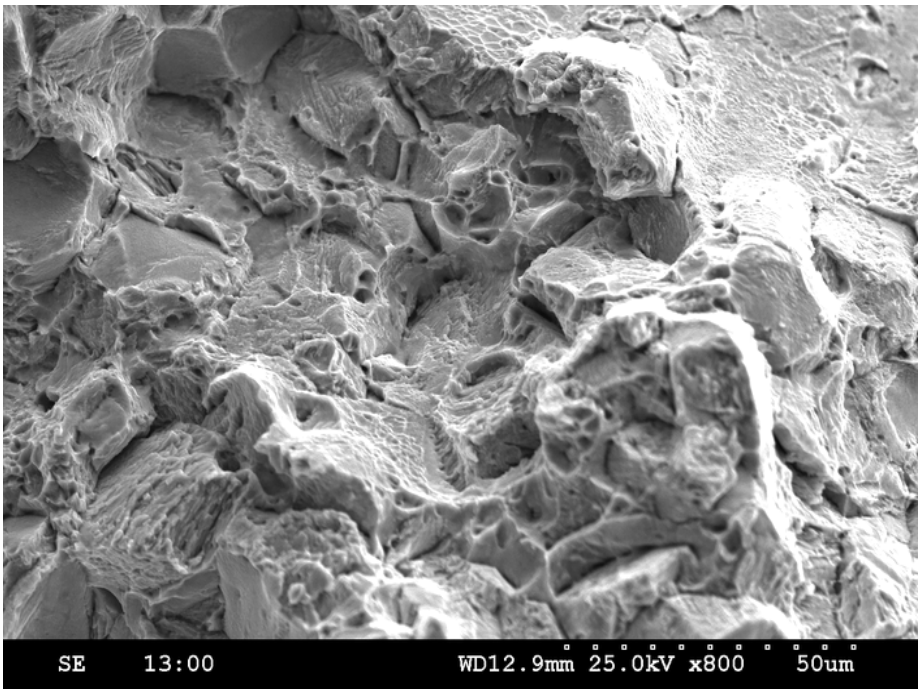

(a)

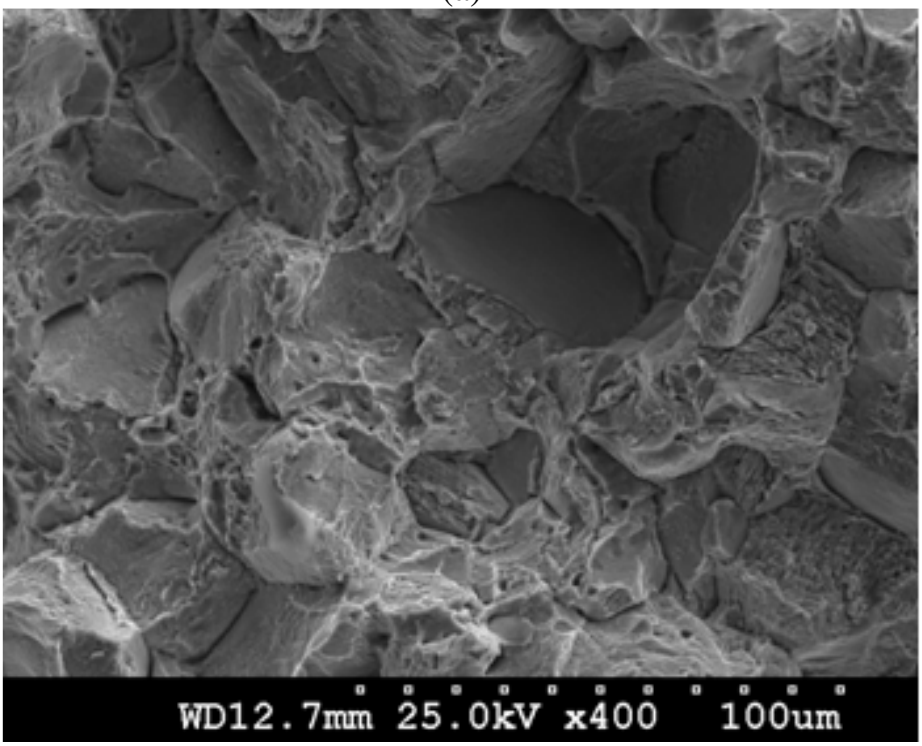

(b)

Figure 4.5.3.1: Secondary Electron SEM micrograph of the fractured EX425 Static Tensile specimen showing both smooth and rough fracture surfaces marking Inter-granular mode of fracture

4.5.4 M_s^{σ} Measurements and Stress-Temperature Dependence

The designation M_s^{σ} comes from the work of Richman and Bolling [13]. As discussed in section 2.2.2, M_s^{σ} is defined as the maximum temperature at which martensitic transformation can be induced by an external stress below the yield stress of the parent phase. The correlation of plastic flow and transformation can be best studied by examining the temperature dependence of the yield strength of the material since the reversal of the temperature dependence of the yield stress occurs at the M_s^{σ}. Having quantitative uniaxial tensile stress data at different test temperatures (as shown in section 4.5.1) not only enables us to determine the temperature of maximum yield stress (which, by definition, must occur at M_s^{σ} temperature) but also by using Leal's analogy [79] where maximum ductility in similar TRIP steel is observed ~ 25°C above M_s^{σ}, an estimate of the correct M_s^{σ} can be made. However, these tests require several test samples and a linear extrapolation of observed $\sigma - T$ curve to arrive at the correct M_s^{σ}. Richman and Bolling proposed a simpler method of determining the critical correct M_s^{σ} using just one specimen. The critical temperature for stress-assisted martensitic transformation M_s^{σ} can be experimentally measured by a reversal of the temperature dependence of the yield stress due to transformation controlled yielding at low temperatures. The following figure 4.5.4.1 show the method used by Richman and Bolling to determine the characteristic M_s^{σ} for paramagnetic austenitic steel.

The figures 4.5.4.1 (a) and (b) represent the different stress-strain plots for a paramagnetic and a ferromagnetic alloy respectively [13]. A small pre-strain is given to the material in the first loading cycle ~ 1 - 3% at or above room temperatures. Then successive cycles of loading are done where first the temperature is reduced in each step and then the loading is done and removed within 0.1% additional strain after reaching yield stress. Richman and Bolling showed

that a distinctive point comes where there is a sharp decrease in the overall yield stress of the material and it keep decreasing on further loading cycles with decrease in test temperature. This critical point is the M_s^{σ} and denotes the transformation region and the transition point.

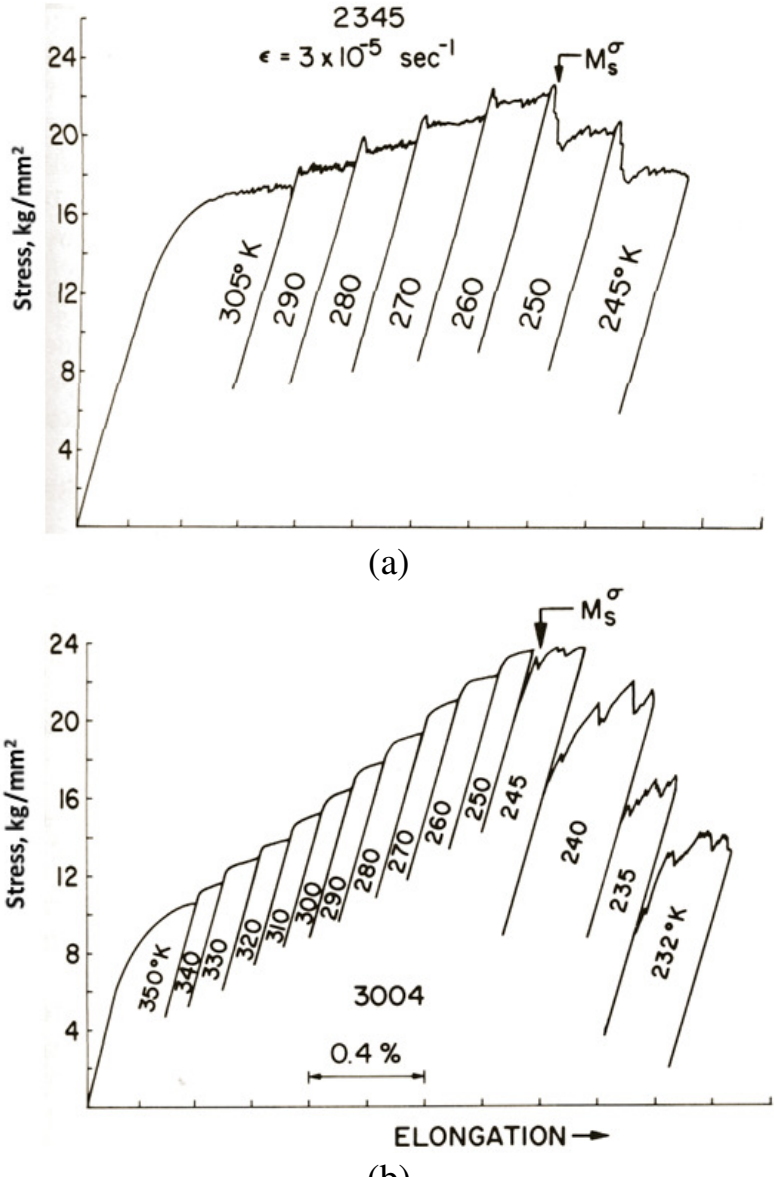

Figure 4.5.4.1: Richman and Bolling method for determination of M_s^{σ} Temperature

Figure 4.5.4.2 shows the Stress – Temperature and Stress – Strain dependence of an EX425 specimen which has undergone a multi-stage temper process (750°C + 700°C + 650°C) in order to achieve the maximum yield stress at room temperature.

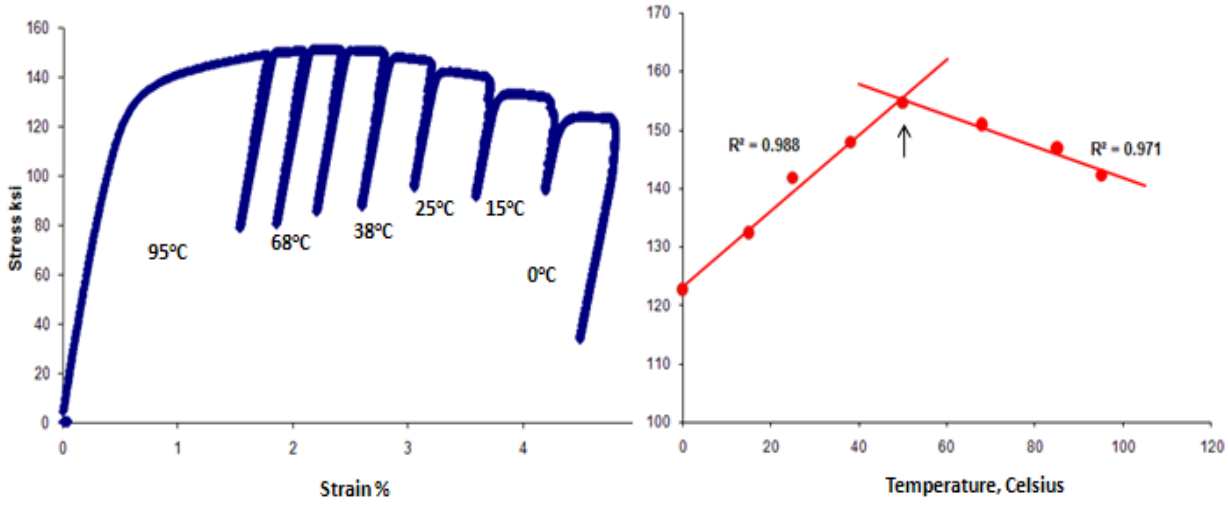

Figure 4.5.4.2: Temperature dependence of Strain and Yield Stress for EX425 aged at 750°C (10hr)-700°C (20hr)-650°C (25hr)

The loading cycle started at a high temperature of 95°C and given a pre-strain of ~1.6% in the first cycle. The loading-unloading cycle was carried out till a temperature of 0°C. It is evident from the figure that the yield strength increases at first and then after a certain point (40-50°C), the yield stress starts decreasing and keeps decreasing till the last test cycle at 0°C. Figure 4.5.4.2 shows the temperature dependence of the yield stress of EX425 for the data obtained in figure 4.5.4.2 (a). A least squares linear trendline is fitted through two series of data points, one with a positive and other with a negative slope. The two lines are extrapolated and the point of intersection can be considered to be the maximum YS; so the M_s^{σ} for the specimen is 46°C.

However, more loading and unloading cyclic tests for different heat treated specimens for measuring M_s^{σ} have shown differing curves.

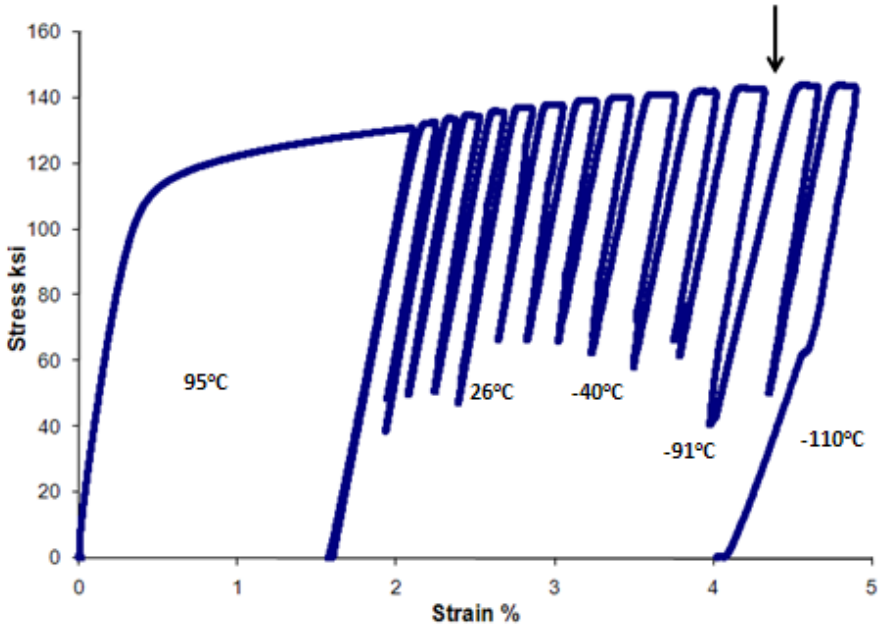

Figure 4.5.4.3: Temperature dependence of Strain for EX425 aged at 755°C for 8.5 hrs

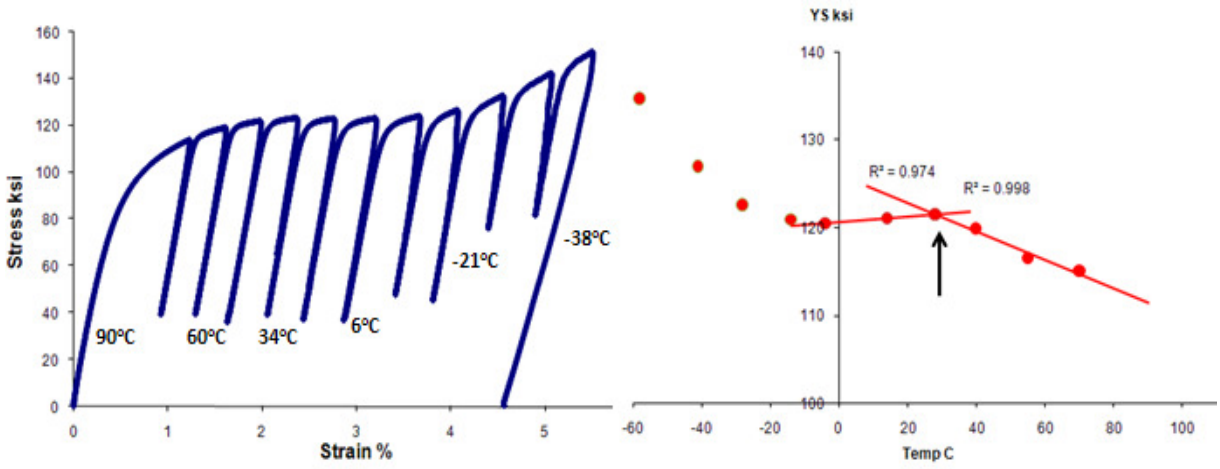

Figure 4.5.4.4: Temperature dependence of Strain and Yield Stress for EX425 aged at 800°C (10hr)-720°C (30hr)-680°C (100hr)

Figures 4.5.4.3 and 4.5.4.4 show the stress – strain and the temperature dependence of yield stress curves for two specimens which were given a) a single step temper of 755^{o}C for 8.5 hours and b) a multi-stage temper (800^{o}C-720^{o}C-680^{o}C). The single step temper was to evaluate a specimen's transformation M_s^{σ} temperature under normal heat treatment conditions and the multi-stage tempered specimen was an attempt to prepare an EX425 specimen which would have an estimated M_s^{σ} close to room temperature.

Figure 4.5.4.4 (b) shows the $\sigma - \varepsilon$ curve for the specimen with single step temper (755^{o}C for 8.5 hours). It shows that on successive cycles with decreasing temperature, the yield stress keep increasing and finally becomes constant and the curve flattens out in the region of test temperature of ~ -95^{o}C. There is clearly no sharp decrease in the observed yield stress as proposed by Richman and Bolling [13]. However since the area under the curve increases with a shift in loading cycle with respect to the unloading cycle corresponding to the sudden increase in slope, it is taken to be indicative of a transformation since for extreme low temperature regimes when the austenite matrix is too stable, the transformation occurs without any significant change in yield stress. In figure 4.5.4.4 for the specimen with multi-step temper, it is seen that the yield stress increases in the first few cycles and then decreases, indicating a clear transformation and an M_s^{σ} temperature. However, on further cyclic loading, it is seen that the yield stress again starts increasing. This again differs from the earlier cases as seen in figure 4.5.4.2, but is indicative of an iso-thermal stress-assisted transformation behavior.

The measured M_s^{σ} temperature of 25^{o}C tallies very well with the predicted M_s^{σ} temperature of 27^{o}C, which was the goal of the 3-step temper process with the final aging temperature of 680^{o}C.

M_s^{σ} temperature was also measured for the standard EX425 specimen aged at 736°C for 16.25 hours by platting the $\sigma - T$ dependence as shown in figure 4.5.4.5. This aging condition gives as Yield Stress of 130 ksi at room temperature for EX425. Table 4.5.4.1 lists the data from all M_s^{σ} temperature measurement tests.

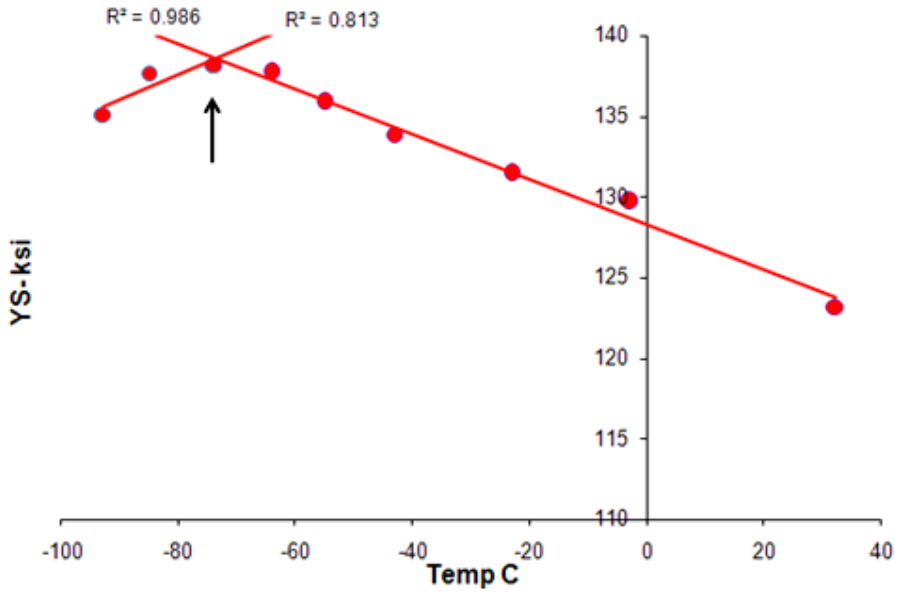

Figure 4.5.4.5: Temperature dependence of Yield Stress for EX425 aged at 736°C for 16.25 hrs

EX425 – Aging Temperature	Measured M_s^{σ}
755°C (8.5 hr)	-95°C
736°C (16.25 hr)	-70°C
750°C(10) + 720°C(20) + 680°C(25)	25°C
750°C(10) + 700°C(30) + 650°C(100)	46°C

Table 4.5.4.1: M_s^{σ} temperature measurement results for EX425

4.6 Martensitic Transformation Modeling

The data obtained from the tensile tests including the measured M_s^{σ} temperatures, have been used to calculate the Austenite Stability Parameter and compare it with the theoretical model

predicted by equation 2.3.5 in section 2.3. Light optical microscopy has also been used to measure the fraction of transformed martensite in the specimens. Using data points of yield stress measured for EX425 under slip as well as transformation regimes at different test temperatures, a $\sigma - T$ curve is generated to predict the entire behavior of the TRIP steel under uniaxial tensile loading.

4.6.1 Observed Transformation Microstructure

Hime [166] used the broken EX425 tensile specimens of both static isothermal and dynamic adiabatic tests and analyzed the polished section of the gage length under an optical microscope to determine the amount of the transformed martensite. Since the specimens have gone through stress-assisted transformation prior to failure, the analysis of the gage section of the specimens is important to evaluate the formation of martensite regions within the austenite matrix. The etchant used in this case is a solution of 0.5 g sodium metabisulfite + 33 cc HCl + 167 cc H_2O, which is known to darken the martensite regions while the austenite remains bright. This etchant has been used earlier by Olson and Azrin [53] to differentiate the martensite morphology within the austenite matrix in 0.27C TRIP Steels. Figure 4.6.1.1 (a) and (b) represent the observed morphology of martensite in the broken Static and Dynamic tensile test specimens respectively. These specimens were aged at 736^{o}C for 16.25 hours and the both tensile tests were done at room temperature.

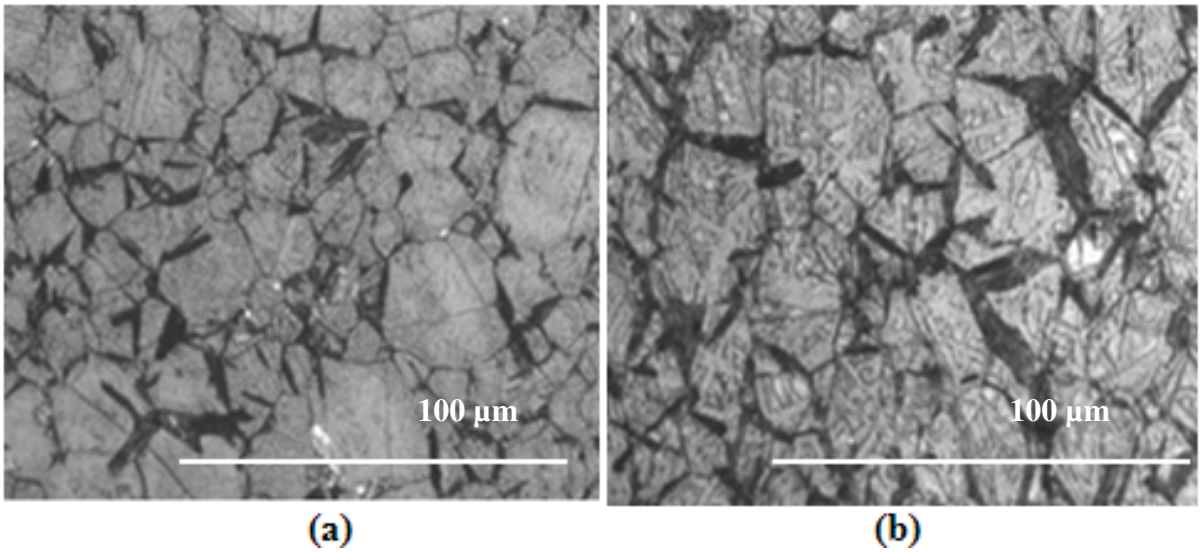

Figure 4.6.1.1: Optical Microscopy images of the dark transformed martensite regions within the bright austenite matrix for a) fractured EX425 static uniaxial test specimen and b) fractured EX425 dynamic tensile test specimen, aged at 736^{o}C for 16.25 hrs and tested at 27^{o}C [166]

From the figure 4.6.1.1, it is observed that there is higher fraction of transformed martensite after the dynamic Kolsky bar tensile tests than the static uniaxial test. This would mean more transformation leading to higher strain hardening, which is correctly observed in figure 4.4.2.1, where EX425 shows higher strain hardening under dynamic tensile loading leading to higher UTS than Static uniaxial loading.

4.6.2 Experimental values of Austenite Stability Parameter (ASP)

One of the primary goals of measuring the M_s^{σ} temperature of EX425 under various aging conditions is to get data points to build a mathematical/quantitative model for the stability of the austenite matrix, which determines the transformation characteristics. The concept of Austenite Stability Parameter has been previously introduced and discussed in detail in section 2.3.1. It has also been used to create the theoretical model for matrix stability and transformation requirements for our new alloy designs. In the current section, the values of M_s^{σ} temperature obtained experimentally by single specimen Richman and Bolling method as well as multi-specimen isothermal tests at different test temperatures has been used as data points to study the dependence of M_s^{σ} with Aging temperature and also the variance of the Austenite Stability Parameter (ASP) values with Yield Strength and Temperature. Figure 4.6.2.1 shows the variation of experimentally observed M_s^{σ} temperature with their corresponding specimen aging temperature.

The data points used in this plot uses both single-step tempers as well as multi-stage tempers and that a linear relationship is observed between the two parameters. For the multi-stage tempers are 3 different aging temperatures, the temperature of the 3rd-stage is considered since it is the last stage of aging that determines the final austenite stability. This also shows that EX425 specimens can be appropriately heat-treated to have an M_s^{σ} around room temperature, but its uniform ductility and fracture strain is limited due to inter-granular fracture (section 4.6.2). However, the aging temperature corresponding to an M_s^{σ} close to room temperature is low (~ 680^{o}C) which

leads to very slow kinetics and hence it takes a very long time (> 100 hr) of aging to reach equilibrium phase composition.

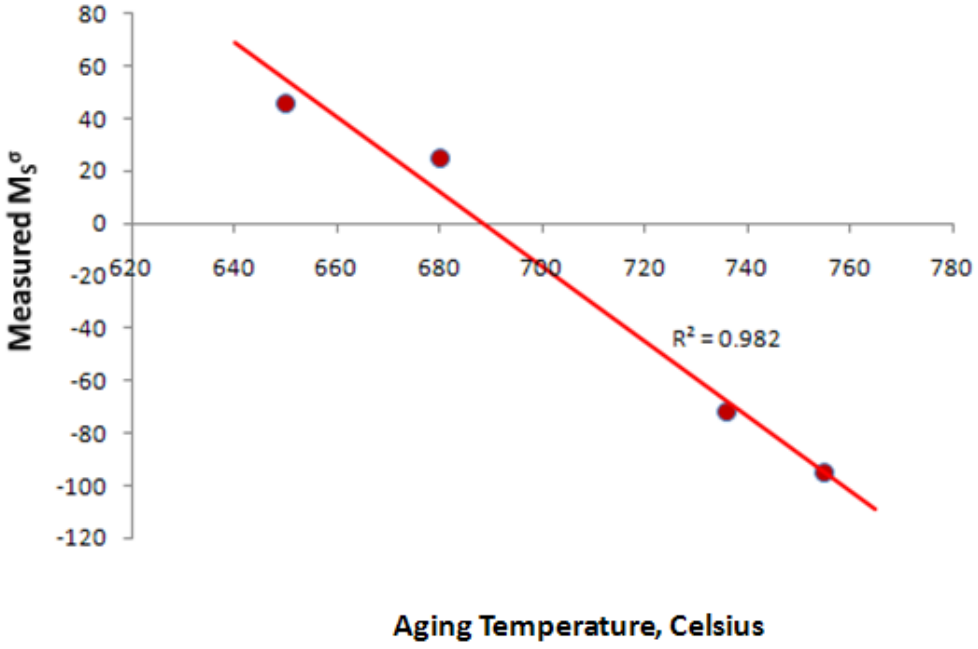

Figure 4.6.2.1: Linear relationship between measured M_s^σ temperature and aging temperature for EX425

Since the M_s^σ temperature for the single step tempered specimens above 700^{o}C lies significantly below 0^{o}C (very stable austenite phase), we cannot determine the Gibb's free energies associated with the BCC and FCC phases using the MART5 database. Although MART5 was designed for low temperature thermodynamics, it has a range of only till ~ 0^{o}C or higher. Hence, only experimental M_s^σ data points above 0^{o}C have been considered while calculating the experimental Austenite Stability Parameter (ASP) values using Thermo-Calc and CMD. The plots showing variance of ASP values with Aging temperature and measured M_s^σ for EX425 is shown in figures 4.6.2.2 and 4.6.2.3. Higher aging temperatures would mean more austenite phase fraction

and lesser gamma prime phase (figure 4.1.1). This would in-turn lead to increase in austenite stability, thereby making ASP values less negative for increasing aging temperatures.

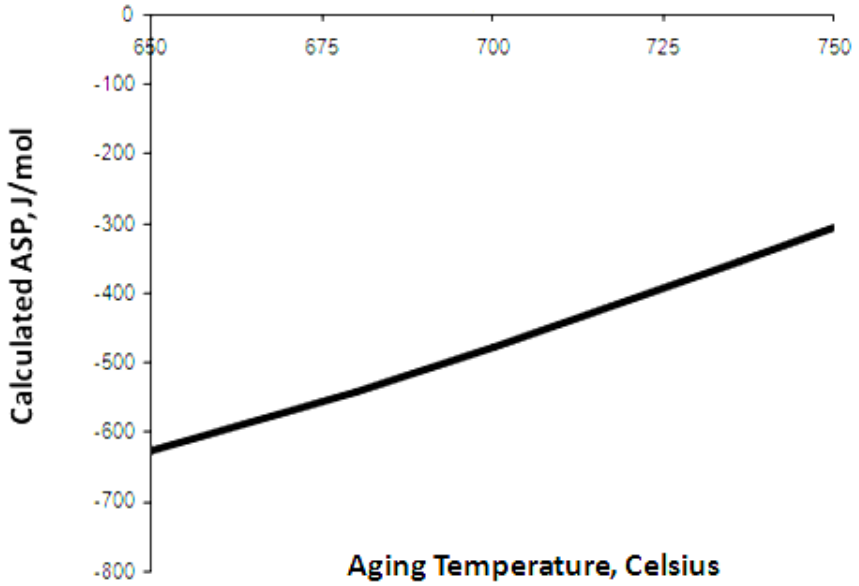

Figure 4.6.2.2: Aging temperature dependence of calculated ASP for EX425

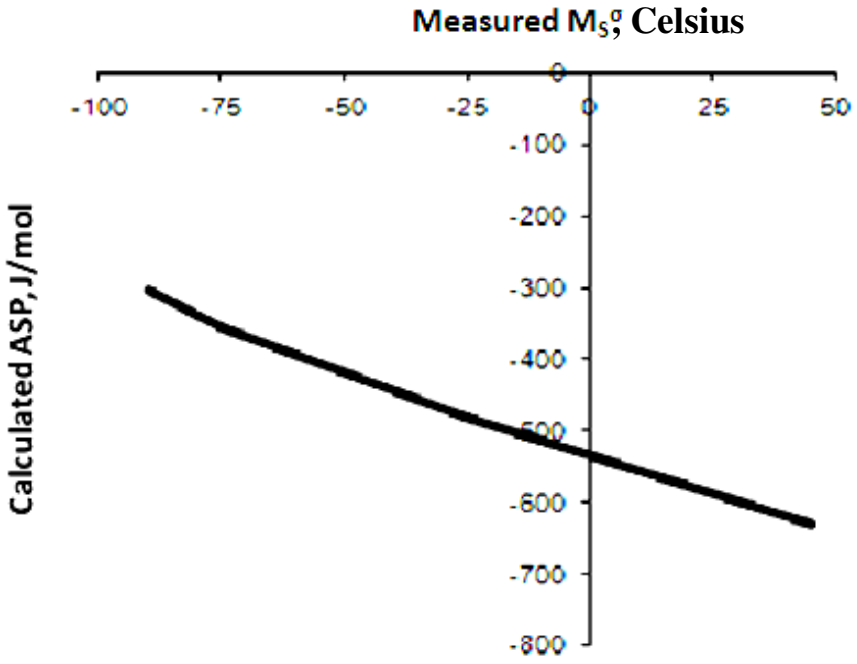

Figure 4.6.2.3: Relation between measured M_s^σ temperature and calculated ASP for EX425

The higher (more positive) the ASP values, more stable is the austenite matrix phase, and this correlation can be extended to the yield strength and hence higher the yield strength (and lower aging temperature), higher the M_s^{σ} temperature. The latter can be explained by the simple analogy that higher yield strength implies more gamma prime fraction and less of austenite fraction, which leads to easier transformation due to less stable matrix and hence higher M_s^{σ} temperature.

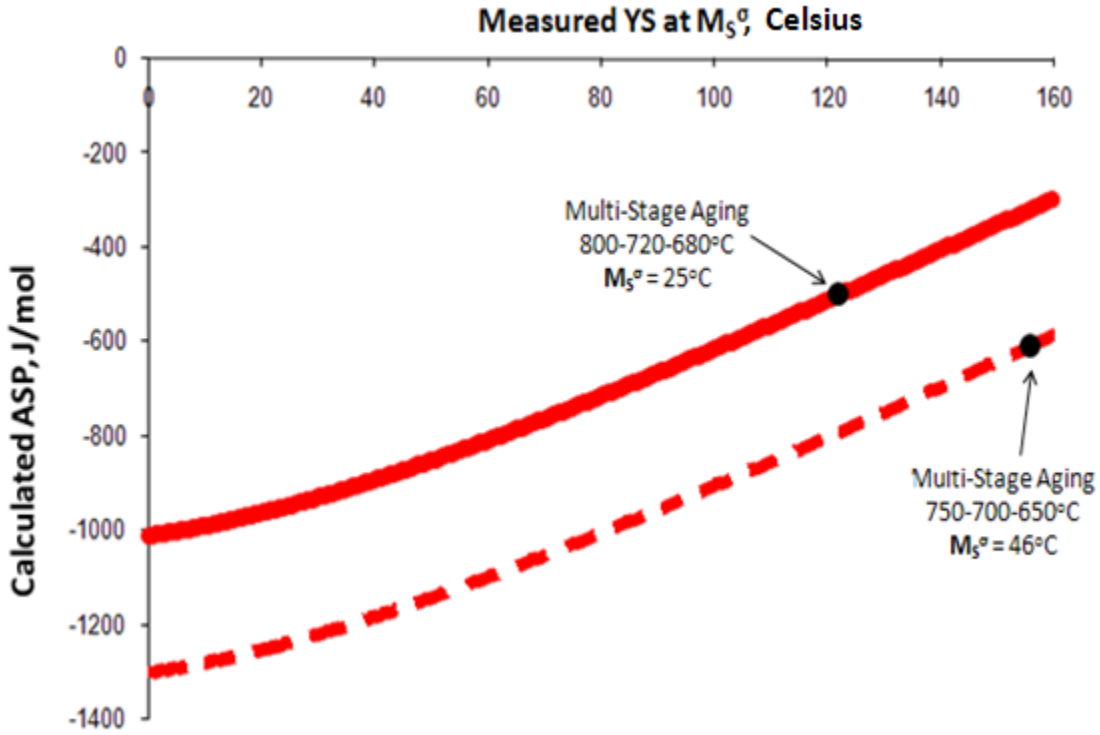

Figure 4.6.2.4: Comparison of measured and theoretical calculated ASP values as a function of the measured Yield Stress at M_s^{σ}, for EX425

Figure 4.6.2.4 shows the comparison of the calculated ASP values from the measured M_s^{σ} temperatures for EX425 with those obtained by theoretical Austenite Stability equation 2.3.7 for uniaxial tension. Since the M_s^{σ} temperature for the 3-step tempered EX425 with a final aging temperature of 680^{o}C resulted in a measured M_s^{σ} of 25^{o}C, which is very close to the expected

value of 27°C, the respective data point shows a very good match with the red line for theoretical M_s^{σ} model. However for the other 3-step temper process which was done to maximize the yield stress for EX425, the measured M_s^{σ} falls out of line with the theoretical model, requiring a revised g_n of 1300 J/mol.

CHAPTER 5: ALLOY DESIGN

The major objective and challenge of this design is to achieve a high ductility level in austenitic TRIP steels while maintaining a high level of yield strength under the same operating conditions. The current design is based on a structural hierarchy of systems design as reviewed by Jenkins [167] which describes the whole process as a sequence of four steps –

Systems Analysis → Systems Design → Implementation → Operation

While the first step of analysis involves identification of applications defining the materials properties and performance objectives, the second step of design characterizes the subsystems and their interactions to create models required to achieve the properties. Once the models are in place, their integration enables design of the new materials for specific properties. Once the composition of the new alloy designs are set, the implementation step involves validation of the prototypes and finally putting the new systems into live operation. This validation helps in characterization of the alloys as well as verifies the effectiveness of the design criteria and models used. These steps or levels are underlined in the systems design chart shown in figure 1.5.1 in section 1.5 where the Processing – Structure – Property – Performance relationship was established with adequate description of the substructure present within each microstructural level.

5.1 Approach

The sequential steps of complete alloy design are shown in figure 5.1.1.

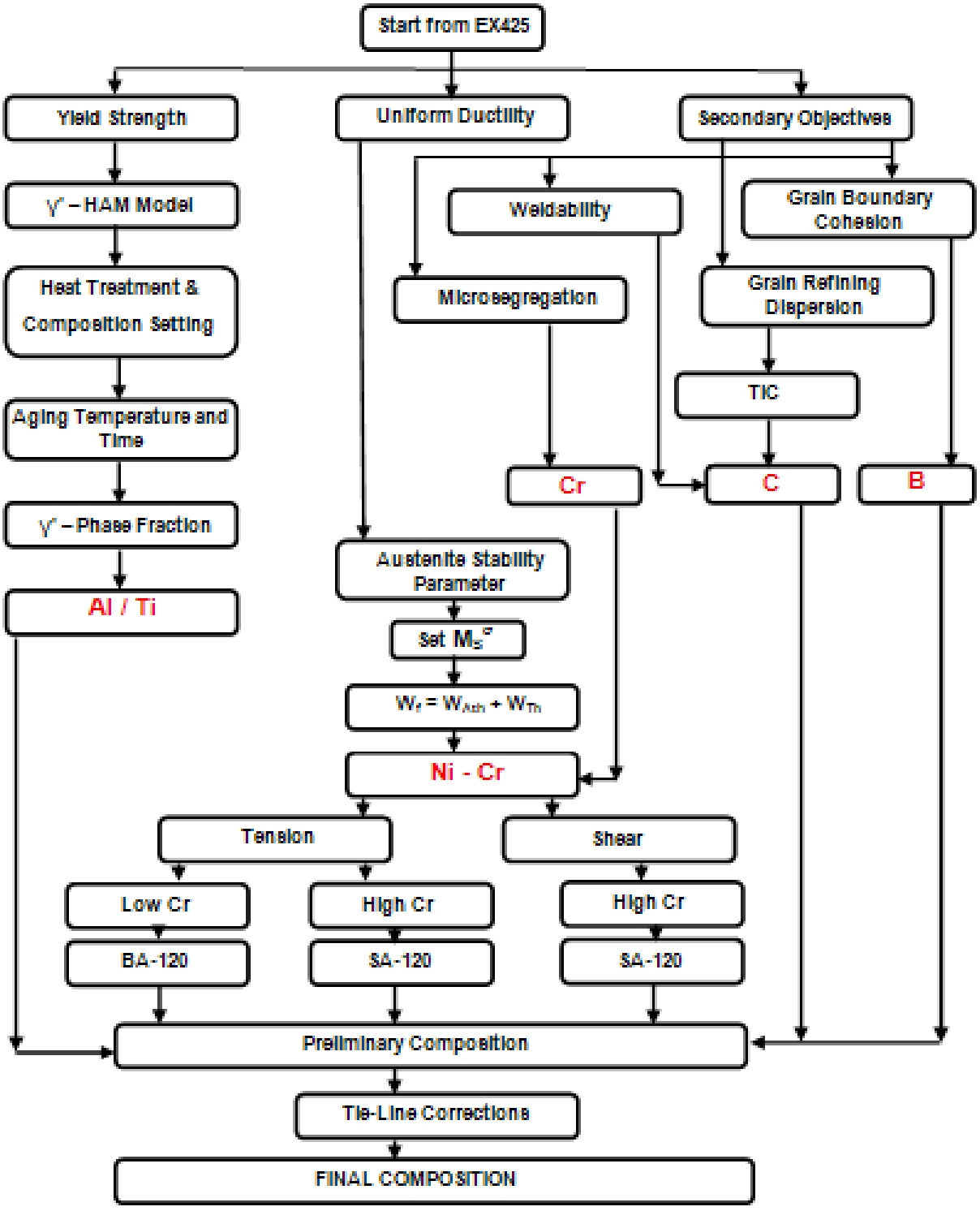

Figure 5.1.1: Design Optimization Process for new alloy designs: BA120 and SA120

As discussed earlier, the basis of these new alloy designs stems from the experimental data points obtained from an earlier TRIP prototype EX425 which helped build quantitative parametric models for optimizing both strength and uniform ductility in this class of steels. The design of new high strength high ductility (under both tension and shear stress states) austenitic steel has been attempted in 3 steps – First, one of the primary objectives was having a yield strength of 120 ksi (827 MPa) at room temperature. Experimental static tensile test data points for the EX425 TRIP prototype alloy aged at different temperatures have been used to calibrate the phase fraction of gamma prime (**γ'**) and corresponding yield strength. This model has been used to determine the optimum amount of gamma prime needed at equilibrium with the f.c.c austenite matrix at a given temperature to yield the desired strength level of 120 ksi (827 MPa). The strength model has been calibrated against both the experimental data as well as the theoretical predictions from the Ham model, which has been discussed earlier in section 2.4. The key to obtaining the right amount of gamma prime (**γ'**) phase fraction is optimal amounts of Al and Ti in the alloy as well as selection of aging temperature post solution treatment to control the phase fraction.

The second step is to optimize the composition of the alloy to achieve maximum uniform ductility under operating conditions. Two alloy designs have been conceptualized in this research and prototypes of both have been made for experimental analysis. Prototype '*A*', named '*Blastalloy 120 or BA120*' is a non-stainless (low Cr) design which has been optimized to achieve maximum uniform ductility under tension while maintaining yield strength of 120 ksi (MPA), both at room temperature. The second prototype B, named '*Shearalloy 120 or SA120*' is a high chromium design which has been optimized to achieve high uniform ductility under both

tension as well as shear (or torsion) stress states while again having yield strength of 120 ksi at room temperature. The high ductility under two different stress states for the same alloy is achieved by varying the aging temperature and time, to vary the austenite stability to meet the necessary performance requirements. The key to optimizing the ductility is based on the concept of austenite stability parameter which defines the matrix transformation characteristics, as introduced and discussed in section 2.3.1, which in turn is derived from fundamental models of transformation-Induced plasticity (section 2.2). The two most important components of the alloy which govern the matrix stability and transformation characteristics are Ni and Cr. The amounts of Ni and Cr have been modeled based on at a pre-destined temperature (M_s^{σ}) which would in-turn lead to high ductility at room temperature. The calculation process of amounts of Ni and Cr for optimum M_s^{σ} temperature is detailed in section 5.3. Adequate amounts of C and B are considered for grain refinement and grain-boundary cohesion. There is no initial change in Mo and V for the new alloy design, although final Mo and V concentration might differ from that of EX425. No Mn is considered in our designs since Mn is known to reduce uniform ductility in austenitic TRIP steels. Finally, validation of final calculated compositions for both alloys (BA120 and SA120) have been done using Thermo-Calc and CMD, for expected gamma prime phase fraction as well as austenite stability after aging, to show that theoretically, both alloy designs do conform to all desired design objectives.

5.2 Strength Goal

The strengthening mechanism employed in this alloy design is precipitation of the **γ'** intermetallic phase. Using the Ham model and equations 2.4.1 and 2.4.2 of precipitation

strengthening of γ' particles as shown in section 2.4, a theoretical dependence of the yield strength of the TRIP alloy can be predicted for varying levels of Gamma Prime phase fraction.

5.2.1 Gamma Prime Precipitate Strengthening Model

Figure 5.2.1.1 shows the calculated precipitation strengthening model based on Ham's single and paired dislocation cutting model and compared with the experimentally determined yield strength's for EX425 aged at different temperatures to vary the equilibrium gamma prime phase fraction. The red solid curve in Figure 5.2.1.1 represents the theoretically predicted dependence of γ'-phase fraction on the total overall yield. The green denote the actual experimental data points for EX425. The equilibrium phase fraction of gamma prime is determined from Thermo-Calc for respective aging temperatures.

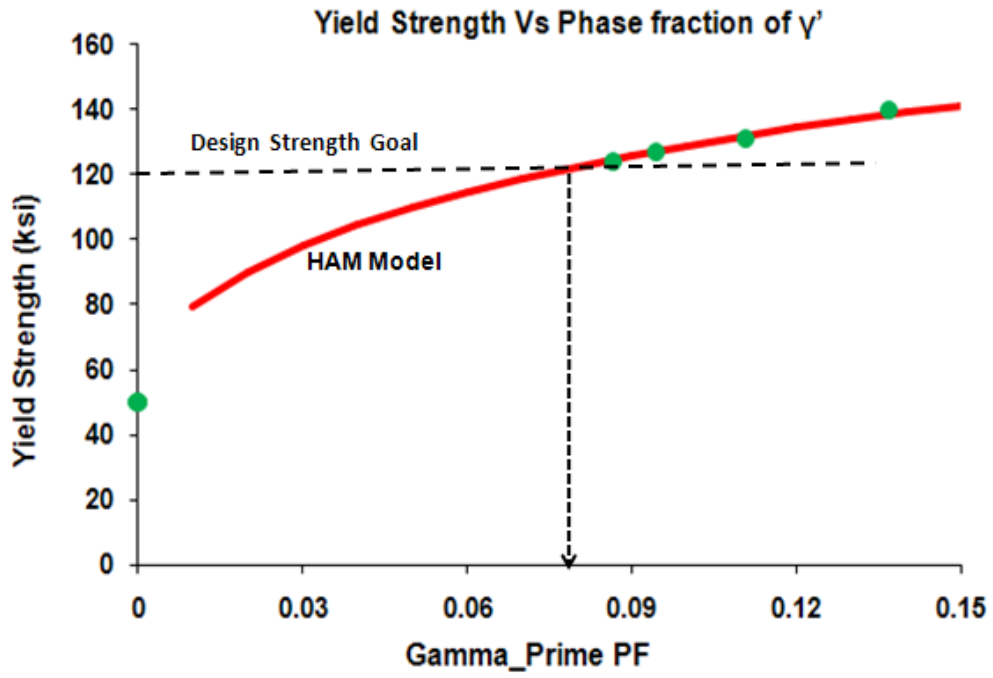

Figure 5.2.1.1: Comparison of Theoretical/Calculated and measured phase fraction of Gamma prime and its effect on Yield Stress in EX425 Austenitic TRIP steel, as compared with the HAM model (Red line) using APB energy (γ_o) of 0.22 mJ/m^2. The green dots represent the measured values from quasi-static uniaxial tensile tests at room temperature

To determine the base yield strength of the austenite matrix, Vicker's microhardness measurements were taken on a fully austenized (solution treated at 950°C for 1 hour) specimen of EX425 and then converted to expected Yield Stress based on Saha's relationship shown earlier in equation 3.3.1. The Yield Stress for Austenite matrix is determined to be ~ 49.5 ksi (340 MPa). This data point is shown in figure 5.2.1.1 as the Yield Stress at zero **γ'-** phase fraction. The rest of the yield strength requirement is fully controlled by the amount of gamma prime phase fraction allowed to precipitate at equilibrium which in turn is controlled by the heat treatment conditions post austenization. The other four data points for EX425 have been determined by uniaxial tensile tests at room temperature. Table 5.2.1.1 shows the experimentally measured values of yield strength of EX425 for varying amounts of Gamma Prime phase fraction with their respective heat treatments. The Antiphase boundary (APB) energy of the **γ'** phase is taken to be ~ 220 J/m^2 to fit the data.

Temper Condition		Calculated y' phase fraction	Room Temperature Measured Yield Strength (ksi)/(MPa)
Temperature, °C	Time (hr)		
950	1.0	0.000	49.5*
750	10.0	0.087	122.0
735	16.8	0.095	127.0
702	55.7	0.111	131.0
600	200.0	0.137	142.0*

Table 5.2.1.1: Calculated gamma prime phase fraction and respective measured tensile yield stress for EX425 for different aging conditions. The yield stress data marked * are computed from measured VHN numbers

The high temper time of 200 hr is for the specimen heat treated at 600°C due to the slow kinetics of gamma prime nucleation at temperatures < 700°C. The low temperature aging is necessitated due to a multi-stage temper starting with high temperature aging in the first steps to speed up the

kinetics of reaching equilibrium. The calculated phase fraction in table 5.2.1.1 and figure 5.2.1.1 has been computed using the final-step equilibrium aging temperature of 600^{o}C only.

5.2.2 Composition and Heat Treatment for required Strength

From figure 5.2.2.2, it is seen that the experimental evaluation of EX425 gives yield strength of 123 ksi for gamma prime phase fraction equal to 0.0867. Using Thermo-Calc with the Ni-data7 database, the variation of phase fraction of **γ'** in EX425 with varying aging temperature has been shown in figure 5.2.2.2. The composition setting to achieve the appropriate amount of the gamma prime phase fraction and the relevant heat treatment has been done in three steps – First, the optimum heat treatment temperature and time are set, then the required amount of gamma prime in equilibrium at the set temperature and time in step 1 is defined and finally the amounts of Al and Ti are calculated to achieve the correct amount of **γ'-**phase at the given aging temperature.

Step 1: Setting optimum Temperature and Time of Aging

As discussed earlier in section 4.1, Stavehaug [13] recorded the temper times needed to achieve maximum hardness in EX425 through optimum austenite grain size resulting in maximum yield strength. Two distinct data points were measured for peak hardness – 700^{o}C for 60 hours and 750^{o}C for 10 hours. An Arrhenius log plot relating the inverse of time and temperature was fitted to these reference points as shown in figure 4.1.2. This relationship is based on the temper times needed to achieve maximum hardness relating to optimum particle size as discussed in section 2.4 using Silcock and Williams theoretical quantitative model. Thus, to obtain the optimum temper time for heat treatment or aging at any temperature (to achieve the required **γ'** phase

fraction), the trendline in the figure 4.1.2 is extrapolated to give the relevant time. The temperature of **750°C and 10 hours** of aging has been kept as the standard aging condition for our new alloy designs. This is because it was observed that the kinetics of gamma prime nucleation as well as time needed to reach equilibrium composition is too slow at 700°C (described in Appendix I) while temperatures above 780°C result in the high probability of transformation of metastable gamma prime (**γ'**) to the undesired equilibrium **η** phase (section 4.3.2.1). 750°C is optimum for gamma prime nucleation kinetics and the aging time of 10 hours required for peak hardness/YS is practically and industrially feasible.

Step 2: Setting required Gamma Prime Phase Fraction

From the theoretical strength model shown in figure 5.2.1.1, it is estimated that a **γ'** phase fraction of 0.083 (8.3%) is required to achieve a room temperature tensile yield strength of 120 ksi (827 MPa).

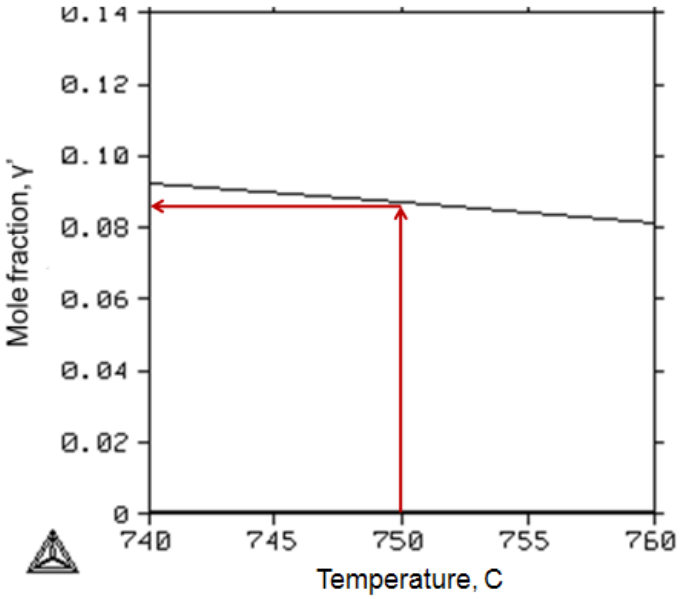

Figure 5.2.2.2: Calculated temperature dependence of **γ'** phase fraction for EX425

However, from figure 5.2.2.2, we see that the amount of gamma prime in equilibrium at 750°C is slightly higher at ~ 0.087 (8.7%) leading to a higher yield strength of ~ 123 ksi. The solid line in figure 5.2.2.2 represents a magnified view of the **γ'-** gamma prime phase fraction with respect to aging temperature.

Step 3: Setting Al and Ti

Keeping the desired phase fraction of gamma prime (0.083) in mind, the amounts of Al and Ti have been altered. Since a lower amount of **γ'** is needed at 750°C than is observed in EX425, the Al and Ti amounts have been reduced slightly. There is no need for high APB energy for the current strength levels as proven by the experimental analysis of EX425 and thus the Al/Ti weight ratio is kept same as that of EX425 and A286, ~ .054 while decreasing the Al and Ti concentrations.

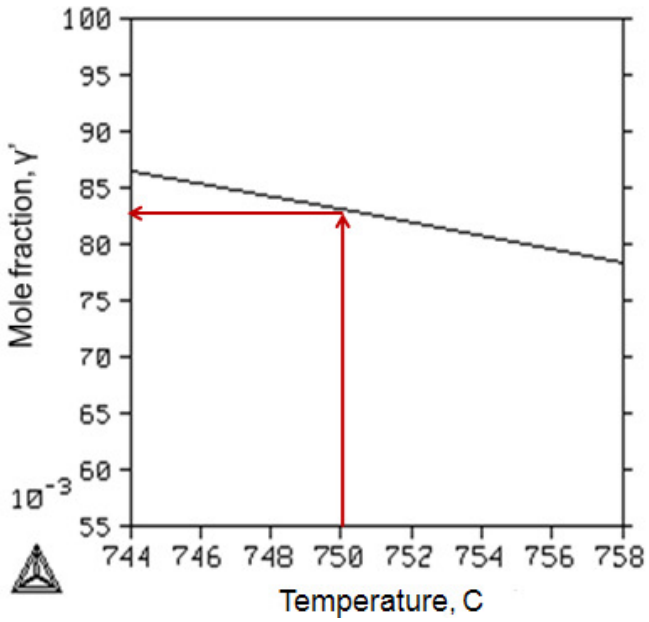

Figure 5.2.2.3: Calculated temperature dependence of **γ'** phase fraction for EX425 with modified Al and Ti contents as 0.156 and 2.9 wt% respectively

Again, using Ni-data 7 database in Thermo-Calc, it is calculated that the Al and Ti amounts of **0.156** and **2.9** (wt %) respectively would be enough to achieve the desired 0.083 phase fraction of gamma prime (**γ'**) while maintaining the ratio of 0.054, as shown in figure 5.2.2.3. It is to be noted that the final amounts of Al and Ti would change once the Ni and Cr levels are set for optimum austenite stability. The computed Tie-line will be used to correct any anomaly in the calculated gamma prime phase fraction once all the components of the alloy design have been set.

5.3 Uniform Ductility

As discussed earlier in section 2.2.4, the principle of transformation induced plasticity is used to achieve the desired property of improved uniform ductility in our new alloys where the stress-assisted transformation of austenite to martensite is controlled suitably to occur at a specific pre-determined temperature (M_s^{σ}). The stability of the austenite matrix plays a very important role in determining the ease of transformation and the related stress required. Quantitative models have been put together (presented earlier in section 2.3) which define the stability of the austenite in terms of its inherent negative free energy and the stability is controlled by the compositions of its alloying elements, stress states and temperature of operation. The computational design of the new alloys to optimize for maximum uniform ductility has been done in the following four stages –

Stage 1: Setting Austenite Stability Levels for Tension and Shear

The dependence of the mechanical driving force of isothermal martensitic nucleation on the applied external stress is shown by equations 2.3.5 and 2.3.6 for the tension and shear stress

states respectively. Figure 5.3.1 shows the yield strength (ksi) dependence of ΔG^{σ} for both tension and shear stress states. The solid curve in brown and blue denotes the mechanical driving force for tension and shear stress states respectively. Since at the transformation temperature of M_s^{σ}, the total driving force of stress-assisted isothermal martensitic transformation is equal to the critical driving force of transformation, the austenite stability parameter ($\Delta G^{Chem} + W_f^{Sol}$) is represented as a summation of the total mechanical driving force due to the applied external stress and the constant term G_n (1010 J/mol), as represented earlier in equation 2.3.12.

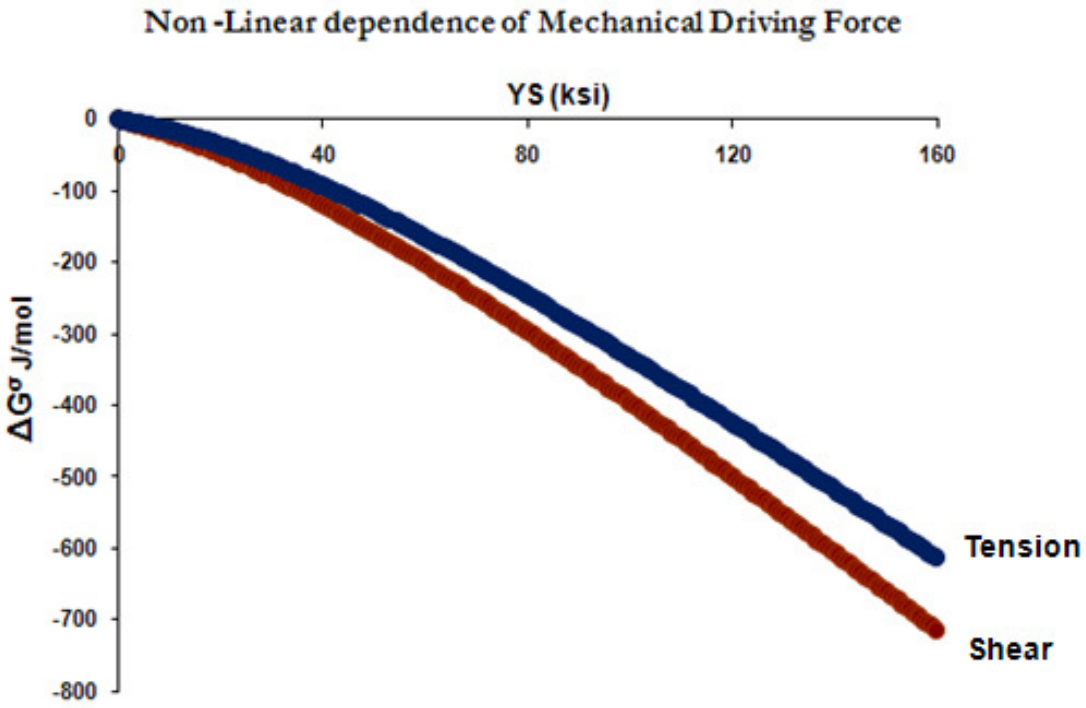

Figure 5.3.1: Theoretical Dependence of the Mechanical driving force of martensitic transformation on the yield stress of TRIP Steels

Re-writing equation 2.3.12, (*at* $T = M_s^{\sigma}$)

$$\Delta G^{Chem} + W_f^{Sol} = -[g_n + \Delta G^{\sigma}]$$

All terms in equation 2.3.12 are expressed in SI units; thus Yield stress used in calculations is in MPa and later converted to ksi to plot the stress dependence. Thus, including the term G_N to the ΔG^{σ} relationship in figure 5.3.1 gives the required quantitative values of austenite stability for our desired yield strength of 120 ksi. Figure 5.3.2 shows the predicted dependence of the austenite stability parameter $(\Delta G^{Chem} + W_f^{Sol})$ on the yield strength of austenitic TRIP steel at the critical transformation temperature (M_s^{σ}).

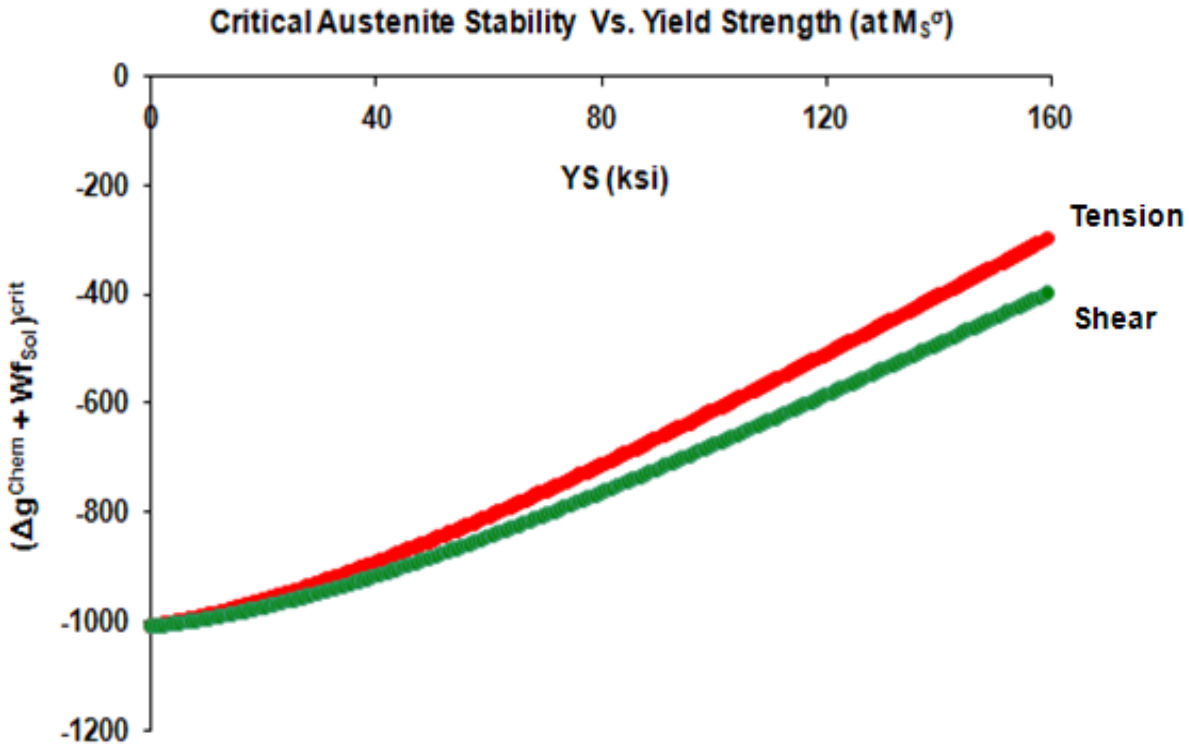

Figure 5.3.2: Theoretical/Calculated Austenite Stability Parameter of TRIP Steels as a function of the Yield Stress at the critical transformation M_s^{σ} temperature

The solid curves in red and green represent the austenite stability parameter dependence on yield strength for uniaxial tension and shear stress states respectively. The required austenite stability,

for a yield stress of 120 ksi (827 MPa) for both tension and shear designs, can then be determined from the respective curves in figure 5.3.1 as the following –

Critical required Austenite Stability Parameter (ASP) under tension: **- 508 J/mol**

Critical required Austenite Stability Parameter (ASP) under Shear: **- 584 J/mol**

Stage 2: Setting Design M_S^{σ} temperatures

For the case of both alloy designs (Blastalloy and Shearalloy) the need is to maximize the uniform ductility at room temperature. Since the maximum uniform ductility under tension in similar classes of TRIP steels like EX425 have been experimentally found to be ~ 25 to 30^{o}C higher than the measured M_S^{σ} temperature (as discussed in section 2.2.4.1), as well as in other austenitic TRIP steels [79], the design M_S^{σ} temperature for the case of stretch ductility under tension for Blastalloy needs to be close to ~ 0 – 5^{o}C. It is seen from figure 2.2.12 in section 2.2.4.1 that there is a very sharp decline in the overall uniform ductility of the material just beyond the maximum point, thus it is safer to design the M_S^{σ} temperature to be slightly higher than 0^{o}C so ensure a larger range of use temperature for the new Blastalloy. Hence, the M_S^{σ} temperature for the *Blastalloy* (BA120) design is kept at **5^{o}C (or 278 K).**

For the case of the second alloy design, which is to be optimized for maximizing ductility under both tension and shear stress states, the design M_S^{σ} (tension) temperature is kept same at **5^{o}C (or 278 K)**. However this would mean a decrease in M_S^{σ} (shear) temperature under shear loading for the same alloy if the aging heat-treatment is kept same (based on figure 2.2.18). Now experimental analysis of the measured M_S^{σ} temperatures for pure shear from the work of Haidemenopoulos [80] in addition to the constitutive transformation theories of Olson and Cohen

(figures 2.2.17 and 2.2.18) leading to the prediction of the stress dependence of temperature for pure shear in TRIP steels have been used to effectively predict the behavior of these materials under pure shear, and thus design an optimum M_S^{σ} temperature for maximizing the shear ductility, without compromising on the mechanical properties of the alloy under tension. The M_S^{σ} temperature under pure shear needs to be close to or even higher than room temperature to alloy desired properties for shear state. Thus, the M_S^{σ} *(shear)* temperature for Design B (Shearalloy, SA120) has been kept at 27°C or 300K. To achieve this dual performance criteria, the aging temperature for SA120 needs to be different for each of the two cases since in general for TRIP steels with same aging treatment, the M_S^{σ} *(shear)* temperature is lower than the M_S^{σ} *(tension)* temperature (figure 2.2.18). For optimized performance under tensile loading applications, the aging can be the same as the standard 750°C for 10 hours. However for optimized performance under shear loading, the aging temperature needs to be modified so as to achieve the required Austenite Stability Parameter value of -584 J/mol at the critical temperature of 27°C instead of 5°C used for tension. The only way this can be done is by lowering the aging temperature. Figure 5.3.3 shows a diagram of the typical dependence of Austenite Stability parameter on the critical temperature (M_S^{σ}) for any stress state.

The calculated Austenite Stability Parameter curve shifts upward (more positive) with increase in critical temperature. Thus in order to keep the required ASP for shear design, but at a higher critical temperature, we need to bring the ASP curve down (more negative), as shown by the blue arrow in figure 5.3.3. This can be achieved by lowering of aging/temper temperature. Now lowering of aging temperature would lead to more gamma prime phase precipitation (figure 5.2.2.2) thereby increasing the yield stress. This can be controlled by over-aging; so instead of

using the peak hardness times (Arrhenius relationship, figure 4.1.2 we need to overage the specimen (leading to increased size of gamma prime precipitates) so that the yield stress can be kept close to 120 ksi while maintaining the desired shear ASP.

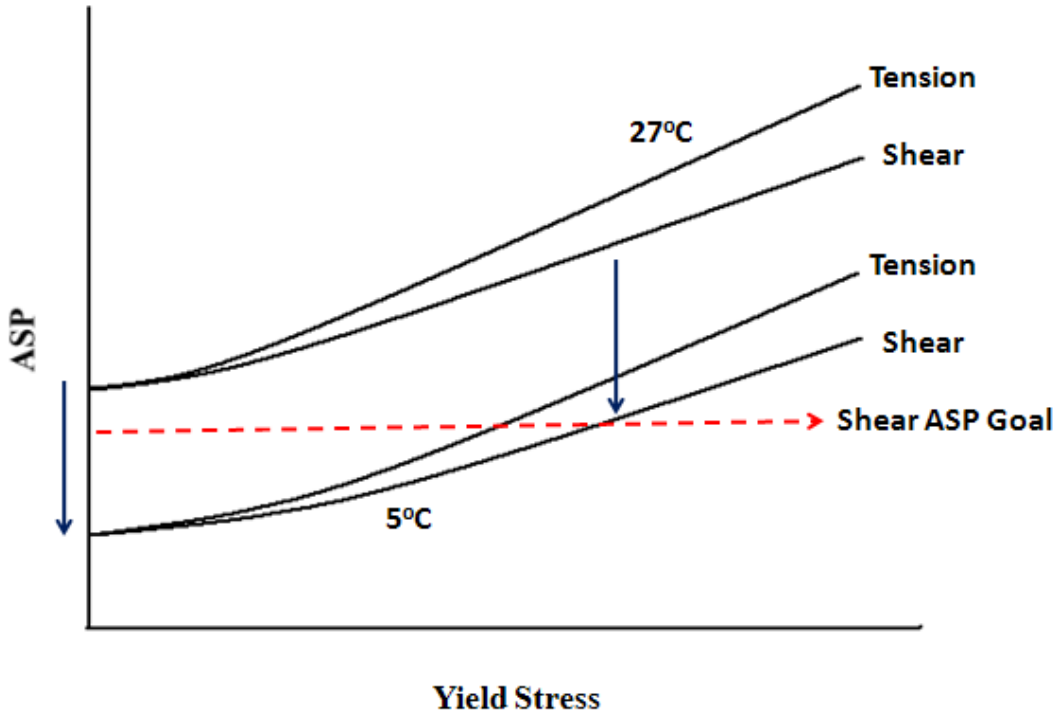

Figure 5.3.3: Variation of Austenite Stability Parameter on the critical transformation temperature for tension and shear in TRIP Steels

Stage 3: Calculating Frictional Work of Martensite Interface Motion

As introduced by equation 2.3.14 in section 2.3.2, the total frictional work of martensite interface motion is the sum of its athermal and thermal contributions. While the athermal contribution to the total frictional work (W_{Th}) is pure composition dependant as represented by equation 2.3.15, the thermal contribution to the total frictional work is dependant on both composition and critical transformation temperature, as represented by equations 2.3.16 and 2.3.17. Figure 5.3.4 shows

the dependence of the Thermal part of the frictional work due to martensite interface motion on the critical transformation temperature.

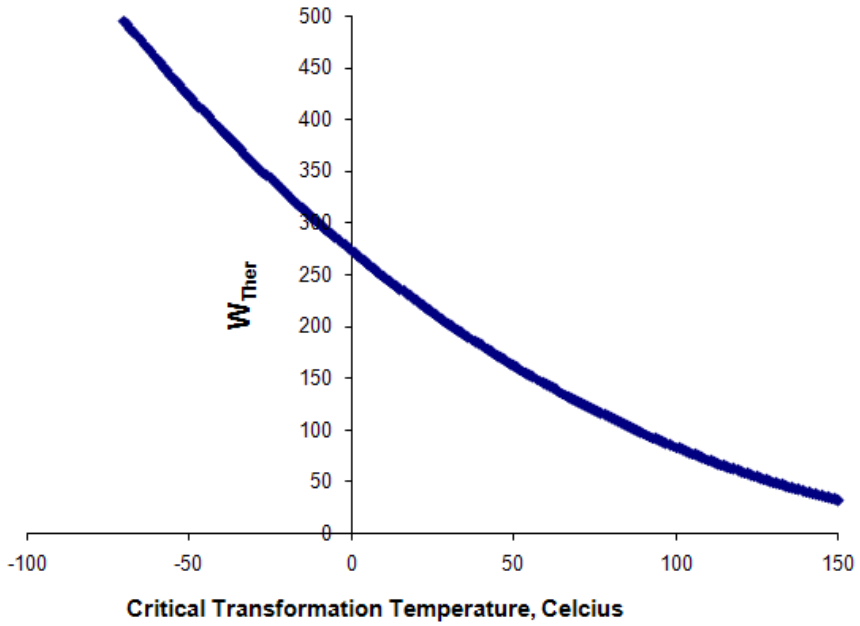

Figure 5.3.4: Variation of the Thermal contribution to the total frictional work of martensite interface motion with respect to the critical FCC→BCC transformation temperature

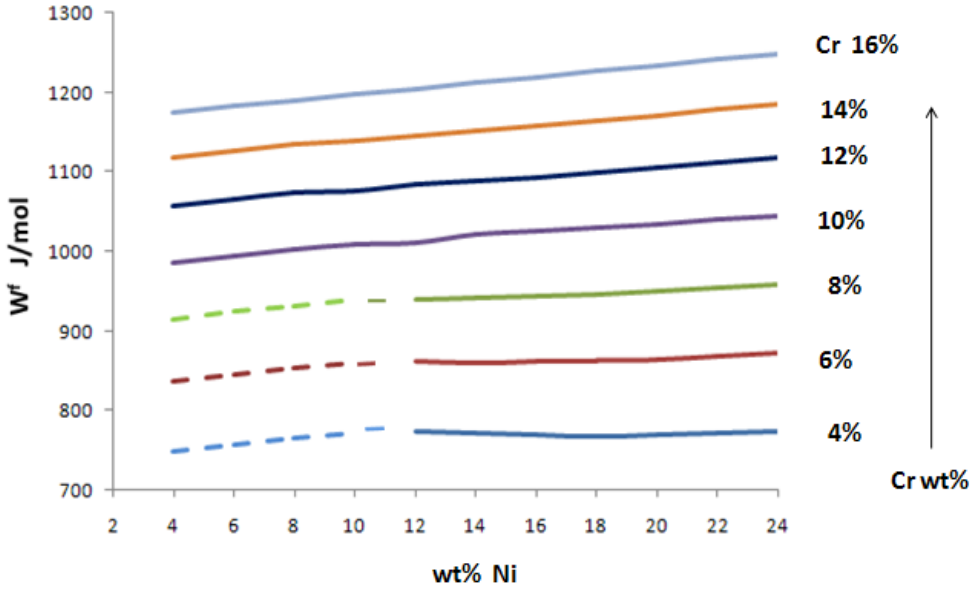

Figure 5.3.5: Variation of the Total frictional work of martensite interface motion with change in Ni and Cr concentrations

The aging temperature for the alloy (for γ-γ' equilibrium) does not have much effect on the W_{Ath} values. Figure 5.3.5 shows the variation in the total frictional work due to martensite interfacial motion as a function of change in Ni and Cr concentration in the alloy. Al and Ti are taken as 0.156 wt% and 2.9 wt% respectively based on the strength goal (section 5.2.2). All other components are same as in EX425.

The regions of the series for Cr 4%, 6% and 8% for Ni concentrations less than 12% is represented as a series of dotted lines as compared to the solid lines for other series of Cr. This is because for these low values of Ni there is no γ' (gamma prime) precipitation at equilibrium with the Austenite matrix at 750^{o}C for these Ni-Cr concentrations, so it's a fully austenitic microstructure.

Stage 4: Calculating Ni and Cr ranges for target ASP values

Similar to figure 5.3.5, the quantities of Ni and Cr are varied from 6 wt% - 26 wt% and 0 wt% - 16 wt% respectively to obtain the data points for calculating the variation of the total Austenite Stability Parameter (***ASP***) with composition. As the first step, equilibrium composition of the austenite matrix at 750^{o}C using Thermo-Calc is determined. Then the difference of the Gibb's free energies for the BCC and FCC phases is obtained by using the same equilibrium matrix composition calculated in the first step in CMD. The critical input temperature in CMD is the desired M_S^{σ} temperature. As discussed in earlier in section 2.2.4.2, by maximizing the thermal contribution to the frictional work of martensite interface motion while keeping the overall ASP constant helps in increasing the slope of the $\sigma - T$ curve for shear stress state adequately thereby improving the temperature range of shear performance for the alloy. By varying the heat

treatment for Shearalloy, it can be optimized for both fragment protection/shear resistance as well as the normal blast protection (high stretch ductility under tension).

W_{Ath} and W_{Th} can be calculated using the equations 2.3.15, 2.3.16 and 2.3.17 in section 2.3.2 from the equilibrium composition of the austenite matrix at the equilibrium temperature of 750^{o}C. Figure 5.3.6 shows the variation in ASP (J/mol) with change in Ni and Cr.

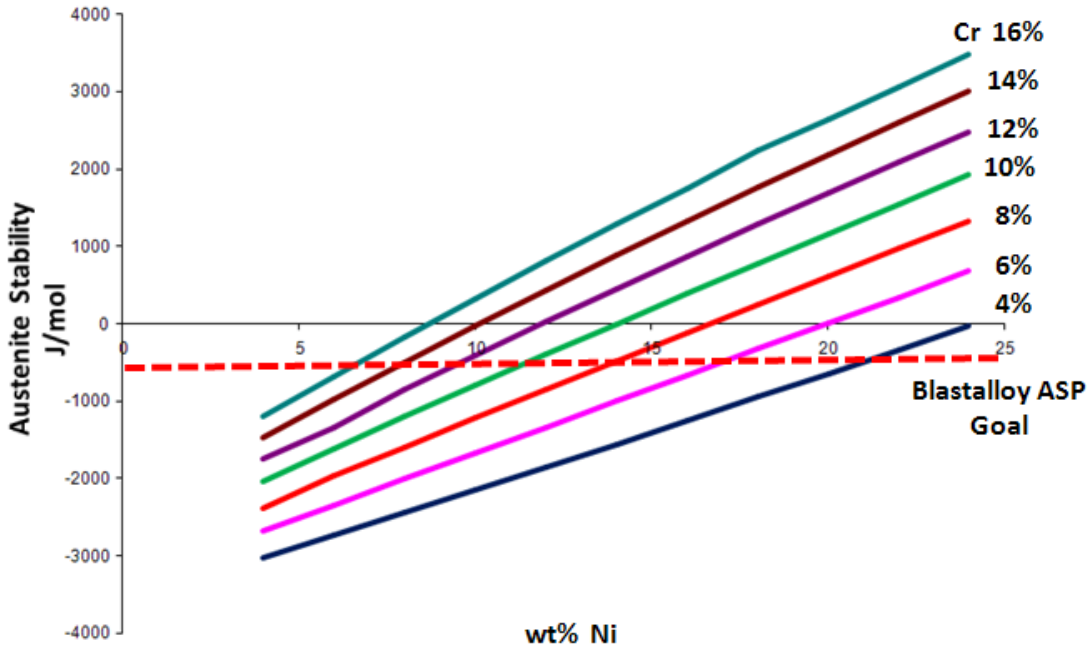

Fig. 5.3.6: Variation of Austenite Stability Parameter with respect to variation in Ni and Cr contents in alloy EX425. The red dashed line shows the goal (-508 J/mol) for Blastalloy

The Cr has been varied in intervals of 2 wt% with each solid curve and color representing a unique constant value of Cr wt% while the Y-axis shows the variation of the Ni content in the calculations. The horizontal red dashed line represents the target ASP values necessary to meet the stability requirements of the matrix phase with respect to transformation, as determined in section 5.3 (stage I).

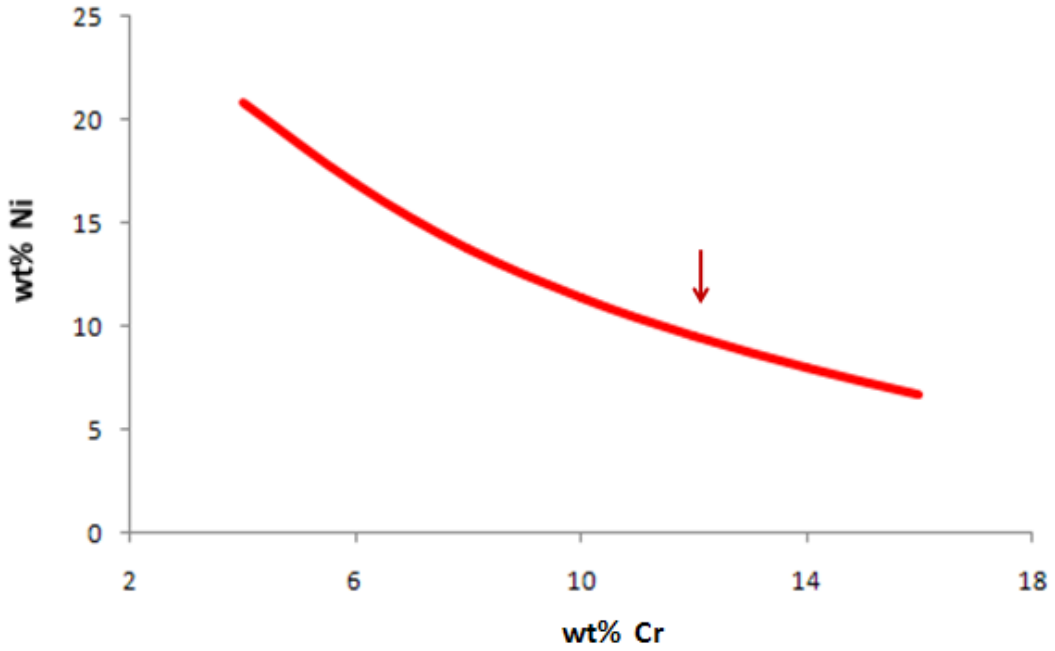

Fig. 5.3.7: Variation of Ni with respect to Cr for constant ASP of -508J/mol for EX425. The brown arrow points to the maximum Cr (and minimum Ni) allowed in alloy for precipitation of γ' in the system in equilibrium with the austenite matrix

The appropriate data points of Ni for each Cr curve were taken which had an intersection with the red target ASP line. The Ni-Cr curve was then plotted where each point on the curve has the same ASP value. There is an obvious inverse relation between the quantities of Ni and Cr to maintain the same matrix stability.

After obtaining the Ni content of each Cr curve that exhibited the target ASP, the wt% Ni values were plotted against their respective wt% Cr for each alloy. A 2^{nd}-order polynomial least-squares trend was fitted in order to predict the Ni and Cr content that satisfies the target ASP value throughout the spectra. Figure 5.3.7 represents an '*Iso-ASP*' curve showing the variation of Ni and Cr for Blastalloy design with each point on the curve having the constant ASP value, equal to -508 J/mol. The brown arrow represents the minimum Ni level required to form Gamma Prime (γ') precipitate in equilibrium within the matrix.

By the above steps 1-4 we obtain the appropriate quantities of Ni and Cr for optimizing austenite stability for maximum ductility. It was observed that data points from the trendline for the Ni-Cr plots resulted in a small discrepancy (± 10 J/mol) between the calculated and expected values for the Austenite Stability Phase (ASP) for the high Cr regimes, due to the use of the trendline for cases where the statistical R-squared is not 1. The tie-line adjustment affected these regimes much more than the others, therefore changing the ASP by a significant amount. Ni, in particular, has been seen to affect ASP the most. Therefore, by taking discrete points of the plot and using a MATLAB program, a better fitting trendline is found. This trend was used to find the required Ni value for each of the Cr regimes that satisfied the target ASP and the relative error between desired and calculated ASP was less than 5J/mol which is acceptable. As a result, the final proposed alloy compositions, as listed later in section 5.5 closely matches the target ASP. This iterative process can be repeated in order to attain an even closer approximation.

From section 5.2.2 we already have the necessary quantities of Al and Ti for the optimum phase fraction of Gamma Prime precipitate at equilibrium at 750^{o}C for desired strength levels. Considerations for grain refining dispersions and grain boundary cohesion are discussed in section 5.4 followed by other secondary property objectives for the designs. The final alloy compositions are consolidated and validated in section 5.5. Finally the set alloy compositions for Blastalloy BA120 and Shearalloy SA120 are evaluated to validate if they meet all secondary design objectives.

5.4 Grain-Refining Dispersion and GB cohesion – Control of C and B

As discussed in section 2.5, the presence of small quantities of fine grain refining dispersion phase (likes secondary carbides) and additional Boron for improved grain boundary cohesion is very important in order to achieve improved uniform ductility in TRIP steels. In our alloy design, we will implement the presence of fine TiC as the dispersed phase which would remain out of solution during solution treatment of the alloy and has a particle size < 1 μm. The amount of the FCC dispersed phase (TiC) after solution treatment and quench and control of the required carbon is described next. As previous described in section 2.5.1, addition of more Boron has been considered for improved grain boundary cohesion in order to avoid inter-granular fracture as observed in EX425 (section 4.5.3).

TiC Grain Refining Dispersion and Control of Carbon

Weldability concerns constrain the carbon content in austenitic TRIP steels to below 0.01 weight % in order to suppress formation of certain carbide particles. In principle, designing the alloy to have a specific TiC dispersion phase fraction at the alloy solutionizing temperature can further dictate the alloy's carbon composition. Generally ~ 0.15 - 0.2 at% of TiC dispersed phase is enough to aid grain-refining. Of all the elements in our design based on EX425, Titanium has the greatest affinity for carbon and so the goal is to have enough carbon to form TiC but without having excess carbon that would form other undesirable particles. Since addition of more carbon by small amounts does not have a considerable effect on the phase fraction of Gamma Prime or the Austenite Stability Parameter, the effect of adding more Carbon in the system has been evaluated independently of the strength and ductility requirements. Figure 5.4.1 shows the Thermo-Calc computed variation in the mole fraction of TiC (represented as the solid red line

FCC_A1#2 in Thermo-Calc output) with aging temperature for EX425 composition, in equilibrium with FCC austenite matrix and γ' Gamma Prime precipitated phase.

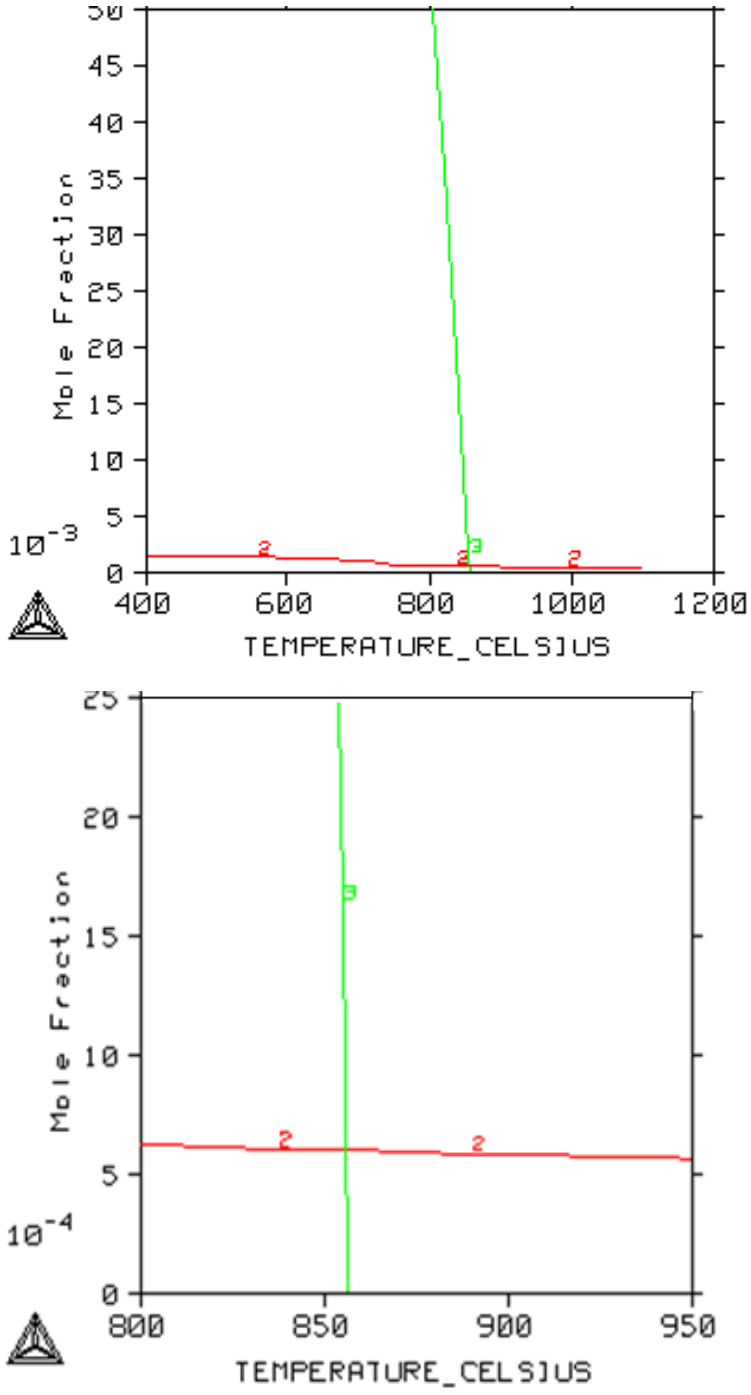

Figure 5.4.1: Calculated temperature dependence of TiC (FCC) mole fraction for EX425

At the point where Gamma prime phase goes to zero (existence of only single austenitic phase → minimum solutionizing temperature) and at the preset austenizing temperature of 950°C, the calculated amount of TiC phase is extremely low, ~ 0.06 at. %, which is less than the desired 0.2 at% needed for optimum refinement. This means more carbon is necessary to increase the TiC formed at 950°C, however we cannot go too high on C to maintain good weldability of the alloy.

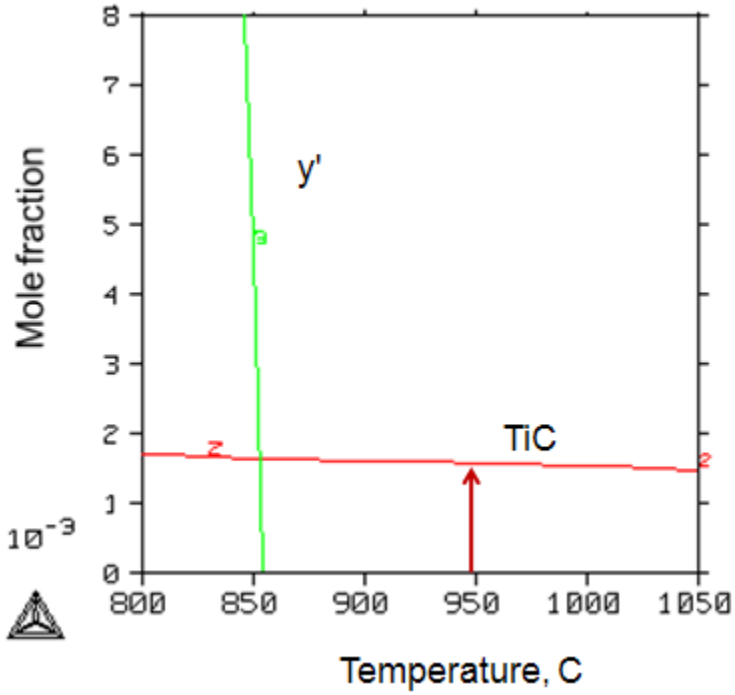

Figure 5.4.2: Calculated temperature dependence of TiC (FCC) mole fraction for EX425 for carbon level 0.014 wt%

Figure 5.4.2 above shows the variation of TiC phase with temperature for a carbon level of 0.014 wt%. This shows that now the carbon level is high enough to form ~ 0.15 atomic % TiC dispersed phase at the solutionizing temperature of 950°C. So preliminary Carbon level is set at 0.014 wt%. It is not desirable to go much higher in carbon levels due to concerns regarding weldability and intergranular corrosion due to formation of other secondary carbides.

Grain Boundary Cohesion and Control of Boron

Studies by Krasko and Olson [129] has shown that addition of Boron to austenitic TRIP steels tend to strengthen the bonding in the grain boundary and across it thereby improving cohesive properties to help reduce inter-granular fracture. This has been discussed earlier in section 2.5.1. The typical amount of Boron in commercially available TRIP steels varies from 50 - 150 ppm (0.015 wt %) with 125 ppm being considered ideal for optimum grain boundary cohesion. Since the level of boron in EX425 is ~ 93 ppm and inter-granular (IG) fracture has been observed at room temperature, the boron content is increased to ~ 125 ppm for design considerations to reduce IG fracture.

5.5 Final Design Composition

While the amounts of Al and Ti were set in section 5.2 using Gamma Prime strengthening model, the preliminary amounts of Ni and Cr were picked from the 'iso-ASP' curve in figure 5.3.7 in section 5.3. For the Blastalloy 120 design, a non-stainless design with Cr ~ 4wt% was selected. For the case of Shearalloy120, a high Chromium design was selected so as to enable maximization of the thermal contribution to the frictional work of martensite interface motion, necessary for optimization of performance under shear loading. It is seen that on using the maximum allowable Cr from the Ni-Cr curve and then using the lever rule to match the desired gamma prime phase fraction, it leads to a very high amount of Ti in the system, which is highly undesirable due to microsegregation issues. Figure 5.5.1 shows the necessary amount of Ti required in the system for increasing Cr content, keeping the gamma prime phase fraction and ASP values constant at 0.083 and -508 J/mol respectively.

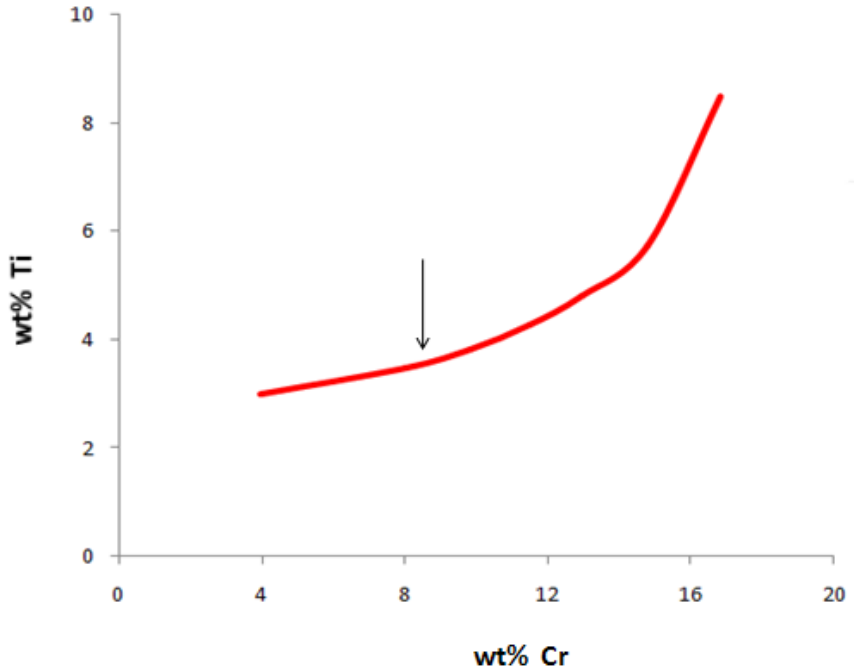

Figure 5.5.1: Calculated variation of required Ti in the system for increasing levels of Cr, while maintaining constant values of gamma prime phase fraction and Austenite Stability Parameter. The brown arrow represents the design constraint for Ti in the system.

Figure 5.5.1 shows that there is a sharp increase in the slope of the Ti-Cr curve beyond 8.5 wt% Cr in the system, marked by the brown arrow. To enable increase in Cr content, we introduce additional Al in the system while maintaining the same ratio for $\left(\frac{Al}{Ti}\right)$ as 0.054 so as not to affect the level of gamma prime strengthening. It is seen that using an Al/Ti content of 0.1885/3.5, a fairly high chromium level of ~ 10 wt% is achievable, for the case of SA120.

The amounts of Mo and V have been kept same as in EX425 which is optimal for stability and other secondary objective criteria, discussed in section 5.6. The amount of N is considered to be the minimal impurity level of 0.001 wt%. Strict control of S and P has to be observed while vacuum induction melting and trace amounts of these can be expected. Table 5.5.1 shows the preliminary amounts for the respective components in wt% of alloy –

Wt %	Al	Ti	Ni	Cr	C	B
BA-120	0.156	2.90	23.60	4.00	0.014	0.0125
SA-120	0.189	5.50	13.65	10.00	0.014	0.0125

Table 5.5.1: Preliminary component settings for new alloy designs

When all these components and their respective preliminary quantities (as determined) are used together to validate the gamma prime phase fraction obtained at equilibrium at 750°C using Thermo-Calc, it is observed that they are slightly shifted from their target levels. The target gamma prime phase fraction is 0.083 at 750°C for Yield Stress of 120 ksi (MPa). In order to correct the γ' phase fraction in equilibrium with the matrix austenite phase at 750°C, we used the following 3-phase lever rule along a Tie line for multi-phase equilibrium system

$$X_i^{Alloy} = f^{\gamma}.X_i^{\gamma} + f^{\gamma'}.X_i^{\gamma'} + f^{TiC}.X_i^{TiC'} \quad (5.5.1)$$

Where:

X_i^{Alloy} = Composition of component '*i*' in Alloy

f^{γ}, $f^{\gamma'}$, f^{TiC} = Phase fraction of Gamma Prime/Gamma (Matrix)/TiC phases, and

X_i^{γ}, $X_i^{\gamma'}$, X_i^{TiC} = Composition of component '*i*' in γ / γ'/TiC Phase

Using the above equation 5.5.1 for each component for both alloy designs, we arrive at the final design compositions for Blastalloy BA120 and Shearalloy SA120. Table 5.5.2 represents the final design components and their amounts in each of the two alloys designed, BA120 and SA120, along with the calculated values of Gamma Prime phase fraction at equilibrium at 750°C, and their Austenite Stability Parameter Values for critical transformation temperatures of 5°C for tensile ductility and 27°C for shear ductility (SA120 only).

wt %	BA – 120	SA - 120	
Al	0.163	0.210	
Ti	3.029	3.809	
Cr	3.986	9.802	
Ni	23.542	14.538	
Mo	1.245	1.225	
V	0.319	0.313	
C	0.01	0.01	
B	0.0125	0.0125	
N	0.001	0.001	
Fe	Balance	Balance	
	Blast Protection	**Blast Protection**	**Fragment Resistant**
Aging	750°C – 10 hr	750°C – 10 hr	726°C – 50 hr (overaging)
γ' – mole fraction	0.083	0.083	0.09
YS (ksi/MPa)	120/827	120/827	130/896
Calculated ASP	-507 J/mol	-510 J/mol	-585.5 J/mol
Desired ASP	-508 J/mol	-508 J/mol	-584 J/mol

Table 5.5.2: Final Design Composition and Properties for BA120 and SA120

5.6 Secondary Design Objectives

Secondary design objectives include properties like good weldability, non – magnetic behavior at operating conditions (Curie temperature of the alloy composition should be lower than room temperature), easily weldable, resistant to environmental hydrogen, stress-corrosion cracking and fatigue initiation and finally, to be affordable since huge quantities of the material is required to

construct the hulls of Naval ships thereby making cost a very important factor for the practical application of these alloys.

5.6.1 Weldability

For any structural material, the heat-affected zones (HAZ) adjacent to the welded joints are considered to be the weakest links. Both the matrix and the strengthening dispersion structures control weldability of austenitic steels. As a rule of thumb, for adequate weldability of martensitic steels C content of the alloy should be kept below 0.15 wt %. For prevention of Intergranular corrosion, discussed later in section 5.6.4, the carbon levels are usually kept lower than 0.05wt%. In our designs, we have much lower carbon content (0.01 wt %) since we don't want to have any carbide dispersions, other than a small amount of grain refining dispersion. For higher carbon amounts, after solidification, welds are very hard and can show a brittle behavior. The hardness of the heat affected zone of the welds can even exceed 500 VHN and cold cracking phenomena is prone to occur. Several methods have been investigated for improved welding of austenitic TRIP steels, including spot welding [168], whereby the reduction of carbon in the weld has been studied.

5.6.2 Control of Microsegregation Behavior

Even if we maintain low carbon levels, steels containing higher alloying content reduce the weldability of the material by microsegregation. Micros**e**gregation is a separation of impurities and alloying elements in different regions of solidified alloy and is caused by the rejection of the solutes from a solidified alloy into the liquid phase. This rejection is a result of different solubility of impurities in liquid and solid phases at the equilibrium temperature. Comparisons of the chromium content in FCC austenite phase with respect to the mole fraction of the solid phase

have been made. Figures 5.6.2.1 (a) and (b) show the mole fraction of Cr in γ - Austenite phase as the alloy solidifies for A286 and EX425.

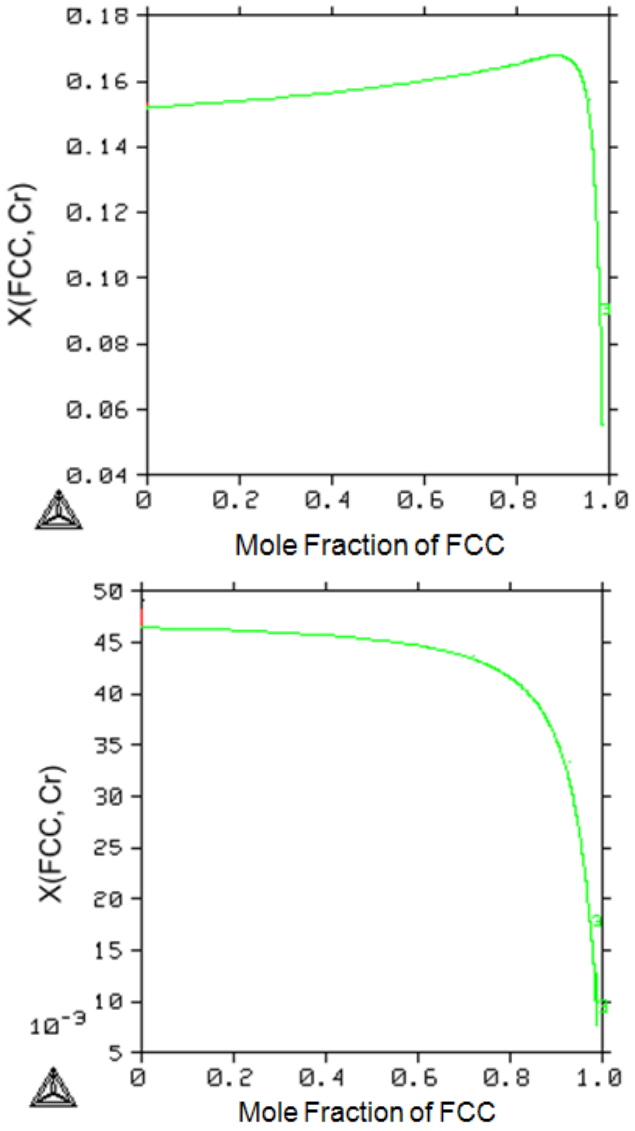

Figure 5.6.2.1: Variation of chromium content in solid as a function of mole fraction of solid phase showing microsegregation in Austenitic TRIP Steels a) A286 b)EX425

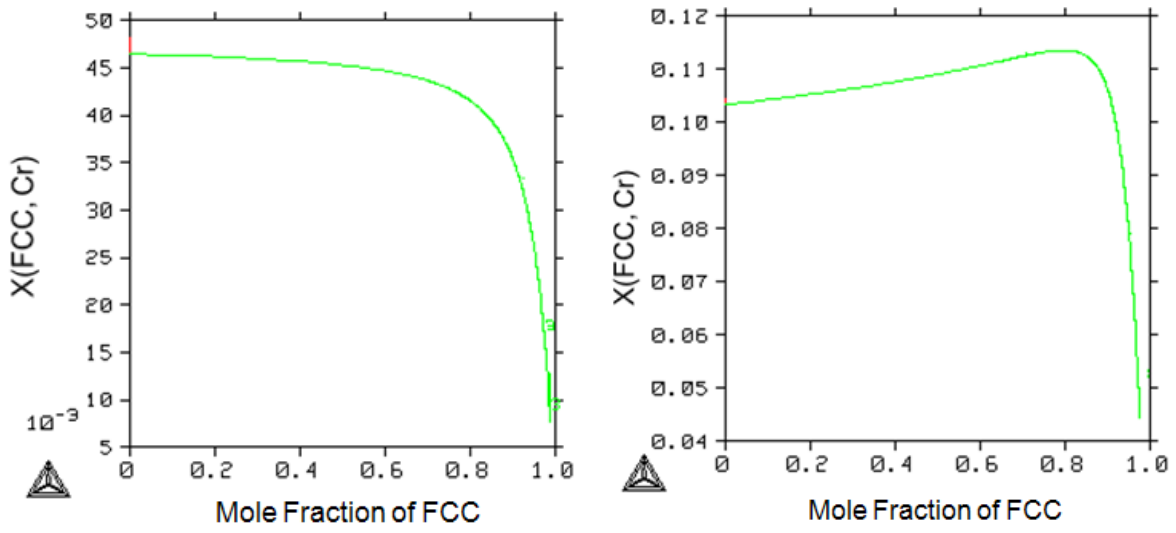

Figure 5.6.2.2: Variation of chromium content in solid as a function of mole fraction of solid phase showing microsegregation in Austenitic TRIP Steels **a)** BA120 **b)** SA120

Figures 5.6.2.2 (a) and (b) are Scheil diagrams for BA120 and SA120 respectively. The figures have been calculated using the Thermo-Calc Scheil model. However, for most compositions, Thermo-Calc would only display the Cr in the liquid phase. The Cr at 90% and 95% solid were calculated and compared with those for Cr 0%. These values are summarized in the table 5.6.2.1.

Alloys	X_{Cr} at 0% Solid	X_{Cr} at 90% Solid	X_{Cr} at 95% Solid
A286	0.1520	0.1650	0.1550
EX425	0.0465	0.0360	0.0270
BA-120	0.0467	0.0370	0.0280
SA-120	0.1030	0.1050	0.0820

Table 5.6.2.1: Comparison of mole fraction of chromium present in FCC phase as the alloys solidify

From table 5.6.2.1, it is observed that the microsegregation level in the new designed alloys BA120 and SA120 are much lower as compared to that of the commercially available austenitic TRIP A286 alloy. BA120, which is non-stainless and whose composition is close to EX425, shows very similar microsegregation characteristics as EX425. Whereas for SA120, being a high chromium design, the microsegregation level is higher than that of BA120 and EX425, but lower than that of the stainless A286 alloy.

5.6.3 Hydrogen resistance and Stress-Corrosion Cracking (SCC)

Ultra-high strength steels are prone to decrease of ductility and fracture toughness in aqueous environments due to hydrogen assisted cracking. The reduction of toughness is caused by inter-granular brittle fracture associated with impurity segregation to grain boundaries, which may not only reduce the uniform elongation by ~ 10-20% but also toughness of the steel by as much as 80% under a corrosive environment. The common impurities in steel are P and S, both of which are embrittlers since they have lower free energy on a free surface than at a grain boundary. So the most effective way of avoiding them is by having clean processing techniques or impurity gettering. Impurity gettering can tie up *P* and *S* as stable compounds formed during solidification. La and Zr have been found to be effective impurity gettering elements. Another approach to minimize impurity effects is by design of grain boundary chemistry. By placing elements like W and B preferentially on the grain boundaries that enhance grain boundary cohesion is beneficial to the stress corrosion cracking resistance. Addition of more Boron has discussed in section 5.4.

Under the combined effects of stress and certain corrosive environments, austenitic stainless and non-stainless steels can be subject to this very rapid and severe form of corrosion. The stresses are usually tensile and may result from loads applied in service, or from residual stresses resulting from the method of fabrication such as cold working. The most damaging environment is a solution of chlorides in water such as sea water, particularly at elevated temperatures. As a consequence stainless steels are limited in their application for holding hot waters (above about 50°C) containing even trace amounts of chlorides (more than a few parts per million). This form of corrosion is only applicable to the austenitic group of steels and is related to the nickel content. Grade 316 is not significantly more resistant to SCC than is 304. The ferritic stainless steel grades do not generally suffer from this problem at all. It has been found possible to improve resistance to SCC by applying a compressive stress to the component at risk; this can be done by *shot peening* the surface for instance. Another basic alternative is to ensure the product is free of tensile stresses by austenizing as a first operation. This has been done for all our new prototype alloys prior to aging to relieve the internal stresses built up from forging and hot rolling.

5.6.4 Corrosion resistance

Due to the formation of passive films and nanometer scale oxide layers that naturally form on the metal surface and greatly reduce the rate of corrosion of the alloys in an aqueous environment, stainless steels are more resistant to corrosion than non-stainless steels. This corrosion resistance can be shown in a Pourbaix diagram, which is a thermodynamic representation of the stability of the oxide films formed at a given pH and potential for a specified aqueous solution [169]. There are three regions in a Pourbaix diagram: *Immunity*, where there is no metal dissolution,

Corrosive, in which there is active metal dissolution, and *Passivation*, where the formation of a protective oxide prevents further metal dissolution. As shown by the Pourbaix diagram in figure 5.6.4.1 calculated using Thermo-calc, the addition of ~ 10.6wt% Cr to the iron matrix shifts the passivation boundary to the left, decreasing the corrosive region of the Pourbaix diagram considerably [169]. A direct result of this relationship between matrix Cr content and Cr partitioning to the oxide film is that the corrosion resistance for an alloy with a fixed Cr content can be improved by increasing the activity of Cr in the matrix, essentially promoting partitioning to the oxide film. This is useful in having corrosion resistance in non-stainless steels whereby all the Cr activity is confined to the matrix (γ – FCC) while the precipitates (γ') is Cr free. Occurrence of pitting corrosion, or localized corrosion on the open surface, is dependent on the chromium content of the alloys, and decreases with increase in Cr levels. However Ni and Mo improve the pitting resistance in steel [172].

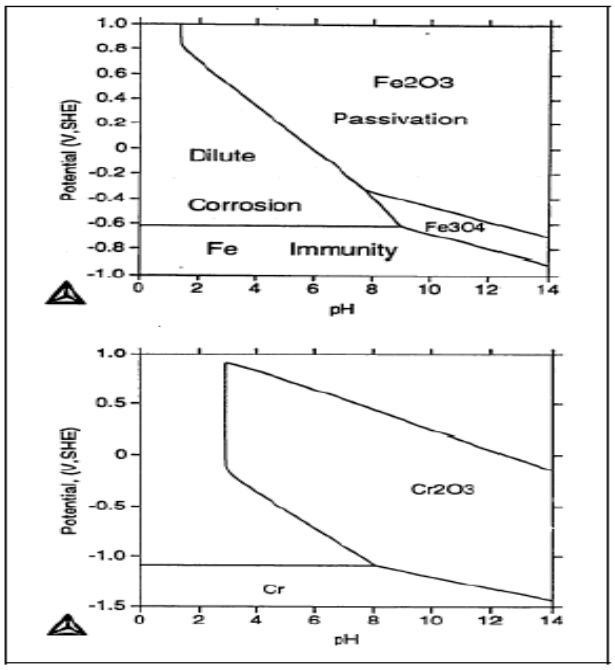

Figure 5.6.4.1: (a) Pourbaix diagrams for Fe and Cr in water. (top) 10^{-6} molal of Fe^{+2} (bottom) 10^{-6} molal of Cr^{+3} [169]

From figure 5.6.4.1 (a) it is seen that the addition of extra Cr shifts the passivation potential of the alloys to the left, thereby increasing the corrosion resistance. However higher chromium is known to lead to increased microsegregation, discussed earlier in section 5.6.2. A comparison of the Cr and Mo levels in commonly used commercial austenitic steels is presented in table 5.6.4.1. While the AISI 3XX steels are austenitic and stainless, AL6XN is a "super austenitic" stainless high Chromium-Nickel alloy steel used in marine applications for extreme resistance to corrosion.

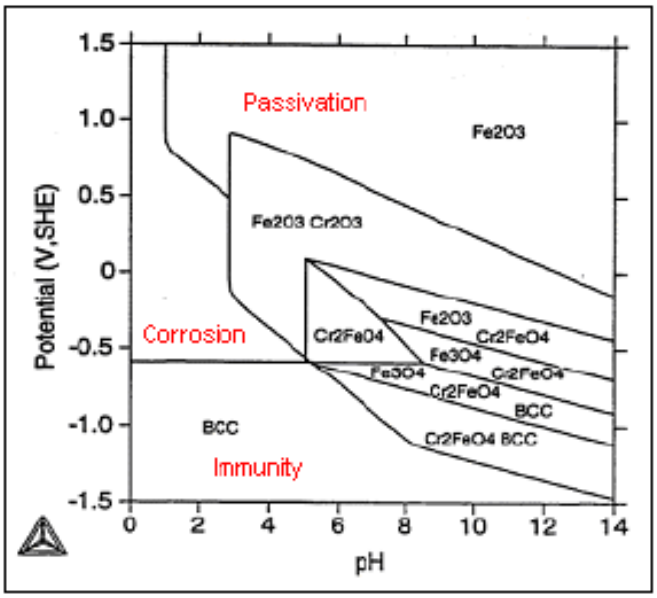

Figure 5.6.4.1: (b) Pourbaix diagram for Fe-10.6Cr considering stoichiometric oxides [169 -170]

Alloy	Cr	Mo	C	Ni
301	16-18%	N/A	<0.15%	6-8%
304	17.5-20%	N/A	<0.8%	8-11%
316L	16-18.5%	2-3%	<0.03%	10-14%
321	17-19%	N/A	<0.8%	9-13%
AL6XN	20-22%	6-7%	<0.3%	23.5-25.5%

Table 5.6.4.1: Comparison of Cr, Mo, C and Ni content for common austenitic steels [169]

Since a thick passive protective layer can also be deposited on the surface of these alloys using high Cr containing paints, non-stainless steels are being considered more and more for corrosive environments.

Intergranular (IG) corrosion is one of the primary concerns governing the amount of carbon in the new alloy designs. This is a form of relatively rapid and localized corrosion associated with a defective microstructure such as carbide precipitation. When austenitic steels have been exposed for a period of time in the range of approximately $500^{o}C$ – $850^{o}C$, or when the steel has been heated to higher temperatures and allowed to cool through that temperature range at a relatively slow rate (such as occurs after welding or air cooling after annealing), the chromium and carbon in the steel combine to form chromium carbide particles along the grain boundaries throughout the steel. Formation of these carbide particles in the grain boundaries depletes the surrounding metal of chromium and reduces its corrosion resistance, allowing the steel to corrode preferentially along the grain boundaries. Steel in this condition is said to be "*sensitized*".

However formation of some carbide is allowed for grain refinement; in our case ~ 0.15wt% of FCC TiC is allowed to precipitate at austenizing temperature. Carbide precipitation depends heavily upon carbon content, temperature and time at temperature and steels with < 0.03 wt% carbon do not show this issue at all.

5.6.5 Non – Magnetism and Curie temperature

Having a non-magnetic behavior at a broad range of operating temperatures is a very important requirement for any naval hull steel and hence it is important to determine the Curie temperature of our designed alloy compositions. Curie temperature defines the limit of Ferro-magnetism in

materials and as the temperature is increased towards the Curie point (T_C), the alignment (magnetization) within each magnetic domain decreases and so above T_C the material becomes paramagnetic. By using the γ (FCC Austenite) phase composition in CMD basic model and Mart5 database and using TC (FCC) as an extra CMD output, the Curie temperatures were obtained for each alloy. Table 5.6.5.1 lists the calculated Curie temperature for the new alloy compositions for BA120 and SA120 and compares them with those of EX425 TRIP prototype as well as the commercial A286 austenitic TRIP steel.

Alloys	A286	EX425	BA-120	SA-120
T_C	48.39 K	131.42 K	102.14 K	39.56 K

Table 5.6.5.1: Curie temperature of different Austenitic TRIP Steels

From table 5.6.2.1, it is seen that the Curie temperature is well below the limit of 300 K (Room temperature) for both our new alloys BA120 and SA120. So the behavior of the new alloys would be paramagnetic at use temperatures.

CHAPTER 6

NEW PROTOTYPE EVALUATION

Evaluation and characterization of the designed alloys BA120 and SA120 have been carried out to verify the various design models used in this research. The design models, for both strength and uniform ductility under tension and shear stress states, have been integrated via the Structure – Property – Performance relationships, as outlined in section 1.5. The quantitative evaluation of the new alloys will be used as added data points in improving our parametric models which can be used as basis for further design model improvements and calibrations and can be extended to shear and compressive loading states. The major evaluation parameters are the matrix stability (measurement of M_s^{σ} under uniaxial tension) and uniform ductility along with gamma prime precipitation strengthening. The composition of the alloy has been verified by an independent laboratory using spectroscopy and gas analysis. Composition analysis using 3-D LEAP tomography has also been performed at Northwestern University. Evaluation of microstructure and variation of microhardness with aging time and temperature have been done to study the austenite matrix and grain size characteristics. Most of the mechanical testing and analysis has been restricted to BA120. Due to improper conditioning of the SA120 during forging post homogenization, the presence of cracks and high number density of inclusions is seen which led to premature fracture of the SA120 tensile specimens. However, nanoscale 3-D LEAP tomographic analysis of the gamma prime distribution in austenite matrix for both alloys BA120 and SA120 has confirmed the presence of adequate precipitate phase fraction at equilibrium.

6.1 Materials

The composition of the two alloys BA120 and SA120, as shown earlier in table 5.5.2, have been conceptualized using parametric models developed from experimental data points obtained by the characterization of an earlier designed austenitic TRIP steel EX425. The specific goal of the designs is to have a stress - assisted martensitic transformation at an optimum pre-determined temperature so as to result in maximization of uniform ductility at room temperature, while maintaining a high strength level at he same time. *Smart Metals (SAES) Corporation* at New Hartford produced the two alloys as 300 lb heats each of 8" diameter ingots by multiple melting techniques using Vacuum Induction Melting (VIM) of raw virgin materials followed by Vacuum Arc Remelting (VAR), according to the specifications in tables 6.1.1 and 6.1.2.

Element	min	Target	max
Carbon	--	0.01	0.02
Manganese	--	--	0.1
Silicon	--	--	0.1
Copper	--	--	0.01
Phosphorus	--	--	0.01
Sulfur	--	--	0.004
Chromium	3.8	4.0	4.2
Nickel	23.5	23.6	23.9
Molybdenum	1.1	1.2	1.3
Vanadium	0.29	0.3	0.31
Titanium	2.8	3.0	3.2
Aluminum	0.14	0.16	0.18
Boron	0.01 (100 ppm)	0.0125 (125 ppm)	0.015 (150 ppm)
Oxygen	--	--	0.0040 (40 ppm)
Nitrogen	--	--	0.0040 (40 ppm)
Other Tramp:	--	--	0.002 (each)

Table 6.1.1: Specified composition and variance for each component for BA120

Element	min	Target	max
Carbon	--	0.01	0.02
Manganese	--	--	0.1
Silicon	--	--	0.1
Copper	--	--	0.01
Phosphorus	--	--	0.01
Sulfur	--	--	0.004
Chromium	9.6	9.8	10.0
Nickel	14.3	14.4	14.6
Molybdenum	1.1	1.2	1.3
Vanadium	0.30	0.31	0.32
Titanium	3.6	3.8	4.0
Aluminum	0.19	0.21	0.23
Boron	0.01 (100 ppm)	0.0125 (125 ppm)	0.015 (150 ppm)
Oxygen	--	--	0.0040 (40 ppm)
Nitrogen	--	--	0.0040 (40 ppm)
Other Tramp:	--	--	0.002 (each)

Table 6.1.2: Specified composition and variance for each component for SA120

Post secondary melting, the ingots were shipped to *Special Metals Corporation* unit at Huntington where the two alloy ingots were coated with anti-oxide barrier paint prior to homogenization to minimize oxidation and de-carburization. The 8" diameter ingots were homogenized at 1190^{o}C (2175^{o}F) for 24 hours. The temperatures were held within ± 1 hr followed by air cooling. Break down forging was conducted at temperatures below 2000°F (1093°C). Forging at the homogenization temperature is allowed but additional heating was done at a maximum temperature of 2000°F (1093°C). Forging of sizes smaller than 4.5 inch by 4.5 inch square (114 mm x 114 mm square) was conducted at temperatures below 1900°F (1038°C). No forging was allowed below 1700ºF (927ºC). Time at forging temperature was kept to a minimum to allow the forging sequence to be completed as quickly as possible. No furnace cooling was done during homogenization and forging. If the forging sequence is interrupted for a

prolonged time the material is air cooled to room temperature and reheated when the forging sequence continues. Upon completion of forging, the material was air cooled to room temperature. Rolling of the ingots was to be done to product sizes listed below in equal weight, to enable machining samples for all tests, including torsion/shear tests and FSI Ballistic tests.

1.25” x 12” x 12”, 1.0” x 12” x 12”, 0.25” x 12” x 12”

No final annealing or heat-treatment was done on these ingots. However, post forging and hot rolling, some cracking issues were observed in both alloys, although to a much more severe extent in the SA120. Figures 6.1.1 and 6.1.2 show the ‘as received’ materials from Special Metals Huntington for BA120.

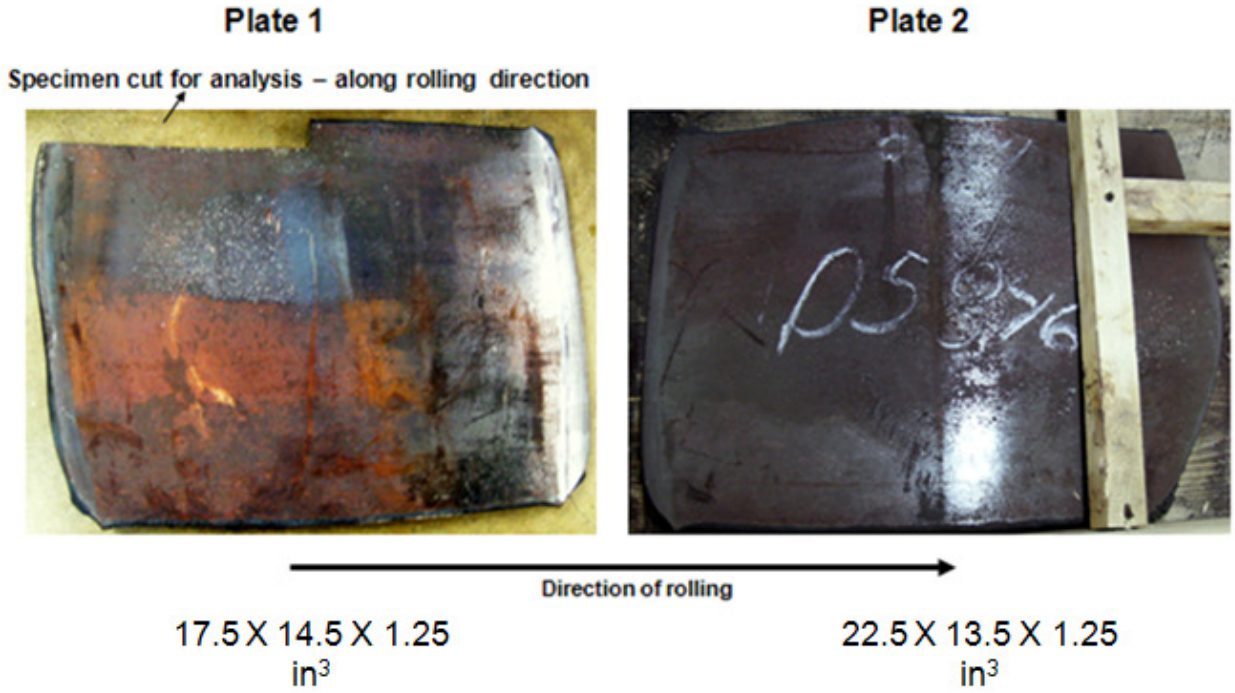

Figure 6.1.1: As-received plates of BA-120 with thickness 1.25 in

While forging and hot press of BA120 to plate/sheets was completed for two thickness levels 0.25” (for FSI tests) and 1.25” (for shear/torsion and other tests), it was observed during

machining of the plates that there was delamination of the sheets (cracking) in the plates with the lesser thickness of 0.25".

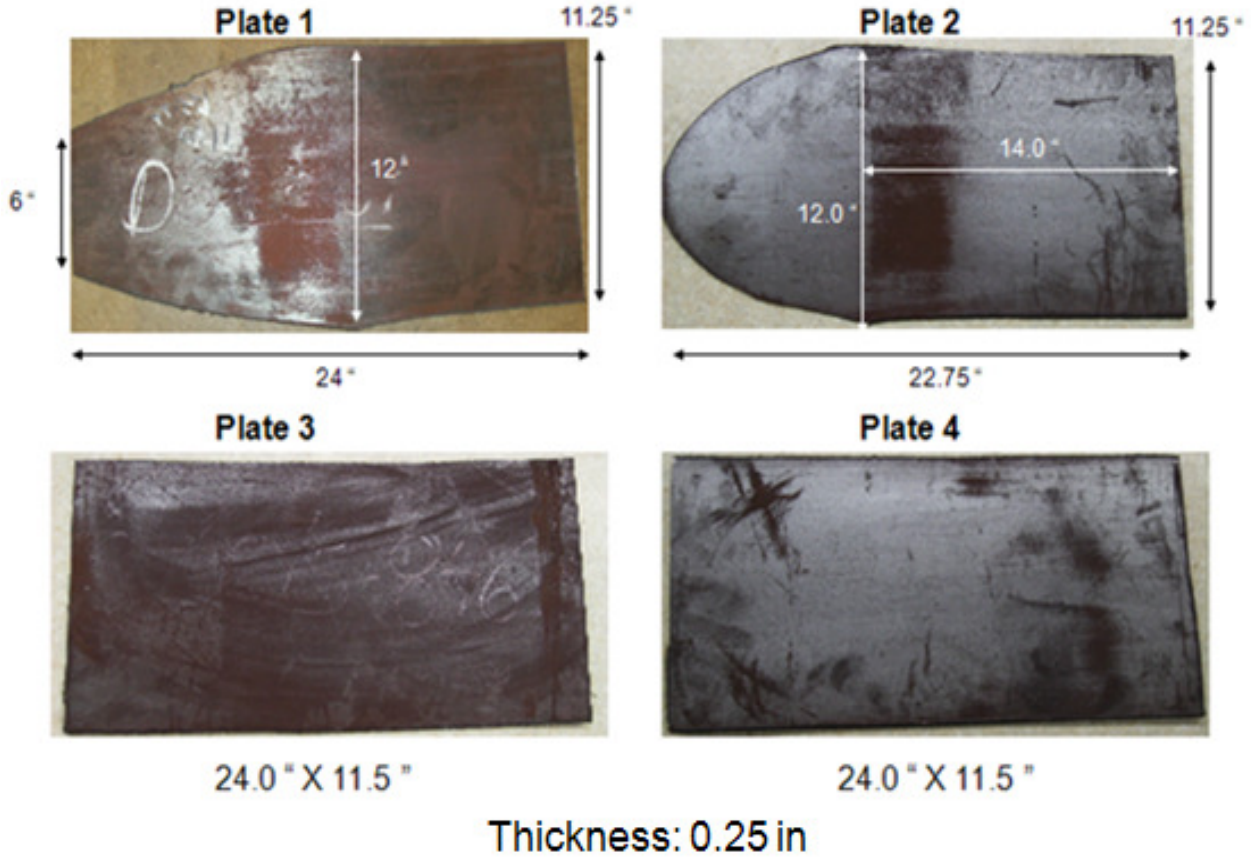

Figure 6.1.2: As-received plates of BA120 with thickness of ¼ in

Figure 6.1.3: Cut-off piece from the as-received plates of BA120 with thickness of ¼ in showing the delamination of the plates being held together by tape

The delamination in the thinner BA120 is thought to be a result of cold working (forging at temperatures lower than expected) leading to extreme high residual stress buildup in the thinner

plates. This is confirmed by the high Vickers microhardness values taken from the surface of the received samples. This is shown in figure 6.3.1.1 in section 6.3. There was no such observed defragmentation in the thicker BA120 plates and thus complete mechanical testing and evaluation of properties for BA120 has been possible.

For the SA120, as seen from figure 6.1.4, the rolling or hot pressing was not completed due to the observed cracks in the ingot which made the ingot bend during rolling. On a closer look at the crack surface, strands of metal are seen sticking out, which suggests some degree of localized melting. The cracks are thought to be caused due to incipient melting of the alloy, possibly due to forging at temperatures close to the melting point of the alloy. On further evaluation upon cutting the large SA120 ingot block into smaller pieces, a large number of inclusions and small cracks were found in the material throughout the interior.

Figure 6.1.4: As-received ingot of SA-120 showing incipient melting and wide-cracks

The calculated equilibrium melting point of the alloys BA120 and SA120 are 1500^{o}C and 1423^{o}C respectively, as compared to 1525^{o}C for EX425. This is calculated from Thermo-Calc by obtaining the temperature where there is only LIQUID phase in equilibrium in the system (both

FCC (TiC and Austenite) as well as Gamma Prime phase fractions are already zero). These values are much higher than the maximum forging temperature of 1190^{o}C. So the condition of the SA120 ingot is most likely associated with the non-equilibrium solidification segregation, due to which the evaluation of this prototype SA120 is limited.

6.2 Composition Analysis and Verification

During VIM/VAR process, the composition specifications have been set to meet the requirements of AMS 2248. No variation is permitted for oxygen and nitrogen. Due to the cracking issue stemming from improper homogenization and forging of the alloys post arc-remelting, it is important to determine the composition uniformity of the materials received. Two different methods of composition analysis have been used to verify the as received specimens –

6.2.1 Chemical Analysis using Spectroscopy

As received samples of both new alloys BA120 and SA120 were sent to *Evans Analytical Group (EAG Labs)* in Syracuse, NY for materials characterization and composition analysis. Interstitial Gas Analysis (IGA) has been used to determine the amounts of C, S, N and O in the alloys while Inductively coupled Plasma-Spectroscopy (ICP) was used to determine the amounts of bulk elements like Fe, Ni, Cr, Ti, Mo, V and Al. For high accuracy of Boron detection, a plasma emission spectroscopy with ICP (ICP-OES) has been used. In the IGA method, the specimens are rapidly heated in high temperature furnaces to convert then in volatile gaseous forms which assist in separating them from the mixture and measure them. Carbon and sulfur mass fractions are measured based on combustion and infrared technology. The analytical method is based on the complete and instantaneous oxidation of the solid sample by combustion in oxygen (above

2000°C). Nitrogen, Oxygen and Hydrogen mass fractions in solid samples are evaluated using the principles of inert gas fusion or solid carrier gas heat extraction. Inductively Coupled Plasma Spectroscopy techniques are the so-called wet-sampling methods whereby samples are introduced in liquid form for analysis. In plasma emission spectroscopy (OES), a sample solution is introduced into the core of inductively coupled argon plasma (ICP), which generates temperature of approximately 8000°C. At this temperature all elements become thermally excited and emit light at their characteristic wavelengths which can be analyzed using a spectrometer. Table 6.2.2.1 shows the comparison of the desired (designed) compositions and the measured compositions (by EAG labs and by 3D-LEAP tomography) for both BA120 and SA120.

6.2.2 Composition analysis using 3D – LEAP

The 3-D Local Electrode Atom probe at the Northwestern University Centre for Atom Probe Technology (*NUCAPT*) has been used to study the composition of the matrix austenite phase after solution treatment (950^{o}C for 1 hr) and quench. 2-D cylindrical profiling parallel to the z-axis direction has been used to define the volume of analysis. Table 6.2.2.1 shows the comparison of the desired (designed) compositions and the measured compositions (by LEAP) for both BA120 and SA120.

	Alloys					
	BA120 (wt%)			SA120 (wt%)		
Components	Designed	LEAP (Solution Treated)	Spectroscopy (EAG)	Designed	LEAP (Solution Treated)	Spectroscopy (EAG)
Fe	67.82	68.28 ± 0.15	68.29	70.25	71.03 ± 0.23	70.25
Al	0.16 ± 0.021	0.152 ± 0.013	0.15	0.21 ± 0.02	0.189 ± 0.02	0.211
Ti	3.00 ± 0.22	2.90 ± 0.24	2.97	3.80 ± 0.20	3.45 ± 0.14	3.79
Ni	23.50 ± 0.11	23.0 ± 0.07	23.00	14.40 ± 0.10	14.20 ± 0.12	14.40
Cr	4.00 ± 0.20	4.11 ± 0.11	4.08	9.80 ± 0.20	10.01 ± 0.15	9.88
Mo	1.20 ± 0.12	1.18 ± 0.12	1.20	1.20 ± 0.10	1.19 ± 0.05	1.15
V	0.30 ± 0.011	0.30 ± 0.04	0.29	0.31 ± 0.01	0.31 ± 0.05	0.30
B	0.0125 ± 0.0.002	-	0.0046	0.0125 ± 0.0.002	-	0.0052
C	0.01 (+ 0.01)	-	0.0082	0.01 (+ 0.01)	-	0.0014
N	0.001 (+ 0.003)	-	< 0.001	0.001 (+ 0.003)	-	0.0024
O	-	-	0.0017	-	-	0.0068
S	-	-	0.0032	-	-	0.0032

Table 6.2.2.1: Comparison of the designed and measured alloy compositions for BA120 and SA120. The measured compositions have been obtained using LEAP as well as Spectroscopy analysis by EAG Shiva Technology Labs.

From table 6.2.2.1 it is seen that there is a good composition match for the new alloys with the designed concentration of individual components, for both BA120 and SA120. However, the measured Boron from ICP Spectroscopy analysis shows that for both BA120 and SA120, the boron content is much lower than the desired amount of 125 ppm. Table 6.2.2.2 shows the results of trace element analysis done by Special Metals during post arc-melting of the alloys.

	C		N		O		S	
Wt %	Desired	Measured	Desired	Measured	Desired	Measured	Desired	Measured
BA120	0.01	0.008	Max 0.004	0.0005	Max 0.004	0.0014	-	0.0031
SA120	0.01	0.009	Max 0.004	0.0006	Max 0.004	0.0027	-	0.003

Table 6.2.2.2: Comparison of the desired and measured concentrations of trace elements C, N, O and S by Special Metals, Huntington during Alloy melting

6.3 Surface Characterization

Since cracking and defragmentation has been observed in the 'as received' materials, it is important to study the surface characteristics of both alloys to investigate any abnormality in its compositions or properties or presence of unwanted inclusions etc. Surface micro-hardness measurements as well as light optical microscopy have been done on the surface of the 'as received' materials.

6.3.1 Micro-hardness measurements

For the BA120, fragmentation of the plates has been seen as an issue caused probably due to cold working (forging at lower temperatures than expected) which would lead to build up of high stresses within the plates. Vicker's micro hardness measurements were taken on specimens cut

from the surface of both BA120 (both 1.25' and 0.25' plates) and SA120 '*as-received*' plates and compared with the micro hardness measurements of solution treated fully austenitic specimens of EX425, BA120 and SA120 to evaluate the extend of residual stresses. Figure 6.3.1.1 shows the comparative results of the micro hardness tests on the aforementioned specimens.

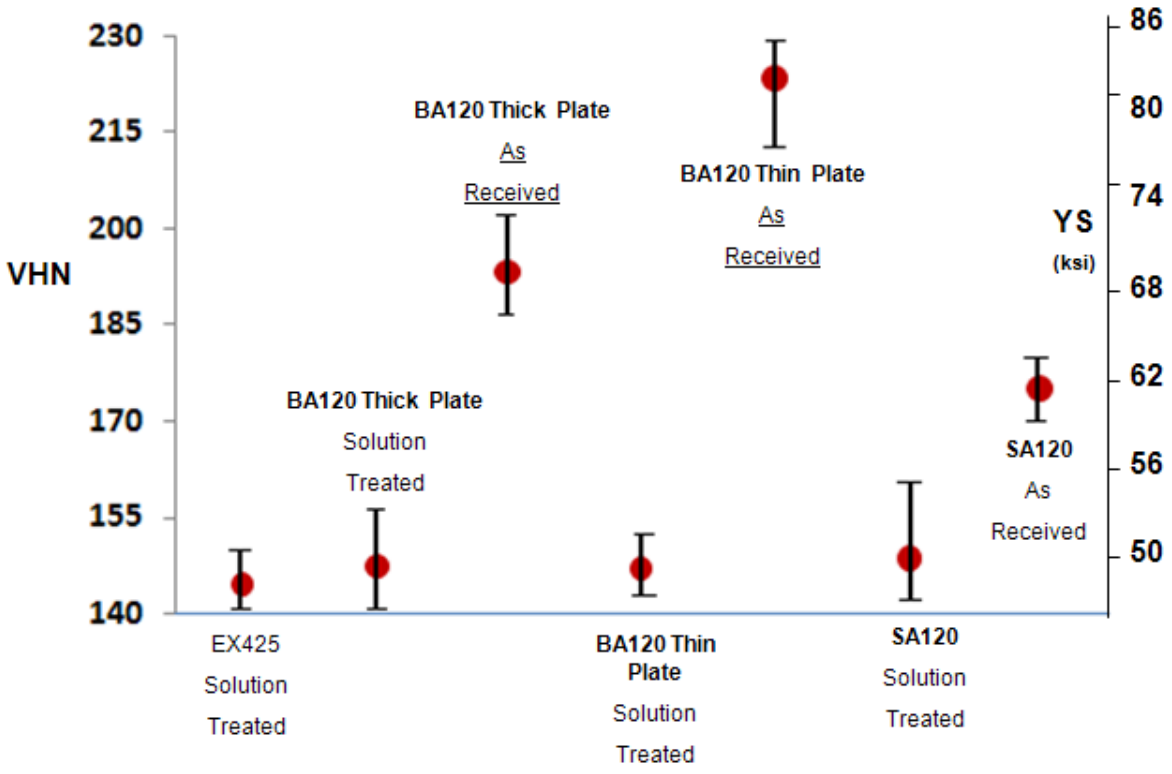

Figure 6.3.1.1: Comparison of the measured surface microhardness for 'as-received' and solution treated specimens of BA120, SA120 and EX425 to compare the relative internal stress build up during forging/rolling in new alloys.

It is seen clearly from the figure 6.3.1.1 that the surface hardness of the material increases with increased cold rolling (lower thickness of plates → higher the hardness). It is also observed that post solutionizing treatment and quenching, the hardness numbers for BA120 and SA120 are close to those expected for a fully austenitic sample, similar to EX425 of 145-150 VHN (~ 48-

50ksi). Austenizing heat treatment at 950^{o}C for 10 hours relieves the stresses built up within the materials. As expected, the BA120 plates of thickness ¼' show the maximum residual stresses due to the high degree of rolling. SA120 does not show presence of much residual stresses due to the incomplete forging/rolling process.

A time – temperature study of the Vickers micro hardness was also done for BA120 to evaluate the variation of hardness and expected yield strength with aging time. The specimens were first solution treated at 950^{o}C for 1 hour and quenched in oil. Then aging was done at a constant temperature of 750^{o}C while the time of aging was varied at 0 hours, 1 hr, 5 hr, 10hr and 20 hours. All heat treatments have been performed under vacuum to avoid surface oxidation. Figure 6.3.1.2 shows the hardness trends measured for BA120 and SA120 specimens in a dual-axis plot along with the expected yield strength numbers determined from the VHN data by using the equation 3.3.1 in section 3.3.

It is observed that a peak hardness of 316 VHN leading to expected yield strength of 124 ksi (855 MPa) is obtained at the aging time of 10 hours, which is close to the expected value from our time – temperature kinetics model, based on optimizing the gamma prime precipitate radius to yield peak hardness. The estimated yield strength of 124 ksi (MPa) is slightly higher than the designed room temperature BA120 yield strength of 120 ksi (MPa).

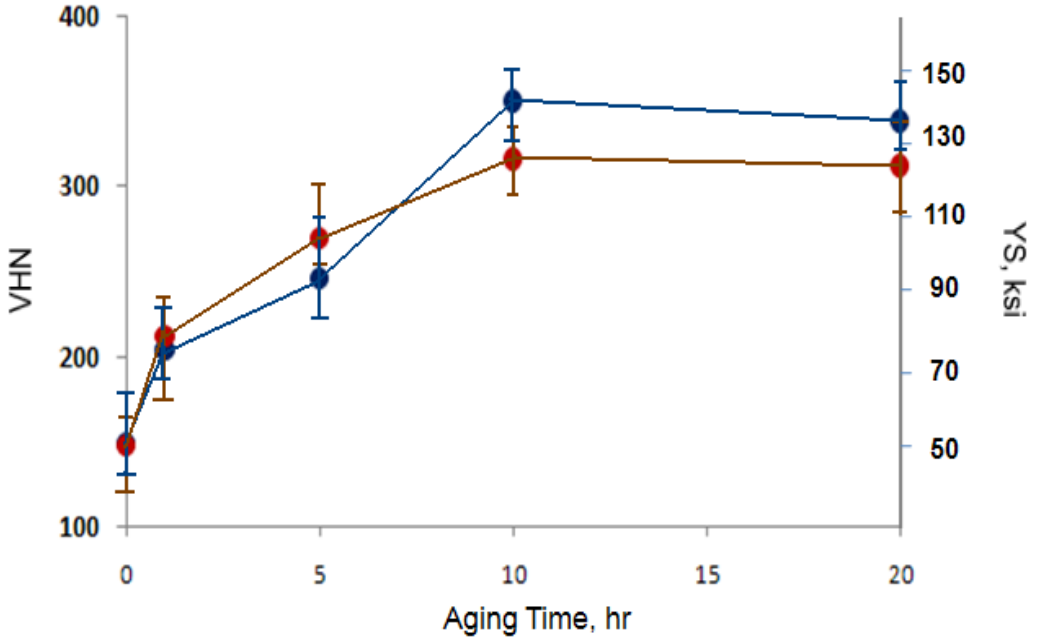

Figure 6.3.1.2: Aging time dependence of surface Vickers Microhardness of for BA120 and SA120 specimens solution treated at 950°C for 1 hr and then aged at 750°C

The measured microhardness (350 VHN) and corresponding yield stress (140 ksi/965 MPa) for SA120 for the standard aging time of 10 hours is higher than that of BA120 as well as the expected value. For both alloys, it is confirmed that the design aging time of 10 hours leads to peak hardness.

6.3.2 Optical Microscopy of Sub-Surface

Light Optical microscopy was done on the etched surface of the BA120 and SA120 specimens post solutionizing heat treatment and quench. The major intent on studying the microstructure of the BA120 solutionized and quenched specimen was to verify the austenite grain structure and size and compare it with those of EX425 to evaluate optimum refinement of grains. Figures 6.3.2.1 and 6.3.2.2 show the austenite grains for the two alloy designs BA120 and SA120 respectively.

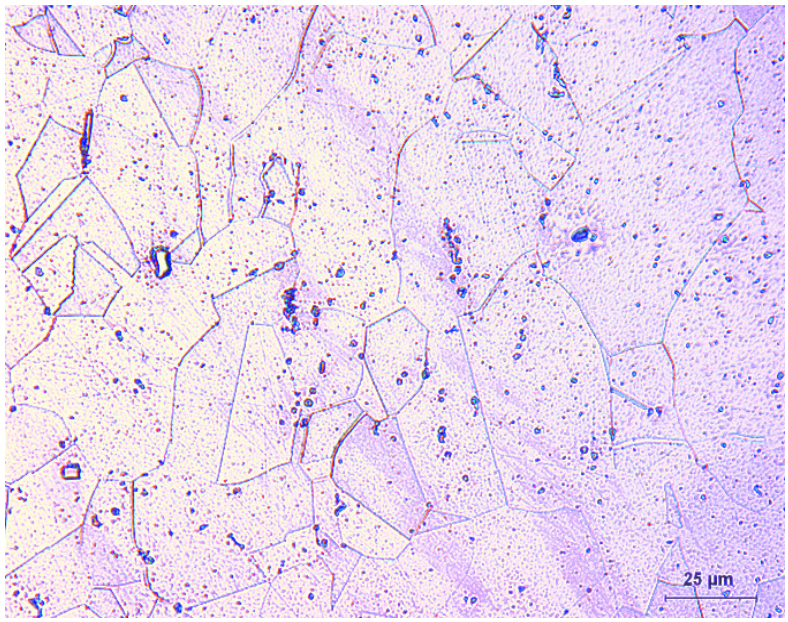

(a)

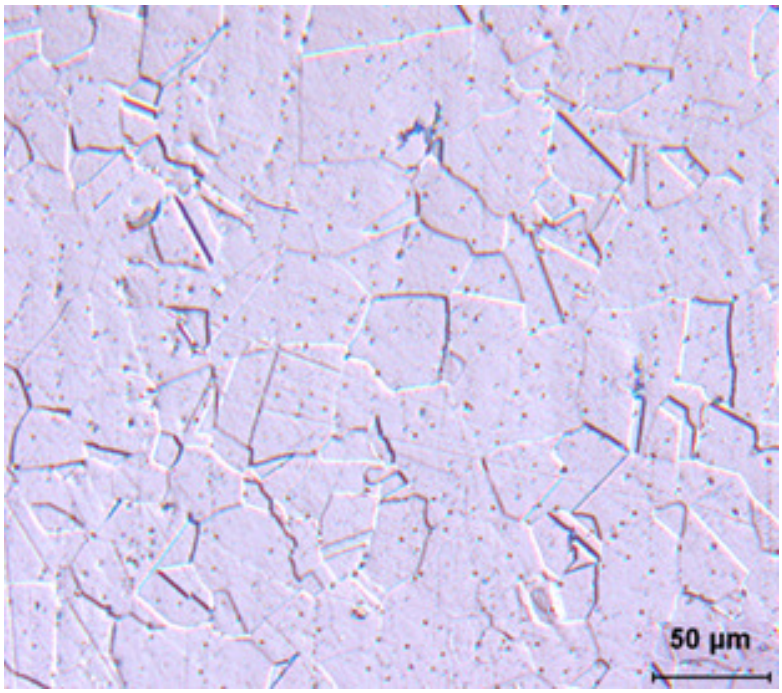

(b)

Figure 6.3.2.1: Optical microscopy of solution treated fully austenitic microstructure of BA120 using a) light etching with 2% Nital showing austenite grain boundaries and b) etching with 10% Nital to show formation of twinned austenite grains

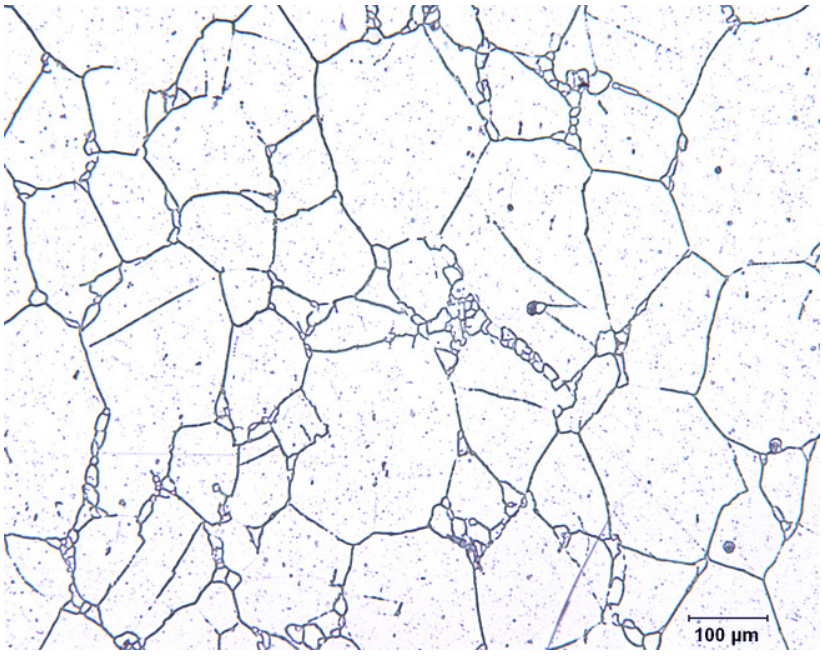

(a)

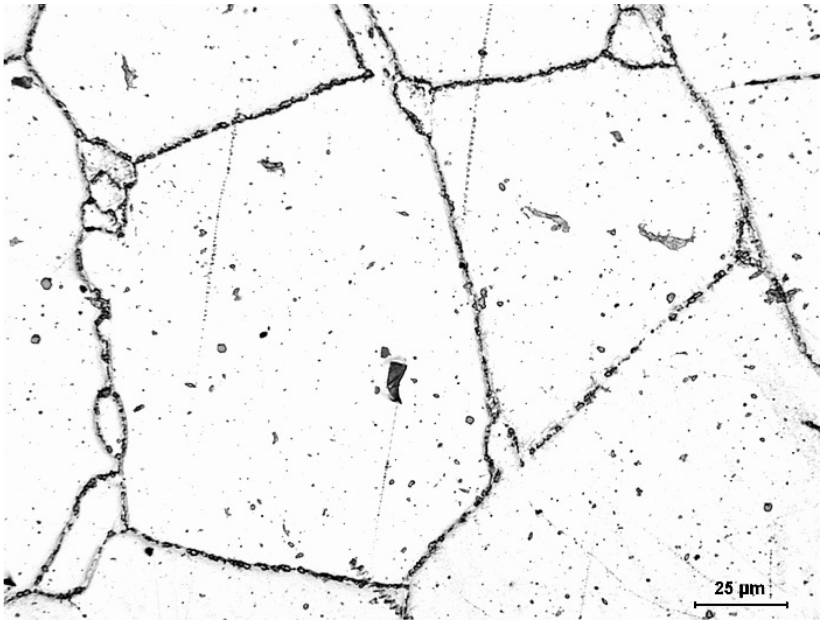

(b)

Figure 6.3.2.2: Optical microscopy of solution treated fully austenitic microstructure of SA120 using light etching with 2% Nital showing austenite grain boundaries a) magnification of 25X and b) magnification of 100X

From figures 6.3.2.1 and 6.3.2.2 it is seen that the diameter of austenite grains of BA120 are smaller than for SA120. SA120 shows a high segregation of smaller austenite grains (d < 10 μm) near the boundary of larger grains (d ~ 100 μm). While BA120 average austenite grain diameter is limited to ~ 40 - 50 μm, the average grain size for SA120 is > 75 μm.

6.4 3-D LEAP (Atom Probe) Tomography

3-D Local electrode Atom Probe Tomography has been used to characterize the nano-scale γ' – precipitates within the austenite matrix for both prototypes BA120 and SA120. This is an extremely important tool to determine the size and distribution of the precipitates in the aged alloy. Accurate compositional analysis has also been done by measuring the proximity histogram [152] for the TiNi Iso-concentration surfaces. Calculation of volume fraction of precipitate and their number density is done using precipitate phase separation by Envelop method [151].

6.4.1 Precipitate Analysis

BA120 blocks were solution treated at 950^{o}C (1 hr) and aged at 750^{o}C for 10 hours. Then small blanks measuring 1mm in thickness and 1cm in length were cut. The tips for the LEAP were prepared using the same technique used for EX425 and described in detail in section 3.3.9.3 and figure 3.3.9.4. Laser mode of LEAP operation was used to determine the γ'-phase distribution, at an operating temperature of 60K and Pulse energy of 0.6 nJ. The laser pulse rate used was 500 kHz which allows for a larger cross-section of volume to be analyzed. Figure 6.4.1.1 show the γ' within the austenite matrix in an aged BA120 specimen. The gamma prime precipitates in figure 6.4.1.1 are represented by the red iso-surfaces for 50% TiNi concentration boundaries. The background austenite matrix is represented by the predominant Fe and Ni ions. The size and

distribution of the gamma prime (red spheroids) within the austenite matrix is very similar to that of EX425 for its standard aged specimens.

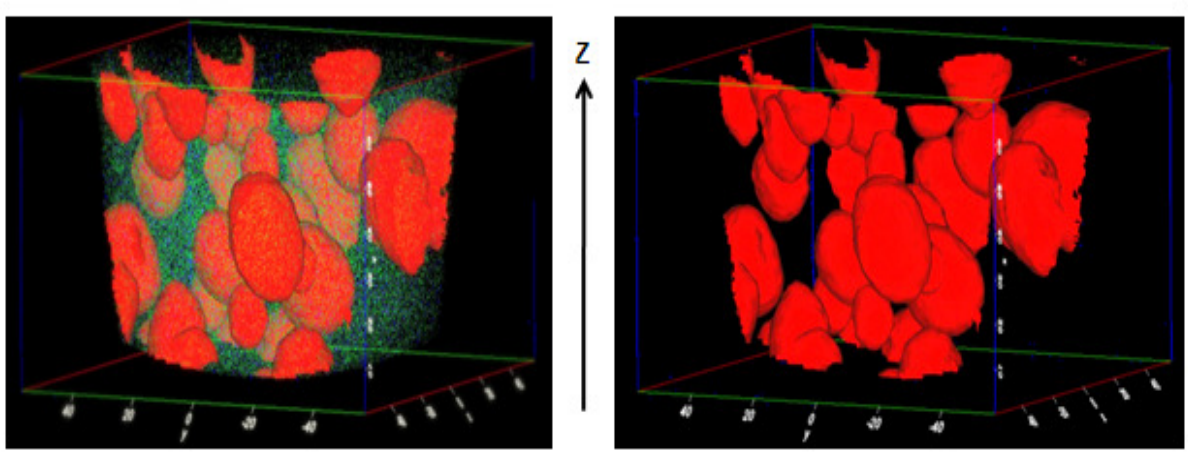

Figure 6.4.1.1: 3-D LEAP reconstructed image of the distribution of Gamma Prime γ' precipitates (Red) within the austenite matrix for BA120. The γ' precipitates are separated from the matrix by an iso-concentration surface defined by a 50% TiNi concentration boundary. **[**40 M ions**]** [80nm X 80nm X 70nm]

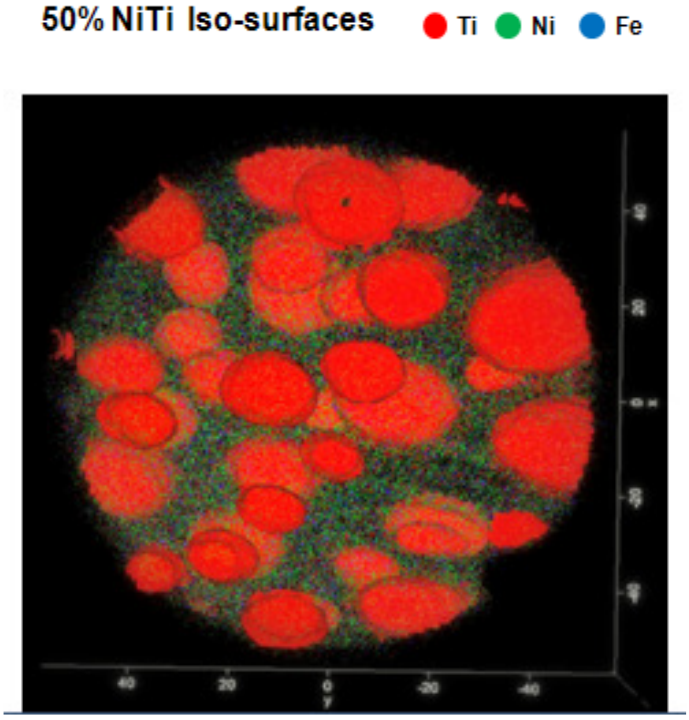

Figure 6.4.1.2: (a) A 2D view of the Gamma Prime γ' precipitates (Red) within the austenite matrix, as viewed along the Z-axis for BA120

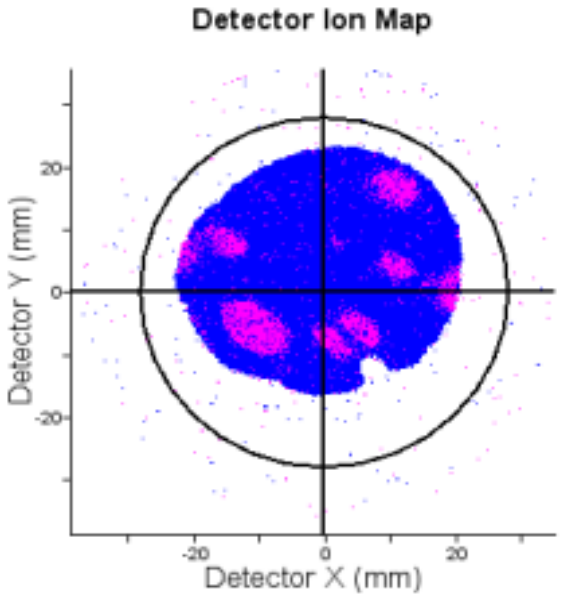

(b)

Figure 6.4.1.2: (b) live image recorded during actual LEAP run showing the Detector Ion map. The evaporation of ions from the Gamma Prime γ' precipitates (pink) within the Blue Fe ions of austenite matrix is clearly demonstrated

The composition Proxigram is computed for all interfaces marked by the iso-concentration surfaces. Figure 6.4.1.3 shows the Proxigram concentration profile for Fe, Ni, Cr and Ti ions.

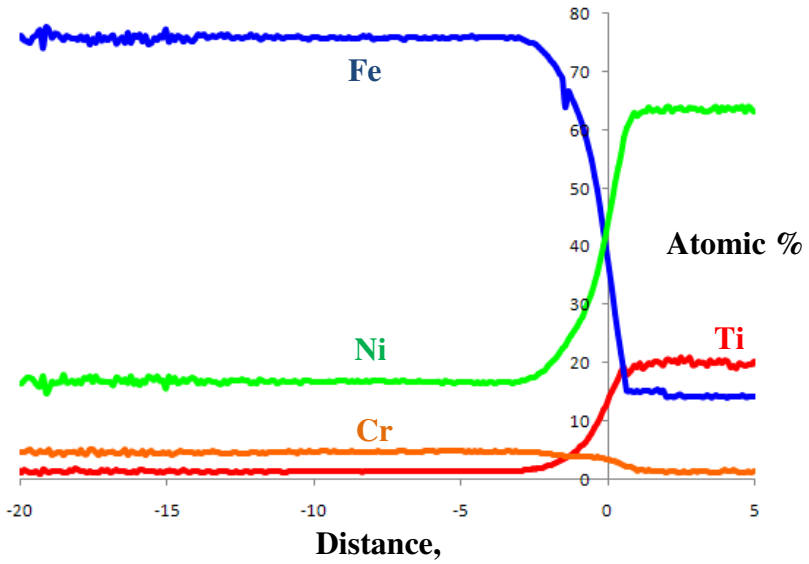

Figure 6.4.1.3: Proxigram analysis of BA120 for all TiNi interfaces shown in figure 6.4.1.1

Using the Envelope method, described in detail in Appendix I, the gamma prime precipitates can be separated into clusters of Ti ions and each cluster would represent one single precipitate. Thus each precipitate can be analyzed for its compositions. The average of concentrations across precipitates can also be taken as a measure of the gamma prime overall composition. Figure 6.4.1.4 shows the creation of clusters using envelope program.

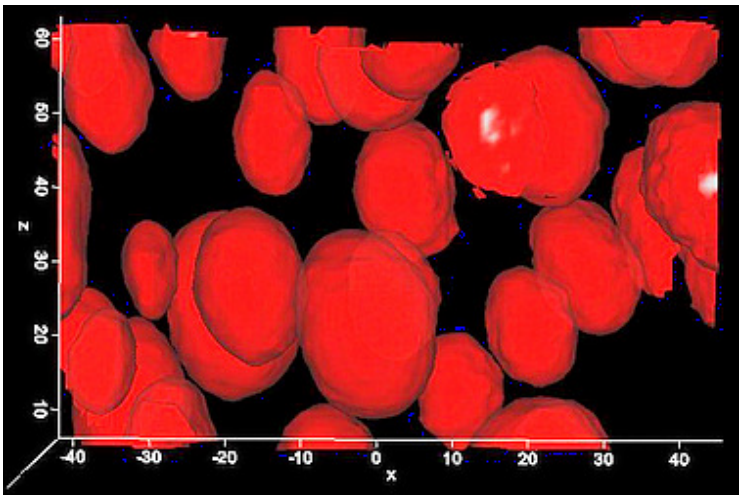

(a)

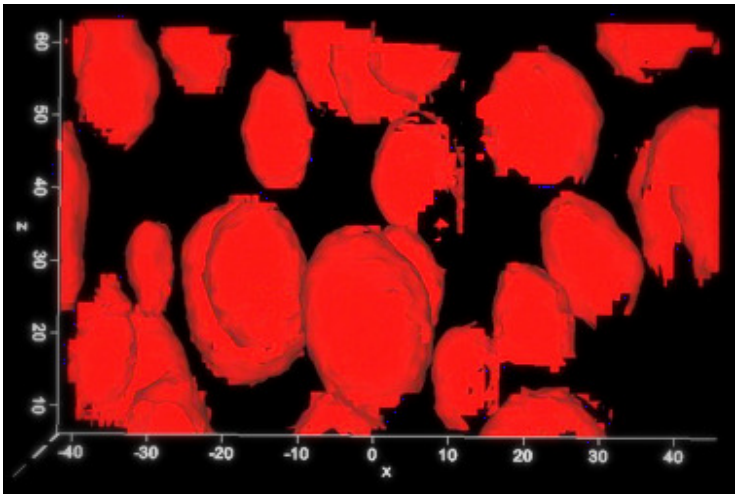

(b)

Figure 6.4.1.4: Comparison of the effectiveness of Envelope algorithm in separating clusters matching the original iso-concentration surfaces: **a)** 3D reconstructed image from LEAP for isolated **50% TiNi iso-concentration surfaces** from figure 6.4.1.1 **b)** Reconstructed Clusters of Ti with separation distance of 50 using the Envelope Program

The accuracy of the envelope program setting can be determined by comparing the clusters formed by the program with the original iso-concentration surfaces created by the IVAS analysis software. Figure 6.4.1.4 shows all precipitates recreated with high accuracy. To determine the volume fraction of precipitates using the envelope program, the number of atoms within the clusters is measured and compared to the total number of atoms in the whole analysis volume.

The ratio between the number of atoms within the clusters and total number of atoms in the whole analysis volume is the calculated volume fraction of Gamma Prime in the system. Thus,

$$Volume\ fraction\ _{\gamma'} = \frac{\{No.of\ atoms\ in\ Clusters\}}{\{Total\ no.of\ atoms\}} \tag{6.4.1}$$

The number density of the precipitates can be determined by taking the ratio of the number of clusters identified by the program having a minimum critical diameter and the effective volume of the sample size.

$$Number\ Density, N_v = \frac{\{No.of\ Clusters\}}{\{Effective\ Volume\}} \tag{6.4.2}$$

Or, mathematically,

$$Number\ Density, N_v = \frac{\{No.of\ Clusters\} \times \varphi}{\{Total\ no.of\ atoms \times Average\ Atomic\ Volume\}} \tag{6.4.3}$$

Where φ is the detection efficiency of a single ion detector, the value of which is 0.5 - 0.6. Table 6.4.1.1 lists the quantities Volume Fraction, Number density and diameter of the gamma prime precipitates in the matrix at equilibrium post aging at 750^{o}C for 10 hours, for both BA120 and SA120.

Two separate experimental runs were done to validate the bigger gamma prime precipitates observed in case of SA120. Figures 6.4.1.5 and 6.4.1.6 show the distribution γ'-precipitates

within the austenite matrix in an aged SA120 specimen for the first and the second experimental runs respectively. Laser evaporation of ions was used with other LEAP parameters being same as in BA120 as well as EX425.

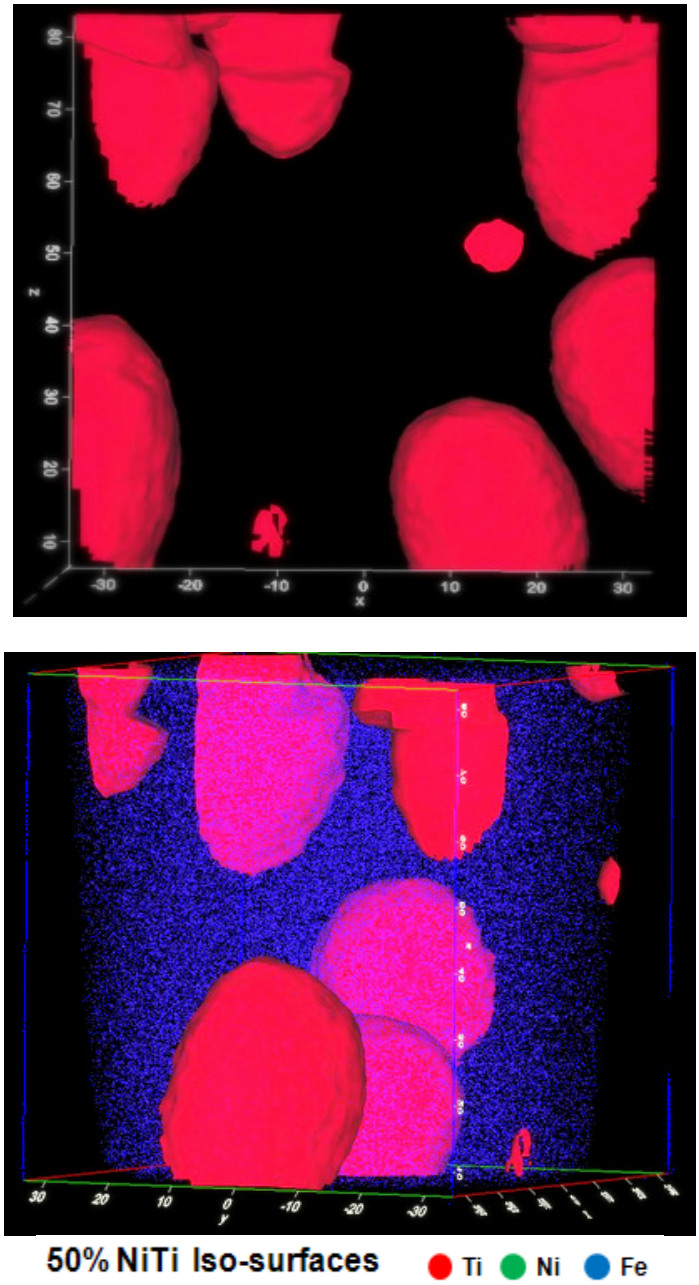

Figure 6.4.1.5: 3-D LEAP reconstructed image of the distribution of Gamma Prime γ' precipitates (Red) within the austenite matrix for SA120. The γ' precipitates are separated from the matrix by an iso-concentration surface defined by a 50% TiNi concentration boundary. **[**28 M ions**]** [70nm X 70nm X 70nm]

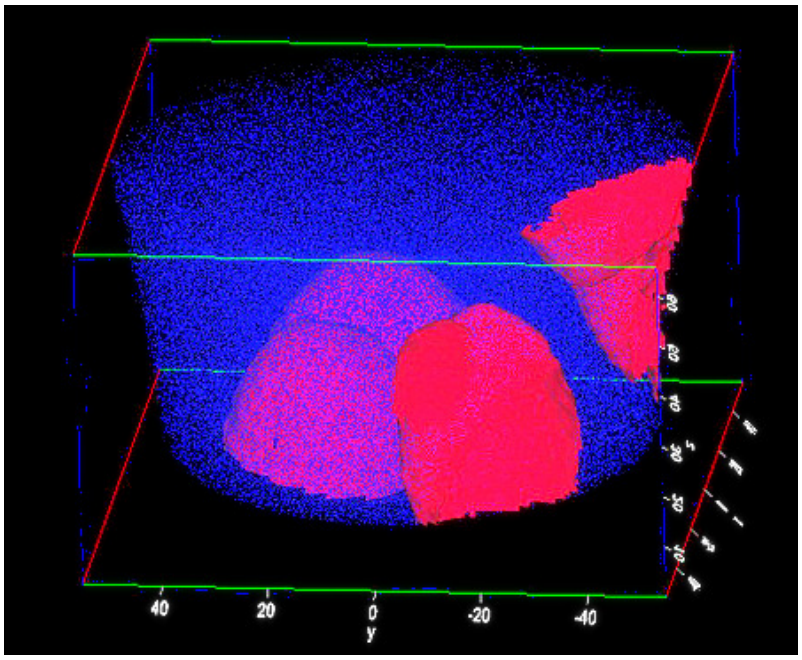

(a)

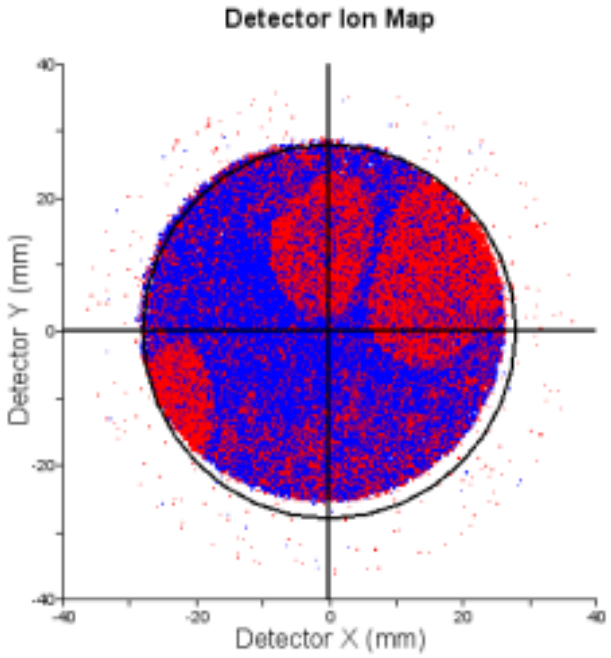

(b)

Figure 6.4.1.6: A 3D view of the Gamma Prime γ' precipitates (Red) within the austenite matrix as viewed along the Z-axis [25 M ions], and **(b)** live image recorded during actual LEAP run showing the Detector Ion map. The evaporation of ions from the Gamma Prime γ' precipitates (pink) within the Blue Fe ions of austenite matrix is clearly demonstrated

From figures 6.4.1.4 and 6.4.1.5 it is clearly seen that the gamma prime precipitates are much larger in size and lower in number density in terms of distribution, as compared to that of BA120 as well as EX425. This can be observed by the comparison of the precipitates observed during the actual running of the LEAP experiment for SA120 and BA120 from the detector ion maps in figures 6.4.1.6 (b) and 6.4.1.2 (b) respectively. The observed large precipitate size may be attributed to overaging – leading to lower number density of precipitates and lower hardness in the material. Proxigram analysis of the composition variation of the components was done and shown in figure 6.4.1.7. The compositions are listed in section 6.4.2. It is interesting to note that the precipitate sizes are comparable to the '*eta* - η' phase precipitates observed in EX425 on prolonged aging at lower temperatures. Due to the high chromium and lower Ni content in the SA120 prototype, the size and distribution of the gamma prime precipitates is affected. The volume fraction, number density and diameter of the gamma prime precipitates is compared in table 6.4.1.1 with that of BA120.

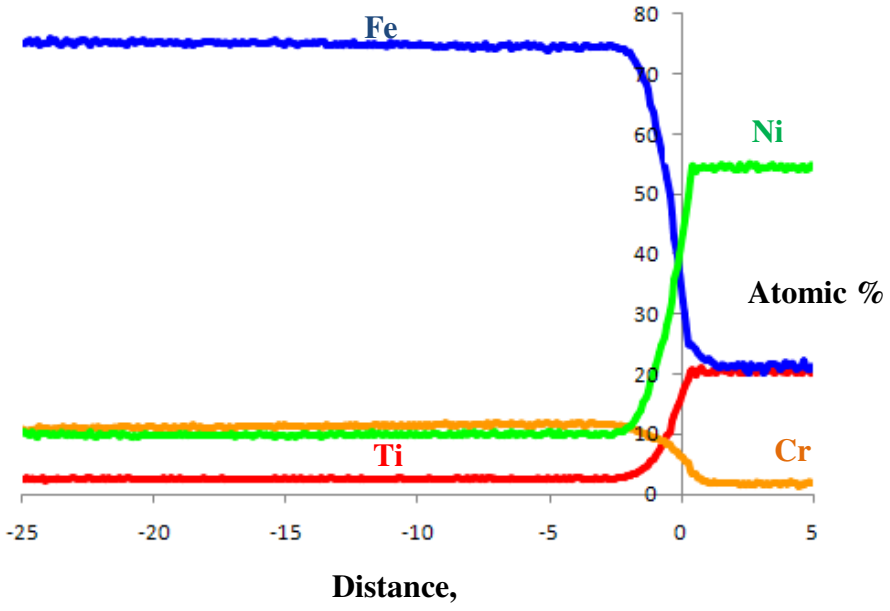

Figure 6.4.1.7: Proxigram analysis of SA120 for all TiNi interfaces shown in figure 6.4.1.5

γ' (Gamma Prime)	BA120	SA120
Average Diameter, nm	15.2	26.4
Measured Volume Fraction	0.102	0.094
Number Density, m^{-3}	2.33×10^{23}	8.16×10^{22}

Table 6.4.1.1: Comparison of properties of Gamma Prime precipitate distribution for BA120 and SA120 specimens aged at 750°C for 10 hours

6.4.2 Composition Validation

The average matrix and precipitate concentration near the matrix/precipitate interface has been measured by the proximity histogram or the Proxigram method [152]. Throughout the current research, all iso-concentration surfaces of bins have been created for TiNi concentration limit of 50%, within and outside the precipitates. As in all Proxigram profile figures before, the negative values of distance in the X-axis represent the matrix region while the positive values of the X-axis represent the precipitate region. The intersection point however is not an accurate measure of the interface composition. The slope of the concentration in the interface should ideally be sharp, however in most cases, a gradual slope is seen. This may be attributed to ion trajectory overlap. Tables 6.4.2.1 and 6.4.2.2 list the composition of various components in the gamma prime precipitates and the matrix respectively for BA120 and SA120 specimens aged at 750°C for 10 hours. The austenite composition has been derived from the proxigram profiles shown in section 6.2.2 for BA120 and SA120.

γ'	BA120	SA120
Calculated	$(Ni_{0.79}Fe_{0.20}Cr_{0.01})_3 (Ti_{0.95}Al_{0.05})$	$(Ni_{0.69}Fe_{0.30}Cr_{0.01})_3 (Ti_{0.94}Al_{0.06})$
Measured	$(Ni_{0.80}Fe_{0.18}Cr_{0.02})_3 (Ti_{0.96}Al_{0.04})$	$(Ni_{0.71}Fe_{0.27}Cr_{0.02})_3 (Ti_{0.96}Al_{0.04})$

Table 6.4.2.1: Gamma Prime precipitate composition for BA120 and SA120 specimens aged at 750°C for 10 hours

Atomic %	BA120		SA120	
Components	Calculated	Measured	Calculated	Measured
Fe	0.731	0.742 ± 0.0287	0.743	0.751 ± 0.0201
Ni	0.192	0.19 ± 0.0214	0.103	0.099 ± 0.0178
Cr	0.047	0.047 ± 0.0076	0.114	0.113 ± 0.0089
Ti	0.017	0.014 ± 0.0078	0.027	0.025 ± 0.0064
Al	0.002	0.0015 ± 0.0002	0.003	0.002 ± 0.0002
Mo	0.008	0.007 ± 0.0003	0.008	0.007 ± 0.0004

Table 6.4.2.2: Measured austenite matrix composition and concentrations of individual components compared to the calculated FCC Matrix composition from Thermo-Calc for BA120 and SA120 specimens aged at 750°C for 10 hours

From table 6.4.1.2 it is seen that there is a very good composition match for BA120 for the measured gamma prime composition with respect to the gamma prime composition calculated using Thermo-Calc for γ – γ' equilibrium at 750°C. However for the case of SA120, a higher amount of Ni and Ti is measured for the precipitate than predicted for γ – γ' equilibrium, and tending more towards a γ – η state rather than a γ – γ' equilibrium. However since mechanical

tensile tests could not be performed for SA120, the exact morphology of the precipitates seen cannot be confirmed without diffraction/TEM.

Using laser mode of evaporation of ions in the atom probe results in a very clear spectrum which yields low concentration variances while determining the composition of matrix or precipitates. For both BA120 and SA120 the matrix composition shows rich in Fe and lower in Ni, which is consistent with the results obtained for EX425. It has been observed that using Laser mode gives a very good match for Cr in the austenitic TRIP steels whereas for Voltage mode of ion evaporation, the Cr was always found to be depleted in the matrix.

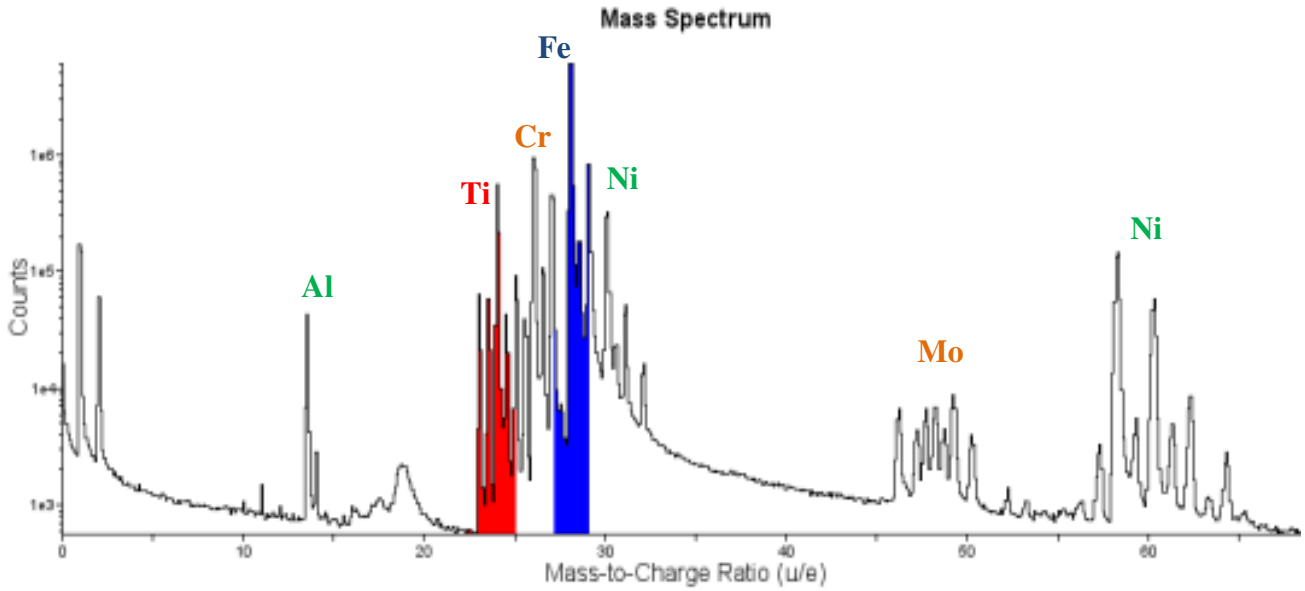

Figure 6.4.1.8: Observed mass spectrum for BA120 using laser mode for 3D-LEAP run at 60K and using 500 pulse rate and 0.6nJ of pulse energy for the laser beam

Mo and V concentrations are very stable for both materials and thus little variance in observed for those. Ti and Cr concentrations have often led to a slight mismatch due to one another since both share the common isotope of 25. However it has been observed over time that in Laser

mode of operation, Cr only exits in the isotopes states of 26 and 26.4. Figure 6.4.1.8 shows the observed mass spectrum for the laser mode of analysis for BA120 aged specimen. The mass spectrum obtained for laser operation of LEAP results in much sharper peaks as compared to voltage mode. H and He peaks are always observed in the system irrespective of the alloy content. As can be seen from the figure 6.4.1.7, all peaks of the common constituents of BA120 are seen in the spectrum, for Fe, Ni, Mo, Cr, Ti and Al. It has been noted that higher order peaks of Ni are observed only for laser mode and not for voltage method, and the intensity of the higher order peaks increases with increase in pulse energy of the laser beam.

6.5 Mechanical Testing

Isothermal static uniaxial tensile tests has been done for BA120 specimens aged at 750^{o}C for 10 hours to evaluate the variation of yield stress, UTS, uniform ductility and fracture strain at various test temperatures. These results have been compared to those of EX425 for performance evaluation. Dynamic (adiabatic) Kolsky bar tensile tests have also been done for BA120 specimens at room temperature for the same aging conditions and compared with those of the current HSLA100 in application in Navy's blast protection alloys. Shear/Torsion tests have been performed on the Kolsky bar setup for dynamic loading, and the performance of BA120 is evaluated at room temperature. The test processes and system setup have been discussed earlier in section 3.3.5 and 3.3.6. The specimen geometry and dimensions have been shown in figures 3.3.5.1, 3.3.5.3 and 3.3.6.1 for static, dynamic tensile and shear/torsion tests respectively. While using the intersection of linear fits to the measured σ – T curve from Isothermal tensile tests is a more accurate method of determining the M_s^{σ} temperature, it has also been measured using

Richman and Bolling's method as verification. Using the measured M_s^{σ} temperature for the alloys, the parametric model for austenite stability has been updated and presented in section 6.5.3. This would be used as a future reference for TRIP alloy designs and can be extended to shear and compression stress states as well.

6.5.1 Static Tensile Tests

Static tensile tests have been done on aged BA120 specimens at temperatures in the range -5^{o}C to 65^{o}C with an applied strain rate of 1mm/min. For temperatures below room temperature, liquid nitrogen gas is used to cool the specimen in an enclosed chamber upto the required temperature. The specimen geometry and dimensions are the same described in section 3.3.5 figure 3.3.5.1 and is same as used for EX425 static tensile tests. All static tensile tests have been performed by using an extensometer fitted to the gage length section of the tensile specimens to enable actual strain measurements of the specimen gage, like in EX425, instead of using the crosshead displacement. The extensometer gives the correct values for the calculation of true stress-strain response of the specimen for the tensile test. Figure 6.5.1.1 shows the true stress – true strain curves for the tensile tests conducted at various temperatures; all specimens aged at the same temperature of 750^{o}C for 10 hours.

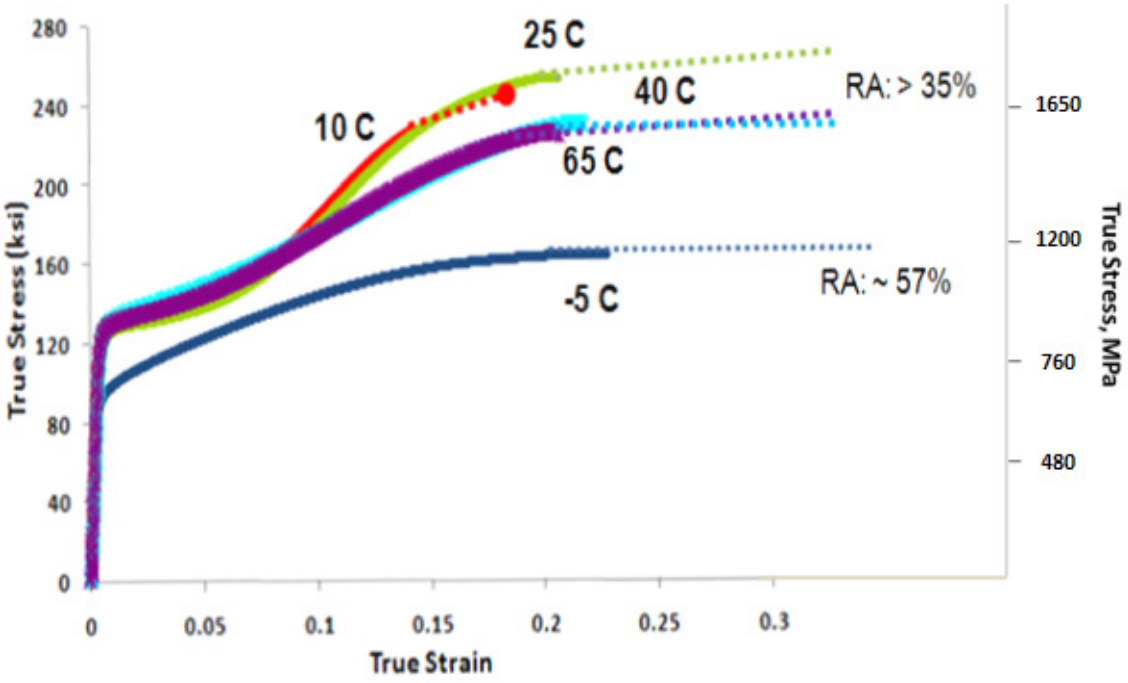

Figure 6.5.1.1: Comparison of True Stress-Strain static uniaxial tensile tests for BA120 specimens aged at 750°C for 10 hours. The test temperature is indicated in bold across each curve. The solid curves indicate the elastic range and the dotted lines show the plastic strain till the point of fracture, thereby indicating final fracture strain

The solid curves in figure 6.5.1.1 represent the region of uniform ductility and extend upto the onset of necking in the specimens while the dotted curves indicate fracture strain. Maximum strain-hardening is observed for BA120 at room temperature while the maximum yield stress is observed at the temperature of 40°C which suggests that the M_s^{σ} temperature would be in the vicinity. A consistent uniform ductility of > 20 % is observed for BA120 for a significant temperature range. For the temperature range 10°C to 65°C, there is very little variation in the yield stress and for the temperature range 25°C to 65°C, the uniform ductility is very similar. This shows the applicability and performance of BA120 over a large range near the room temperature, which is the objective for the blast protection alloy design. Figure 6.5.1.2 shows the engineering stress – engineering strain curves for the same conditions.

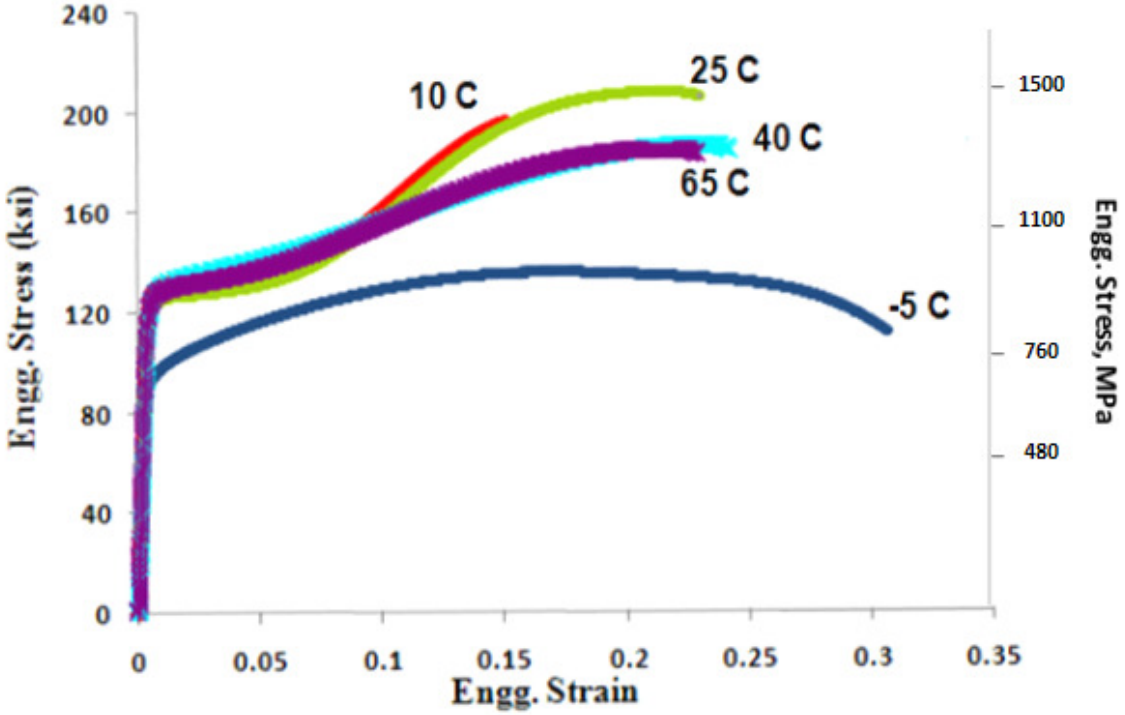

Figure 6.5.1.2: Comparison of Engg. Stress-strain static uniaxial tensile tests for BA120 specimens aged at 750°C for 10 hours. The test temperature is indicated in bold across each curve.

The reduction in area is calculated from the radius of the fracture surface and comparing it to the original radius of the specimen to determine the change in area. This value is indicative of the fracture strain and gives an idea of the order of necking for the specimen. For BA120, it is seen that the reduction in area of the fracture surface (fracture strain) is ~ 37%, which is twice higher than EX425 (~18%) under the same aging and test conditions. For uniform ductility, BA120 reaches an estimated 21% at room temperature as compared to 16% for EX425. Figure 6.5.1.3 shows the comparison of the true stress-strain curves for BA120, EX425 and HSLA100 at room temperature. As seen from the data in table 6.5.1.1, the lowest ratio of YS/UTS is achieved at room temperature for BA120. This ratio, as mentioned earlier in section 4.4.1, gives an idea of the strain-hardening in the specimen. The high strain hardening observed at room temperature for

BA120 is ideal since it shows transformation plasticity at the expected temperature for optimizing and improving mechanical properties. Figure 6.5.1.3 shows that BA120 outperforms the austenitic EX425 and the martensitic HSLA100 in terms of yield stress, uniform ductility and strain hardening, although the maximum fracture strain is observed for HSLA100.

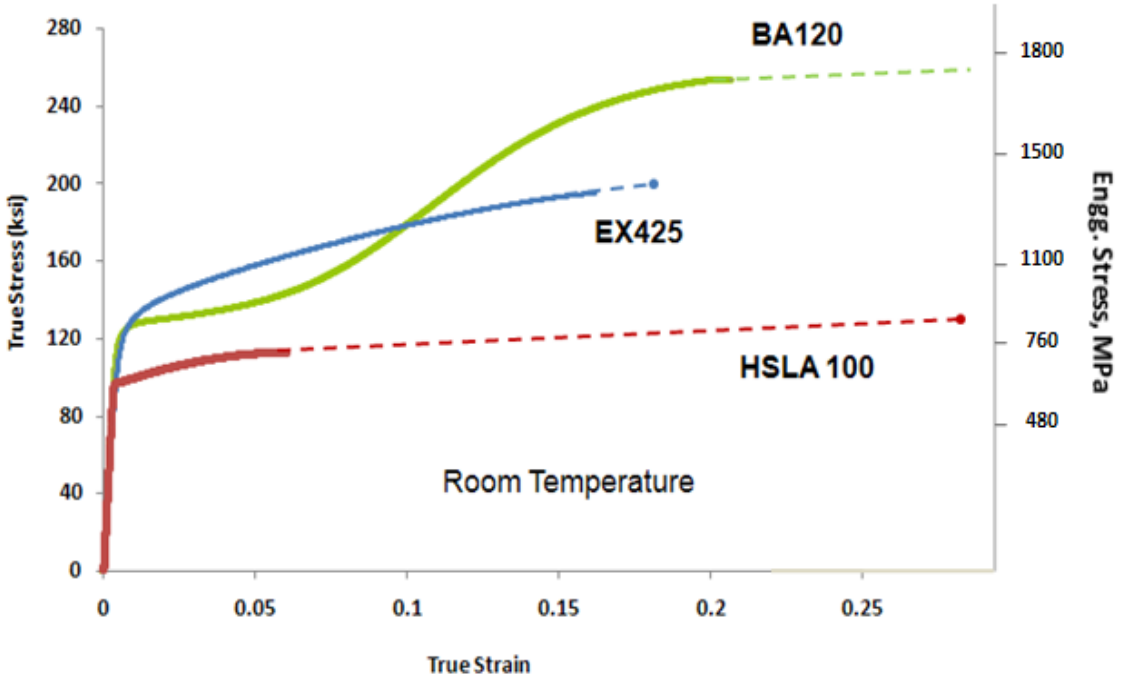

Figure 6.5.1.3: Comparison of True Stress-strain static uniaxial tensile tests at room temperature for BA120 and EX425 specimens of comparative yield stress

Test Temperature	YS (ksi)	UTS (ksi)	YS/UTS	Uniform Elongation	Reduction in Area
-5°C	97	157	0.618	0.235	0.574
10°C	127	230	0.552	0.144	0.183
25°C	127	246	0.516	0.212	0.374
40°C	133	227	0.586	0.223	0.383
65°C	128	223	0.574	0.207	0.358
70°C	123*	-	-	-	-

Table 6.5.1.1: Iso-Thermal Static Uniaxial tensile test properties of BA120 aged at 750°C for 10 hours. The data for 70°C is obtained from the first cycle loading during M_s^{σ} test

Figure 6.5.1.4 shows the optical micrographs of the fractured tensile specimens for the tests done at temperatures 25^{o}C and -5^{o}C, taken by Hime [166]. From figure 6.5.1.1, we have seen that the former shows high transformation strain hardening leading to higher stretch ductility as compared to the latter. This is also observed in the micrographs in figure 6.5.1.4, where the figure (a) shows darker martensite regions as compared to (b) which means more transformation occurred in sample (a).

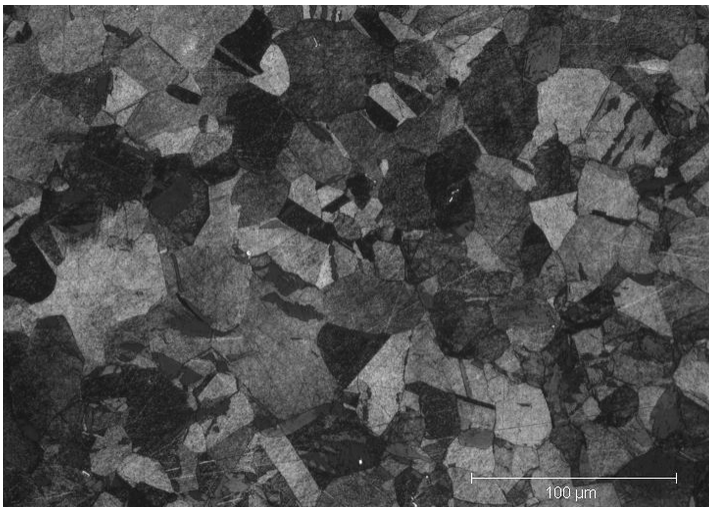

(a)

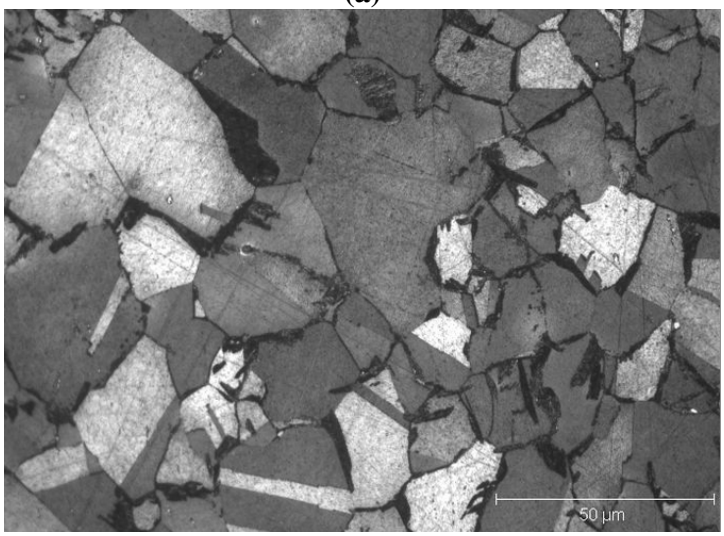

(b)

Figure 6.5.1.4: Comparison of observed transformed martensite in BA120 fractured quasi-static tensile specimens aged at 750^{o}C for 10hours and tested at (a) 25^{o}C and (b) – 5^{o}C. The darker regions represent the transformed martensite. Etchant used: 0.5 gm of Sodium Metabisulfite, 33 cc HCL and 167 cc H_2O [166]

6.5.2 M_s^{σ} Measurements and Stress-Temperature Dependence

Using Richman and Bolling's method where the critical temperature for stress-assisted martensitic transformation M_s^{σ} can be experimentally measured by a reversal of the temperature dependence of the yield stress due to transformation controlled yielding at low temperatures, the M_s^{σ} temperature for BA120 and SA120 have been measured. The figure 6.5.2.1 shows the loading-unloading cycle for BA120 with changing temperature to determine the point of peak yield stress. Both BA120 and SA120 specimens were austenized at 950^{o}C for 1 hr prior to aging at 750^{o}C for 10 hour. Both heat treatments were done in vacuum under sealing. However, it should be noted that Richman and Bolling's method is only a quick screening method of finding the vicinity of M_s^{σ} temperature, as can be seen from figure 6.5.2.1 that the M_s^{σ} temperature lies between 30^{o}C and 40^{o}C.

A more accurate method of determining the M_s^{σ} temperature is from single-specimen isothermal tests; and the value obtained by this method has been used for further matrix stability calculations in section 6.5.3 instead of using the value from Richman and Bolling's loading-unloading method. For the latter case, the actual yield stress is only correct for the first cycle, in this case 70^{o}C as shown in figure 6.5.2.1. However for lower temperatures the yield stress takes into account the additional strain in the material (pre-strain) and hence is higher than the actual yield stress of BA120 at that test temperature. Thus for actual calculation of M_s^{σ} temperature, the $\sigma - T$ stress temperature dependence of BA120 was plotted using the data obtained from isothermal tensile tests and least squares trendline is fitted for the data points, as shown in figure 6.5.2.2. The intersection of the two linear fits is taken as the measured M_s^{σ} temperature for the material. In the case of BA120, the M_s^{σ} temperature comes out to be 36^{o}C.

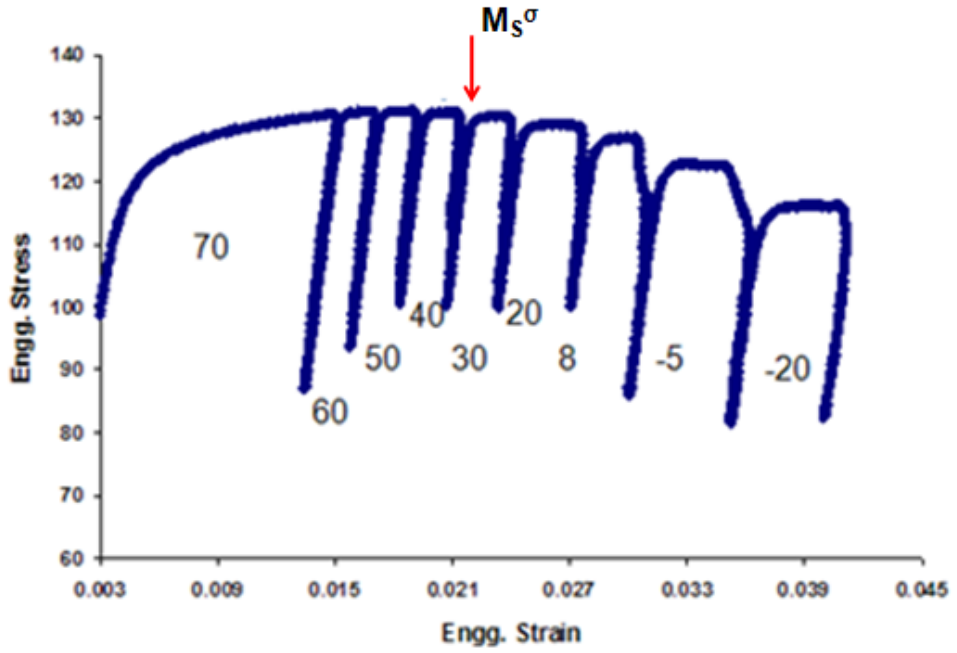

Figure 6.5.2.1: Stress Strain plot for the determination of M_s^σ temperature for BA120 using Richman and Bolling's method of loading and unloading stress cycles at successively decreasing temperatures. The peak yield stress is the measure of the M_s^σ temperature

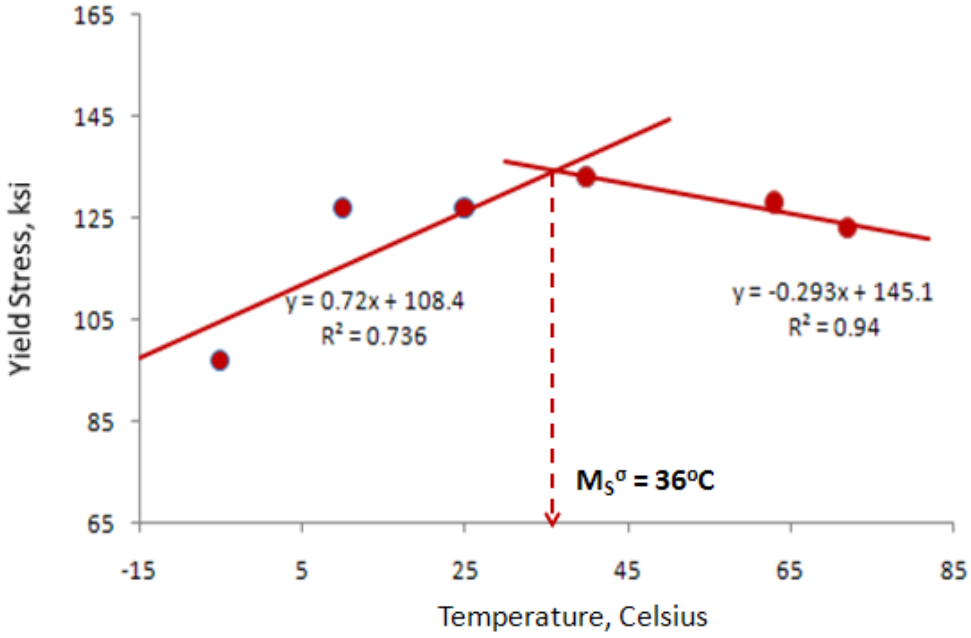

Figure 6.5.2.2: Temperature dependence of Yield Stress for BA120 from the Iso-thermal tensile tests data. Linear trends to the data points if fitted and the intercept is taken as the M_s^σ temperature

For the case of SA120, no accurate isothermal tests could be performed due to presence of defects in the alloy. However, using Richman and Bolling's method, an estimate of the M_s^σ temperature was done. Figure 6.5.2.3 shows the result of the M_s^σ temperature measurement for SA120. The yield stress values obtained at loading are significantly lower than expected due to the defecting nature of the alloy forging. However since the main objective is to determine the critical temperature of change in slope in $\sigma - T$ dependence, (temperature of maximum yield stress) this method is sufficient to determine the range of the M_s^σ temperature for SA120. Due to the premature fracture observed in SA120, the amount of pre-strain given to the specimen in the first cycle is restricted to only 1.6%. The M_s^σ temperature for SA120 lies in the range 5°C to 20°C, which is close to the designed M_s^σ temperature of 5°C. On further evaluation, the M_s^σ temperature for SA120 is taken to be 21°C. This value has been used as a measure of matrix stability for ASP calculations in section 6.5.3.

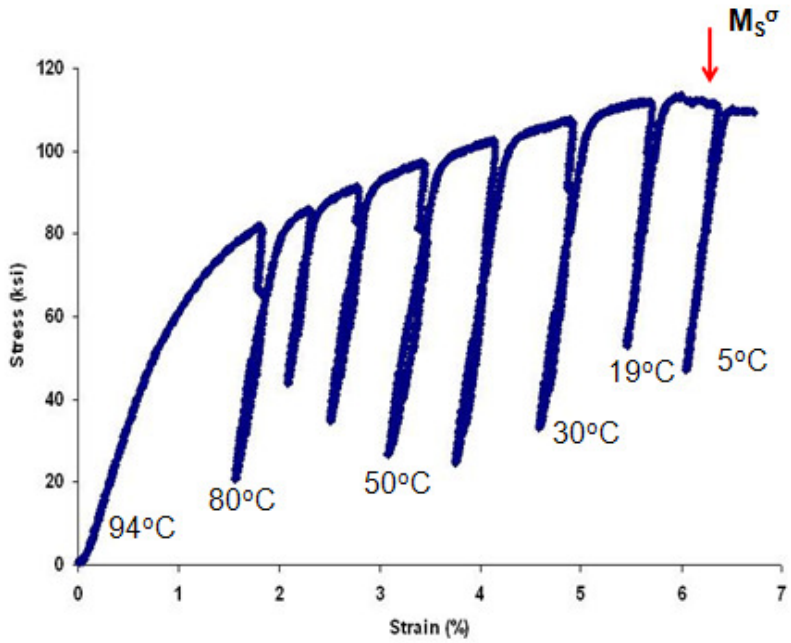

Figure 6.5.2.3: Stress Strain plot for the determination of M_s^σ temperature for BA120 using Richman and Bolling's method of loading and unloading stress cycles at successively decreasing temperatures.

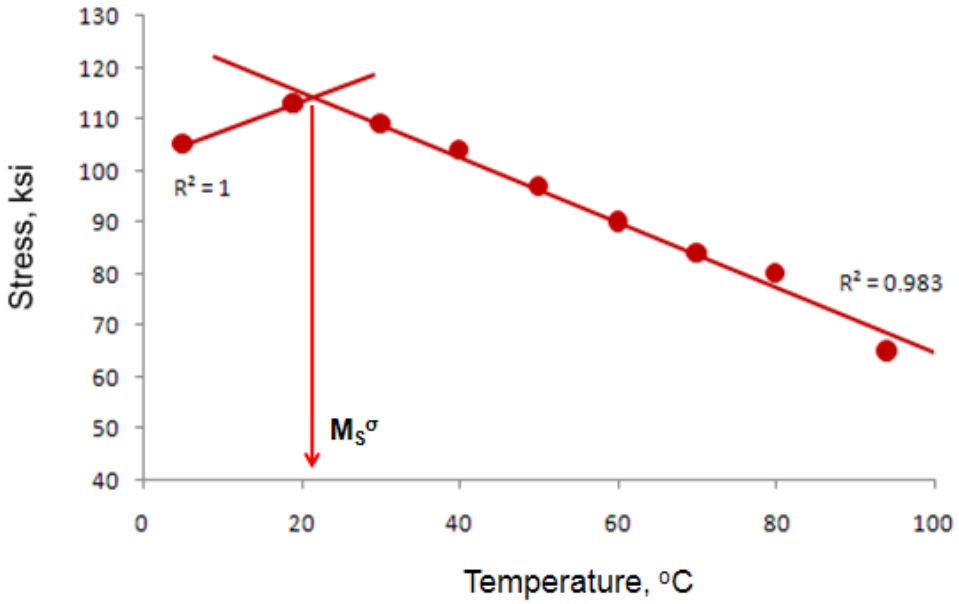

Figure 6.5.2.4: Temperature dependence of Yield Stress for BA120 from the Iso-thermal tensile tests data to determine the M_s^{σ} temperature

6.5.3 Modification of Austenite Stability Model

Using the measured value of M_s^{σ} temperature under tension for BA120 (M_s^{σ} = 36°C) and SA120 (M_s^{σ} = ~ 21°C), the experimental values for the respective Austenite Stability Parameter (ASP) was calculated using Thermo-Calc in conjunction with Ni-Data7 and CMD interfaces with Basic model and MART5 thermodynamic database. The expected Yield stress for SA120 is taken as 130 ksi (896 MPa) since the microhardness measurements show the prototype SA120 as having higher YS than BA120 (124 ksi – 855 MPa) at room temperature for the same aging conditions. Figure 6.5.3.1 shows the modified Austenite stability model, as compared with the original model used to formulate the designs.

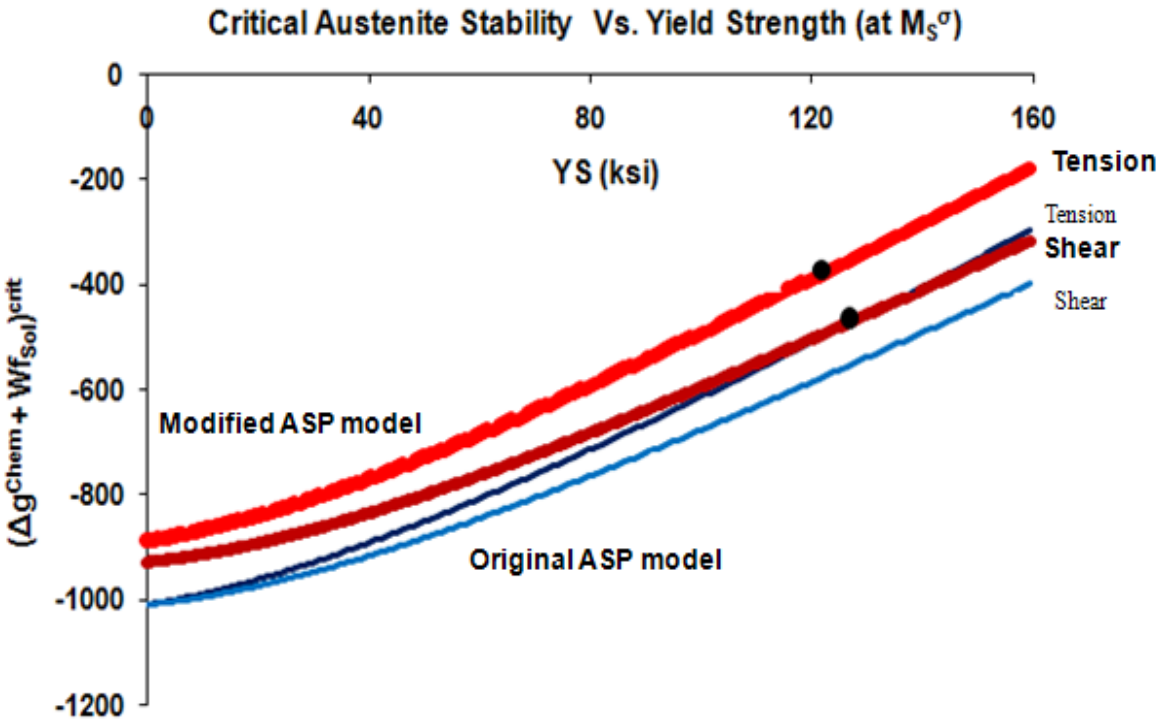

Figure 6.5.3.1: Comparison of the modified Austenite Stability Parameter model for Tension and Shear stress states with the earlier model. The new model is shown in red (Tension) and Brown (Shear). The black solid points represent the calculated ASP values for BA120 and SA120 from the measured M_s^σ temperatures of 36°C and 21°C, respectively

The black solid points represent the experimental ASP values calculated for BA120 and SA120. Since the measured M_s^σ temperatures were higher than the designed M_s^σ temperatures for both BA120 and SA120, the experimental values of ASP would be more positive and thus lie above the original Tension and Shear ASP curves.

To calibrate the Austenite Stability model to the new experimental data points for BA120 and SA120, the curves for the Tension Shear ASP values needs to be shifted towards a more positive value. For this, a positive addition to the constant free energy term g_n is needed as per equation 2.3.9 discussed in chapter 2. To compensate for this additional term to the required total critical

transformation free energy, an additional contribution to the frictional work of martensite interface motion is necessary. Now in our theoretical considerations for the total frictional work of martensite interface motion, we have considered the composition and temperature dependence of the matrix. However motion of the strengthening precipitates also form a constant additional input to the total frictional work of martensite interface motion. This additional term is represented as $W_{\gamma'}$, owing to the contribution from the Gamma Prime precipitates in impeding the motion of the martensite interfaces. The value of would be $W_{\gamma'}$ would be constant for a given stress state because under varying stress states, the interaction of the gamma prime with the martensite motion would vary. Fitting the experimental data points to the Austenite Stability parameter curves for tension and shear stress states gives the following values for $W_{\gamma'}$ –

$W_{\gamma'}$ (Tension) = 120 J/mol, and $W_{\gamma'}$ (Shear) = 80 J/mol

The final equation for Austenite stability Parameter can thus be represented as a modified form of equation 2.3.14 and can be re-written as –

$$W_f^{Sol} = W_{Ath} + W_{Th} + W_{\gamma'} \qquad (6.5.1)$$

6.5.4 Dynamic Tests – Tension and Shear

Dynamic tensile and torsion/shear tests were done for BA120 specimens at room temperature. The specimens were solution treated at 950^{o}C for 1 hour and then aged at 750^{o}C for 10 hours prior to tests, with both heat treatments done in vacuum sealed glass ampoules. The combined

results for Tension and Torsion were plotted in a True stress-strain curve and compared with that of HSLA 100, as shown in figure 6.5.4.1.

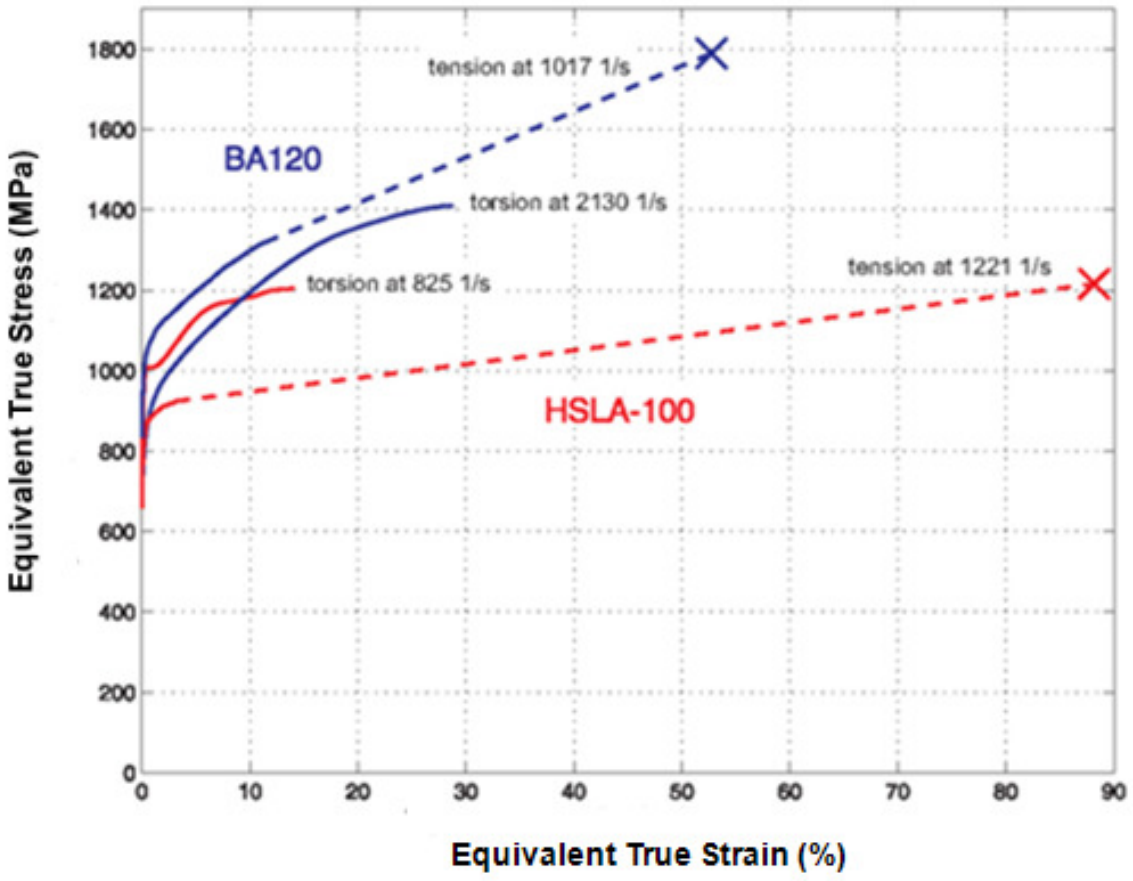

Figure 6.5.4.1: Comparison of True Stress-strain curves for Dynamic tensile and Torsion/Shear tests for BA120 and HSLA100 at room temperature [160]

Figure 6.5.4.1 shows a direct comparison of the dynamic behavior of BA120 with respect to the martensitic HSLA100 steel currently used in blast protection applications. It clearly demonstrates that BA120 provides higher strength with high strain hardening, with the corresponding increase in uniform ductility leading to improved performance at room temperature. As expressed in all true stress-strain curves shown in earlier chapter 4, the solid lines in figure 6.5.4.1 represent the region of the curve with uniform elongation while the dotted lines represent the region of plastic

strain or necking till the point of fracture. The final point in the true stress-strain curve can be taken as the fracture strain of the specimen.

For dynamic tensile loading comparison at room temperature, BA120 has a higher yield stress 150 ksi (~1040 MPa) for high strain rates > 1000 s^{-1} as compared to 125 ksi (860 MPa) for HSLA 100. It also shows strain hardening leading to UTS of ~ 195 ksi (1344 MPa). The fracture strain for BA120 under dynamic loading is as high as 53 %, which is much higher as compared to the earlier austenitic TRIP prototype EX425. The uniform elongation obtained is ~ 14%, which is similar to EX425 (13.5%), as compared to ~ 1% in the case of HSLA100 which shows a lot of plastic strain due to necking till the point of fracture.

Figure 6.5.4.3 shows the SEM micrographs of the fractures surface of the dynamic tensile specimens of BA120. The SEM micrographs show presence of necking in the specimen, validated by the high fracture strain observed in the specimen, although not as high as HSLA 100 which exhibits mostly post-uniform strain. The level of intergranular fracture is much less than that of EX425 (figure 4.5.3.1) and the fracture surface is smoother. Addition of boron for better cohesion between austenite grain boundaries and the presence of adequate fine TiC grain-refining dispersions have resulted in better mechanical properties for BA120.

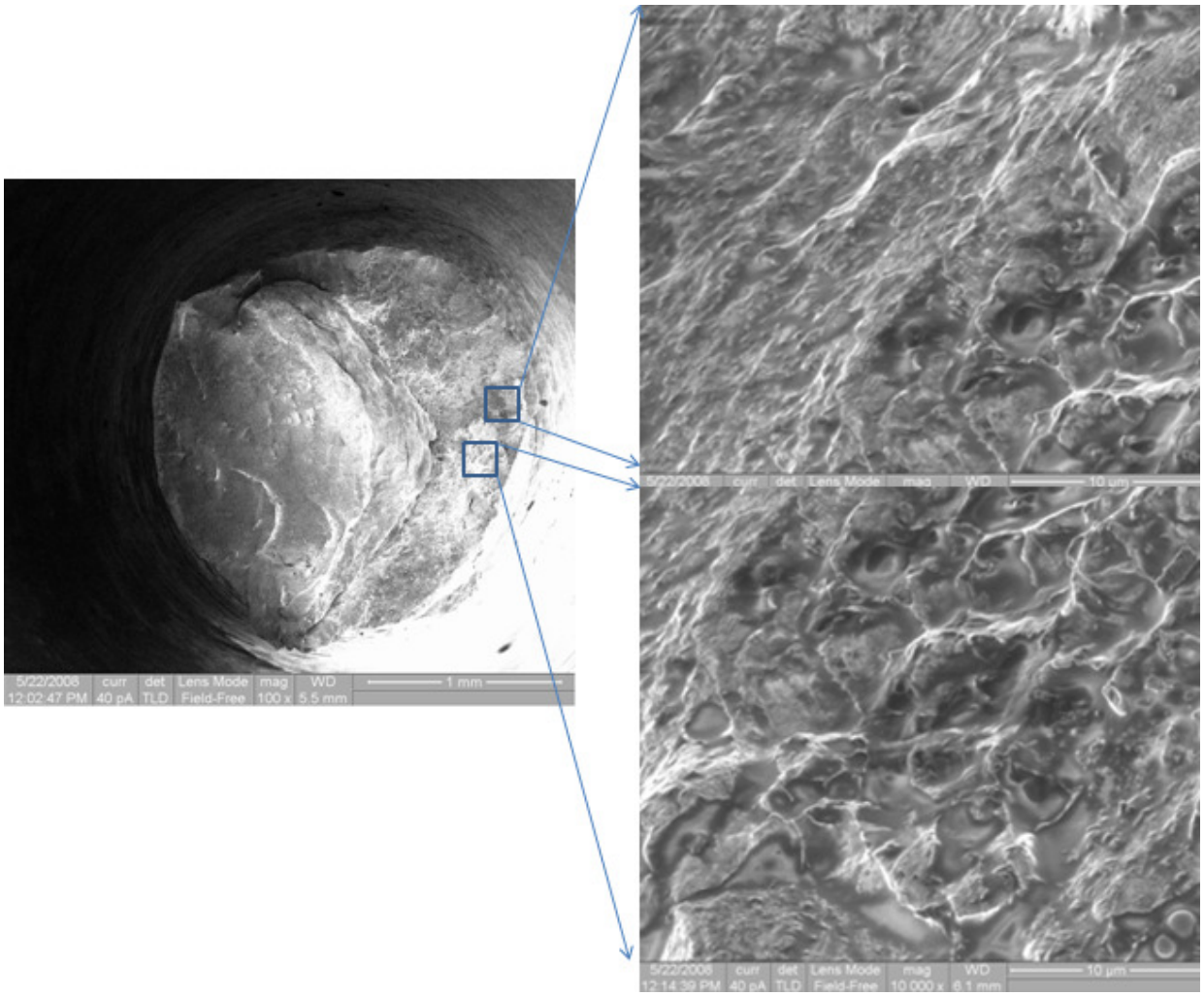

Figure 6.5.4.2: SEM Micrographs of the fractured end of dynamic tensile test specimens for BA120 [160]

Figure 6.5.4.3 compares the optical micrographs of the fractured dynamic tensile specimens of BA120 for high and low strain rate tests. High strain rates have shown higher transformation strain hardening as compared to the lower strain rates. This is also confirmed from the micrographs showing more transformed martensite (darker regions) for the high strain rate test as compared to the lower one.

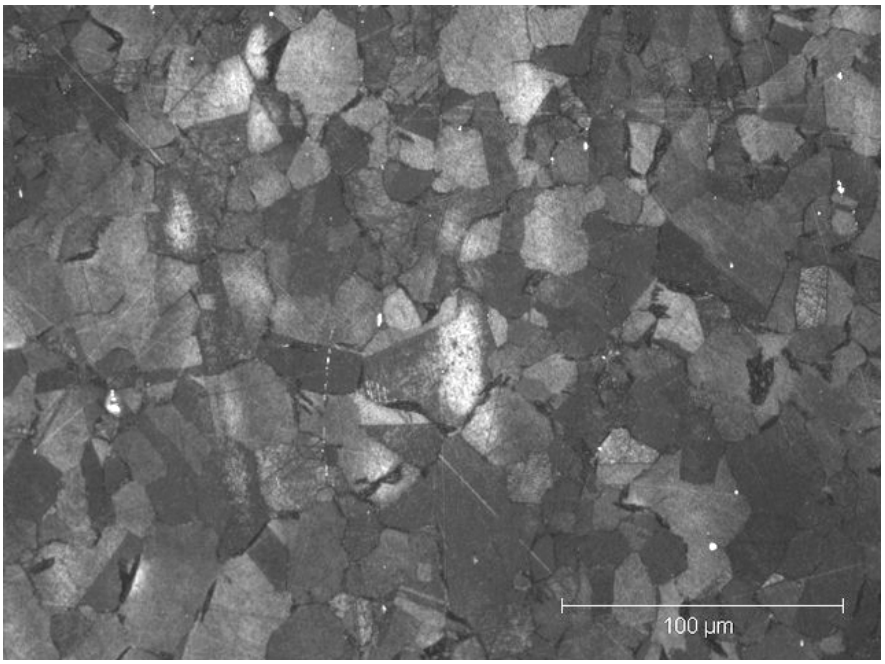

(a)

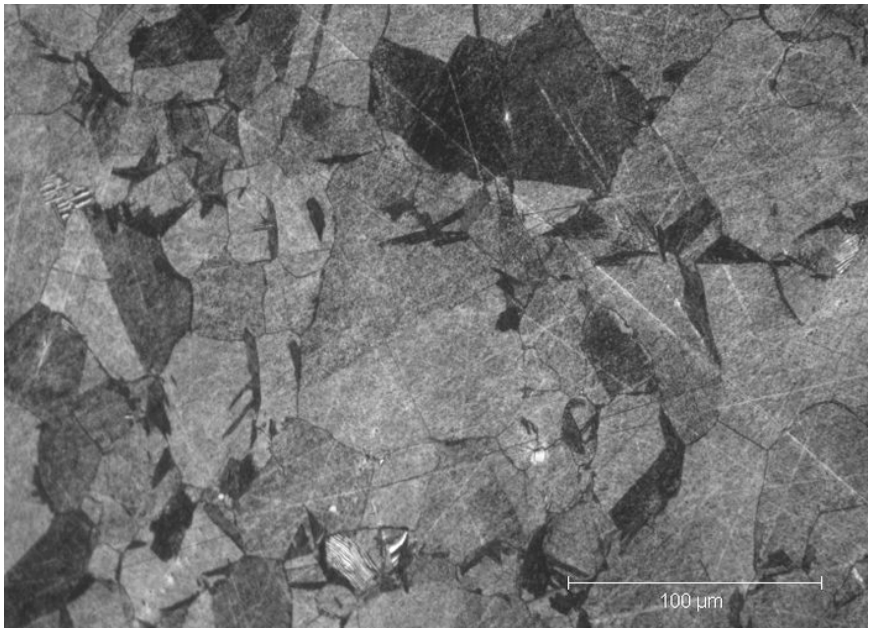

(b)

Figure 6.5.4.3: Comparison of observed transformed martensite in fractured BA120 dynamic-static tensile specimens aged at 750^{o}C for 10hours and tested at room temperature using a strain rate of (a) 1017 s^{-1} (b) 500 s^{-1}. The darker regions represent the transformed martensite. Etchant used: 0.5 gm of Sodium Metabisulfite, 33 cc HCL and 167 cc H_2O [166]

Dynamic shear/torsion tests have been performed on BA120 specimens at room temperature using a setup similar to the dynamic tensile loading Kolsky bar apparatus by Mori [160]. The specimen geometry and dimensions have been shown earlier in section 3.3.6 figure 3.3.6.1. The specimens were marked with grid along the thin wall as shown in figure 6.5.4.4 (a). The distortion of the grids is seen in figure 6.5.4.4 (b) after the shear test specimen fracture. The resultant shear strain has been computed using both a) displacement of bars as well as b) grid method.

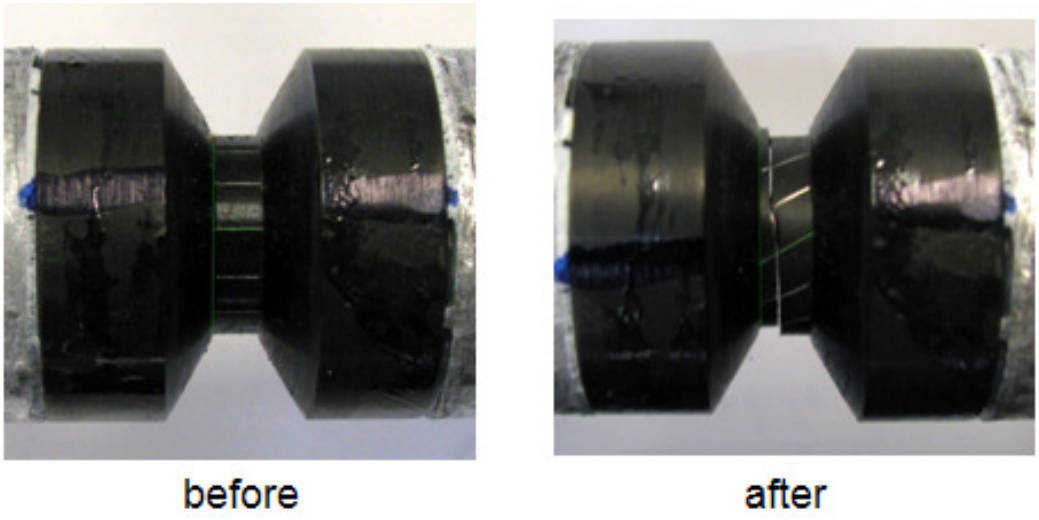

Figure 6.5.4.4: Dynamic Torsion/Shear BA120 test specimen with marked grid-lines in the inner wall as shown before and after the test [160]

	Bars	Grid
HSLA	23%	36%
BA120	41%	53%

Table 6.5.4.1: Measured Shear strains for Dynamic Shear tests done on BA120 specimens shown in figure 6.5.4.3 [160]

Table 6.5.4.1 shows the comparative measured shear strains for BA120 and the martensitic HSLA100 using grids and bars. The data is converted to equivalent true stress-strain from the σ_{XY} component by multiplying the stress by a factor of $\sqrt{3}$ for figure 6.5.4.1.

The equivalent shear yield stress measured is ~ 135 ksi (930 MPa), under dynamic shear loading. The measured shear strain for BA120 is ~ 53% with the equivalent strain being ~ 30%. The shear strain and strain hardening is much higher than observed for HSLA100. Figure 6.5.4.5 shows the SEM images of the fracture face of the torsion specimens after the dynamic torsion tests. The surface shows presence of microvoids.

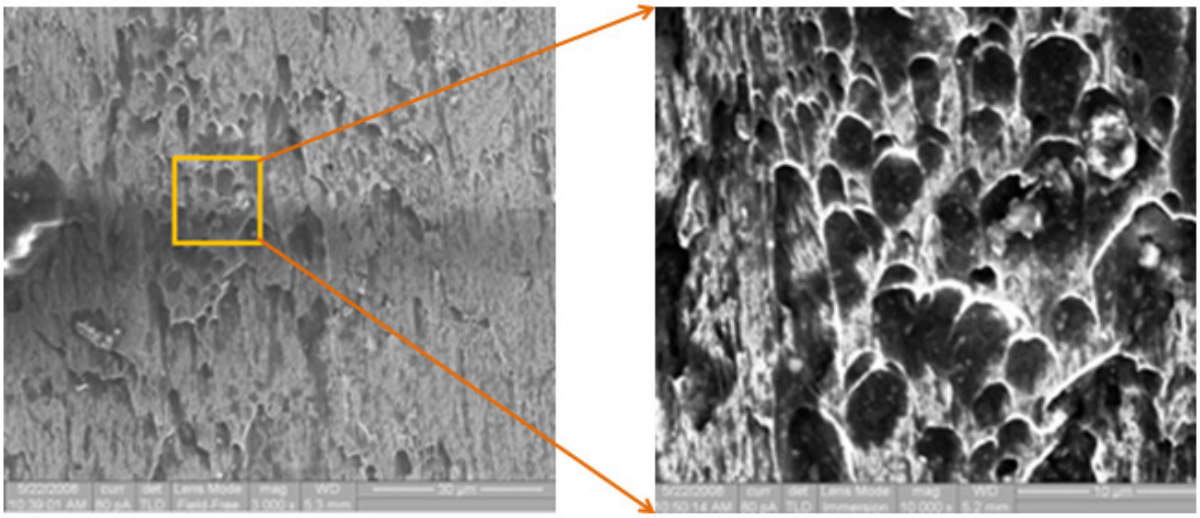

Figure 6.5.4.5: SEM Micrographs of the fractured face of the BA120 Shear specimens [160]

6.5.5 FSI Ballistic Simulation

Fluid-Structure Interaction tests for BA120 were conducted in a system described in section 3.3.7. BA120 plates were solutionized at 950^{o}C for 1 hr at an independent external metal working company. They were then machined according to the specifications as described in figure 3.3.7.3. After machining, the plates were sent to the same metal working company for the

standard heat treatment at 750^{o}C for 10 hours. A first blast impact with an applied pressure of ~84 MPa led to a maximum deflection of ~ 9mm (d_{max}/L = 0.119) [160]. The thickness of the flyer plate used for impulse is 4.84 mm. A comparison of the normalized deflection of the plate with respect to its position with the FEM simulated deflection profile yielded very close match between experimental and predicted models. Inspite of showing an improvement of over 38% in terms of normalized deflection as compared to the AISI 1018 monolithic plate, the BA120 plate did not show any fracture or formation of necks in the region of maximum deflection. Due to this, a second impulse was used with a pressure of ~ 78 MPa which resulted in a maximum deflection of 16.6 mm.

Figure 6.5.5.1 shows the deflection profile with local plate position for BA120 for the first and the second impulses. It is clearly observed that the second impulse leads to a more profound deflection occurs away the central region. The deflection caused by the second impulse is smaller than the first impulse due to strain hardening and the deflection bulge occurring outside the gage section prevents stress concentration near the edges/boundary which would otherwise lead to premature fracture. The high strain observed without any sign of fracture in BA120 under dynamic ballistic loading provides encouraging results leading to improved blast protection applicability of this material.

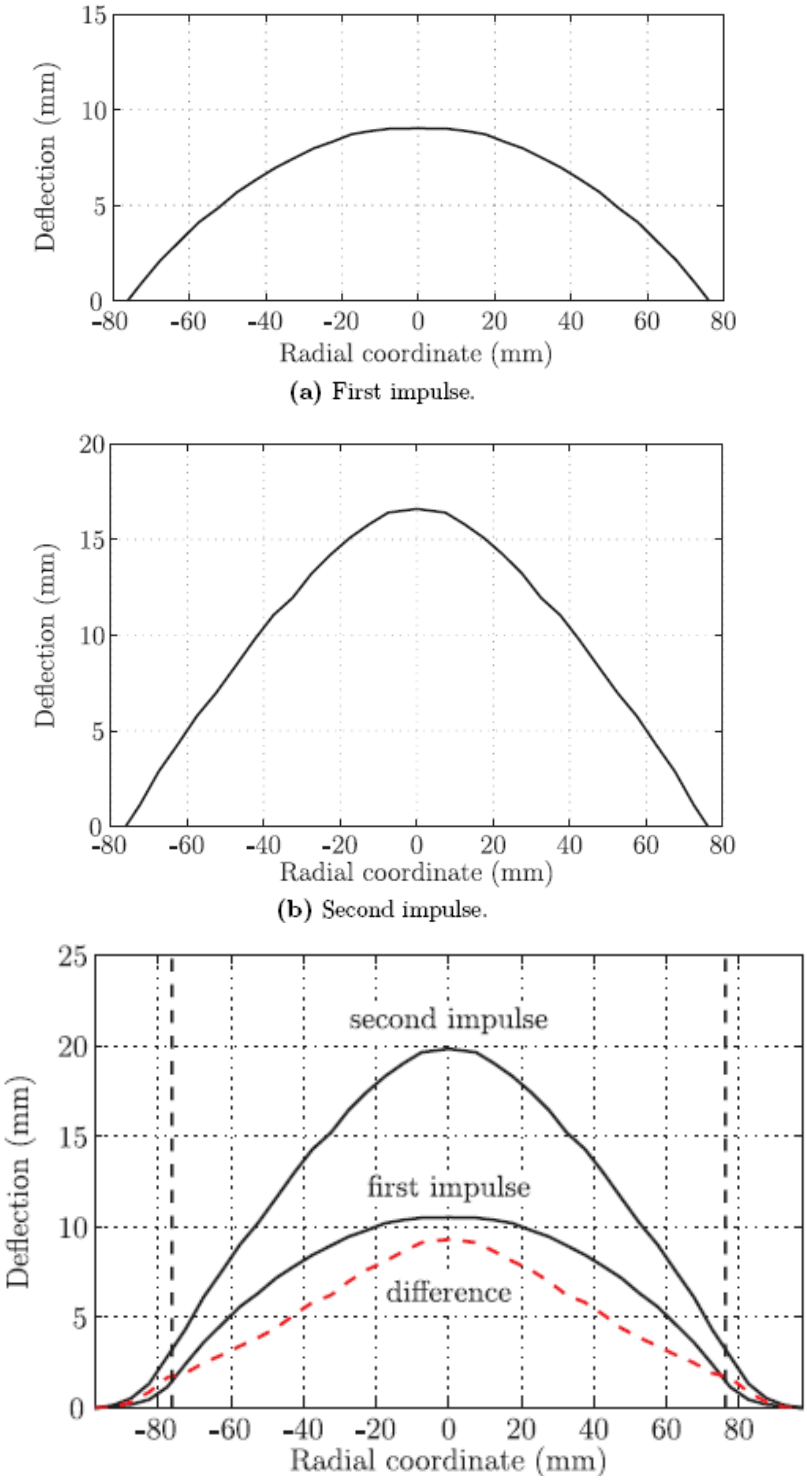

Figure 6.5.5.1: Deflection profiles obtained for BA120 post FSI-ballistic tests on subsequent impulses a) showing deflection profile post 1st impulse and b) deflection profile post second impulse. The lowermost figure shows the combined effect of the impulses, with the calculated difference in impulses [160]

CHAPTER 7

CONCLUSIONS

Evaluation of a first prototype alloy BA120 has confirmed the simultaneous improvement in uniform ductility under tensile and shear loading in austenitic TRIP steels. The design of high strength austenitic TRIP steels for Blast resistant applications has been approached in 4 steps. The first step comprised identification of property objectives and necessary improvements needed over currently used steels for similar application. Once the objectives were set, the second step included analysis of earlier model alloy EX425 to obtain data for both strength calibrations as well as transformation stability of the matrix. These experimental data from EX425 were then used to calibrate parametric models for similar classes of austenitic TRIP steels, as the third step, to define the austenite stability which is the most critical parameter governing the martensitic transformation characteristics. The new alloy designs have been based on extrapolations of these models in order to meet the desired property objectives. Finally as the fourth step, prototypes of the newly designed alloys were melted and forged and specimens of these were used for mechanical tests as well as being subjected to microscopic and surface analysis techniques.

Prototype evaluation of the new designed alloy BA120 has validated the design process. Mechanical testing and nano-scale characterization of these prototypes have confirmed improvements in yield strength as well as uniform ductility at room temperature due to transformation strain hardening, leading to higher uniform ductility under tension as well as

shear/torsion loading. The performance has been compared to the currently used steel for blast-resistant applications like HSLA100 and significant improvements have been shown for the new alloy BA120. Although modifications have been made to the existing stability models based on the results obtained for the new alloy BA120 to make them more accurate and consistent, the design process has nonetheless proven to be a successful demonstration of the various parametric design models and their integration in the systems based approach to materials design.

7.1 Property Objectives and Evaluation of Earlier Prototype

While earlier alloy designs under the Navy's CyberSteel 2020 program focused on transformation toughening of the alloys to build materials having high fracture toughness and necking which demonstrated the successful design of BA160 [8], evaluation of recent needs of the Navy had resulted in the necessity for designing alloys with improved uniform stretch ductility under tension for blast protection and under shear loading for fragment resistance at room temperature, while maintaining high levels of yield stress (>100 ksi/690Mpa). While toughness was not the primary design criteria as in case of the martensitic BA160, sufficient toughness requirement is necessary for all blast protection applications. Secondary design objectives included non-magnetic (paramagnetic) property at room temperature, high resistance to corrosion (H and Stress assisted cracking), good weldability and low microsegregation levels.

7.2 Alloy Design

Using a systems engineering framework to meet the desired property objectives, a flowchart depicting the Structure→ Property → Performance relationship was developed. The yield strength requirements have been met by the precipitation of γ'-intermetallic phase during aging.

The strength model used has been created using the measured yield stress of EX425 for calculated phase fraction of the γ'-phase in the system at equilibrium, leading to a $\sigma - f_{\gamma'}$ plot showing the relationship between the two factors. The austenite matrix has been shown to contribute ~ 49 ksi (338 MPa) of the required strength and the rest is contributed by appropriate mole fraction of γ'-phase precipitation. Al and Ti content of the alloy was varied to achieve the right amount of γ'-phase needed, while maintaining a constant ratio of Al/Ti in the alloy. Proper heat treatment steps were determined for the alloys based on required phase fraction of γ' at equilibrium with the matrix. Solutionizing temperature and time were set based on earlier study on EX425 austenitic TRIP steel at 950°C for 1 hr.

The theoretical formulation for all kinetics based models describing the austenite stability and the associated transformation plasticity comes from the early works of Olson and Cohen and their model of heterogeneous martensitic nucleation. By relating the stress-assisted martensitic transformation to the critical transformation temperature (M_s^{σ}), the stability of the austenite has been defined through a set of quantitative models. The critical value of the Austenite Stability Parameter (ASP) at the M_s^{σ} temperature is defined as the sum of the mechanical driving force of transformation (ΔG^{σ}) and a constant critical free energy term (g_n). The ASP term is then equated to the composition and temperature dependence of the frictional work of martensitic interface motion (W_f^{Sol}) and the change in Gibb's free energy associated with the FCC → BCC martensitic Transformation (ΔG^{Chem}).

The concept of Transformation-Induced Plasticity (TRIP) has been used to achieve the desired mechanical properties in the alloys. The design M_s^{σ} temperature for each alloy was set according to the optimum performance (maximum uniform ductility) evaluated from earlier austenitic

TRIP Prototype EX425. Ni and Cr contents were varied to determine their optimum concentrations so as to meet the necessary ASP requirements at the pre-determined critical temperature.

The design revealed that Ni has a very strong effect on the matrix stability in austenitic TRIP steels. This was the case as observed in EX425 where the critical transformation M_s^{σ} temperature was measured at -70^{o}C. By lowering the Ni content and adjusting the Cr levels suitably, the stability of the matrix was decreased, which is observed by the high transformation M_s^{σ} temperature measured for BA120 and SA120. SA120 was designed to have a high chromium content in order to optimize its performance for shear resistance as well, which can be attained by an increase in the thermal contribution to the frictional work of martensite interface motion. This design concept is based on the dependence of the critical Gibb's free energy on the temperature for transformation (Figure 2.2.19) and the temperature dependence of yield stress (Figure 2.2.18).

Carbon content is controlled by the amount of the fine grain refining FCC dispersion phase TiC desired in the alloys. The presence of ~ 0.15 atomic % TiC in the matrix during solution treatment is enough for this purpose which leads to a carbon level of ~ 0.014wt% in the alloy. During tensile tests of the prototype EX425, intergranular fracture was seen to occur in the specimens which restricted its uniform ductility. To enhance grain-boundary cohesion in order to reduce the occurrence of intergranular fracture, more Boron has been added in the system. The average range of Boron content in austenitic steels is from 50 ppm to 150 ppm, so a level of 125 ppm was taken in the alloy design for optimum cohesion of austenite grain boundaries. All other

components like Mo and V were kept the same as in A286 and EX425. However Mn was removed from the design consideration as it is known to reduce uniform ductility in TRIP steels.

7.3 New Prototype Evaluation

Using precipitation strengthening and matrix stability thermodynamic design models, two prototype alloys were made – ***BA120*** which is a non-stainless (Cr = 4 wt%) austenitic steel optimized for adequate Blast Protection by having high Strength and High ductility and ***SA120***, which is a high chromium (Cr = 9.8 wt%) austenitic steel optimized for adequate shear and fragmentation resistance at room temperature.

300 lb heats each of 8" diameter ingots were prepared by multiple melting techniques using Vacuum Induction Melting (VIM) of raw virgin materials followed by Vacuum Arc Remelting (VAR), with strict control over composition. Surface microscopy and Vickers Microhardness measurements were done on austenized as well as aged specimens and a surface microhardness of 317 VHN (leading to an expected 124 ksi YS) was measured for BA120 specimens aged at 750^{o}C for 10 hours. Microhardness measurements were also taken for aged specimens at various times to determine the variation of hardness with temper time. Isochronal tempering study confirmed that the peak hardness (leading to maximum yield stress) occurs at 10 hours of aging time, at the standard temperature of 750^{o}C.

The strength model (Yield Stress vs. Gamma prime phase fraction) developed using data points from the earlier TRIP prototype EX425 has been confirmed to be very accurate. However the time-temperature Arrhenius relationship for peak hardness might differ for Low-Cr and High-Cr austenitic steels, the current model being more favorable to low-Cr designs.

The characterization of the low chromium prototype BA120 yielded encouraging results. Static as well as dynamic tensile tests have confirmed high strength and high ductility due to the occurrence of strain hardening at room temperature. The principle design objective was to attain the combination of high strength and high ductility at room temperature under tensile loading. The room temperature tensile yield stress for BA120 was measured to be ~ 124-127 ksi (855-875 MPa). The measured yield stress under dynamic tensile and shear loading were 150 - 152 ksi (1049 MPa) and 160 ksi (1100 MPa). High strain hardening was confirmed leading to UTS of 246 ksi (1696 MPa) under quasi-static loading and a UTS of ~ 195 ksi (1344 MPa) under dynamic loading. These values are much higher than HSLA100 and comparable to EX425 austenitic TRIP alloy. The uniform ductility under uniaxial tension for BA120 is 21% with a fracture strain of ~ 37% as compared to 16% uniform ductility and ~17% fracture strain for EX425. Fracture strain improved by as much as 100% over the EX425 prototype alloy. The equivalent shear yield stress measured is ~ 135 ksi (930 MPa), under dynamic shear loading. The measured uniform shear strain for BA120 is ~ 53% with the equivalent strain being ~ 30%. The shear strain and strain hardening is much higher than observed for HSLA100. Thus the thermodynamic constitutive models demonstrated adequate feasibility of combining γ' – precipitation strengthening along with transformation plasticity leading to optimum austenite matrix stability to design an austenitic TRIP steel with improved mechanical properties over the currently used austenitic steels for blast protection applications.

The results from the dynamic shear tests have shown that BA120 has very good fragment protection properties. The Fluid-Structure Interaction (FSI) ballistic test results have also shown that underwater dynamic impact of blast leads to a very high strain in BA120 without fracture at

higher multiple impulses, leading to improved blast-protection application especially for naval applications.

The matrix was found to be slightly more unstable than desired with the measured M_s^{σ} temperature for BA120 and SA120 being 36°C and 21°C respectively, which although higher than the desired 5°C, leads to a good performance of the alloy under shear stress loading.

Due to improper forging and rolling process, the SA120 prototype alloy ingots had many cracks and inclusions which restricted its mechanical evaluation. However, surface microhardness tests and an isochronal study similar to that of BA120 was done which confirmed the peak hardness (leading to highest Yield Stress) at 10 hours of aging at 750°C. The hardness numbers obtained for 10 hours was ~ 350 VHN (which translates to a expected YS of 140 ksi).

3-D LEAP (Atom Probe) Tomography of the prototype BA120 has confirmed good compositional accuracy of the matrix and gamma prime phase with those predicted using Thermo-Calc for the $\gamma - \gamma'$ phase equilibrium post aging. The measured average particle diameter of 15 nm matches well with the optimum gamma prime precipitate size for peak hardness. The predicted number density of γ' was also verified using the envelope method of cluster separation for precipitates. However for the case of SA120, the average diameter of the gamma prime precipitates was calculated at much higher values as ~ 26nm leading to lower number density of these precipitates, which implies overaging of the specimen at the 10 hour aging time.

Finally, using the measured M_s^{σ} temperatures for both prototypes, a modification has been made to the Austenite Stability Parameter model and calibrated to accurately reflect these latest data

points for further design iterations. The properties demonstrated for BA120 are an improvement over HSLA100 and EX425 in terms of uniform ductility under tension as well as shear with a high strain hardening at room temperature, leading to a significant progress in the field of Systems Computational approach to Materials Design.

CHAPTER 8

FUTURE WORK

The first prototype BA120 has demonstrated the right direction taken in terms of using constitutive and parametric models based on stability of the matrix and kinetics of martensitic transformation, to design steels with high strength and high ductility under any stress state. However, there is always the necessity for improvement, not only in terms of performance capabilities of austenitic steels, but also in terms of the equations and model used to design the alloy. Since these current models have successfully shown the application of systems based Structure-Property-Performance approach to materials design, using the experimental data points from this research, better calibration and modification of the models can be pursued for next design iterations.

8.1 Evaluation of Current Prototypes

For this thesis, an earlier austenitic TRIP prototype EX425 was used extensively to design the models for precipitation strengthening and matrix austenite stability parameter to define

appropriate transformation characteristics. The current prototypes BA120 and SA120 provide further material to base future designs by extending the limits of the current models to including performance evaluation under shear and compression stress states as well.

8.1.1 BA120

Detailed analysis of the transformed martensite volume fraction could not be pursued in this current research. Comparison of the transformed martensite regions using X-Ray diffraction to measure the intensities of the observed austenite and martensite peaks and by using preferential etching techniques to identify the martensite regions within the austenite matrix is currently being pursued by Feinberg [157]. Volume fraction of transformed martensite in the fractured specimens would be proportional to the observed strain-hardening in BA120, which is observed for both static as well as dynamic tensile tests. This may be done for torsion test specimens as well. Iso-thermal tensile tests under dynamic loading would be an ideal measure of the dynamic M_s^{σ} temperature and whether it varies from the quasi-static M_s^{σ} temperature. Since the final performance under dynamic loading is critical to the overall performance of the alloy, these tests would be necessary in the immediate future.

The performance of BA120 under quasi-static torsion loading could not be evaluated at Northwestern University. Collaboration with external testing facility at *Illinois Institute of Technology, Chicago* has been made for future tests.

More detailed analysis of BA120 is needed with regards to property changes with variation in heat treatment. EX425 has shown that with an appropriate heat treatment (single step or via

multi-stage), any M_s^{σ} temperature can be obtained. Using the new M_s^{σ} temperatures for different aging temperatures, the Austenite Stability Parameter model can be further calibrated.

8.1.2 SA120

Due to the improper forging technique used during manufacturing of SA120, the final ingot consists of large number density of inclusions, voids and cracks visible on the surface and spreading to the interiors. Therefore mechanical testing and evaluation of expected properties could not be completed. While the M_s^{σ} temperature for SA120 under tension has been measured, the M_s^{σ} temperature under Shear stress needs to be validated experimentally since. SA120 has been optimized for performance under both stress states. There is a need for experimental capability to run Kolsky bar dynamic adiabatic tests at different temperatures. Finally FSI ballistic tests need to be performed on SA120 to confirm the initial performance objective of improved blast resistance for these alloys.

Only surface microscopy and microhardness measurements have been made possible for SA120 along with 3D-LEAP tomography analysis of the distribution of precipitates. Growth kinetics of Gamma Prime nucleation in EX425 has been extensively studied [159] and presented in appendix I. For BA120 the observed gamma prime distribution and size is very similar to that of EX425. However for SA120 the size of the gamma prime is larger and the number density is lower than that of BA120 and EX425. This suggests overaging leading to coarsening of the gamma prime beyond its optimum size for peak hardness. Thus a study of the precipitation kinetics for SA120 similar to EX425 would be ideal.

Measurement of transformed martensite volume fraction is necessary for SA120, as in case of BA120 to determine the relative transformation for the two alloy classes (BA120 – Low Cr and SA120 – High Cr) under static as well as dynamic loading.

8.2 Next Generation Design

The next iteration of Design would be based on optimum combination of performance under tensile and shear at room temperature, with importance given to increased fracture strain (plastic strain/necking) under dynamic loading. Calibration of the gamma prime precipitation strengthening has been shown to be very accurate and consistant; however further calibrations are necessary for the Austenite Stability models, especially for the shear stress state. Since no experimental validation for performance under shear loading is available for austenitic TRIP steels, the detailed evaluation of SA120 becomes more critical. Using the measured shear M_s^{σ} temperature and determining stability of the austenite matrix for different heat treatments (leading to varying yield stress) can lead to important data to fit to the updated ASP model shown in figure 6.4.4.1. Thus using the current design as a building block, the next generation of High Strength Austenitic TRIP steels can be designed with improved shear resistance and matrix stability optimized for shear stress- assisted transformation.

REFERENCES

[1] "*Science of Steel*," G. B. Olson, in *Innovations in Ultra-High Strength Steel Technology*, ed. G. B. Olson, M. Azrin, and E.S. Wright, Sagamore Army Materials Research Conference Proceedings: **34th** (1990) 3-66

[2] G. B. Olson, "*Computational Design of Hierarchically Structured Materials*", *Science* **277** (1997) 1237-1242

[3] G. B. Olson, "*Designing a New Material World*", *Science* **288** (2000) 993-998

[4] Materials Technology Lab (MTL), Department of Materials Sc. And Engg, Northwestern University, *http://mtl.northwestern.edu/homebody.htm*

[5] G. B. Olson, *J. Materials. Ed.* ***11*** (1989) 515-528

[6] G. B. Olson, "*Materials Design: An Undergraduate Course*", Morris E. Fine Symposium, TMS-AIME, Warrendale, PA, 1991, p. 41-48

[7] C. S. Smith, "*A search for Structure*", 1988, MIT

[8] Saha, Arup. "*Systems Design of Ultra-tough High Strength Steels for blast-Resistant Naval Hull Application"*. Doctoral Thesis, 2004, Northwestern University

[9] V.F Zackay, E.R Parker, D.Fahr, and R.Busch: Trans. ASM, 1967, **vol. 60**, pp. 252- 59

[10] J.R. Patel and M. Cohen, "*Criterion for the action of Applied Stress in the Martensitic Transformation*", *Acta Metall.* **1** (1953), pp. 531–538.

[11] T. Angel, *J. Iron Steel Inst.* (1954), pp. 165–174

[12] G.B. Olson and M. Cohen In: S.C. Antolovich, R.O. Ritchie and W.W. Gerberich, Editors, *Mechanical properties and phase transformations in engineering materials*, Met. Soc. AIME, New Orleans (1986), pp. 367–390.

[13] Stavehaug, F., "*Transformation toughening of γ'–strengthened metastable austenitic Steels"*. Doctoral Thesis, 1990, MIT

[14] Kohn, G., "*Effects of TRIP phenomenon on the toughness of Heat Treatable Alloy Steels"*. Doctoral Thesis, University of California, Berkeley, 1976

[15] D. Bhandarkar, V.F. Zackay and E.R. Parker, *Metall. Trans.* **3** (1972), pp. 2619–2631

[16] McCarren M, Chardon M, Chuu K, Forbes T, Fruth S, Haro E, Kuou D, Lee C. *BlasTruss: Civil Shield Technologies*. IDEA 398, March 2004, Northwestern University

[17] M. F. Ashby, *Materials Selection in Mechanical Design*, Pergamon, Tarrytown, NY, 1992.

[18] K. C. Hsieh, "*Fracture Toughness of Ti-modified Air-melted UHS Steels*", Doctoral Thesis Proposal, Department of Materials Science and Engineering, Northwestern University, Evanston IL (2000)

[19] Lee, Sungsoo, "*Dynamic Failure of Blast-Resistant Structures subjected to Impulsive loading*". Doctoral Thesis 2006, Northwestern University

[20] Xue, Zhenye and John W. Hutchinson, '*Preliminary Assessment of Sandwich Plates Subject to Blast Load'*. Division of Engineering and Applied Sciences, Harvard University, Cambridge, MA 02138

[21] Evans, A.G. and John W. Hutchinson, "*The Structural Performance of Near-Optimized Truss Core Panels",* International Journal of Solids and Structures volume 39 (2002).

[22] Belytschko, Ted. *Computational Fluid-Structure: Interaction and Homogenization*. Department of Mechanical Engineering, Northwestern University

[23] McCarren, M. *BlasTruss: Validation of Structural Model Predictions* IDEA 398, 2004, Northwestern University

[24] Jacques, P., Q. Furnemont, T. Pardoen, and F. Delannay, *on the role of martensitic transformation on damage and cracking resistance in TRIP-assisted multiphase steels*, Acta mater. 49 (2001) 139-152.

[25] Echt J, Edelman L, McCarren M, Stempel K, Tu W, M. Bender, "*Civil Shield: Materials and Structures for Anti-Terrorism Blast Protection*", MSE-390, Northwestern University 2004

[26] K C Russell, 'Nucleation theory under metastable and dissipative conditions', *Phys. Scr.* T44 15-22

[27] G.B. Olson and M. Cohen: *Met Trans. A*, vol. 7A, 1976, pp 1897

[28] G.B. Olson and M. Cohen: *Met Trans. A*, vol. 7A, 1976, pp 1905

[29] A. J. Bogers and W. G. Burgers: Acta Met., 1964, vo. 12, p. 255

[30] L. Kaufman and M. Cohen: Prog. Metal Phys., 1958, vol. 7, p. 165

[31] V. Raghavan and M. Cohen: *Acta Met.*, 1972, vol. 20, p. 333

[32] C. L. Magee: Phase Transformations, p. 115, ASM, 1970

[33] G.B. Olson and M. Cohen: *Met Trans. A*, vol. 7A, 1976, pp 1915

[34] J.W. Gibbs: *The scientific papers of J. Willard Gibbs*, Dover, 1961

[35] H. Conrad: J. Metals, July 1964, pp. 582

[36] J.E. Dorn: *Dislocation Dynamics*, p 27, McGraw-Hill, NY 1968

[37] V. Raghavan and M. Cohen: *Met. Trans.*, 1971, vol. 2, p. 2409

[38] J. F. Breedis and W. D. Robertson: *Acta Met*., 1963, vol. 11, p. 547

[39] P. L. Magnanon and G. Thomas: Met Trans., 1970, vol. 1 p. 1577

[40] G.B. Olson and M. Cohen, "*A General Mechanism of Martensitic Nucleation: Part III. Kinetics of Martensitic Nucleation*", *Met Trans.*, 1976, vol. 7A p. 1915

[41] A. H. Cottrell and B. A. Bilby: *Phil Mag*., 1951, vol. 42, p 573

[42] N. Thomas and D. J. Millard: *Phil Mag*., 1952, vol. 43, p 422

[43] J. A. Venables: *Phil Mag*., 1961, vol. 6, p 379

[44] J. P. Hirth: *Deformation Twinning*, R. E. Reed-Hill, J. P. Hirth, and H. C. Rogers, eds., p. 112, Gordon and Breach, New York, 1964

[45] G.B. Olson: Sc.D. Thesis, Appendix C, MIT, June, 1974

[46] P. C. Clapp: *Phys. Status Solidi* (b), 1973, vol. 57, p. 561

[47] D. deFontaine, N. E. Paton, and J. C. Williams: *Acta Met*., 1971, vol. 19, p. 1153

[48] V. F. Zackay, E. R. Parker, D. Fahr, and R. Busch, "*Enhancement of Ductility in High-Strength Steels*", Trans. ASM, 7 (1967) pp. 252-259

[49] J. P. Bressanelli and A. Moskowitz, "*Effects of Strain Rate, Temperature and Composition on Tensile Properties of Metastable Austenitic Steels*", *ASM Trans. Quart.* 59, 1966, p. 223

[50] G. B. Olson, "*Transformation Plasticity and the Stability of Plastic Flow*", in *Deformation Processing and Structure*, pp. 391-424, ASM, Metals Park, OH, 1983

[51] D. Bhandarkar, V. F. Zackay, E. R. Parker, "*Stability and Mechanical Properties of some Metastable Austenitic Steels*", Met. Trans. A, (1972) pp. 2619

[52] J.M. Rigsbee and P.J. VanderArend: in *Formidable HSLA and Dual Phase Steels*, A.T. Davenport, ed., TMS-AIME conf. Proc., 1977, pp. 56-86

[53] G.B. Olson and M. Azrin, "*Transformation Behavior of TRIP Steels*", *Met. Trans.* **9A** (1978), 713

[54] A. R. Marder: ibid, pp. 87-98

[55] G.B. Olson and M. Azrin *Met. Trans.* A, 1978 vol. **9A**, pp. 713-21

[56] G.B. Olson and M. Cohen, *J. Less-Common metals*, 1972, vol. **28**, pp. 107-18

[57] S.R. Pati and M. Cohen, *Acta Met.*, 1969, vol. **17**, pp. 189-99

[58] S.R. Pati and M. Cohen, *Acta Met.*, 1971, vol. **19**, pp. 1327-32

[59] G.B. Olson and M. Cohen, "*Stress-Assisted Isothermal martensitic transformation: Application to TRIP steels*", *Met. Trans.*, 1982, vol. **13A**, pp. 1907-14

[60] Richman, R.H. and Bolling, G.F, "*Stress, Deformation and Martensitic Transformation*", *Met. Trans*. 2 (1971) Sept, 2451-2462

[61] G.B. Olson and M. Cohen, *Proc. Intl. Conf. Solid-Solid Phase Transf*. (Carnegie Mellon) AIME, 1982, p. 1145

[62] G.B. Olson and M. Cohen, "*Principles of Martensitic Transformations*" in Frontiers of Materials Science, ed. M. A Meyers and O. T. Inal, 1985, p. 43-87

[63] M. Suezawa and H. E. Cook, Acta Met., Vol. **28**, 1980, p. 423

[64] H. C. Ling and G. B. Olson, *Proc. Intl. Conf. Solid-Solid Phase Transf*. (Carnegie Mellon) AIME, 1982, p. 1171

[65] A. L. Roitburd, Dok. Akad, Nauk SSR, vol. **256**, 1981, p. 80

[66] Richman, R.H. and Bolling, G.F: Scripta Met., 1970, vol. **4**, pp. 539-44

[67] P. J. Fisher: "*The effects of Stress on the martensitic transformation*," PhD Thesis, University of New South Wales, 1974

[68] G.B. Olson and M. Cohen, "*A General Mechanism of Martensitic Nucleation: Part II. FCC → BCC and other Martensitic Transformations*", *Met Trans.*, 1976, vol. **7A** p. 1905

[69] R. E. Cech and D. Turnball, Trans. AIME, **206** (1956) 124.

[70] M. Cohen and G. B. Olson, "*Martensitic Nucleation and the Role of the Nucleating Defect*", in *New Aspects of Martensitic Transformations*, First JIM International Symposium (JIMIS-1) Kobe, Japan. Suppl. Trans. JIM 17 (1976) 93

[71] J. R. Patel and M. Cohen, *Acta Met.* **1** (1953) 531

[72] G. B. Olson, K. Tzusaki and M. Cohen, "*Statistical Aspects of Martensitic Nucleation*", Turnball Symposium*: Phase Transformations in Condensed Systems* ed. G. S. Cargill, F. Spaepen, and K. N. Tu, MRS

[73] G.B. Olson and M. Cohen, "*Martensitic Transformation as a Deformation Process*", MIT, 1982

[74] G.B. Olson and M. Cohen "*Kinetics of strain-Induced martensitic Nucleation", Met. Trans.* A, 1975 vol. **6A**, pp. 791

[75] G.B. Olson and M. Azrin, AMMRC, 1977

[76] G.B. Olson, M. Azrin and H. Band: *AC-Permeability Measurement of Strain-Induced Martensite during tensile Deformation of TRIP Steels*, AMMRC TR **77-10**, March 1977

[77] T. Narutani, G. B. Olson and M. Cohen. *J. de. Physique* **43** (1982) C4-429 – 434

[78] G. B. Olson, "*Mechanically-Induced Phase Transformation in Alloys*", Encyc. Mat. Sci. and Engg. Pergamon Press, 1982

[79] R. H. Leal: "*Transformation Toughening of Meta-stable Austenitic steels*," PhD Thesis, MIT, 1984

[80] G. N. Haidemenopoulos: "*Dispersed-phase Transformation Toughening in Ultra-High Strength Steels*," PhD Thesis, MIT, 1988

[81] C. C. Young: "*Transformation Toughening in PhosphoCarbide Strengthened Austenitic Steels*," PhD Thesis, MIT, 1988

[82] M. Grujicic, "*Stabilization of Precipitated Austenite in Tempered Fe-Mn-C Steels*", Mater. Sci. & Engg. A **127** (1990) 79-84

[83] C. J. Kuehmann: "*Thermal Processing Optimization of Nickel-Cobalt Ultrahigh-Strength Steels*," PhD Thesis, Northwestern University, 1994

[84] A. P. Miodownik and M. Hillert, "*A thermodynamic Treatment of the Ferromagnetic Transition in Alloys*", CALPHAD **4 #2** (1980) 143-153

[85] R. J. Weiss, "*The origin of the INVAR effect*", Proc. Phys. Soc. London **82** (1963) 281-299

[86] W. Bendick, H. H. Ettwig, and W. Pepperhoff, "*Thermally Excited Electron Transitions in FCC Iron Alloys*", *J MMM* 10 (1979) 214-216

[87] M. Matsui and S. Chikazumi, "*Analysis of Anomalous Thermal Expansion Coefficient of Fe-Ni Invar alloys", J. Phys. Soc. Japan* **45 #2** (1978) 458-465

[88] M. Matsui, K. Adachi and S. Chikazumi, "*Magnetic and Thermal Anomalies of Invar alloys", J. Phys. Soc. Japan* **51 #12** (1980) 6319-6325

[89] H. E. Lippard: "*Micro-analytical Investigations of Transformation-Toughened Co-Ni Steels*," PhD Thesis, Northwestern University, 1999

[90] R. J. Arsenault, S. Patu and D. M. Easterling, *Metall. Trans.* **20A**, 1419 (1989)

[91] R. J. Arsenault and S. Li, *Metall. Trans.* **20A**, 1429 (1989)

[92] U. F. Kocks, A. S. Argon and M. F. Ashby, in *Thermodynamics and Kinetics of Slip, Progress in Materials Science*, Vol. **19**. (1975)

[93] K. Ishida and T. Nishizawa, Trans. *Japan Inst., Metals* **15**, 217 (1974)

[94] G.B. Olson, k. Tzusaki and M. Cohen, in *Turnball Symposium.: Phase transitions in Condensed Systems*, p.129, Materials Research Society, PA (1987)

[95] G. Ghosh, G. B. Olson, "*Kinetics of FCC → BCC Heterogeneous Martensitic Nucleation – I. The Critical Driving Force for Athermal Nucleation*", *Acta Mater.* **42** (1994) 3361-3370

[96] G. Ghosh, G. B. Olson, "*Kinetics of FCC → BCC Heterogeneous Martensitic Nucleation – II. Thermal Activation*", *Acta Mater.* **42** (1994) 3371-3379

[97] Silcock, J.M. and Williams, N.T. "*Precipitation during aging at 700^0C of a commercial Austenitic steel containing titanium and aluminum*", *Journal of the Iron and Steel Institute*. 1966. November: pp. 1100-1107.

[98] Y. Liu, K. Ullakko, V. Gavriljuk, V. Nadutov and J. Pietikainen, *Proc. ICOMAT – **89** (edited by B. C. Muddle)*, p. 56. Trans. Tech. Publication, Zurich 1990

[99] S. Asgari, "*Structure and strain hardening of Superalloy AEREX 350*", Journal of Materials Processing Technology **118** (2001) 246-250

[100] N.S. Stoloff, in: C.T. Sims, W.C. Hagel (Eds.), *The Superalloys*, Wiley, New York, 1972, p. 361.

[101] R.W.K. Honeycombe, *The Plastic Deformation of Metals*, **2nd ed**., Edward Arnold, London, 1985

[102] L.M. Brown, R.K. Ham, *Strengthening Methods in Crystals*, Elsevier, Amsterdam, 1971, pp. 9–135.

[103] R.K. Ham, Ordered Alloys: *Structural Applications and Physical Metallurgy*, Claitors, Baton rouge, Louisiana, 1970, pp. 365–373.

[104] D. Raynor, J.M. Silcock, Met. Sci. J. **4** (1970) 121–130

[105] B.H. Kear, J.M. Oblak, A.F. Giamei, Metall. Trans. **1** (1970) 2477–2486.

[106] M. Safarzadeh, *MS Thesis*, Sharif University of Technology, 2004

[107] C. L. Briant and S. K. Banerji, in *Embrittlement of Engineering Alloys*, Academic Press, NY 1983

[108] D. Y. Lee, E. V. Barrera, J. P. Stark and H. L. Marcus, Metall. Trans. A, **15A**, 1415 (1984)

[109] C. L. Meyers, Jr., G. Y. Onoda, A. V. Levy and R. J. Kotfila, *Transactions of the Metallurgical Society of AIME*, 233, 720 (1965)

[110] J. Komedo and C. J. McMohan, Jr, *Metall. Trans.* ***12A***, 31 (1981)

[111] M. P. Seah, *J. Phys. F*, **10**, 1043 (1980)

[112] W. T. Geng, A. J. Freeman and G. B. Olson, "*Influence of alloying additions on grain boundary cohesion of transition metals: First Principles determination and its phenomenological extension*", Phys. Rev. B, **63**, 2001, p. 165415 1-9

[113] R. H. Doremus, *J. Appl. Phys.* **47**, 1833 1976)

[114] J. P. Stark and H. L. Marcus, *Metall. Mater. Trans. A* **8A** 1423 (1977)

[115] D. Y. Lee, E.V. Barrera, J. P. Stark and H. L. Marcus, *Metall. Mater. Trans. A* **15A** 1415 (1984)

[116] M. P. Seah, *Acta Metall.*, **28**, 955 (1979)

[117] P. Wynblatt and R. C. Ku, *Surf. Sci.* ***65***, 511 (1977)

[118] J. R. Rice and J. S. Wang, *Mater. Sci. Eng*., **A 107**, 23 (1983)

[119] M. S. Daw and M. I. Baskes, *Phys. Rev. Lett*. **50**, 1285 (1983)

[120] T. McMullan, M. J. Scott and E. Zaremba, *Phys. Rev. **B35***, 1076 (1987)

[121] G. S. Painter and F. W. Averill, *Phys. Rev. Lett.* **58**, 234 (1987)

[122] M. E. Eberhart and D. D. Vvedensky, *Phys. Rev. Lett*. **58**, 61 (1987)

[123] R. Wu, A. J. Freeman and G. B. Olson, Science **265**, 376 (1994)

[124] L. P. Sagert, G. B. Olson, and D. E. Ellis, Philos. Mag. B **77**, 871, 1997; L. P. Sagert, Ph. D Thesis, Northwestern University, 1995

[125] L. P. Zhong, R. Wu, A. J. Freeman and G. B. Olson, *Phys. Rev. **B** **55***, 11 133 (1997)

[126] W. T. Geng, A. J. Freeman, R. Wu, C. B. Gellar, and J. E. Raynolds, *Phys. Rev. B* **60**, 7149 (1999)

[127] W. T. Geng, A. J. Freeman, R. Wu, and G. B. Olson, *Phys. Rev. **B** **62***, 6208 (2000)

[128] E. Wimmer, H. Krakauer, M. Weinert and A. J. Freeman, *Phys. Rev. **B** **24***, 864 (1981)

[129] G. L. Krasko and G. B. Olson, "*Effect of Boron, Carbon, Phosphorus and Sulfur on Intergranular Corrosion in Iron*", U.S Army Materials Technology Lab, MTL, Solid State Communications, **Vol. 76**. No. 3, pp. 247-251, 1990

[130] J. G. Cowie, M. Azrin and G. B. Olson, "*Microvoid formation during Shear deformation of Ultrahigh strength steels*", *Met. Trans. A*, Vol. 20, **1**, 1989, 143-153

[131] C. Zener, *quoted by C. S. Smith*, Trans. A.I.M.E., **175**, 15 (1948)

[132] M. J. Gore, G. B. Olson and M. Cohen, "*Grain-Refining Dispersions and Properties in Ultrahigh-strength Steels*", in *Innovations in Ultrahigh-Strength Steel technology*, Sagamore Army Materials Research Conference Proceedings, **34**, pp. 425

[133] R. Stringfellow and D. M. Parks, "*Strain-Induced Transformation Toughening in Metastable Austenitic Steels*", Int. J. Plasticity **7** (1991) 529

[134] R. Stringfellow, "*Mechanics of Strain-Induced Transformation Toughening in Metastable Austenitic Steels*", Ph. D Thesis, MIT, Nov. 1990

[135] B. Sundman, B. Jansson, J. O. Andersson, "*The Thermo-Calc databank System*", *CALPHAD* **9** (1985) 153-190

[136] H. J. Jou, L. Li, C. J. Kuehmann, G. B. Olson, "*User Guide for CMD™ (Computational Materials Dynamics) Software*", Version 3/31/03, Questek Innovations LLC, Evanston, IL (2003)

[137] H. J. Jou, "Application *of Computational Materials Design Tools*", Questek Innovations LLC, Evanston, IL (2003)

[138] *Computer Coupling of Phase Diagrams Thermo-chemistry* (CALPHAD), http://www.calphad.org/; P.J. Spencer, "*A Brief History of CALPHAD*", Calphad, Vol. **32**, 2008, Pages 1-8,

[139] F. Latourte, *Ongoing Research*, Northwestern University, 2008

[140] ASTM E92 "*Standard test methods for determining Vickers Hardness of Metallic Materials", 2003*

[141] H.D. Espinosa and S. Nemat-Nasser, *Low-velocity impact testing*, *ASM Handbook* **8** (2000), pp. 539–559;

[142] L. Mori, *Doctoral Qualifying Exam*, 2006, Northwestern University

[143] H.D. Espinosa, A. Patanella and M. Fischer, *A novel dynamic friction experiment using a modified Kolsky bar apparatus*, *Experimental Mechanics* **40** (2000) (2), pp. 138–153

[144] S. Vaynman, M. E. Fine, S. Lee, and H. D. Espinosa, "*Effect of strain rate and temperature on mechanical properties and fracture mode of high strength precipitation hardened ferritic steels*", Scripta Materialia, **55(4)**:351–354, (2006)

[145] F. Barthelat, K. Malukhin and H. D. Espinosa, "*Quasi-Static and Dynamic Torsion testing of ceramic coatings using High-Speed photography*", In *Recent Advances in Experimental Mechanics*, Gdoutos, E.E. (Ed.). Kluwer Academic Publishers (2002)

[146] B. D. Cullity, in: *Elements of X-Ray Diffraction*, Addison-Wesley Publishing Co. Inc. Reading MA (1978) 412

[147] D. Ishiem and D. N. Seidman, "*Microstructural Characterization at the Atomic Level in Three Dimensions by 3D Local Electrode Atom Probe Tomography*", Presentation in Seidman Research Group, 2004, Northwestern University

[148] A. Cerezo, T. J. Godfrey, and G. D. W. Smith, *Rev. Sci. Instrum*. **59**, 862 (1988)

[149] M. K. Miller, A. Cerezo, M. G. Hetherington, and G. D. W. Smith, *Atom Probe Field Ion Microscopy,* (Oxford University Press, 1996)

[150] Imago Scientific Instruments Corp., Madison, WI, *http://www.imago.com/imago/*

[151] R. A. Karnesky, C. K. Sudbrack and D. N. Seidman, "*Best-fit ellipsoids of atom-probe tomographic data to study coalescence of γ' (L12) precipitates in Ni–Al–Cr*", *Scripta Materialia*, **57**, (2007), 353-356

[152] O. C. Hellman, J. A. Vandenbroucke, J. Rusing, D. Isheim and D. N. Seidman, "*Analysis of Three Dimensional Atom Probe data by Proximity Histogram*", Microscopy and Microanalysis **6** (2000) 437-444

[153] M. K. Miller, G. D. W. Smith, in: *Atom Probe Microanalysis: Principles and Applications to Materials Problems*, MRS Publications, Pittsburgh, PA (1977)

[154] M. Mulholland, *Ongoing Doctoral Research*, Northwestern University, 2007

[155] *Imago Visualization and Analysis Software (IVAS) Release 3.0*, Imago Scientific Instruments Corp., Madison, WI, September 2006

[156] *ASTM E 112-96 standard test methods for determining average grain size*, 1996

[157] Z. Feinberg, *Ongoing Doctoral Research*, Northwestern University, 2008

[158] M. K. Miller, G. D. W. Smith, in: *Atom Probe Microanalysis: Principles and Applications to Materials Problems*, MRS Publications, Pittsburgh, PA (1977)

[159] P. Sadhukhan, R. Glamm, J. Sebastian and G. B. Olson, "*Kinetics of γ' Nucleation and PrecipiCalc simulation of Capillary Energy in Ni-rich Austenitic TRIP Steels using 3-D Local Electrode Atom Probe Tomography*", *In Review Process*, 2008

[160] L. Mori, "*Lightweight Structures and Novel Steel Alloys Resistant to Blast and Fragments*", Doctoral Thesis, 2008, Northwestern University

[161] B. Hopkinson, *A method of measuring the pressure produced in the detonation of high explosives or by the impact of bullets*, Proceedings of the Royal Society of London. Series A, 89(612):411–413, (1914)

[162] R. M. Davies, *A critical study of the Hopkinson pressure bar. Philosophical Transactions of the Royal Society of London*, Series A, Mathematical and Physical Sciences (1934-1990), **240**(821):375–457, (1948).

[163] R. M. Davies. *A simple modification of the Hopkinson pressure bar*. In **24** *Proceedings of the 7th International Congress on Applied Mechanics*, volume 1, page 404, (1948)

[164] H. Kolsky. *An investigation of the mechanical properties of materials at very high rates of loading*. *Proceedings of the Physical Society*, **62**(11):676–700. doi:10.1088/0370-1301/62/11/302, (1949)

[165] V. P. Muzychenko, S. I. Kashchenko, and V. A. Guskov. *Use of the split Hopkinson pressure bar method for examining the dynamic properties of materials*: *Review. Industrial Laboratory*, 52:72–83, (1986)

[166] E. Hime, *Senior Thesis*, Dept. of Materials Sc. and Engg. Northwestern University, 2008

[167] G. M. Jenkins, "*The Systems Approach*" in: *Systems Behavior*, J. Beishon, G. Peters, eds., Open University Press, Birmingham, UK, (1972) 56-79

[168] G. Shi and S. A. Westgate, "*Techniques for Improving the Weldability of TRIP Steels using Resistance Spot Welding*", *TWI Research Reports*, 798, 2004, TWI Ltd, Cambridge, UK

[169] Echt J, Edelman L, McCarren M, Stempel K, Tu W, M. Bender, "*Civil Shield: Materials and Structures for Anti-Terrorism Blast Protection*", TMS 2004

[170] S. Chan, K. D'Aquilla, F. Du, J. Lee, P. Sadhukhan, "*Civil Shield: Blastalloy*", *Materials Design (MSE 390)*, Northwestern University, spring 2007

[171] C. Campbell, "*Systems Design of High Performance Stainless Steels*", Doctoral Thesis, 1997, Northwestern University.

[172] Frankel, G.S, *Pitting Corrosion*, *ASM Handbook*, Vol. **13A**. 2003.

[173] S. L. Sheets, R. Glamm, D. Cechetti, A. Ball, J. Li and P. Sadhukhan, "*Blastalloy II: Austenitic TRIP Steels*", *Materials Design (MSE 390)*, Northwestern University, spring 2008

[174] A. J. Goldman and W. D. Robertson, *Acta Metall.* **12**, 1265 (1964)

[175] M.K. Miller, Atom Probe Tomography: *Analysis at the Atomic Level*, Kluwer Academic/Plenum, New York, 2000

[176] M.K. Miller, E.A. Kenik, *Microscopy and Microanalysis* **10** (2004) 336–341

[177] J.M. Hyde, C.A. English, in: G.E. Lucas, L. Snead, M.A. Kirk, R.G. Ellman (Eds.), *Microstructural Processes in Irradiated Materials* – 2000, Materials Research Society Symposia Proceedings, vol. 650, Materials Research Society, Warrendale, PA, 2001, pp. R.6.6.1–R.6.6.12.

[178] E.A. Marquis, "*Microstructural evolution and strengthening mechanisms in Al–Sc and Al–Mg–Sc alloys*", Ph.D. thesis, Northwestern University, 2002

APPENDIX I

Experimental characterization of γ' $Ni_3(Ti_XAl_{1-X})$ precipitation: Evolution and coarsening of strengthening precipitates in non-stainless Austenitic TRIP Steels

Abstract

The 3D-Local electrode atom probe with voltage pulse method has been used to characterize and study the nucleation and coarsening of γ' strengthening precipitates in an austenitic TRIP Steel. Fully austenized specimens were heat-treated at 700°C for various times. Nucleation and subsequent coarsening of the γ' precipitate phase was measured by using a 50% TiNi iso-concentration surface boundary to separate the precipitates from the matrix. The *envelope*^{TM} method has been used to separate the precipitate clusters from the matrix to evaluate each precipitate property in detail. The variation in precipitate size (diameter), volume fraction of gamma prime and concentration of components has been measured and compared with those predicted by equilibrium thermo-calc calculations.

1. INTRODUCTION

Many Ni-rich austenitic TRIP steels such as the commercially used A286 and the recently developed BA120 [1] are age-hardenable by a fine dispersion of nanometer sized γ' precipitates. The strengthening mechanism employed in these alloys is the precipitation of the γ' intermetallic phase in equilibrium with the matrix phase, which impedes dislocation shear through APB formation. The γ', represented as Ni_3 (Ti, Al), is an ordered super lattice phase and has an $L1_2$ structure (ordered face centered cubic) [2] with very small lattice parameter misfit. Mechanical properties such as yield strength, UTS and creep resistance are strongly dependent upon the size and distribution of the γ' precipitates within the matrix [2, 3]. The low energy of its coherent interface with the matrix promotes precipitation by homogenous nucleation reaction. The coherency strain resulting from a lattice mismatch and existence of order in the particles is the major contributor to the strengthening mechanism. Earlier studies of high strain hardening due to

θ – particles [4] have shown that these precipitates are not cut by the dislocations due to deformation. The study on precipitation-hardened alloys with small coherent precipitates such as γ' in high Ni alloys have shown that precipitates are usually sheared by dislocations. The quantitative effect of the strengthening due to γ' precipitation in austenitic steels is documented by Silcock and Williams [5] on the commercial A286 austenitic steel. Their results provide a relationship between aging times, aging temperature, solution treatment temperature and γ' particle size which has been used effectively to model the amount of strengthening achieved in similar austenitic TRIP steels, per unit mole fraction of γ' phase present in the system at equilibrium [1].

In most Ni-rich alloys, the lattice misfit due to these coherent γ' precipitates is nearly zero [6]. In case of austenitic TRIP steels the precipitates have been found to be spheroidal in shape upto 750^{o}C for aging times less than 50 hours, although prolonged aging at higher temperatures have shown the f.c.c γ' precipitates to transform morphologically into undesired h.c.p plate-like $\boldsymbol{\eta}$ precipitates [1]. Thus, the classical theories of nucleation and coarsening such as the Langer-Schwartz supersaturation model [7] and the Olson – Umantsev [8] temporal power law model are applicable to these $\gamma - \gamma'$ equilibrium systems. To enable a successful computation system based design of optimum strengthening by γ' phase, it is necessary to have a better understanding of the kinetics of nucleation and coarsening of these precipitates in austenitic TRIP steels, under isothermal conditions.

Several studies of the thermodynamics of γ' precipitate nucleation and coarsening have been studied using conventional techniques such as the TEM [9, 10] and HREM [11]. However the nano-scale size of these precipitates makes them very difficult to analyze in detail using standard SEM and TEM characterization techniques, specifically in terms of distribution densities, inter-precipitate distance calculations and accurate analysis of the precipitate composition profiles. The need to view the precipitate distribution on a large scale and get quantitative analysis of its size, number density and intrinsic composition makes the 3-D LEAP much more viable option than a TEM or any other high resolution microscopy technique. The 3-D Local electrode Atom Probe ($LEAP^{TM}$) is a highly sophisticated imaging technique that combines the capabilities of chemical and analytical analysis at the atomic level and allows 3-D reconstruction of the volume

of material under study, thereby allowing an atom-by-atom investigation of its inherent intrinsic properties. Since it has such a high atomic scale resolution, it provides an accurate determination of the composition of any phase, using either the 1D profiling technique or the more stochastic proximity histogram or *proxigram* calculations [12]. Sudbrack et al. have earlier studied the temporal evolution of the smaller γ' Ni_3 (Al_xCr_{1-x}) precipitates in an f.c.c chromium rich solid-solution in a Ni-Al-Cr system using 3D Atom probe tomography [13].

With the advancement of predictive science-based computational materials engineering concepts, the use of thermodynamic software have been increasingly used to predict diffusive nucleation kinetics in multi-phase systems. In a continuation of this work, sophisticated PrecipiCalc^{TM} [14] software based on Thermo-Calc^{TM} [15] has been used to calculate and predict the 3D equivalent diffusive precipitation kinetics of the γ' phase [28]. The calibration and validation protocols for PrecipiCalc for γ' precipitation in Ni-based alloys has already been developed by Olson et al. [29] funded by the NASA-DARPA initiative. The output of PrecipiCalc includes the time evolution of Precipitate microstructure (size distribution, number density, and fraction); compositions of matrix and precipitate; driving forces, nucleation rates, and critical radii. Thus, PrecipiCalc allows the direct comparison of the predicted equilibrium concentration levels of different species based on its diffusion mobility databases and models and the data obtained from the 3D-LEAP tomography, and the difference in the predicted and measured concentrations has been used to define the capillary energy in the system for the two-phase $\gamma - \gamma'$ equilibrium for mass balance. The Kuehmann - Voorhees model [16] for isothermal coarsening in ternary Ni-rich alloys includes the effects of capillarity on the precipitate composition, such that both the matrix and precipitate compositions can deviate from their equilibrium thermodynamic values.

2. EXPERIMENTAL

The material used in this study is the alloy EX425. EX425 is a fully austenitic non-stainless TRIP steel developed by Dr. Stavehaug at MIT [17]. It is strengthened by precipitation of intermetallic **γ'** Ni_3 [Ti, Al] phase in metastable equilibrium with the f.c.c austenite matrix, the size and phase fraction of the precipitates being a function of the aging temperature and time. The composition of EX424 is shown in table 1.

	Ni	Cr	Ti	Mo	Al	V	Mn	C	B	Fe
EX425	25.04	3.93	2.91	1.25	0.16	0.32	0.09	.005	.0093	Bal

Table 1: Composition in wt% of alloy EX425

As reported by Stavehaug [17], the original EX425 was melted by Vacuum Induction at *Carpenter Technology Corp* into 100 lb ingots which were homogenized at 1190^{o}C for 24 hours, cooled to 1149^{o}C and forged into 3-inch square bars. They were further reduced in form of billets of 2.875 X 1.5 inch cross section. Before any heat-treatment, the billets were cut into smaller blanks and solution treated at 950^{o}C for 1 hr and quenched in oil to ensure a fully austenitic microstructure free from any precipitates. The as-quenched samples were then aged at 700^{o}C for various times – 5 min, 30 min, 1 hr, 5 hr, 10 hr, 25 hr, 50 hr, 100 hr and 200 hours. The reported measured yield stress and critical transformation temperature for aging at 700^{o}C for 50 hours is 130 ksi and -10^{o}C respectively [1]. All heat treatments have been done in vacuum, by encapsulating the samples in a glass ampoules and pumping down to ~10^{-6} torr, to avoid formation of any oxides on the surface [1]. Post aging and quench, blanks of size (0.2mm X 0.2 mm X 10 mm) were cut from the sections for the use in Atom Probe Tomography. These were then fixed into small copper crimps and sealed at one end. Then microtips were prepared using electropolising in two steps – first step involved macro-polishing using 10% perchloric acid in butoxyethanol solution at room temperature with a DC voltage of ~ 10-16 V enabling a steady current of 0.1-0.2 mA to form a slight taper. After this, the tip is washed very delicately with ethanol solution prior to micro-polishing. Once a nice thin taper is formed, in second stage of micro-polishing, we switch to a 2% perchloric acid in Butoxyethanol with a DC starting voltage of 7-9 V for final necking and slowly bringing down the applied voltage to 4-5V till a very fine layer is formed. At this moment, we switch from automatic voltage control to manual short-pulsing for a better control of the final breaking of the tip edge for a perfect finish of around ~ 40 – 50 nm [1].

Atom Probe analysis has been conducted at the *Northwestern University's Centre for Atom Probe Tomography* (NUCAPT) which houses the next generation LEAP (manufactured by *Imago Scientific Instruments*) [18]. Voltage pulsing is used to evaporate the ions from the

specimen tip surface. The ion evaporation was performed at a temperature of 60k ± 3k. The pulse fraction (ΔV/V – ratio of Pulse voltage to steady-state D.C. voltage) used is 0.20 based on calibration of Ni-ion concentration in austenite matrix, shown in figure 2(a). The pulse frequency and operating pressure were 200 kHz and $< 10^{-11}$ torr respectively. The average detection rate in the area of analysis ranged from 0.04 to 0.08 ions per pulse for the LEAP tomographic analyses [18].

The 3-D reconstruction of the ions evaporated from the analyzed volume is done using a software program IVAS^{TM} 3.0, developed by *IMAGO Scientific Instruments*. IVAS gives the option of selecting ions hit on all or any part of detector and uses a series of automatic time-of-flight and flight path corrections to calculate ion '*hit*' trajectories. Subsequently upon identification of the peaks in the mass spectrum, it gives a reconstructed image of the specimen showing each element/ion type in any specific color as desired. Any precipitates or phase differentials are easily observed due to the color contrasts and creation of concentration surfaces based on ionic segregation. IVAS allows excellent precipitate analysis using the *Envelope*^{TM} algorithm [19-22] method to create '*clusters*' to fit the spheroidal γ' precipitates, interface analysis and composition profiling. The envelope program is a cluster-search routine that uses Hyde's [21] maximum separation distance algorithm and then uses Miller's method [19, 20] to fill in precipitates with those elements which were not part of Hyde's maximum separation distance calculation. Karnesky et al. [23] further created an improved algorithm to fit γ' phase precipitates into equivalent ellipsoids while retaining their moments of inertia and principal axis, in a Ni-Al-Cr superalloy. The envelope algorithm allows the separation of coagulated clusters of γ' precipitates from the γ matrix based on a pre-defined inter precipitate separation distance and a delineating ionic species (*Ti* in this case) which has the highest slope/change in concentration at the γ - γ' interface. Detailed information on each cluster is then available in terms of its intrinsic concentration of all ionic species and the equivalent radius based on its atomic volume can be determined. While Ti is used as the delineating species for all γ / γ' interfaces, the maximum separation distance is taken as 0.6nm. The minimum number of ions for clusters is defined at the standard value of 50 and the grid spacing is taken as 0.12nm.

All γ / γ' interfaces reported in this work are identified by 50% TiNi iso-concentration surfaces [24] and the atoms contained within these isosurfaces were exported and analyzed using the modified envelope algorithm. The critical value of the iso-concentration surface is determined by step-by-step incrementing of the TiNi boundary concentration value till the bounded regions have a clear separation. Composition estimation is done by three different methods – a) 1D composition profiling, and b) Proximity Histogram [12] analysis of Iso-concentration surfaces, c) ion count from each cluster/precipitate. For calculating the 1D composition file, a pre-shaped section (Cylindrical, Cube or Sphere) can be selected with specific diameter/width to encapsulate any region of the reconstructed volume and all ions/atoms within that region selected is used to compute the 1D composition profile (Composition vs. Distance from edge). In this research, a cylindrical section of 20 nm diameter has been used in all 1D profiles generated. In cases where more detailed composition analysis (of precipitates or specific phases) is required, an Iso-concentration Proximity Histogram or '*Proxigram*^{TM}' method is used [12]. In this method, for a specific threshold concentration of a single or group of ions, the program creates contour plots of 3D regions highlighting volumes within the reconstruction where the minimum equilibrium boundary concentration is restricted by the threshold equilibrium concentration of ions specified. This method uses bins to identify each ion within their boundary, and computes the contours based on concentration differentials. All proxigram analysis plots in this work show the matrix austenite concentrations to the left of the interface (axis x<0) and the γ' precipitate concentration profiles to the right of the interface represent the precipitate composition (axis x>0). The standard deviation of the measured compositions of each ion/atom is calculated using the following equation [25].

$$\sigma = \sqrt{\frac{c(1-c)}{N}} \tag{1}$$

where c is the measured composition of the specific ion and N is the total number of ions. From the precipitate clusters obtained for each aging condition using the *envelope* algorithm, the 95% statistical confidence interval and average was taken for each ionic species to compute the mean precipitate composition.

Vickers Microhardness measurements have been taken on the aged specimens using an applied load of 200gm-f for 10s. The microhardness numbers (VHN) have been converted to estimated yield stress values for TRIP steels using Saha's relationship [26]. Microhardness measurements have allowed a direct quantitative relationship between the phase fraction of γ' precipitates and the corresponding estimated yield stress of the alloy.

3. RESULTS

3.1 Microhardness:

Before reporting the γ' precipitate analysis of nucleation and coarsening, the Vickers hardness results are presented. Microhardness measurements were taken on the fully austenized specimen (to determine the base strength of the austenite matrix) as well as all specimens aged at 700°C for various times listed earlier to determine the aging time corresponding to the peak hardness. Figure 1 presents the results of the Vickers hardness measurements with respect to aging time.

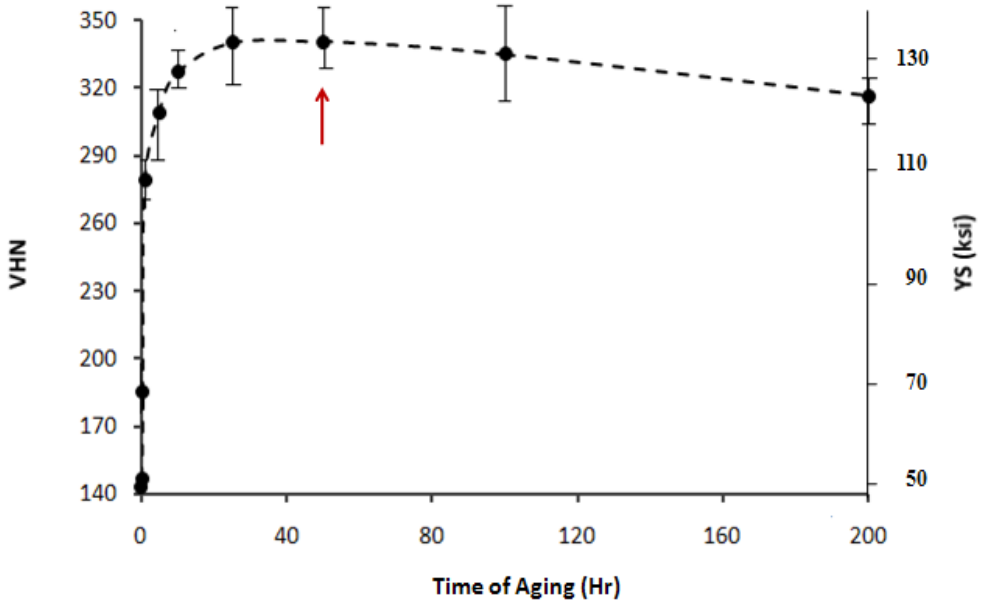

Figure 1: Dual-axis plot showing the variation of measured surface Vicker's microhardness of EX425 with aging time for EX425 specimens aged at 700°C, with the red arrow marking the time for peak hardness [1]. All specimens were solution treated at 950°C for 1 hr and quenched prior to aging. The figure shows rapid increase in surface hardness for times t = 0.083 hr to t = 1 hr due to γ' precipitation – nucleation. The predicted yield stress (ksi) is based on Saha's analogy of hardness vs. YS (ksi) for transformation toughened steels [1].

It is observed that the base hardness of the matrix austenite is ~ 148 VHN corresponding to a yield stress of ~ 49 ksi. During the nucleation stage of the γ' precipitation, the microhardness increases at a very steep rate, reaching 300 VHN (~ 116 ksi) in only 1 hr of aging. The peak hardness in EX425 is observed at 50 hr. The corresponding equivalent predicted yield stress is 130 ksi. Although the peak hardness is observed for ~ 50 hr, the range of aging time from 25 hr to 100 hours has comparable microhardness. Overaging leads to decrease in microhardness due to the coarsening of the γ' precipitates to large sizes and reduced number density within the matrix. The precipitation kinetics till $t = 1hr$ is expected to be very high.

3.2 Pulse Fraction Calibration:

The first step to LEAP usage is to calibrate the optimum pulse fraction necessary with uniform evaporation and minimization of ion loss during voltage pulsing. Usage of lower pulse fractions has previously shown loss of Ni in the measured composition for the matrix in EX425 [1]. Microtips prepared for fully austenized specimens of EX425 were run in the LEAP at a constant temperature (60k) and frequency (200kHz), but varying the pulse fraction from 0.15 to the max of 0.20. Fully austenitic specimens were used since they provide the best basis for calibration of the matrix Ni content when there are no γ' precipitates in equilibrium in the system. Figure 2 presents the variation of measured austenite matrix Ni content with LEAP pulse fraction and aging temperature.

It is seen from figure 2(a) that the minimum pulse fraction required for best Ni detection is 0.17. However similar runs for Cr and Ti have shown that using the maximum pulse fraction of 0.20 gives the best result in terms of concentration of ionic species [1]. Figure 2(b) shows the comparison of the measured Ni content with the predicted Ni content (using Ni-Data 7 [27] thermodynamic database in conjunction with Thermo-Calc^{TM} [15]) in the austenite matrix at different aging temperatures. Very good correlation between the predicted and measured concentration for Ni is observed for the Ni-data7 database, which has also been used later in PrecipiCalc simulations.

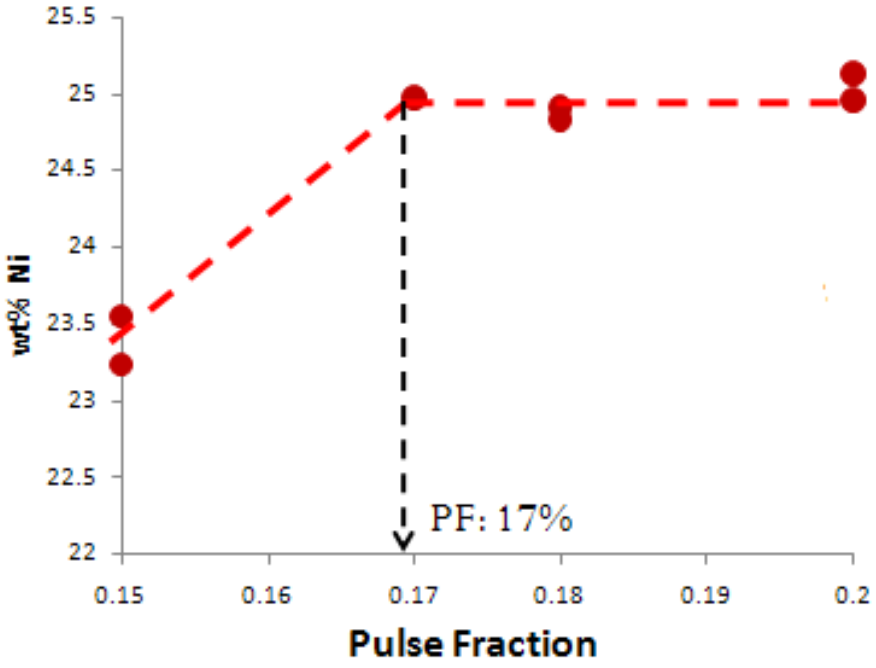

(a)

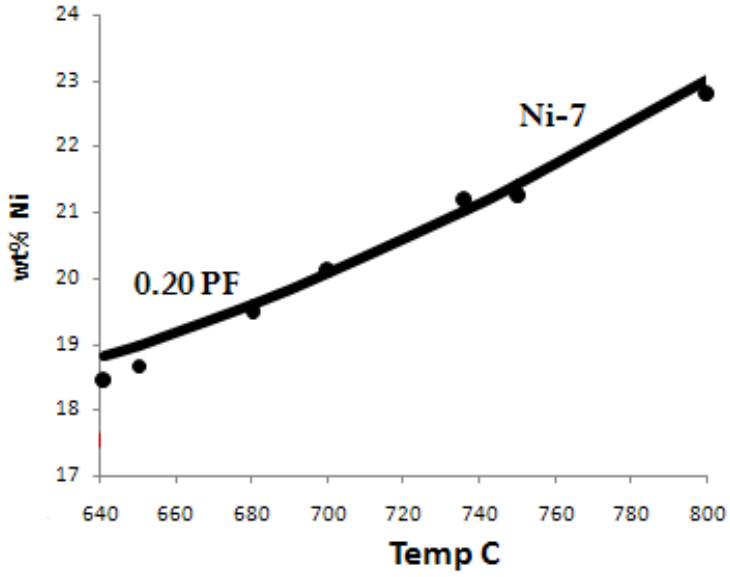

(b)

Figure 2: (a) Variation of measured Ni concentration in the austenite matrix with change in voltage pulse fraction using LEAP tomography. The brown dots represent actual experimental data **(b)** Variation of measured Ni in the austenite matrix using LEAP with a PF of 0.20, as a function of specimen aging temperature. The black dots represent the experimental data while the solid line represents the ThermoCalc predicted Ni equilibrium concentration at specific aging temperatures. All specimens used in this test have fully solution treated at 950^{o}C for 1 hr and quenched immediately in oil, to obtain a fully homogenous austenitic matrix, to enable calibration for Ni concentration [1].

3.3 Evolution of γ' precipitates

For *t = 0 hr* (no aging → fully austenized as-quenched sample), the 3D reconstruction of the analysis volume shows uniform distribution of the Ti and Ni ions without any segregation. No γ' precipitate can be resolved using TiNi iso-concentration surfaces, even with low threshold concentration limits (~ 5%), which shows that the specimen is homogenous f.c.c austenite microstructure. Earlier X-ray diffraction measurements using Cu K-α irradiation had shown presence of only austenite {220} peaks for the fully austenized specimen [1]. Figure 3 (a) shows the LEAP reconstruction of the specimen volume showing uniform distribution of the ions. Figure 3 (b) shows the cylinder for 1D composition profiling. From the 1D profile (fig. 4), no change in ionic compositions of the main components is observed, confirming the presence of a homogenous austenite matrix throughout.

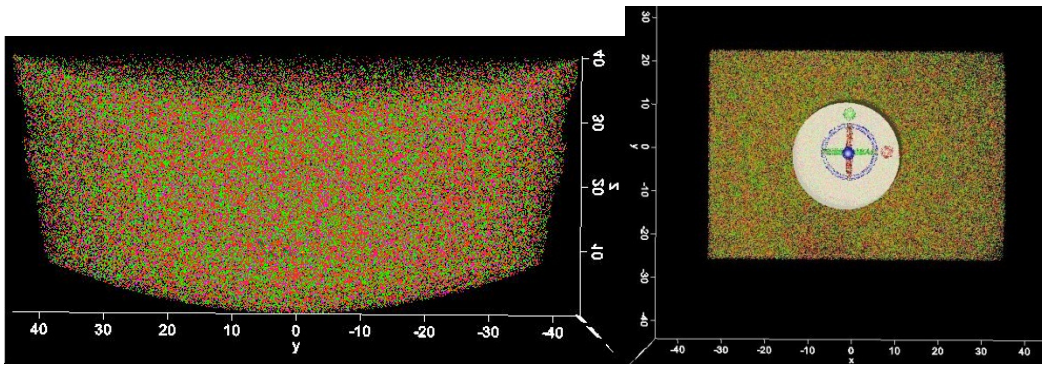

Figure 3: 2D Sections of the austenite matrix in EX425 from the 3-D reconstruction of the analyzed volume using LEAP^{TM}. The specimen microtip was prepared from a fully austenized (950^{o}C for 1 hr) blank of EX425, without any aging (*t = 0*). The images show only Ni (green) and Ti (red) ion distribution/ No segregation of Ti and Ni or formation of interfaces was observed on analysis of the reconstructed volume.

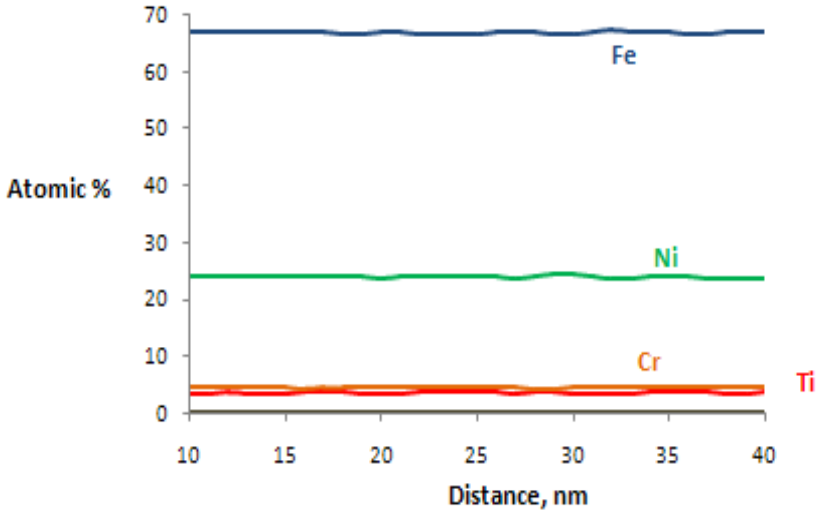

Figure 4: 1-D Composition profile of major constituents for figure 3 measured using 3-D LEAP Tomography. The length of 30 nm is for analysis along z-axis, as shown in figure 3 (b)

Figure 5 shows the evolution of the γ' precipitates in EX425 at 700°C as a function of aging time. All images represent a partial 2D section [50 nm X 45 nm] showing the precipitates represented in red using a 50% TiNi iso-concentration boundary surface. The background is austenite matrix represented primarily by Fe ions in blue, Ni ions in green and Ti ions in red. Analysis of LEAP reconstruction did not show any precipitates at t = 0.083 hr (5 min) using the 50 % TiNi iso-concentration interface binding method. However statistical analysis of the 1D concentration profile showed a minor decrease in Ni and Ti content from that of the predicted austenitic Ni and Ti contents, leading to the belief that segregation of Ni/Ti ions to form precipitate clusters have begun. Vickers microhardness measurements had earlier confirmed increase in the VHN number for the *t =0.083 (5 min)* stage as compared to the *t = 0* stage which also confirms the nucleation of the precipitate embryos at its sub-critical stage. However, the precipitate size is too small (< 0.1 nm) to be resolved even by the LEAP, thereby requiring more conventional methods such as the TEM/neutron scattering to detect actual presence of the precipitate clusters at these low times. For *t = 0.5 hr* (30 min) of aging, distinct small spheroids of γ' precipitates have been detected, with average diameter of 2-3 nm, using 50% NiTi iso-concentration surface binding. The small size led to a high number density of the precipitates (5.0×10^{24} m^{-2}); however the kinetics is still in the nucleation stage. Since there is a observed increase in the size of the

precipitates as well the number density, this stage is nucleation and coalescence. Rapid increase in size of the precipitate (high dR_{ppt}/dt) occurs till $t = 1\ hr$ after which the kinetics slow down and reaches a steady metastable equilibrium at ~ $t = 10\ hr$. At $t = 50\ hr$ (aging time for peak hardness), the spheroidal γ' precipitates are seen to be well developed with average diameter close to ~ 13nm and number density of precipitates being of the order of ~ 10^{24} m^{-2}.

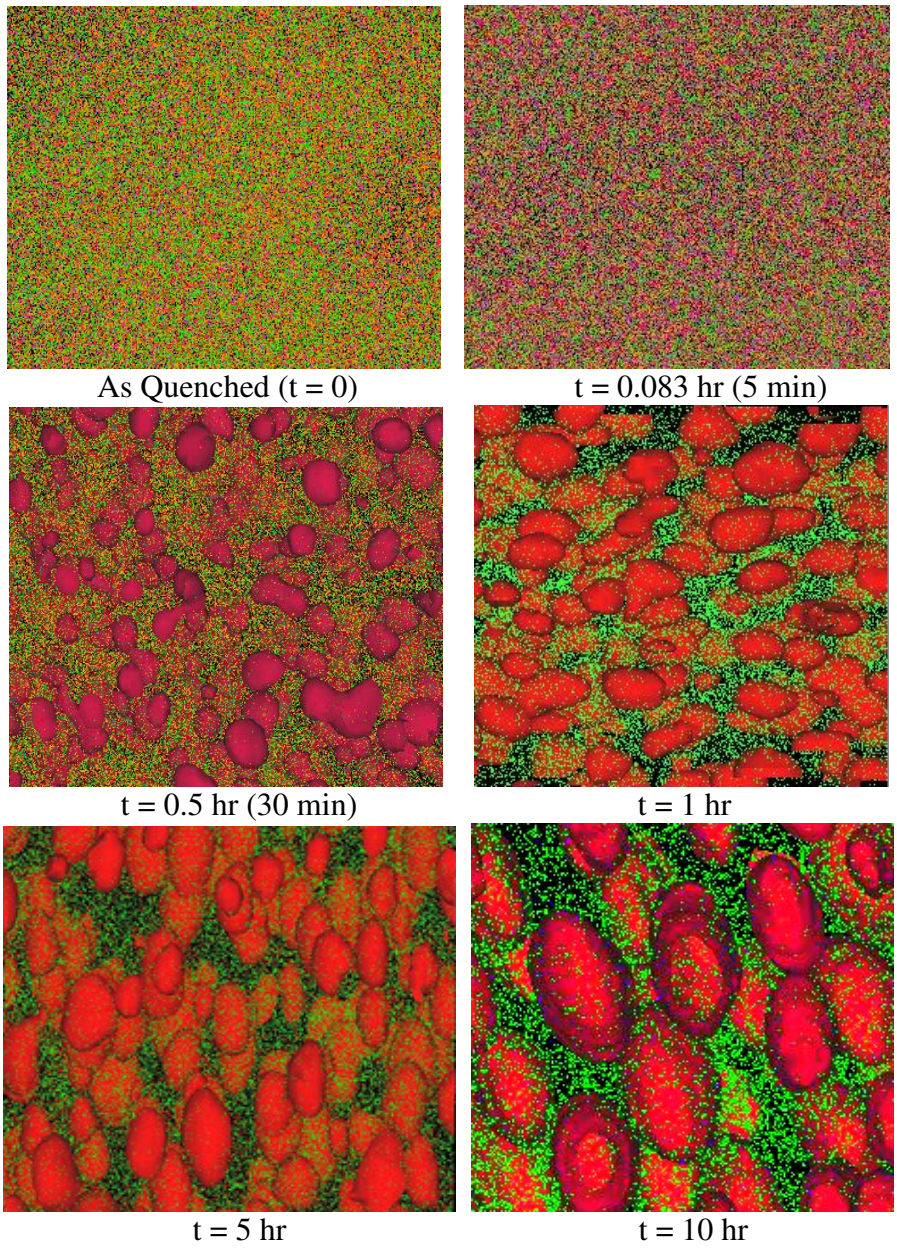

As Quenched (t = 0)

t = 0.083 hr (5 min)

t = 0.5 hr (30 min)

t = 1 hr

t = 5 hr

t = 10 hr

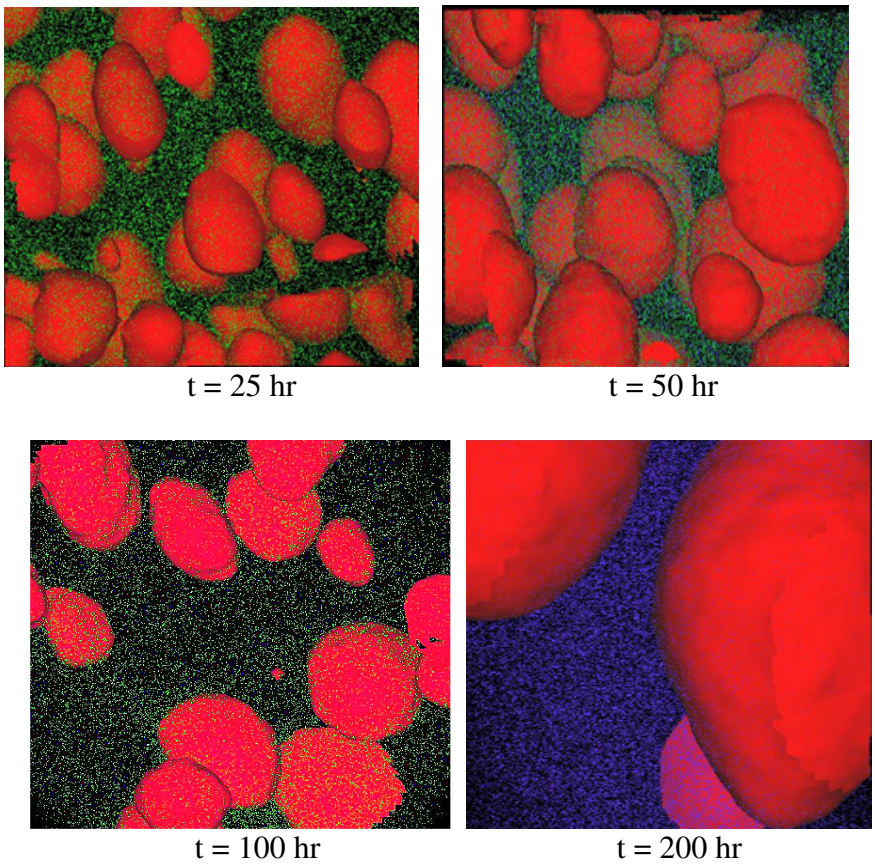

Figure 5: Clipped images of the 3-D LEAP reconstructions of the analyzed volumes for EX425 specimens aged at 700°C for various time. The red spheroids represent the 50% TiNi iso-concentration surfaces to show the γ' precipitates within the austenite matrix, which is primarily represented by the Fe (blue) and Ni (green) ions. In using the envelope method to form precipitate clusters, the entire dataset of the reconstructed volume is not used due to processing time constraints for datasets > 25 M ions. So a clipped dataset is used for all cases, with ion count 10-14 M for all cases while using the envelope algorithm.

The Ti-rich regions are clearly visualized in the reconstructed volume even without creating iso-concentration regions and the interfaces are highlighted by a sharp change in concentration profile for Ti, Ni and Fe ions – these ions show that highest change in their concentration levels. At $t = 100\ hr$, slight increase in precipitate size in noted although its distribution number density decreases by almost half. However on prolonged aging to times $t > 200\ hr$, precipitates as large as ~ 27 nm (d_{max}) in diameter is observed. On further analysis of the precipitate composition, they are observed to be higher in Ti and Ni contents and significantly lower in Al contents than what is predicted by Thermo-Calc for equilibrium γ - γ' system. It is also observed that the rate of

increase in γ' precipitate size (dR_{ppt}/dt) is maximum in the range $t = 0.083$ to $t = 1.0$ hr. From $t = 10.0$ *hr* to $t = 100.0$ hr, there is not much change in the sizes and the system is recognized to be in a metastable γ - γ' equilibrium, until the $t = 200$ *hr* stage. γ' precipitates are known to transform morphologically to h.c.p $\boldsymbol{\eta}$ structure at high temperatures for prolonged aging times and a higher Ti and Ni with lower Al content is predicted for these **η** precipitates thereby leading to the belief that the equilibrium is shifting towards γ - η system than staying at γ - γ' equilibrium. Formation of $\boldsymbol{\eta}$ precipitates but with a plate/band morphology has earlier been observed for EX425 at higher temperatures of 800°C using Laser pulse LEAP method [1]. This is a highly undesired phase as it reduces the uniform ductility of the TRIP steels under quasi-static and dynamic loading.

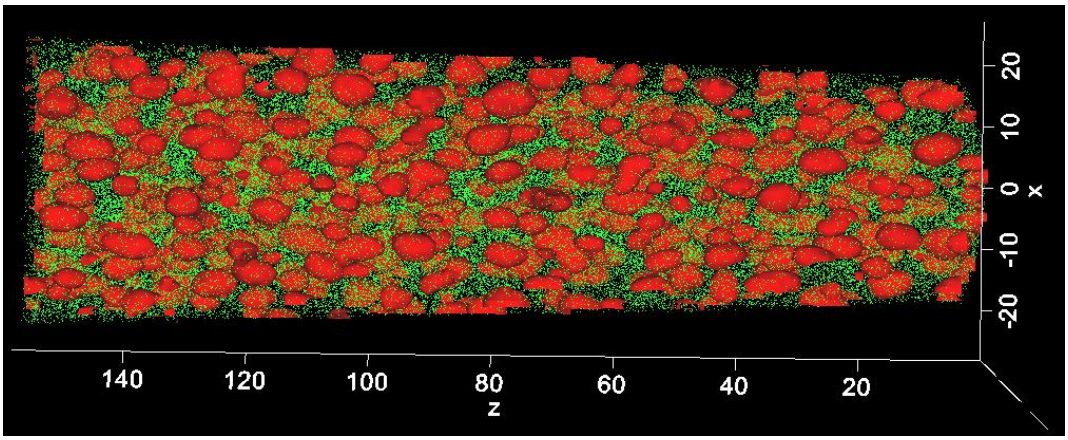

Figure 6: 3D reconstructed volume of the γ' precipitate distribution within the austenite matrix for EX425 specimen aged at 700°C for t = 1 hr. The red spheroids represent 50% TiNi iso-concentration surfaces which define the γ' precipitate clusters. The background is austenite matrix represented by the green Ni ions [40nm X 40nm X 160 nm]. To evaluate individual precipitates, a clipped file having only ~ 15 M ions is exported for analysis using the envelope algorithm to minimize processing times.

Figure 6 shows the full reconstruction of the analyzed volume of EX425 for t = 1hr. The complete size of the dataset is ~ () millions ions [40nm X 40nm X 160 nm]. It is observed that the precipitates are distributed evenly over the volume with a very high distribution number density at this aging time. From table 5 it is seen that the number density decreases post t = 1hr, thereby signaling the start of the pure coarsening stage. Upto this point, both nucleation and coarsening were observed.

3.4 Quantitative Precipitate Analysis

Austenite and Precipitate Composition

Atomic % - T(hr)	C_{Fe}^{γ}	C_{Ni}^{γ}	C_{Cr}^{γ}	C_{Ti}^{γ}	C_{Al}^{γ}	C_{Mo}^{γ}	C_{V}^{γ}
0	67.04 ± 2.33	24.11 ± 2.13	4.35 ± 1.14	3.43 ± 1. 44	0.34 ± 0.23	0.75 ± 0.40	0.36 ± 0.14
0.083	67.10 ± 2.63	23.92 ± 1.78	4.25 ± 1.01	3.39 ± 1. 26	0.33 ± 0.18	0.73 ± 0.51	0.35 ± 0.11
0.5	69.52 ± 3.03	22.14 ± 2.45	4.26 ± 1.08	2.74 ± 1. 12	0.30 ± 0.11	0.74 ± 0.15	0.33 ± 0.08
1.0	70.67 ± 2.73	21.61 ± 2.08	4.38 ± 0.87	2.01 ± 0. 76	0.22 ± 0.15	0.77 ± 0.37	0.37 ± 0.07
5.0	71.54 ± 2.15	21.33 ± 1.97	4.44 ± 0.98	1.42 ± 0. 68	0.18 ± 0.09	0.79 ± 0.46	0.38 ± 0.10
10.0	72.63 ± 2.27	20.32 ± 2.10	4.57 ± 1.24	1.18 ± 0.61	0.14 ± 0.13	0.80 ± 0.42	0.38 ± 0.06
25.0	73.03 ± 1.89	19.94 ± 2.03	4.67 ± 1.45	1.09 ± 0. 67	0.13 ± 0.10	0.80 ± 0.23	0.38 ± 0.08
50.0	73.12 ± 2.83	19.81 ± 1.67	4.71 ± 1.04	1.05 ± 0. 71	0.13 ± 0.07	0.81 ± 0.37	0.36 ± 0.05
100.0	73.25 ± 3.11	19.68 ± 1.85	4.68 ± 0.78	1.04 ± 0. 46	0.13 ± 0.06	0.81 ± 0.55	0.39 ± 0.11
200.0*	73.60 ± 3.63	18.79 ± 2.56	5.08 ± 1.71	1.03 ± 0. 61	0.12 ± 0.07	0.89 ± 0.61	0.42 ± 0.19

* represents γ - η system

Table 2: Measured austenite composition as a function of time for EX425 showing the migration of the ions, specifically Ni, Ti, Fe, Al and Cr towards the matrix-precipitate interface. Proximity histogram method has been used to obtain the concentration levels of each ionic species at a give aging time. The rate of change in concentration for Ti, Al and Ni $[(dC_{Ti}^{\gamma}/dt),\ (dC_{Al}^{\gamma}/dt)\ and\ (dC_{Ni}^{\gamma}/dt)]$ in the austenite matrix is maximum for the range $t = 0.083$ to $t = 1.0$ hr. All concentrations were calculated by taking a 95% statistical confidence interval of the measured proxigram profile starting from atleast 5nm from the interface boundary to allow for a steady state profile to develop. The error is calculated using equation (1), which are close to the limits obtained by the statistical analysis

The concentration of the ionic species in the matrix austenite and the γ' precipitates has been reported in tables 2 and 3 respectively. Only the data from the Proxigram analysis for all 50% TiNi iso-concentration surfaces have been reported, since the calculated error limit of 2σ is least for the proxigram method, as compared to the 1D-profiling and the ionic count from precipitate clusters. For the γ' precipitate composition analysis, the results are reported in terms of the concentration in the respective sub-lattice site fractions. From table 2, it is observed that the rate of change in concentration for Ti, Al and Ni $[(dC_{Ti}^{\gamma}/dt),\ (dC_{Al}^{\gamma}/dt)\ and\ (dC_{Ni}^{\gamma}/dt)]$ in the

austenite matrix is maximum for the range $t = 0.083$ to $t = 1.0$ hr. Rapid segregation of the Ti and Ni ions out of solution and towards the γ' precipitate interface can be seen from the LEAP reconstructions of the analyzed volume. Figure 7 shows the full reconstructed volume for $t = 1.0$ hr. From figure 10, the number density of the precipitates in this stage ($t = 1.0$ hr) is the maximum as compared to the other aging times signifying the nucleation stage. Post $t = 1.0$ hr, coarsening of the precipitates take place till it reaches the saturation equilibrium far-field matrix composition for 1/d → 0, for infinite diameter of the precipitates. The equilibrium extrapolated composition of the matrix is reported in table 4.

t (hr)	$C_{\gamma'}$ $(Ni_XFe_YCr_{1-X-Y})_3(Ti_ZAl_{1-Z})$
0	-
0.083	*- Not Detected -*
0.5	$(Ni_{0.547}Fe_{0.434}Cr_{0.019})_3(Ti_{0.941}Al_{0.059})$
1.0	$(Ni_{0.654}Fe_{0.338}Cr_{0.008})_3(Ti_{0.921}Al_{0.079})$
5.0	$(Ni_{0.765}Fe_{0.232}Cr_{0.003})_3(Ti_{0.920}Al_{0.080})$
10.0	$(Ni_{0.810}Fe_{0.187}Cr_{0.003})_3(Ti_{0.920}Al_{0.080})$
25.0	$(Ni_{0.816}Fe_{0.182}Cr_{0.003})_3(Ti_{0.919}Al_{0.081})$
50.0	$(Ni_{0.823}Fe_{0.175}Cr_{0.002})_3(Ti_{0.912}Al_{0.088})$
100.0	$(Ni_{0.835}Fe_{0.163}Cr_{0.002})_3(Ti_{0.907}Al_{0.093})$
200.0*	$(Ni_{0.901}Fe_{0.097}Cr_{0.002})_3(Ti_{0.927}Al_{0.073})$

* represents γ - η system

Table 3: Measured γ' precipitate composition reported in terms of its respective sub-lattice site fractions with Ni-Fe-Cr and Ti-Al as the two lattices. For $t = 0$, there is no γ' precipitate as it is a fully austenitic microstructure. For the case of $t = 0.083$ *hr* (5 min), the presence of γ' precipitates can be determined by the measured change in microhardness and the austenite/ γ' precipitate concentration, however due to their extreme small sizes (~ 0.1 nm), it could not be resolved by LEAP using iso-concentration surfaces.

It is to be noted that while using the envelope method to form precipitate clusters, the entire dataset of the reconstructed volume is not used due to processing time constraints for datasets > 25 M ions. So a clipped dataset is used for all cases, with ion count 10-14 M for all cases while using the envelope algorithm.

Precipitate Size

The arithmetic mean of the measured volume-equivalent radii for only single γ' precipitates, i.e., non-coalesced precipitates, contained fully within the volume, is used to calculate the precipitate radius for each aging time [13]. Thus, the radius of each precipitate cluster is calculated as,

$$R_{ppt.} = \left[\frac{2.n}{(equivalent\ atomic\ volume)}\right]^{\frac{1}{3}} \quad (2)$$

where 'n' is the total number of ions in the cluster. To determine the equivalent atomic volume, we use the Fe ionic volume of 84.9 nm^3. Since the detection efficiency is only 50-60%, a factor of 2 is included in the numerator of equation (2). For each aging time $t > 0.083\ hr$, two sets of precipitate cluster sizes have been observed. Along with the larger set of precipitates each with a defined critical ion count (n > 10k ions for t > 5hr), few smaller precipitates of ion count n < 1000 have been detected throughout the analysis volume, which can be seen in figure 5 for the images representing aging times $t = 10\ hr$ to $t = 100\ hr$. These two distinct classes of precipitate sizes have been treated separately, since the smaller clusters cannot be considered as fully developed and hence including their radii would give a lower estimate of the actual mean radii of the precipitates in the system. The precipitate diameters for each aging time are reported in table 5.

Figure 8 shows the semi-log plot of the variation of the austenite ionic concentrations as a function of the inverse of the precipitate size/diameter. As expected, the maximum slope is seen for the Ti ions, since these ions represent the highest change in concentration profiles for the γ - γ' interface and Ti acts as the delineating constituent between the two phases in envelope algorithm for precipitate cluster separation.

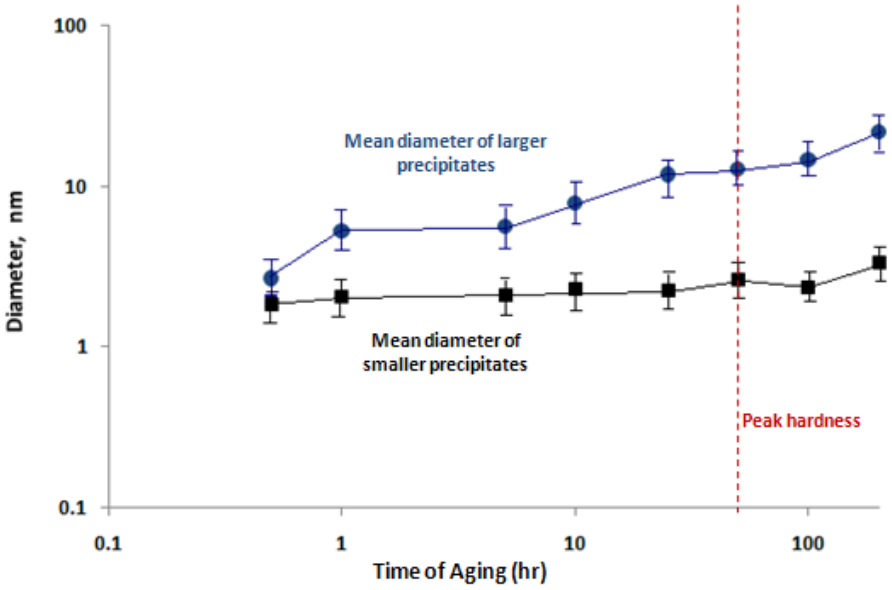

Figure 7: Variation of the measured γ' precipitate diameter as a function of aging time for EX425 specimens aged at 700°C. The variation is measured for two sets of precipitates defined by a preset critical size (n > 10k ions for t > 5hr). Most of the precipitates (70-80%) have n > 10k ions; however smaller precipitates are observed to be present throughout. It is observed from the data in table 4 that the average size of these smaller growing precipitates do not change much with aging time, although the size of the larger precipitates are directly related to the aging time.

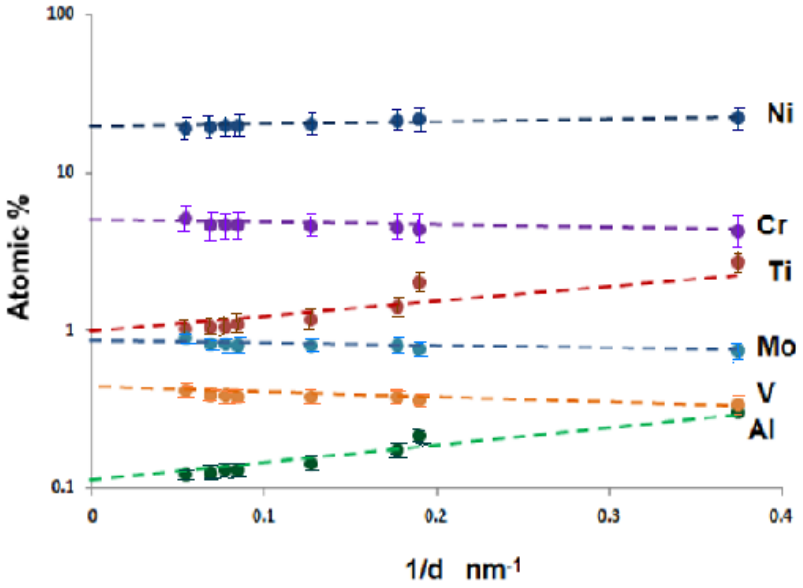

Figure 8: Variation of the austenite ionic concentration as a function of the inverse of precipitate size. The maximum slope is seen for Ti and Al ion concentrations, as two delineators of the γ - γ' interface. The linear extrapolation of these functions for each ionic concentration gives the predicted equilibrium concentration at **t = α** (1/d → 0).

To determine the predicted equilibrium concentration of the austenite matrix, a linear extrapolation of the concentration profiles for each ionic species is taken from figure 7. The equilibrium concentration at infinite time ($t = \alpha$) is represented as the time for the precipitate size to be infinite, d → α *(or, 1/d → 0).* In using the extrapolation, the data for $t = 200\ hr$ is not considered since it represents a shift in equilibrium from a γ - γ' system to a γ - η system due to the morphological transformation of the γ' precipitates into η. Table 4 presents the comparison of the predicted equilibrium concentration of the ions based on the linear extrapolation of the LEAP data and the predicted equilibrium concentration using Thermo-Calc in conjunction with Ni-Data7 thermodynamic database.

atomic %	C_{Fe}^{γ}	C_{Ni}^{γ}	C_{Cr}^{γ}	C_{Ti}^{γ}	C_{Al}^{γ}	C_{Mo}^{γ}	C_{V}^{γ}
t = α LEAP extrapolation	73.627	19.327	4.683	1.041	0.109	0.822	0.391
t = α Thermo-Calc	73.566	19.308	4.772	1.035	0.105	0.824	0.397

Table 4: Comparison of the predicted equilibrium concentration of EX425 at 700°C using LEAP extrapolation to *1/d → 0* from figure 9 and that predicted by Thermo-Calc using Ni-Data7 thermodynamic database

The optimum precipitate size for peak hardness at aging temperatures of 650°C, 736°C and 750°C have been previously measured to be 14.1, 14.0 and 14.5 nm respectively [1]. Thus very small change in optimum precipitate size is observed for different aging temperatures signifying that the Brown and Ham model of paired dislocation cutting has the same dependence on volume fraction (*f*) as the single-dislocation cutting model, for appropriate strengthening. The variation of a normalized precipitation strengthening term using phase fraction of gamma prime with respect to Precipitate radius was earlier calculated and shown in figure 9. The normalized strength of EX425 is calculated for the measured precipitate cluster diameter. The precipitate diameter is determined by first calculating the average effective volume of the clusters in each state, with Ti ions acting as the differentiating constituent from the matrix. Then using equivalent sphere geometry for each cluster, the average cluster radius is calculated. Figure 9 shows the

intersection of the best fit $r^{1/2}$ and $1/r$ curves for optimum radius. The optimum precipitate radius for maximum strengthening is calculated to be ~ 7.4 nm.

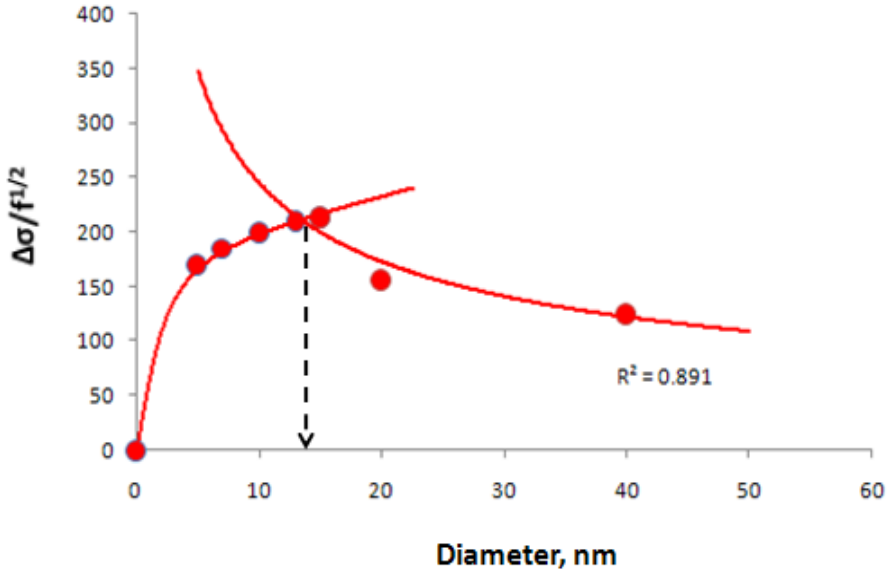

Figure 9: Determination of optimum precipitate diameter using normalized stress function with respect to measured gamma prime phase function [1].

The optimum diameter of 14.8 nm calculated using this model is related to the peak hardness assumption for similar classes of austenitic TRIP steels and is based on the Arrhenius time-temperature relation for peak hardness based on Stavehaug's data for EX425 [17].

Precipitate Phase fraction (f) and Number density (N_V)

The phase fraction and number density of γ' precipitates are important parameters in the strengthening mechanism of austenitic TRIP steels, based on the optimum stress required for dislocation shear [30, 31]. The ratio of the number of atoms within the clusters (or iso-concentration surfaces) and total number of atoms in the whole analysis volume is the calculated volume fraction (f) of γ' precipitates in the system. The number density, N_V, of the precipitates can be determined by taking the ratio of the number of clusters identified by the program having a minimum critical diameter and the effective volume of the sample size. This must include the

detection efficiency of a single ion detector, φ, the value of which is 0.5 - 0.6. The calculated phase fraction and number density for each aging time is reported in table 5.

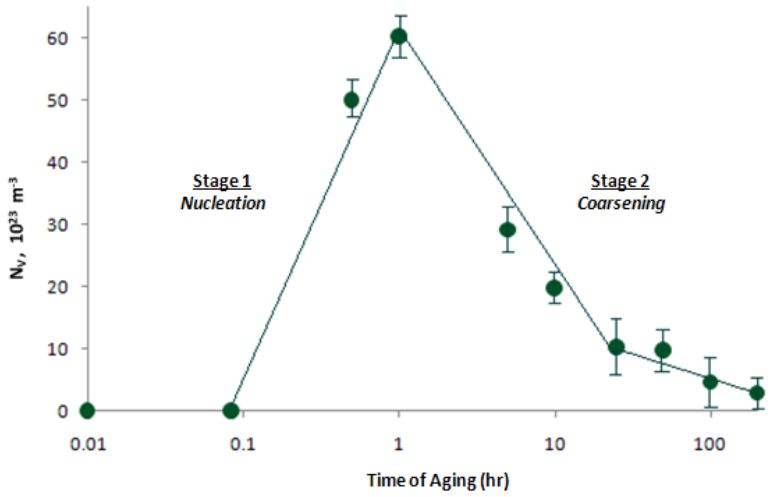

Figure 10: Variation of the calculated number density of γ' precipitates in EX425 specimens aged at 700°C as a function of the aging time. The peak number density is calculated for aging $t = 1hr$. Since there is both increase in size of precipitates as well as number density till $t = 1hr$, this stage is controlled by both nucleation and coarsening mechanism. However, for $t > 1hr$, only coarsening takes place which leads to the decrease in the overall number density of the precipitates.

The peak hardness is a function of both the optimum size of the precipitates as well as its number density (or volume fraction). This can be observed by comparing the results of the plots shown in figure 8 and 10. The peak hardness occurs at a time $t = 50\ hr$ as determined by the Vickers microhardness results shown in figure 1. The aging time $t = 50\ hr$ does not represent the peak number density however due to the combination of the appropriate precipitate size it results in maximum hardness, leading to the highest yield stress for the specimen. Figure 11 shows the calculated variation in the precipitated mole fraction of the γ' phase with aging temperature using Thermo-Calc. The predicted equilibrium phase fraction of the γ' precipitates at 700°C for EX425 is ~ 0.105. The measured volume fraction of the γ' precipitates for different aging times is reported in table 5 and plotted in figure 12.

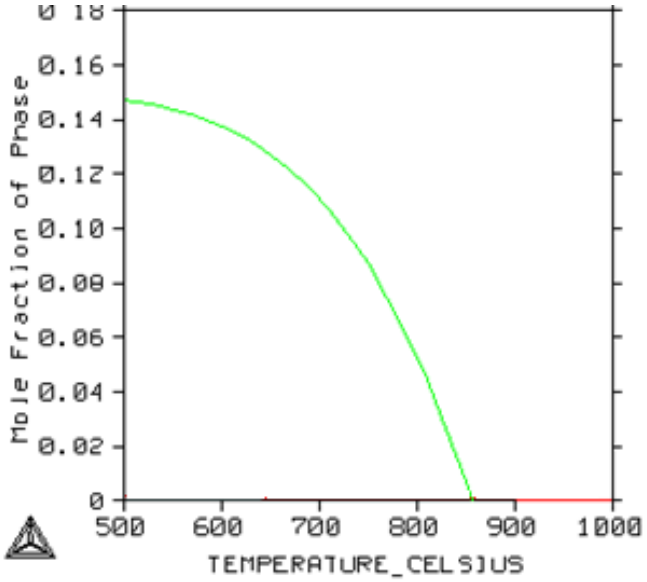

Figure 11: Temperature dependence of the mole fraction of gamma prime precipitate phase in equilibrium with matrix FCC austenite for EX425 calculated using Thermo-Calc software in conjunction with the thermodynamic database Ni-Data7 [1]

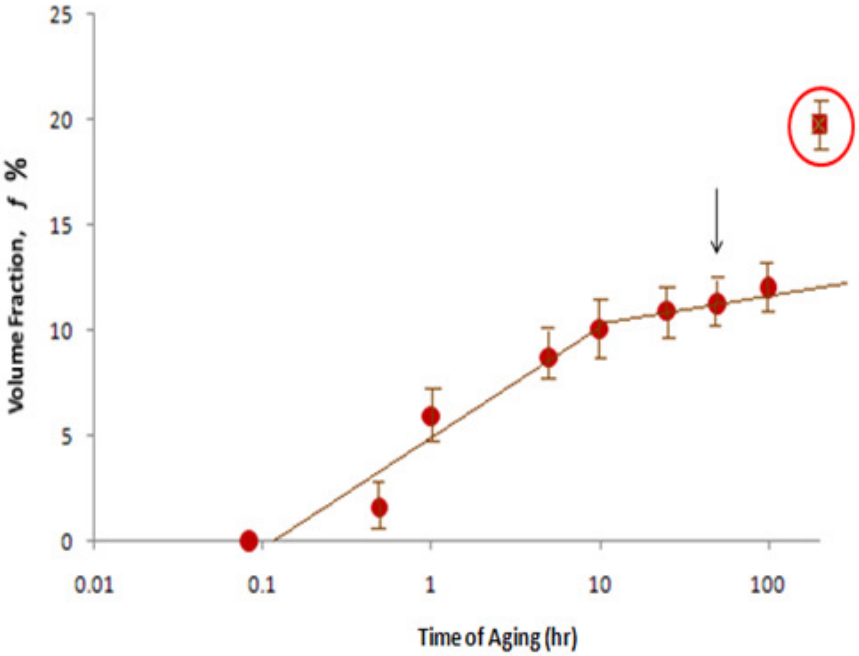

Figure 12: A semi-log plot showing the variation of the calculated volume fraction of γ' precipitate phase as a function of aging time. The calculated volume fraction at $t = 200\ hr$ is much higher than the trend for γ - γ' system due to the formation of η precipitates, and the respective datapoint is thus separated and marked in red circle. It is observed that the precipitate volume fraction reaches a steady state at $t > 1hr$

Interprecipitate Distance (IPD)

The mean edge-to-edge interprecipitate distance ($\lambda_{e-e}^{Ave.}$) for the precipitates within the analyzed volume can be determined by the equation [13, 23],

$$\lambda_{e-e}^{Ave.} = mod[(2.\frac{4}{3}\pi.N_V)^{-\frac{1}{3}} - R_{Ave}] \quad (3)$$

where R_{ave} is the mean radius of the precipitates for the given equilibrium aging temperature and time. The interprecipitate distance for each aging time is reported in table 4. The effort limit 2σ is determined from the limits for the radius R_{Ave} while using the 95% statistical confidence interval for the respective aging time (*t*) dataset.

Aging time *t*, hr	$d_{ppt}^{\gamma'}$, nm	$N_V \times 10^{24}$, m^{-3}	f	$\lambda_{e-e}^{Ave.}$, nm
0	-	-	-	-
0.083	*-Not Detected-*	*-Not Detected-*	*-Not Detected-*	*-Not Detected-*
0.5	2.671 ± 0.96	5.008 ± 0.45	0.016 ± 0.007	5.340 ± 2.02
1	5.288 ± 1.63	6.023 ± 0.92	0.059 ± 0.006	10.576 ± 2.87
5	5.644 ± 1.67	2.905 ± 0.85	0.087 ± 0.007	11.280 ± 3.71
10	7.892 ± 2.38	1.973 ± 0.18	0.100 ± 0.011	15.780 ± 4.06
25	11.849 ± 2.73	1.023 ± 0.21	0.109 ± 0.096	23.700 ± 6.33
50	13.764 ± 3.51	0.972 ± 0.13	0.112 ± 0.016	27.520 ± 6.20
100	14.923 ± 4.34	0.451 ± 0.17	0.120 ± 0.038	31.780 ± 6.89
200*	21.891 ± 6.78	0.276 ± 0.25	0.198 ± 0.059	43.780 ± 11.52

* represents γ - η system

Table 4: Calculated γ' precipitate phase properties within the austenite matrix for EX425 aged at 700°C for varying aging times. For *t = 0*, there is no γ' precipitate as it is a fully austenitic microstructure. For the case of *t = 0.083 hr* (5 min), the presence of γ' precipitates can be determined by the measured change in microhardness and the austenite/ γ' precipitate concentration, however due to their extreme small sizes (~ 0.1 nm), it could not be resolved by LEAP using iso-concentration surfaces.

3.5 Nucleation and Coarsening - Discussion

Although a detailed discussion of the capillary energy fit to the kinetics of the nucleation and coarsening of the γ' precipitation and a computational predictive methodology of using PrecipiCalc to determine coarsening in these precipitates using data from this work is presented in a continuation of this work [28], a brief discussion of the general theoretical dependence of the precipitate size and density is presented hereof. Langer and Schwartz [7] formulated basic kinetic rate equations to define the nucleation and separation of a secondary phase starting from the quenched state to supersaturation, in conjunction with the classical nucleation theory. Using Binder and Stauffer's [31] analogy where it was argued that the time required for nucleation reaction completion is more significant than the nucleation rate, Langer and Schwartz (LS) made several assumptions regarding the statistical properties of nucleation and growth of droplets in metastable supersaturated fluids, resembling the same kinetics as outlined in the two phase γ - γ' system described in this work. According to the LS model, a droplet of radius R (in this case a γ' precipitate cluster) and uniform concentration C immersed in a matrix phase A with supersaturation δC will grow at a rate given by [7] -

$$\frac{dR}{dt} \cong \frac{D}{R}\left(\frac{\delta C}{\Delta C} - \frac{2d_o}{R}\right) \tag{4}$$

Where D is the diffusion constant and d_o is the capillary length proportional to the surface tension. This equation also forms the basis of Lifshitz-Slyozov model [32] describing the growth of the precipitate/droplet post nucleation stage. In this regime, the time-dependent distribution of the precipitate phase droplets is described as a function of its radius R as [7] –

$$\frac{\partial \vartheta}{\partial t} = \frac{\partial}{\partial R}[v(R)\vartheta(R)] + j(R) \tag{5}$$

Where $v(R)$ is the radial velocity and $\frac{dR}{dt}$ is given by equation 4, $j(R)$ is the distributed nucleation rate. The LS model further derives the variation of the scaled mean radius ρ as a function of time τ, which after several assumptions based on the Lifshitz-Slyozov model, finally reduces to the form of [7] –

$$3\rho^2\frac{d\rho}{dt} \approx K \tag{6}$$

where K is a constant with a value of *4/9* based on Lifshitz-Slyozov analogy. The theoretical calculated aging time dependence of the size and density of the secondary phase droplets in the

supersaturated stage in the LS model can be compared directly with the aging time dependence of the measured precipitate size and number densities as represented in fig. 6 and fig 8 respectively. As presented by Sudbrack et al. [13], the temporal power law defining the coarsening rate constant for the γ' precipitate size derived from the Kuehmann-Voorhees model [16] is represented as –

$$R_t^3 - R_0^3 = K_R t \tag{7}$$

The calculated rate constant K_R is 0.75 × 10^{-30} m^3 s^{-1} for times *t = 1 hr* to *t = 100 hr;* which defines the primary coarsening stage of the process. The predicted model value is (0.56 – 1.3) × 10^{-30} m^3 s^{-1} which agrees very well with the LEAP determined coarsening rate constant. In continuation of this work, Glamm et al. [28] have described thermodynamic modeling using PrecipiCalc simulations to introduce a capillary energy term to have a better fit to experimental values obtained in this work. Detailed discussion of the kinetics with respect to the Langer Schwartz model is presented in the same.

4. CONCLUSIONS

1. Characterization of the γ' precipitate nucleation and coarsening in an experimental TRIP model prototype EX425 has been done in terms of measuring precipitate properties including size and concentration profiles for the γ - γ' interface using 3D Local electrode Atom-Probe tomography technique and voltage pulsing method. Although extreme small sizes of the precipitates at t = 0.083 hr could not be resolved by this method, accurate precipitate size and density measurements were made possible by the using the envelope algorithm to separate the precipitate clusters from the austenite matrix.

2. Using Vickers microhardness measurements, the peak hardness was confirmed for an aging time of t = 50hr for aging temperature 700°C. The optimum precipitate size at 700°C was measured to be 13.76 nm with a calculated volume fraction of 0.112 which compares well with the thermo-calc predicted volume fraction of 0.108. The optimum precipitate size for peak hardness has been shown to be independent of aging temperature; which signifies that nucleation is mainly diffusion controlled with respect to aging time.

3. At t = 0.5 hr, small spheroids/droplets of γ' precipitates are observed within the austenite matrix, with an average size of ~ 2-3 nm and an increasing number density.
4. The maximum number density of the γ' precipitate distribution is calculated to be at t = 1hr; signifying the end of the nucleation phase and start of primarily coarsening stage. For t > 1hr, both nucleation and coarsening is observed. The rate of diffusion kinetics, with respect to concentration and size change, is very high till t = 0.5 hr, as can be observed from the data in table 2,3 and 5 with respect to change in precipitate and far-field austenite compositions and average precipitate diameters. Uniform distribution of the γ' precipitates is seen for times upto 100 hrs and the shape of the precipitates is primarily spheroidal.

5. Two sets of precipitates have been observed for each aging time – one with high number of ions which meets the criteria for a well developed precipitate cluster and the other with relatively smaller number of ions and diffusing boundaries. To calculate the average precipitate sizes and number density, only precipitates with a certain critical number of total ions are considered (n > 10k ions for t > 5hr).

6. Equilibrium composition of the matrix has been calculated by extrapolating the concentration profiles for each ionic species till t = α at which point the precipitate size can be considered to be infinite. The equilibrium composition obtained is then compared with the predicted Thermo-calc equilibrium compositions for EX425 and found to have a good match.

7. The size and composition of the γ - γ' system evolves as a function of time; for prolonged aging the γ' precipitates have been shown to have much higher Ti and Ni and low in Al as compared to the equilibrium predicted value by Thermo-calc, signifying the slow morphological transformation of the γ - γ' system to a $\gamma - \eta$ equilibrium system.

8. The calculated coarsening rate constants K_R is 0.75 × 10^{-30} m^3 s^{-1} which compares very well with the theoretically predicted value of (0.56 – 1.3) × 10^{-30} m^3 s^{-1} from the Kuehmann-Voorhees model [16] thereby suggesting adherence to classical predicted diffusion kinetics.

ACKNOWLEDGEMENTS

Financial support by Office of Naval Research (N00014-0400798) is acknowledged. Atom-probe tomographic analyses were performed at the Northwestern University Center for Atom-Probe Tomography (NUCAPT). The LEAP™ tomograph was purchased with funding from the NSF-MRI (DMR-0420532) program. We extend our gratitude to Dr. Jason Sebastian for his helpful suggestions towards the betterment of this work.

References

[1] Sadhukhan, Padmanava, "*Computational Design and Analysis of high-strength Austenitic TRIP Steels for blast-protection applications"*. Doctoral Thesis, 2008, Northwestern University

[2] S. Asgari, "*Structure and strain hardening of Superalloy AEREX 350*", Journal of Materials Processing Technology **118** (2001) 246-250

[3] N.S. Stoloff, in: C.T. Sims, W.C. Hagel (Eds.), *The Superalloys*, Wiley, New York, 1972, p. 361.

[4] R.W.K. Honeycombe, *The Plastic Deformation of Metals*, **2nd ed**., Edward Arnold, London, 1985

[5] Silcock, J.M. and Williams, N.T. "*Precipitation during aging at 700^{0}C of a commercial Austenitic steel containing titanium and aluminum*", *Journal of the Iron and Steel Institute*. 1966. November: pp. 1100-1107.

[6] Taylor A, Floyd RW. J Inst Met 1952–53; 81:451.

[7] J. S. Langer and A. J. Schwartz, "*Kinetics of nucleation in near-critical fluids*", Phys. Rev. A, **3**, Vol. 21, March 1980

[8] Umantsev A, Olson GB. Scripta Metall 1993;29:905.

[9] Hirata T, Kirkwood DH. Acta Metall 1977;25:1425.

[10] Kirkwood DH. Acta Metall 1970;18:563.

[11] Xiao SQ, Haasen P. Acta Metall Mater 1991;39:651.

[12] O. C. Hellman, J. A. Vandenbroucke, J. Rusing, D. Isheim and D. N. Seidman, "*Analysis of Three Dimensional Atom Probe data by Proximity Histogram*", Microscopy and Microanalysis **6** (2000) 437-444

[13] S. K. Sudbrack, K. E. Yoon, R. E. Noebe and D. N. Seidman, "Temporal evolution of the nanostructure and phase compositions in a model Ni-Al-Cr alloy", Acta Materialia **54** (2006) 3199-3210

[14] PcP

[15] B. Sundman, B. Jansson, J. O. Andersson, "*The Thermo-Calc databank System*", *CALPHAD* **9** (1985) 153-190

[16] Kuehmann CJ, Voorhees PW. Metall Mater Trans 1996;27A:937.

[17] Stavehaug, F., "*Transformation toughening of γ'–strengthened metastable austenitic Steels"*. Doctoral Thesis, 1990, MIT

[18] Kelly TF, Camus PP, Larson DJ, Holzman LM, Bajikar SS.
Ultramicroscopy 1996;62:29.

[19] M.K. Miller, Atom Probe Tomography: *Analysis at the Atomic Level*, Kluwer Academic/Plenum, New York, 2000

[20] M.K. Miller, E.A. Kenik, *Microscopy and Microanalysis* **10** (2004) 336–341

[21] J.M. Hyde, C.A. English, in: G.E. Lucas, L. Snead, M.A. Kirk, R.G. Ellman (Eds.), *Microstructural Processes in Irradiated Materials* – 2000, Materials Research Society Symposia Proceedings, vol. 650, Materials Research Society, Warrendale, PA, 2001, pp. R.6.6.1–R.6.6.12.

[22] E.A. Marquis, "*Microstructural evolution and strengthening mechanisms in Al–Sc and Al–Mg–Sc alloys*", Ph.D. thesis, Northwestern University, 2002

[23] R. A. Karnesky, C. K. Sudbrack and D. N. Seidman, "*Best-fit ellipsoids of atom-probe tomographic data to study coalescence of γ' (L12) precipitates in Ni–Al–Cr*", *Scripta Materialia*, **57**, (2007), 353-356

[24] O.C. Hellman, J. Blatz du Rivage, D.N. Seidman,
Ultramicroscopy 95 (2003) 199–205.

[25] M. K. Miller, G. D. W. Smith, in: *Atom Probe Microanalysis: Principles and Applications to Materials Problems*, MRS Publications, Pittsburgh, PA (1977)

[26] A. Saha and G.B. Olson, "*Computer-Aided design of transformation-toughened blast-resistant naval hull Steels: Part 1*", Journal of Computer-Aided Materials Design, Vol. 14, **2**, July 2007, 177-200(24)

[27] Sente Software, ThermoTech thermodynamic database bank, http://www.sentesoftware.co.uk/databases.html#Ni-DATA

[28] R. Glamm, Z. Feinberg, P. Sadhukhan, and G. B. Olson, "*Kinetics of γ' Nucleation and PrecipiCalc simulation of Capillary Energy in Ni-rich Austenitic TRIP Steels using 3-D Local Electrode Atom Probe Tomography*", *In Process*, 2008

[29] L.M. Brown, R.K. Ham, *Strengthening Methods in Crystals*, Elsevier, Amsterdam, 1971, pp. 9–135.

[30] R.K. Ham, Ordered Alloys: *Structural Applications and Physical Metallurgy*, Claitors, Baton rouge, Louisiana, 1970, pp. 365–373.

[31] K. Binder and D. Stauffer, Adv. Phys. **25**, 343 (1976)

[32] I. Lifshitz and V. Slyozov, J. Phys. Chem. Solids **19**, 35 (1961)

APPENDIX II

Civilian Applications of Blastalloy

While the focus of the research in this thesis has been on systems-based computational design of advanced materials with high strength and stretch ductility for improved blast protection applications, specifically for the U.S. Navy in building ships, several applications of these new alloys related to civilian safety has been explored. In the past few years, several undergraduate design teams (EDC and IDEA) at Northwestern University have investigated the feasibility of using sandwich-laminate structures of these materials for non-military applications using quantitative simulations of 'blast'. Under the umbrella of the project named 'CivilShiled', the following civilian applications have been explored by EDC and IDEA teams since 2004 –

a. Ground Transportation → Commuter Trains and Hummer H2
b. Safe room
c. Trash receptacles

Prior to discussing the design and applicability of each of the above proposed solutions, it is important to quantify a '*blast*'. The impact of an explosion on a surface depends on the amount of explosive material and the distance between the explosion and target, termed as the "*standoff distance*". The velocity of the wave front increases with explosive size and decreases as standoff increases. The wave front velocity perpendicular to a surface creates a large momentary pressure peak, followed by a short time of reduced pressure at the surface [C1-McCarren 398'04].

a. Ground Transportation → Commuter Trains and Hummer H2

One of the first civilian applications explored was to implement the new alloys into commuter trains, inspired by the recent Madrid bombings in March 2004 and the London bombings in July 2005, which brought forth the need for better protection on board commuter trains. In order for this implementation to substantially increase the safety of passengers on the trains in the case of a blast, new physical configurations and train policies had to be implemented. Current train designs include 1-2 doors at either end of the car and a long, open compartment with seats for passengers which expose them to the vulnerabilities of a backpack bomb. These vulnerabilities can be easily decreased by developing new train configurations. Various train configurations have been proposed by an IDEA team in 2005 [C2]. These configurations, in conjunction with the new alloys to make the individual compartments able to protect against internal explosions, will greatly increase the safety of passengers. To make sure the new alloy can be implemented in cabins in such a way that its blast-protective capabilities are maximized, several new cabin layouts for commuter trains have been investigated [C2]. However, there is a tradeoff between safety and comfort in these configurations. After much research and consideration, implementation of the new alloy in overhead bins was determined to not to be feasible. While the addition weight of each train is less than 25% of a current train, which involves extra cost concerns. Therefore, while it is feasible to employ the alloy, the additional requirements may make this option impractical.

To overcome the difficulties of protection in the commuter train application, the armoring of a car was chosen. Using a car as a platform to display improved blast resistance is reasonable because it provides the opportunity for the passengers to be separated from the terrorists at all

times. So ground transportation systems using the example of the Hummer H2 was considered by EDC team in 2005 [C3-Liz Abrahamson]. The H2 seemed like an ideal application due to its reasonably flat side panels and ability to carry the additional weight added by the truss structure. A potential weakness of the application lay in the vehicle's windows, which the Blastalloy could not protect. An armored car application for the proposed technology has been under consideration since the beginning of the project. Marketability of such a product is proven by the success of the Mercedes-Benz S500 Guard series, which is designed to not only protect primarily against ballistic attacks, but also purports to have improved resistance to explosive blasts. Only the passenger cabin could be effectively protected because it is the most critical for rider safety and additional weight will therefore not be wasted on less important sections of the car. It was determined that a mixture of monolithic and sandwich metal structures, with the addition of bulletproof glass, would be the most effective way to efficiently protect the H1 [C3]. Sandwich structures with a relatively thin face sheet thickness (~1.37 mm) on the large, flat, low-impact places, such as the roof, firewall, and rear might be used. This provides lightweight protection in the areas where an explosion would either be deflected by other pieces of equipment (e.g. the engines blocking direct access to the firewall) or a place less likely for a bomb to detonate (e.g. a bomb on the roof). Thicker face sheet (~3.2 mm) sandwich structures could be chosen for the floor pan because the likelihood of a close, large explosion, such as a mine or improvised explosive device (IED), is very high. The doors would be made out of relatively thick (~6.25 mm) monolithic plate due to the complicated shapes necessary for forming the door to accommodate locks and to fit into and around the car frame properly.

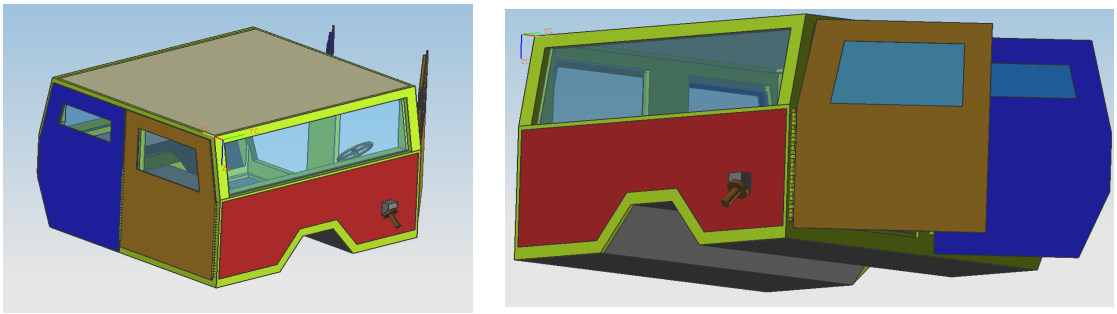

Figure C1: Diagram model of an experimental H2 cabin, as designed by EDC'05, NU

b. Safe Room

Kevlar and Steels are the two most common materials used for building Safe rooms; the former is lightweight but only has half the blast resistant capability of the latter, while the steels are heavy and difficult to customize. An EDC'07 team [C4] at Northwestern looked at the feasibility of used austenitic TRIP 120 alloys in laminate structures for adequate safe room applications. The team built a system for a safe room which showed nearly ten fold increase in blast protection, while showing a major decline in cost and weight. This system has been shown to be easily manufactured, distributed, and installed without destroying and rebuilding the existing structure. The design approach has led to the belief that with the future creation of lighter, stronger, cheaper materials this field of safe room technology will grow and evolve faster than any other field of its kind. The designed saferoom combines numerous technologies and structures to form a room that is strong, secure, lightweight, and effective. The room itself is 8' x 8' x 8' and is made from austenitic TRIP BA120 panels. The corners of the saferoom, as well as the ceiling, are further supported by extra lap joints that buttress the edges of the room. These extra corners are also made from BA120, and will overlap each wall by at least 3 inches. The rooms also welds strong support structures, as well as secure ventilation, which is very important for any safe room design. To ensure proper air flow, there must be at least 1 square inch of air space for each square foot of floor space. Therefore, there must be an opening 8 by 8 inches in size, or at least 64 square inches of ventilation. The folded plate structure of the saferoom is advantageous because the crushing of the internal truss structure absorbs energy, and allows the steel to take more impulse for the same weight, when compared to a solid, monolithic plate of same steel. The weight of the panel is only about 60 pounds each. The size is also useful because it is the standard size for drywall panels, which means that the panels can be easily transported and installed. These features satisfy our requirements for a lightweight and portable, yet strong system. BA120 is selected as the steel of choice because of the high energy absorbance it has, as shown by the area under the stress vs. strain curve in chapter 6. For a maximum stress of 0.2, which was found to be acceptable by users in terms of a survey, BA120 outperforms Blast Alloy 160, Kevlar, and stainless steel in terms of deflection per unit impulse absorbed. This extra impulse absorption capability will allow inhabitants to withstand that much stronger of a blast,

another user requirement. Also, BA120 costs only ~$60 in raw materials, making the room cost effective.

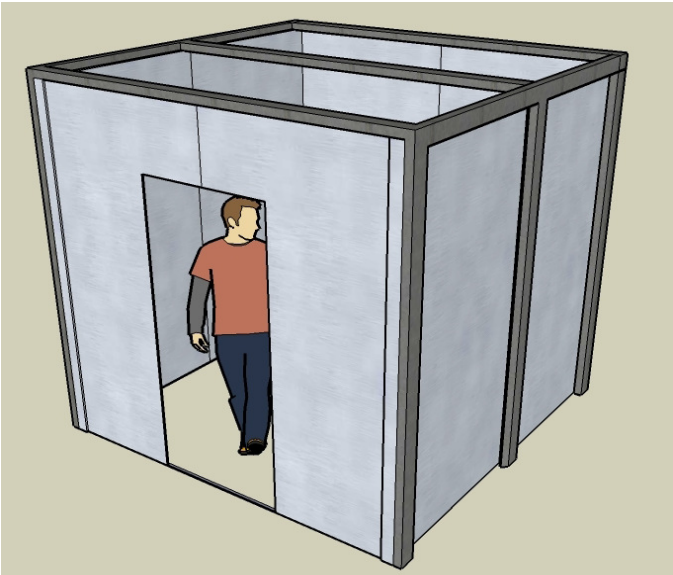

Figure C2: Model of designed Saferoom, EDC spring 2007, Northwestern University

c. Trash Receptacle

The bomb containment trash receptacle option was found to be a viable application for the blast resistant BA120. Currently, similar devices are employed in airports, mass transit systems, mailrooms, courts, military installations, and government buildings. Recently, the Washington Metropolitan Transit Authority spent over $ 1 million installing 400 bomb containment trash receptacles in the DC metro system, proving an evident market for the application. As opposed to the safe room, which only protects the few occupants inside, blast proof trash receptacles have been shown to protect a wider range of users by reducing the blast radius of bombs. There were, however, difficulties with this application like building a live model for simulation, which is required by the receptacle to maximize performance. Also, due to the restrictions of current blast simulations, the effects of a blast within the trash can not be modeled with great accuracy due to the curved geometry of the surface. All simulations done by EDC ’04 teams at Northwestern analyzing the performance of austenitic TRIP 120 steels in case of trash receptacle applications are based on the dimensions of the cylindrical can, modeled as a flat wall. Using the weight (825

lbs) and dimensions (36 gallon capacity, 32" height, 3/8" thick face plates) of a steel trash receptacle designed to withstand blast conditions, a constant weight performance comparison was generated for the proposed folded plate design and square honeycomb design presently employed and it was found that the TRIP 120 steel outperforms the currently used material BMCS M10 by 3 times in terms of impulse absorbed, and the cost of TRIP 120 is only $1/10^{th}$ that of BMCS M10 [C2].

References:

[C1] McCarren M, Chardon M, Chuu K, Forbes T, Fruth S, Haro E, Kuou D, Lee C. *BlasTruss: Civil Shield Technologies*. *IDEA 398, March 2004, Northwestern University*

[C2] L. Abrahamson, D. Becker, S. Bernaz and T. Forbes, IDEA 298/398 Interdisciplinary Design, *Civil Shield Technologies, 2005, Northwestern University*

[C3] D. Schulte, *BlastTruss: Civil Shield Technologies.* IDEA 398 Final Reports, Sep. 2004, Northwestern University

[C4] S. Cho, A. Dai, J. Kim and N. Sethi, "*Design of TRIP 120 Saferoom*", EDC, spring 2007, Northwestern University.